

https://dspace.org/

Fine structure of the Isovector Giant Dipole Resonance: a survey with the (p,p') reaction at zero degrees

Jingo, Maxwell

2014-08-05
http://hdl.handle.net/10539/15122

Downloaded from a DSpace repository. https://dspace.org/

Fine structure of the Isovector Giant Dipole Resonance: A survey with the (p,p′) reaction at zero degrees

Maxwell Jingo

A thesis submitted to the Faculty of Science,
University of the Witwatersrand, Johannesburg, in fulfilment of the
requirements for the degree of
Doctor of Philosophy

Johannesburg, 2014

Declaration

I, the undersigned, hereby declare that the work contained in this thesis is my own original work. It is being submitted for the Degree of Doctor of Philosophy in the University of the Witwatersrand, Johannesburg. It has not previously in its entirety or in part been submitted for any degree or examination in any other University.

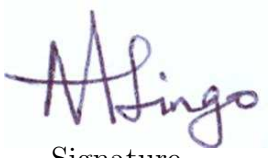

Signature Date: 26 May 2014

Abstract

This investigation involves a survey of the fine structure phenomenon of the Isovector Giant Dipole Resonance (IVGDR) over a wide mass range of nuclei, from ^{27}Al, ^{40}Ca, ^{56}Fe, ^{58}Ni to ^{208}Pb, using inelastic proton scattering at 200 MeV. Proton detection is accomplished using the recently commissioned zero-degree facility of the K600 magnetic spectrometer at iThemba LABS. Inelastic proton experiments at zero degrees are very selective to excitations with low angular momentum transfer, and therefore ideal for studies of the IVGDR. This is because such experiments simplify the analysis of the many contributions to the spectra due to the complex nature of the nuclear interaction. The ability to make precise measurements of the properties of the IVGDR demonstrated by this work opens up new challenges to both experimental and theoretical work in nuclear structure. This is a survey of the (p,p$'$) reaction at zero degrees as a probe to study properties of the GDR and also the low energy $E1$ strength with high energy-resolution. Such a data base will provide more stringent tests of nuclear theory and the progress is seen in the details obtained. These tests can only be described by microscopic models including complex degrees-of-freedom. This should lead to new insights into the underlying interactions responsible for the nature of the electric dipole strength in nuclei.

In the present study, double-differential cross-sections were converted to equivalent photo-absorption cross-sections and their results compared to previously published photo-absorption data. An excellent correspondence in the excitation-energy region of the Giant Dipole Resonance (GDR) was noticed between the two data sets.

The fine structure observed can be described using characteristic energy scales, arising mainly from Landau damping (even though the spreading width may also play a role). The extraction of these characteristic energy scales which are a signature for the decay process was achieved through the use of wavelet analysis. Furthermore, thanks to the recent advances in computational power and techniques, microscopic shell model-based calculations lead to new insights into the underlying properties of the nuclear interaction which are responsible for the collective behaviour evidenced by the existence and properties of the IVGDR.

In addition to the extraction of characteristic energy scales, this study also provides level densities of $J^{\pi} = 1^{-}$ states. In order to extract nuclear level densities, there is need to eliminate instrumental background and other contributions to the spectra from (p,p$'$) scattering using the model-independent Discrete Wavelet Transform (DWT) method. Level densities of $J^{\pi} = 1^{-}$ states are determined using the fluctuation analysis technique and comparisons are made with the phenomenological Back Shifted Fermi Gas (BSFG) model predictions, calculations of the Hartree Fock-Bogoluibov (HFB) microscopic model and Hartree Fock-Bardeen-Cooper-Schrieffer (HF-BCS) predictions. Finally, this survey will simultaneously provide bench-marks on the capabilities and limitations of the new zero-degree facility important for planning of the future experimental work.

This work is dedicated to Praise Jingo and Nicole Rutendo Jingo.

Acknowledgements

The work presented in this thesis resulted from the efforts of many people. I would like to take this opportunity to thank all of you to whom I am greatly indebted.

I would like to express my sincere gratitude to my two university supervisors, namely Prof. J. M. Carter and Prof. E. Sideras-Haddad, who have guided me through the past six years since I began my research career. They have continuously encouraged, advised, and supported me in all the aspects of the present work. I have learned from them not only skillful experimental techniques but also the necessary attitudes to solve scientific problems.

I am deeply grateful to my co-supervisor (iThemba LABS, Cape Town), Dr. R. Neveling for his guidance and encouragement throughout the present work. Especially, he spent a lot of time discussing with me the DATA extraction and analysis procedures. He also gave me many chances to discuss with great scientists in the world.

Dr. I. Usman, who has been a good role model. I appreciate the helpful discussions with her on this present work.

I address my thanks to the collaborators from Research Centre for Nuclear Physics (RCNP), Japan namely Dr. H. Fujita, Prof. Y. Fujita and Prof. A. Tamii, who provided innovative ideas, skill and welcomed work during the fruitful collaboration

period.

I gratefully acknowledge the outstanding contribution of the Germany team from the Technische Universität Darmstadt: Prof. A. Richter, Prof. P. von Neumann-Cosel, Dr. V. Yu. Ponomarev, Dr. I. Poltoratska, Anna-Maria Heilmann and Andreas Krugmann towards achieving valuable theoretical calculations and participation in the experimental shifts at iThemba LABS.

Drs. S. Förtsch, F. Smit and Z. Buthelezi for making sure that all the experimental problems are solved and striving for background-free data.

Yvonne Kheswa, our wonderful target marker, for making beautiful targets.

Dr. R. Newman, our Head of the Department of Nuclear Physics at iThemba LABS, who never failed to cheer me up with his humorous and good natured approach to life.

Dr. J. L. Conradie (The Beam-Bender) and the entire accelerator team, who set up the accelerator and fine tuned the beam as no else can. *Thanks for providing us with good proton beams during the experimental weekends.*

Ackowledgement also goes to Prof. João Rodrigues, the former Head of the School of Physics, WITS, for his contributions towards the achievement of my goals.

I would like to thank all the staff of the School of Physics, WITS, for making life easy for me as an international student, "*Ndinotenda*".

To Mosebetsi Leotlela, I salute you "*ntate*", Thanks for being so kind, I really enjoyed the "*Wimpy lunches*" we shared together.

My fellow iThemba LABS postgraduate students: Innocent Mayida, Dr Joel Mira, Siyabonga Majola and Dr Justin Mabiala. Thank you for your co-operation and contributions in one way or the other towards the success of this work. Special thanks also go to iThemba LABS (Gauteng) staff namely: Ms Daisy Mahlare, Ms Doris Monyamane, Ms Ntombifuthi Radebe, Dr Morgan Madhuku, Mr Motau Maloma and Mr Kamela Sekonya.

I would like to warmly thank my good friend Chamunorwa Oscar Kureba to whom I am deeply grateful for all his expert help, hard work, enthusiasm and for his commitement in the entire project, from the earliest experiment to the finished thesis, and for always being ready to support and discuss any subject. *thanks baba, basa raitwa iri* !!!.

This work was supported in part by iThemba LABS through Top-up grants and Wits University through the Postgraduate Merit Award bursaries. *Thank you.*

I spent six years as a member of the experimental nuclear structure group at Wits University and iThemba LABS. I enjoyed research activities, discussions, recreations and other things in a pleasant and comfortable atmosphere. I am grateful to all my colleagues and friends.

I would like to express my great thanks to my parents (Mr and Mrs P. Jingo), brothers (Francis Jingo, Fortune Jingo and Farai Jingo), sister (Rebecca Jingo), and uncle (Piniel Chiduwa) for their continuous encouragements, patience and support.

Finally, I would like to address my heartfelt acknowledgment to the following most precious people: Brender Nyoni, Praise Jingo and Nicole Rutendo Jingo for their continuous, unwavering and unconditional support throughout these trying years.

Ngiyabonga kakhulu. Inkosi ibusise.

My motivational statement:

"*Each of us is born into genius. Sadly, most of us die amid mediocrity.*" So why is it that we never reach our "full potential"; why do we believe that we don't make a contribution; why do we believe that we have to have a "title" to lead?
Statement by Robin Sharma.

Contents

Titlepage **i**

Declaration **ii**

Abstract **iv**

Acknowledgements **ix**

List of Figures **xiv**

List of Tables **xxv**

List of Figures **xxvi**

List of Tables **xxvi**

1 Introduction **1**

1.1 Historical background 1

1.2 Fine structure 5

1.3 Modern theoretical models 6

1.4 Level densities 8

1.5 This study 8

2 Theoretical considerations **12**

2.1 Classification of giant-resonance modes 13

2.1.1 Macroscopic picture 13

2.1.2 Microscopic picture 14
2.2 Damping of giant resonances 16
2.2.1 Doorway-state picture of giant resonances 16
2.3 Scattering formalism 19
2.3.1 Distorted waves and optical potential 22
2.4 Charged-particle induced reactions 24
2.4.1 Rutherford approach 25
2.4.2 Coulomb excitation 27
2.4.3 Fermi's method 28
2.4.4 Weizsäcker-Williams method 31
2.5 Microscopic models for the calculation of dipole strength distributions 35
2.5.1 Quasi-particle Phonon Model (QPM) 36
2.5.2 Equation of Motion Phonon Method (EMPM) 44
2.6 Extraction of characteristic energy scales 49
2.6.1 Fourier Transform 49
2.6.1.1 Discrete Fourier Transform 50
2.6.1.2 Power spectrum 50
2.6.2 Wavelet transform analysis 51
2.6.2.1 Some advantages of the Wavelet Transform Theory . 51
2.6.2.2 Theory of wavelet analysis 51
2.6.2.3 Continuous Wavelet Transform (CWT) 53
2.6.2.4 Discrete Wavelet Transform (DWT) 55
2.7 Extraction of level densities 56
2.7.1 Level density models 58
2.7.1.1 Back-Shifted Fermi Gas (BSFG) model 60
2.7.1.2 Hartree-Fock-Bogoliubov (HFB) model 62
2.7.2 Fluctuation analysis 63
2.7.2.1 Conditions of applicability 63
2.7.2.2 Methodology 65

3 Experimental equipment, techniques and procedures 68

3.1 The iThemba LABS accelerator complex 70

3.1.1 The second solid-pole injector cyclotron (SPC2): K = 8 MeV 72

3.1.2 The separated-sector cyclotron (SSC): K = 200 MeV 72

3.1.3 General beam setup 74

3.2 K600 magnetic spectrometer 74

3.3 Focal plane detector system 77

3.4 Data acquisition system and electronics 80

3.5 Dispersion matching 81

3.5.1 Faint beam technique 84

3.6 Experimental procedure 85

3.6.1 Targets 85

3.6.2 K600 fields 89

3.6.3 Beam viewers 90

3.6.4 White tune 90

3.6.5 Zero degree beam optimisation 90

3.7 Data extraction 94

3.7.1 Methods of particle identification 95

3.7.2 VDC operation 100

3.7.2.1 Look Up Table (LUT) 100

3.7.3 Position resolution 102

3.7.4 VDC efficiency 104

3.7.5 Background subtraction procedure 105

3.7.6 Horizontal angle calibration 106

3.7.7 Lineshape correction 109

3.7.8 Energy calibration 110

3.8 Experimental cross-sections 114

3.8.1 Error analysis . . . 115
3.8.1.1 Statistical errors . . . 115
3.8.1.2 Systematic errors . . . 116

4 Results, analysis and discussion **117**

4.1 Introduction . . . 117
4.2 Overview of the measured experimental data . . . 118
4.3 Background subtraction in the region of the isovector giant dipole resonance . . . 121
4.4 Photo-excitation and decay of the IVGDR . . . 124
4.4.1 Equivalent photon method . . . 126
4.5 QPM $E1$ strength function for ^{208}Pb, ^{58}Ni, ^{56}Fe and ^{40}Ca . . . 131
4.5.1 $E1$ response: experiment *versus* theory . . . 133
4.6 Characteristic energy scales: experimental *versus* theoretical . . . 138
4.6.1 RPA discussion . . . 146
4.7 Extraction of the level densities . . . 149
4.7.1 Fluctuation analysis technique . . . 149
4.7.2 DWT decomposition and background determination . . . 150
4.7.3 Extraction of 1^- level densities . . . 151
4.7.4 Discussion of extracted $J^\pi = 1^-$ states . . . 155

5 Conclusion **161**

References **164**

List of Figures

2.1 Schematic representation of various collective modes taken from Ref. [Ito05]. 14

2.2 Schematic picture of $E1$ and $E2$ single-particle transitions between shell-model states in ^{90}Zr [She04]. Proton (red arrows with open cicles) and neutron (green arrows with open circles) $1p$-$1h$ transitions from and to corresponding energy levels below and above the Fermi level ε_{F}, which contribute coherently to a given collective mode, are shown. 15

2.3 Schematic representation of the width of the collective $1p$-$1h$ state into a direct component $\Gamma^{\uparrow}$ and a spreading component $\Gamma^{\downarrow}$ of a giant resonance [Har01]. 17

2.4 Damping of giant resonances. A hierarchy of lifetimes and energy scales in the decay of giant resonances as a result of different processes [She05]. 18

2.5 Angular distributions for DWBA07 inelastic proton scattering on ^{58}Ni for GDR, GQR, $M1$ resonance, $M2$ resonance and Low energy Octupole resonance (LEOR) at $E_{\mathrm{p}} = 200$ MeV. There are also results for the 2^{+}_{1} and 3^{-}_{1} states. 25

2.6 Schematic view of the momentum change. Trajectories are symmetric with respect to angle ϕ. 26

2.7 Schematic view of the geometry of heavy-ion-induced electromagnetic excitation. 29
2.8 Equivalent photon number per unit projectile charge, for $E1$ radiation, and as a function of the dimensionless quantity ωR/c. The ratio of the projectile energy to its rest energy is given by γ ($c = 1$). 36
2.9 Illustration of the principles of wavelet analysis and wavelet families. Real (k= 5, see Eq. (2.114)) and complex Morlet (f_c = 1, f_b = 1, see Eq. (2.115)) wavelets are the products of cosine and Gaussian functions. The real and the imaginary parts of the complex Morlet are shown in solid and dashed lines respectively. The Biorthogonal 6.8 wavelet has an antisymmetrical shape but no analytical expression. 53
2.10 Decomposition of the original signal $\sigma(E)$ into approximations and details obtained by using the discrete wavelet transform. 57

3.1 A schematic overview of the cyclotron facility at iThemba LABS. . . 71
3.2 A schematic overview of the SPC2 cyclotron. 73
3.3 The resonance lines of importance for a 200 MeV proton beam in the SSC [Con92]. 73
3.4 The K600 magnetic spectrometer at iThemba LABS shown here in the zero degree mode. 75
3.5 A schematic diagram of the K600 focal plane detector system. 79
3.6 A schematic diagram of the K600 trigger electronics. 82
3.7 Schematic ion trajectories under achromatic (left) and lateral dispersion matching (right) conditions. 85
3.8 *Top panel*: A two-dimensional histogram of the faint beam showing the horizontal scattering angle against the horizontal focal plane position before optimisation. *Bottom panel*: A one-dimensional projection illustrating the horizontal focal plane position of the faint beam (FWHM = 65 keV). 86

3.9 *Top panel*: An improved two-dimensional histogram of the faint beam showing the horizontal scattering angle against the horizontal focal plane position after optimisation. *Bottom panel*: A one-dimensional projection illustrating the horizontal focal plane position of the faint beam (FWHM = 29 keV). 87

3.10 The wire-mesh viewer shown in the in-beam position. The viewer is positioned 45° with respect to the beam. The beam direction is from left to right. Each small square represents 1 mm^2. 91

3.11 The target viewer shown in the in-beam position. 91

3.12 The zero degree viewer shown in the in-beam position. The viewer is positioned 45° with respect to the beam. The beam can be seen as the faint parallelogram in the center. 92

3.13 TRACK ray-tracing results for elastically scattered protons (for E_{p} = 200 MeV) with an angular acceptance of ± 1.91° for the two dipole ratios R = 1.33 and R = 1.49. One should note that in the case of R = 1.33, the two rays shown outside of the focal-plane vacuum chamber represent particles that will re-scatter from the dipole D2 exit flange and vacuum chamber wall. 94

3.14 *Top panel*: A two-dimensional histogram showing the locus of the pulse height of the first scintillator *versus* TOF caused by beam halo. *Bottom panel*: A two-dimensional histogram illustrating the pulse height of the first scintillator *versus* TOF for the ^{56}Fe target. The right locus represents beam halo events, and the left locus represents the protons scattered from the target. 97

3.15 *Top panel*: A two-dimensional histogram of TOF *versus* the horizontal focal position (x_{fp}) showing loci for the inelastically scattered protons (gated part) and beam halo (ungated part). *Bottom panel*: A two-dimensional histogram of the pulse height of the first scintillator *versus* TOF for events selected by the gated region in the top panel. . 98

3.16 *Top panel*: First scintillator pulse height *versus* second scintillator pulse height for all events, without any cut. *Bottom panel*: A typical two-dimensional particle identification (PID) plot that is obtained after applying both the TOF *versus* horizontal focal plane position ($x_{\rm fp}$) and first scintillator pulse height *versus* TOF cuts. 99

3.17 *Top panel*: An example of a one-dimensional histogram showing good drift length characteristics for all the wires of the horizontal focal plane position ($x_{\rm fp}$) wireplane. *Bottom panel*: A two dimensional spectrum that can be obtained for a good LUT and valid VDC events. 101

3.18 Schematic representation of a trajectory associated with a charged particle intersecting the VDC resulting in a six-wire event [New96]. . 104

3.19 *Top panel*: A two-dimensional scatterplot in which the central region represents both physics and background events whereas the two outer Δy sections represent only background events. *Right panel*: Projection of the events onto $y_{\rm fp}$. *Bottom panel*: The red spectrum represents the background of the upper Δy section and the green spectrum represents the background of the lower Δy section as indicated in the top panel. The black spectrum represents the focal plane position spectrum for all selected events in the central Δy region. The blue spectrum represents the background that results from the sum of the two outer Δy sections. 107

3.20 The resultant background subtracted spectrum after subtracting the blue spectrum from the black spectrum as shown in Fig. 3.19. 107

3.21 The pepper-pot collimator. This collimator has the following properties: its first hole from the middle on the x-axis/y-axis is at 0.819° (14.3 mrad), the second is at 1.679° (29.3 mrad) and the third is at 2.251° (39.3 mrad). The holes span 0.41° (7.15 mrad), except for the smaller hole which spans $\sim$ 0.20° (3.57 mrad). The smaller hole, achieved by adding an insert, is not shown. 108

3.22 Focal plane angle ($\theta_{\rm fp}$) pepperpot spectrum with Gaussian fitted on the observed peaks. 108

3.23 *Top panel*: Two-dimensional histogram of $\theta_{\rm scat}$ *versus* $x_{\rm fp}$ for $^{\rm nat}$Ca without lineshape correction. *Bottom panel*: Corresponding horizontal focal position ($x_{\rm fp}$) spectrum before lineshape correction. 111

3.24 *Top panel*: Two-dimensional histogram of $\theta_{\rm scat}$ *versus* $x_{\rm fp}$ for $^{\rm nat}$Ca with lineshape correction. The abberations of $x_{\rm fp}$ for the $\theta_{\rm scat}$ are corrected by software and the excited state has been straightened. *Bottom panel*: Corresponding horizontal focal plane position spectrum after lineshape correction. 112

3.25 Momentum calibration curve for the K600 focal plane Weekend 3. . . 113

4.1 Experimentally measured excitation-energy spectra for ^{208}Pb(p,p′), ^{58}Ni(p,p′), ^{56}Fe(p,p′), $^{\rm nat}$Ca(p,p′) and ^{27}Al(p,p′) at $E_{\rm p}$ = 200 MeV and small scattering angles, $\theta_{\rm Lab} = 0^\circ - 1.91^\circ$. 119

4.2 Experimental double-differential cross-sections for ^{208}Pb(p,p′), ^{58}Ni(p,p′), ^{56}Fe(p,p′), ^{40}Ca(p,p′) and ^{27}Al(p,p′) at $E_{\rm p} = 200$ MeV and small scattering angles, $\theta_{\rm Lab} = 0^\circ - 1.91^\circ$. 120

4.3 Estimated contributions to the excitation-energy spectrum of ^{208}Pb in the GDR region by $E2$ cross-sections and a phenomenological background. **Colour:** The green dash-dotted curve corresponds to the $E2$ contribution, while the blue dashed one shows the phenomenological background. The red continuous curve illustrates the sum of these contributions. 122

4.4 Estimated contributions to the excitation-energy spectrum of ^{58}Ni in the GDR region by $E2$ cross-sections and a phenomenological background. Here the 10.660 MeV magnetic dipole ($M1$) state also reported in Ref. [Fuj07] is very prominent. 122

4.5 Estimated contributions to the excitation-energy spectrum of ^{56}Fe in the GDR region by $E2$ cross-sections and a phenomenological background. Candidates of $M1$ states are indicated by vertical arrows [Nag10]. 123

4.6 Estimated contributions to the excitation-energy spectrum of ^{nat}Ca in the GDR region by $E2$ cross-sections and a phenomenological background. Here the well-known 10.3188 MeV $M1$ state in ^{40}Ca reported in [Ana81], the 0^+ state at 9.304 MeV and 1^+ state at 9.83 MeV in ^{40}Ca are indicated also. 123

4.7 Estimated contributions to the excitation-energy spectrum of ^{27}Al in the GDR region by $E2$ cross-sections and a phenomenological background. 124

4.8 *Top panel*: Total number of virtual photons for the $E1$ multipolarity, created by a proton passing by a lead target at impact parameters $b_{\text{min}} = 12.3$ fm and larger (i.e. integrated over impact parameters), for three typical bombarding energies [Ber09]. *Bottom panel*: Total number of virtual photons for the $E1$ multipolarity, as created by a proton passing by the experimental targets at an incident energy of $E_{\text{p}} = 200$ MeV (see text). 125

4.9 *Top panel*: Total photo-absorption cross-sections for the previous ^{208}Pb nucleus in the GDR region. The red circles denote σ_{abs} obtained in the work at $E_{\text{p}} = 295$ MeV [Pol11], green squares represent the (γ,all) data from [Sch88] and black histogram represents the (γ,xn) data from [Vey70, Bel82]. *Bottom panel*: The blue histogram denotes the total photo-absorption cross-section ($\sigma(\text{p}, \text{p}'_{\gamma\text{corr}})$) obtained in the present work at $E_{\text{p}} = 200$ MeV, green squares represent the σ(γ,ABS) data from [Var03], and black histogram represents the σ(γ,xn) data from [Vey70, Bel82]. 128

4.10 The blue histogram denotes the total photo-absorption cross-section ($\sigma(\mathrm{p}, \mathrm{p}'_{\gamma\mathrm{corr}})$) obtained in the present work at E_p = 200 MeV, green squares represent the $\sigma(\gamma$,ABS) data from [Ish02a], red circles denote $\sigma(\gamma$,n) from [Ful74] and black triangles represent $\sigma(\gamma$,p) data from [Ish70]. 129

4.11 The blue histogram denotes the total photo-absorption cross-section ($\sigma(\mathrm{p}, \mathrm{p}'_{\gamma\mathrm{corr}})$) obtained in the present work at E_p = 200 MeV, red circles denote $\sigma(\gamma$,n) from [Bor00] and black triangles represent $\sigma(\gamma$,p) from [Bor00]. 129

4.12 The blue histogram denotes the total photo-absorption cross-section ($\sigma(\mathrm{p}, \mathrm{p}'_{\gamma\mathrm{corr}})$) obtained in the present work at E_p = 200 MeV, green squares represent the $\sigma(\gamma$,ABS) data from [Ero03], red circles denote $\sigma(\gamma$,n) from [Gor67a] and black triangles represent $\sigma(\gamma$,p) from [Gor67b]. 130

4.13 The blue histogram denotes the total photo-absorption cross-section ($\sigma(\mathrm{p}, \mathrm{p}'_{\gamma\mathrm{corr}})$) obtained in the present work at E_p = 200 MeV, green squares represent the $\sigma(\gamma$,ABS) data from [Ahr75], red circles denote $\sigma(\gamma$,n) from [Vey74] and black triangles represent $\sigma(\gamma$,p) from [Sho62]. 130

4.14 QPM $E1$ strength distributions for the target nuclei after being folded with the corresponding experimental energy-resolutions. 132

4.15 *Top panel*: $E1$ response in experimental ^{208}Pb(p,p$'$) spectrum between 8 MeV and 21 MeV. *Middle panel*: $E1$ response in $^{208}\mathrm{Pb}(\mathrm{p},\mathrm{p}'_{\gamma\mathrm{corr}})$ spectrum between 8 MeV and 21 MeV. *Bottom panel*: QPM theoretical calculations for ^{208}Pb nucleus. 134

4.16 *Top panel*: $E1$ response in experimental ^{58}Ni(p,p$'$) spectrum between 8 MeV and 25 MeV. *Middle panel*: $E1$ response in $^{58}\mathrm{Ni}(\mathrm{p},\mathrm{p}'_{\gamma\mathrm{corr}})$ spectrum between 8 MeV and 25 MeV. *Bottom panel*: QPM theoretical calculations for ^{58}Ni nucleus. 135

4.17 *Top panel*: $E1$ response in experimental ^{56}Fe(p,p$'$) spectrum between 8 MeV and 25 MeV. *Middle panel*: $E1$ response in ^{56}Fe(p,p$'_{\gamma\mathrm{corr}}$) spectrum between 8 MeV and 25 MeV. *Bottom panel*: QPM theoretical calculations for ^{56}Fe nucleus. 136

4.18 *Top panel*: $E1$ response in experimental ^{40}Ca(p,p$'$) spectrum between 8 MeV and 25 MeV. *Middle panel*: $E1$ response in ^{40}Ca(p,p$'_{\gamma\mathrm{corr}}$) spectrum between 8 MeV and 25 MeV. *Bottom panel*: QPM theoretical calculations for ^{40}Ca nucleus. 137

4.19 *Top panel*: CWT analysis of the IVGDR strength distribution from QPM calculations of ^{208}Pb. The power spectrum on the left represents the region $12 \leq E_{\mathrm{x}} \leq 15.5$ MeV. *Bottom panel*: CWT analysis of the excitation-energy spectrum of the ^{208}Pb(p,p$'_{\gamma\mathrm{corr}}$). The power spectrum on the left corresponds to the IVGDR measured and the same region is used in the top part of the figure. **Colour**: The green line in the power spectrum indicates the same characteristic energy scales shown by the blue line but only that they been scaled up by a certain enhancement factor to make them visible and the same applies for all the other nuclei. It should be noted that the scales for the total widths of the GDRs in the table 4.2 are not shown in the other plotted figures except for ^{208}Pb because the scale axis is limited to 5 MeV for better visibility of low-lying wavelet coefficients. 140

4.20 *Top panel*: CWT analysis of the IVGDR strength distribution from QPM calculations of ^{58}Ni. The power spectrum on the left represents the region $14 \leq E_{\mathrm{x}} \leq 24$ MeV. *Bottom panel*: CWT analysis of the excitation-energy spectrum of the ^{58}Ni(p,p$'_{\gamma\mathrm{corr}}$). The power spectrum on the left corresponds to the IVGDR measured and the same region is used in the top part of the figure. 141

4.21 *Top panel*: CWT analysis of the IVGDR strength distribution from QPM calculations of ^{56}Fe. The power spectrum on the left represents the region $14 \leq E_{\mathrm{x}} \leq 24$ MeV. *Bottom panel*: CWT analysis of the excitation-energy spectrum of the ^{56}Fe(p,p$'_{\gamma\mathrm{corr}}$). The power spectrum on the left corresponds to the IVGDR measured and the same region is used in the top part of the figure. 142

4.22 *Top panel*: CWT analysis of the IVGDR strength distribution from QPM calculations of ^{40}Ca. The power spectrum on the left represents the region $14 \leq E_{\mathrm{x}} \leq 24$ MeV. *Bottom panel*: CWT analysis of the excitation-energy spectrum of the ^{40}Ca(p,p$'_{\gamma\mathrm{corr}}$). The power spectrum on the left corresponds to the IVGDR measured and the same region is used in the top part of the figure. 143

4.23 CWT analysis of the excitation-energy spectrum of the ^{27}Al(p,p$'_{\gamma\mathrm{corr}}$). The power spectrum on the left represents the region $14 \leq E_{\mathrm{x}} \leq 24$ MeV. 144

4.24 *Top panel*: CWT analysis of the IVGDR strength distribution from EMPM calculations of ^{208}Pb. The power spectrum on the left represents the region $9 \leq E_{\mathrm{x}} \leq 13$ MeV. *Bottom panel*: CWT analysis of the IVGDR strength distribution from QPM calculations of ^{208}Pb. The power spectrum on the left corresponds to the IVGDR measured and the same region is used in the top part of the figure. 145

4.25 ^{208}Pb equivalent photo-absorption spectrum together with the power spectrum from the CWT analysis in comparison with QPM and RPA predictions. 147

4.26 ^{58}Ni equivalent photo-absorption spectrum together with the power spectrum from the CWT analysis in comparison with QPM and RPA predictions. 147

4.27 ^{56}Fe equivalent photo-absorption spectrum together with the power spectrum from the CWT analysis in comparison with QPM and RPA predictions. 148
4.28 ^{40}Ca equivalent photo-absorption spectrum together with the power spectrum from the CWT analysis in comparison with QPM and RPA predictions. 148
4.29 Decomposition of the ^{208}Pb(p,p′) excitation-energy spectrum with the DWT analysis into approximations A_i and details D_i. The approximation $A9$ describes the total width of the GDR, thus $A10$ can be adopted as background shape. 152
4.30 From top to bottom: Experimental ^{208}Pb(p,p′) excitation-energy spectrum including background obtained with the use of discrete wavelet transform, smoothed spectra g(E_x) and g$_>$(E_x), stationary fluctuating spectrum $d(E_x)$ obtained by dividing the two smoothed spectra, autocorrelation functions from experimental (purple solid line). 153
4.31 Excitation-energy spectrum of ^{208}Pb(p,p′) reaction at 0° before subtracting DWT (A10) background. 157
4.32 Comparison of the experimentally obtained level densities of 1^- states in ^{208}Pb in the energy range from 8 to 17 MeV with predictions from BSFG using the model of [Rau97] (red solid line) or from [Egi05] (green dashed line), HF-BCS [Dem01] (blue dotted line) and HFB [Hil06] (orange dash-dotted line). 157
4.33 Excitation-energy spectrum of ^{58}Ni(p,p′) reaction at 0° before subtracting DWT (A10) background. 158
4.34 Comparison of the experimentally obtained level densities of 1^- states in ^{58}Ni in the energy range from 12 to 20 MeV with predictions from BSFG using the model of [Rau97] (red solid line) or from [Egi05] (green dashed line), HF-BCS [Dem01] (blue dotted line) and HFB [Hil06] (orange dash-dotted line). 158

4.35 Excitation-energy spectrum of ^{56}Fe(p,p′) reaction at 0° before subtracting DWT (A10) background. 159
4.36 Comparison of the experimentally obtained level densities of 1^- states in ^{56}Fe in the energy range from 8 to 20 MeV with predictions from BSFG using the model of [Rau97] (red solid line) or from [Egi05] (green dashed line), HF-BCS [Dem01] (blue dotted line) and HFB [Hil06] (orange dash-dotted line). 159
4.37 Excitation-energy spectrum of ^{40}Ca(p,p′) reaction at 0° before subtracting DWT (A10) background. 160
4.38 Comparison of the experimentally obtained level densities of 1^- states in ^{40}Ca in the energy range from 12 to 20 MeV with predictions from BSFG using the model of [Rau97] (red solid line) or from [Egi05] (green dashed line), HF-BCS [Dem01] (blue dotted line) and HFB [Hil06] (orange dash-dotted line). 160

List of Tables

2.1 Multipole excitations as particle-hole excitations across major shells [Har01]. 16

3.1 General technical specifications of the K600 magnetic spectrometer. . 76

3.2 Ion optical properties of the high dispersion focal plane of the K600 magnetic spectrometer for a dipole field ratio of 1.49. 76

3.3 Technical specifications of the new UX Vertical Drift Chamber. . . . 78

3.4 Technical specifications of the focal plane scintillators. 78

3.5 A summary of the targets used during the present experiment. 88

3.6 Momentum calibration curves for the 3 different weekends. 113

4.1 Neutron and proton thresholds for the 5 target nuclei. 118

4.2 Characteristic energy scales of the GDR in ^{208}Pb, ^{58}Ni, ^{56}Fe, ^{40}Ca and ^{27}Al extracted from the wavelet analysis of equivalent photo-absorption results and QPM calculations. Bold energy scales represent identical scales between "theory" and "experiment", energy scales with horizontal lines over them represent clearly identifiable scales (e.g. $\overline{abc}$), weak scales are not in bold and have no horizontal lines and finally, the energy scales representing the total widths of GDRs are shown in green colour with horizontal lines under them (e.g. $\underline{\text{abc}}$). 144

4.3 List of parameters utilised in the level density extraction of $J^\pi = 1^-$ states. 152

List of Abbreviations

- $1p$-$1h$: One particle One hole
- $\sigma(\gamma$,ABS): Total photo-absorption cross-section
- BLM: Bergoz Beam Loss Monitors
- BSFG: Back Shifted Fermi Gas model
- CWT: Continuous Wavelet Transform
- DAQ: Data Acquisition System
- DFT: Discrete Fourier Transform
- DWBA: Distorted Wave Born Approximation
- DWT: Discrete Wavelet Transform
- ECR: Electron Cyclotron Resonance
- EM : Electromagnetic radiation
- EMPM: Equation of Motion Phonon Method
- ETDHF: Extended Time Dependent Hartree-Fock
- ETFFS: Extended Theory of Finite Fermi Systems
- EWSR: Energy-Weighted Sum Rule
- FFT: Fast Fourier Transform

- FWHM: Full width-at-half-maximum
- GDR: Giant Dipole resonance
- GMR: Giant Monopole Resonance
- GT mode: Gamow-Teller mode
- GT model: Goldhaber and Teller model
- HFB: Hartree Fock-Bogoliubov
- HF-BCS: Hartree Fock-Bardeen-Cooper-Schrieffer
- ISGQR: Isoscalar Giant quadrupole resonance
- IVGDR: Isovector Giant Dipole Resonance
- IVGQR: Isovector Giant Quadrupole Resonance
- IUCF: Indiana University Cyclotron Facility
- KVI: Kernfysisch Versneller Instituut
- LABS: Laboratory for Accelerator Based Sciences
- LUT: Look Up Table
- MIDAS: Maximum Integration Data Acquisition System
- NAC: National Accelerator Centre
- PMT: Photo-multiplier Tube
- QDC: Charge-to-Digital Converter
- QDD: Quadrupole Dipole Dipole
- QPM: Quasi-particle Phonon Model
- RCNP: Research Centre for Nuclear Physics

- RMT: Random Matrix Theory
- RPA: Random Phase Approximation
- SMMC: Shell-Model Monte Carlo calculations
- SRPA: Second Random Phase Approximation
- SPC: Solid Pole injector Cyclotron
- SSC: Seperated Sector Cyclotron
- SJ model: Steinwedel and Jensen model
- TDA: Tamm-Dancoff Approximation
- TDC: Time-to-Digital Converter
- TOF: Time-of-Flight
- TRK: Thomas-Reiche-Kuhn
- VDC: Vertical Drift Chamber
- VME: Versa Modula Europa

Chapter 1

Introduction

Nuclear giant resonances are known to be small-amplitude, high-frequency, simple collective modes of excitations. They have very high vibrational frequencies in the range 2 – $10{\cdot}10^{21}$ Hz and are considered to be the fastest vibrations of any known many-body system. In quantum-mechanical terms, the resonance corresponds to a transition between the ground state and a collective state and its strength is described by a transition amplitude. The vibrations are classified by a change in quantum numbers with respect to the ground state such as angular momentum (ΔL), spin (ΔS), isospin (ΔT) and parity.

1.1 Historical background

The study of giant resonances has been and still is a major topic of research in nuclear physics. Giant resonances in nuclei were first discovered in 1937 by Bothe and Gentner [Bot37], who observed evidence of nuclear vibrations in the measurements of photon absorption from the bombardment of several nuclei with γ-radiation produced in the Li(p,γ) reaction. The measured cross-sections from the various nuclei were at times several orders of magnitude larger than those predicted by the avail-

able theoretical calculations. In 1944, the idea of a dipole oscillation of the nucleus was theoretically predicted by Migdal [Mig44].

This was followed in 1947 by observations of a giant resonance phenomenon made by Baldwin and Klaiber [Bal47]. They measured the photo-fission cross-section in uranium and thorium and observed that the photo-absorption cross-section shows a broad peak near $E_\gamma = 18$ MeV. A scan of most nuclei revealed that the photo-absorption cross-section was dominated by a peak, roughly 5 MeV wide, located anywhere between the photo-disintegration threshold and 30 MeV, and was referred to as the Giant Dipole Resonance (GDR) of the nuclear photo-effect [Ful62]. In 1948, Goldhaber and Teller [Gol48] interpreted the resonance peaks as the Isovector Giant Dipole Resonance (IVGDR) using an early version of the theoretical description known as the Hydro-dynamical model.

An Isovector Giant Dipole Resonance (IVGDR) is described as an electric resonance, typically observed in the nuclear excitation-energy region of 10 to 25 MeV. Electric dipole transitions are populated by the collective motion of the nucleons at these high energies, hence the moving charges lead to dipole oscillations. Note that we distinguish between dipole oscillations and a static dipole field, where the former creates an electric field that will emit electromagnetic radiation while the latter creates an electric field but no emission of electromagnetic (EM) radiation takes place. In the Goldhaber and Teller model (GT model), the oscillation was considered to be due to incompressible, rigid proton and neutron spheres vibrating against each other, with the restoring force being proportional to the surface-symmetry energy in the extended nuclear mass formula of Myers and Swiatecki [Mye74]. In such a case, where the restoring force is proportional to the surface energy, the excitation energy of the GDR is found to be proportional to $A^{-1/6}$, where A is the mass number of the nucleus.

Two years after the publication of Goldhaber and Teller, Steinwedel and Jensen [Ste50] proposed a two-fluid model of the giant resonance (SJ model) based on a similar idea as the GT model. In their model, both the proton and neutron fluids were compressible and oscillated in- and out-of-phase within a sphere with a fixed surface. Here, the restoring force was provided by the volumetric-symmetric energy in the Bethe-Weizsäcker mass formula [Wei35, Bet36]. In the SJ model, the energy of the vibrations is found to be proportional to $A^{-1/3}$.

More recently, the mass dependence of the GDR resonance (centroid) energy is given by a combination of an $A^{-1/3}$ and $A^{-1/6}$ terms [Har01, Ber75]:

$$E_{\mathrm{IVGDR}} = 31.2A^{-1/3} + 20.6A^{-1/6}(\mathrm{MeV}). \tag{1.1}$$

The resonance width can also be described by a semi-empirical function based on the hydro-dynamical model. Auerbach and Yeverechyahu considered two compressible and viscous nuclear fluids, and proposed the following resonance width based on the viscosity terms [Aue75]:

$$\Gamma = 2.3 + 14A^{-2/3} + 21A^{1/2}(\mathrm{MeV}). \tag{1.2}$$

However, from scattering experiments it was confirmed that the mean-free path of the nucleons was of the order of the nuclear radius. Therefore, collisions between the nucleons became rare and the hydro-dynamical model did not describe the conditions in the nucleus very accurately. Without further modifications, neither of the two models (SJ and GT models) agreed particularly well with the experiments.

Giant resonances can also be viewed as damped harmonic oscillations and if such a system is coupled to an external field, e.g., an electromagnetic field, the resonance can be described well by a Lorentzian distribution [Ber94]. Theoretically, a

Lorentzian distribution is symmetric and can extend from -∞ to +∞, hence such a distribution is always non-zero at the origin. However, this is not physically realistic, since the excitation to a giant resonance will not occur in the absence of an energy transfer to the system. Therefore, giant resonances in spherical nuclei are better parameterised by Lorentzian distributions of the Breit-Wigner type [Kne96, Mor76]:

$$\sigma(E) = \frac{\sigma_{\rm m}\Gamma^2 E^2}{(E^2 - E_{\rm m}^2)^2 + \Gamma^2 E^2}, \tag{1.3}$$

where $E_{\rm m}$ is the resonance energy, Γ is the resonance width and $\sigma_{\rm m}$ is the peak cross-section.

Speth and Wambach [Spe91] defines giant resonances as resonance structures in the transition strength distribution of a weak external field which carry a large fraction of the total transition strength (typically 50% or more). The total electric dipole transition strength of a nucleus is determined by the Thomas-Reiche-Kuhn (TRK) sum rule [Are79],

$$\begin{aligned} \int_0^{30\rm MeV} \sigma_{\rm abs}(E_\gamma) dE_\gamma &= \frac{16\pi^3}{9\hbar c} \sum_f (E_f - E_i) B(E1, i \rightarrow f) \\ &= \frac{2\pi^2 e^2 \hbar NZ}{mcA} \simeq \frac{60NZ}{A} (\rm MeVmb) \end{aligned} \tag{1.4}$$

where m, N, Z and A are the nucleon mass, neutron, proton and atomic mass numbers, respectively. In addition, $B(E1,\ i \rightarrow f)$ is either the reduced transition strength or matrix element squared of the dipole operator between the ground state and all the available excited states. The GDR exhausts a major fraction (or possibly more) of this sum rule.

Past studies have shown the existence of various collective modes (e.g. low-lying 0^+, 2^+, 3^- states, monopole, quadrupole, octupole, etc resonances) in atomic nu-

clei in addition to the GDR. Tremendous advancement in comprehending such elementary modes of excitations has been made both experimentally and theoretically [Har01, Spe91]. A remarkable amount of experimental work has been carried out towards the investigation of global dependencies and systematics of these modes in various nuclei. The macroscopic features of giant resonances such as centroid energies and collectivity, measured in terms of sum rules, have been studied and are well understood in microscopic models [Har01, Bor98]. In contrast, giant resonance widths have not been fully understood due to the limitations in the experimental methods. Despite all the experimental and theoretical efforts, there is still very limited knowledge about the internal collective processes in the nucleus [Spe91, Bor98]. One might direct this deficiency in gaining complete understanding of intrinsic damping mechanisms of giant resonances to the lack of a consistent explanation of the corresponding decay widths observed experimentally.

1.2 Fine structure

High energy-resolution electron and proton inelastic scattering experiments revealed that giant resonances additionally carry fine structure. The pioneering work on the fine structure concept was reported a long time ago in high energy-resolution ($\Delta E \simeq$ 50 keV) electron scattering experiments at the DALINAC [Sch75, Kuh81], where the Isoscalar Giant Quadrupole Resonance (ISGQR) of ^{208}Pb was observed. The experimental evidence for fine structure was believed to be related to the coupling between collective states and more complex degrees of freedom. A clear understanding is however a long-standing challenge that in the past led to a serious debate concerning the physical nature of the observed fine structure. It must be noted that at the time when the electron scattering measurements were originally performed, proton and α-particle scattering experiments had failed to detect any fine structure features. However, with the introduction of the high energy-resolution capabilities for proton and alpha scattering measurements, data observed from both hadronic and leptonic

probes showed that the observed fluctuations were to a very large extent similar and therefore, physical in nature [Kam97]. Recent investigations at the Grand-Raiden magnetic spectrometer of RCNP, Osaka, Japan, using the (^{3}He,t) reaction have also confirmed the existence of the fine structure feature in the Gamow-Teller resonances in the medium-heavy nucleus ^{90}Nb region [Kal06].

Choosing a technique for a better quantitative analysis of fine structure still remains a point of contention. One is required to conceive a unique technique that could resolve the position, width and localisation of the quantity in question. Early attempts at the extraction of information on characteristic energy scales of the fine structure involved the use of an entropy index method [Lac99, Lac00] and a multifractal analysis [Aib99, Aib03] of the fluctuating strength function. However, more recently, a method based on wavelet analysis technique has been shown to be the most promising candidate [She04, Kal05]. For more detailed discussion on the comparison of the different methods, see Ref. [She08]. Wavelet analysis technique has been implemented in the analysis of the present experimental and theoretical model predictions results. Moreover, the characteristic energy scales from both the experimental results and theoretical calculations will be extracted using the complex Morlet Mother wavelet.

1.3 Modern theoretical models

In order to gain a better insight of the experimentally observed results, the availability of theoretical model predictions is critical. Even though there is a need to attain a unified, all-encompassing theory of nuclear structure and reaction, numerous sophisticated nuclear models have successfully correlated large amounts of experimental data. For this reason, quite a number of different theoretical models have been proposed in explaining the most suitable results of the experimental data from heavy to light nuclei across the periodic table, partly because of the systematic dependence

on shell structure (open or closed shell). Recently, there have been developments of a nuclear theory based on effective field theory technique. This is a systematic approach with new quality to nuclear structure, but in practice fails to work in heavier nuclei. Here one has to re-route to energy-density functional methods based on Random Phase Approximation (RPA) and its extensions. A variety of theoretical model predictions such as the RPA [Rin80], Second Random Phase Approximation (SRPA) [Lac00], Extended Time Dependent Hartree-Fock (ETDHF) [Kam97] and Extended Theory of Finite Fermi Systems (ETFFS) [Lac01], have been utilised for the microscopic description of the strength functions in nuclei in recent years. The comparison of these microscopic theoretical calculations with the experimental results in order to explain the decay processes of resonance widths is still a crucial question that needs to be addressed. The Quasi-particle Phonon Model (QPM) is one of the models used to describe the $E1$ strength function in heavy and medium-heavy nuclei [Sol92, Ber99]. This model is not based on universal forces but uses effective forces with parameters to be fixed for each individual case. However, because of that it is particularly successful in reproducing collective features of nuclei.

A better understanding of the decay modes, in particular the systematic behaviour of the escape width relative to the spreading width, plays a pivotal role in the complete description of the nuclear giant dipole resonance across the periodic table. This study also focuses on the importance of Landau damping, which does not play a role for the Isoscalar Giant Quadrupole Resonance (ISGQR). This Landau damping is the distribution of the strength of a collective mode between several collective states. The IVGDR therefore provides a test case, where the interplay of all three major decay mechanisms can be investigated.

1.4 Level densities

Another important aspect of the proton inelastic scattering data with high energy-resolution is the fine structure features which can be connected to nuclear level densities in the excitation-energy region of giant resonances. Nuclear level densities are imperative for the study of nuclear reactions. Their applications include astrophysics, the study of nuclei far from the stability line, and reactor physics [Agv03, Tof10]. They are also important to infer nuclear thermodynamic properties. Thermodynamic quantities have been used to investigate phase transition phenomena in nuclei.

The phenomenon of fluctuating cross-sections in compound nucleus reactions in the region of overlapping resonances was first studied theoretically in the early 1960's [Eri63] using the assumption of random phases between the scattering amplitudes. At somewhat lower excitation energies, the levels still do not overlap but states are unresolved because of the limited energy-resolution. Then, level densities can be extracted by means of a fluctuation analysis [Mul82, Han90], provided the background contributions to the spectra can be estimated with reasonable accuracy. In the present work, the extraction of level densities of the dominant 1^- states in the excitation-energy region of GDR in a variety of nuclei is possible and is compared to theoretical values from approaches based on the phenomenological Back Shifted Fermi Gas (BSFG) model, the microscopic Hartree Fock-Bardeen-Cooper-Schrieffer (HF-BCS) and Hartree Fock- Bogoluibov (HFB) calculations.

1.5 This study

High energy-resolution results obtained at intermediate proton beam energies, using the K600 magnetic spectrometer in combination with dispersion matching techniques, provides a promising approach to study the fine structure of the IVGDR in nuclei. The necessary experimental techniques were recently discussed in [Fuj02b]

and are described in Chapter 3. With these techniques the possibility to perform (p,p′) experiments at forward scattering angles with an energy-resolution much better than the energy spread of the incident beam has been demonstrated.

The purpose of this study is to extend the systematic studies of the fine structure to the case of the IVGDR, which may be considered the archetype of giant resonances in nuclei. Albeit being the best studied case experimentally and theoretically, many open questions remain [Har01]. In particular, the observed widths as a function of mass number show strong fluctuations which have never been successfully explained on a microscopic basis [Jun08]. An in-depth analysis of the fine structure can certainly add new and independent information to this problem and permits stringent tests of the available microscopic theoretical models. Therefore, a systematic study of light to heavy nuclei was undertaken using high energy-resolution inelastic proton scattering at $E_{\mathrm{p}} = 200$ MeV with the K600 magnetic spectrometer of iThemba LABS.

The experiment represented pioneering work for zero degrees experiments at iThemba LABS and served as a test to investigate the capabilities and limitations of the newly commissioned zero-degree facility. In the past years impressive progress towards a combination of 0° experiments with high energy-resolution, particularly important for a detailed understanding of the Gamow-Teller (GT) modes, have been witnessed. At the Research Centre for Nuclear Physics (RCNP), Osaka, Japan, the (^{3}He,t) reaction was established as a tool for determination of GT$_-$ (isospin $T = T_0 - 1$, where T_0 is the ground state isospin of the target nucleus) strengths from (p,n)-type reactions reaching typical energy-resolutions $\Delta E \approx 30$ keV FWHM in light and ≈ 50 keV in heavy nuclei [Fuj96, Fuj02a]. At Kernfysisch Versneller Instituut (KVI), Groningen, Netherlands, similar success was also achieved with the (d,^{2}He) reaction as a measure of GT$_+$ strengths from (n,p)-type reactions [Hag04]. A particular advantage of near 0° measurements is the selectivity to low angular momentum transfer ($\Delta L = 0$

or 1) simplifying the analysis of the other additional angular momenta contributions to the spectra due to the complex nature of the nuclear interaction which results in the presence of additional multipolarity modes of excitation.

One important aspect of carrying out an experiment such as the present one is the extraction of complete electric dipole ($E1$) strength distributions (*via* relativistic Coulomb excitation) from excitation energies starting at about 5 MeV across the giant dipole resonance (GDR). This was clearly illustrated for the reference case of ^{208}Pb [Tam11, Pol12], for which the $E1$ strength is well known through studies of the ^{208}Pb(γ,γ) and ^{208}Pb(γ,n) reactions [Rye02]. Historically, dipole strengths were studied by combining data from different reactions such as (γ,xn) and (γ,γ), or particle-γ coincidence reactions such as (^{3}He ^{3}He$'\gamma$). However, (γ,xn) measurements are restricted to the energy region above the neutron-separation energy (S_n), while (γ,γ) reactions yield data for low excitation energies roughly up to the neutron threshold [Rus09]. It was therefore problematic to investigate the GDR with (γ,xn) and (γ,γ) reactions. However, by using (p,p$'$) scattering at small angles including 0° one can probe $E1$ excitations both above and below the neutron-separation energy.

A very important aspect of this work is the possibility to complement it with experiments using photons avalaible in the literature as well as proton scattering results performed at the RCNP in Osaka, Japan, with a similar zero-degree facility. However, experiments at RCNP are performed at higher proton energies of 295 MeV. This allows independent checks of the methods for extraction of the $E1$ strength as well as a better understanding of the contributions to the spectra due to nuclear interaction.

The layout of this thesis is as follows: Chapter 2 is devoted to the description of the theoretical considerations involved in the study of Isovector Giant Dipole Resonances and the quantities extracted, e.g. the fine structure of characteristic energy scales

and level densities. This chapter will give a short overview of the tools used in the extraction of the characteristic energy scales and the associated background subtraction. The theory on the wavelet analysis technique will also be presented. Chapter 3 presents the details of the high energy-resolution experiments using the K600 magnetic spectrometer. This includes the analysis of the experimentally measured (p,p$'$) excitation-energy data and extraction of relevant energy spectra. Chapter 4 presents the results of the analysis of the experimentally measured (p,p$'$) excitation-energy data, theoretical calculations and the application of wavelet transform together with the extracted spin- and parity-dependent level density results. The conclusions of the thesis are presented in Chapter 5.

Chapter 2

Theoretical considerations

Introduction

The first section in this chapter presents the classification of giant resonance modes, where their macroscopic and microscopic pictures are discussed in Sect. 2.1.1 and Sect. 2.1.2, respectively. In Sect. 2.2, the damping of giant resonances is described followed by the scattering formalism in Sect. 2.3. Charged-particle induced reactions by Rutherford scattering as well by Coulomb excitation are discussed in Sect. 2.4. In Sect. 2.5, the microscopic models used in the calculation of giant resonance strengths are discussed. The mathematical tools required to extract the characteristic energy scales from both the experimental data and the theoretical predictions are given in Sect. 2.6. The tools encompass the use of the Fourier Transform and wavelet analysis. Details concerning spin- and parity-dependent nuclear level density extraction are presented in Sect. 2.7.

2.1 Classification of giant-resonance modes

2.1.1 Macroscopic picture

In addition to the Isovector Giant Dipole Resonance (IVGDR), there exits a long list of other collective modes of excitation such as the Giant Monopole Resonance (GMR), Giant Quadrupole Resonance (GQR), etc. These modes of excitation are classified according to their change in angular momentum (L), spin (S) and isospin (T). Depending on the combination of ΔL and parity relative to the ground state, giant resonances are classified in analogy to electromagnetic transitions as electric or magnetic. Figure 2.1 shows schematically examples of oscillations which result from the excitations of the various giant resonances. The $\Delta S = 0$, $\Delta T = 0$ modes are classified as the electric, isoscalar vibrations. The electric, isoscalar vibrations cause the neutrons and protons to oscillate in phase according to a multipole pattern defined by ΔL. Moreover, the $\Delta S = 0$, $\Delta T = 1$ modes are known as the electric, isovector vibrations where the protons and neutrons oscillate out of phase against each other according to a multipole pattern defined by ΔL. From past studies, it has been observed that for the same multipole mode the isovector resonances are at higher excitation energy than the isoscalar resonances due to some extra energy required to separate neutron and proton distributions in the isovector case.

On the otherhand, the $\Delta S = 1$, $\Delta T = 0$, modes are classified as the magnetic, isoscalar vibrations in which nucleons with spin$\uparrow$ vibrate against nucleons with spin$\downarrow$. Oscillation modes with $\Delta S = 1$, $\Delta T = 1$, are known as the magnetic, isovector. In these particular vibrations the protons with spin$\downarrow(\uparrow)$ oscillate against neutrons with spin$\uparrow(\downarrow)$.

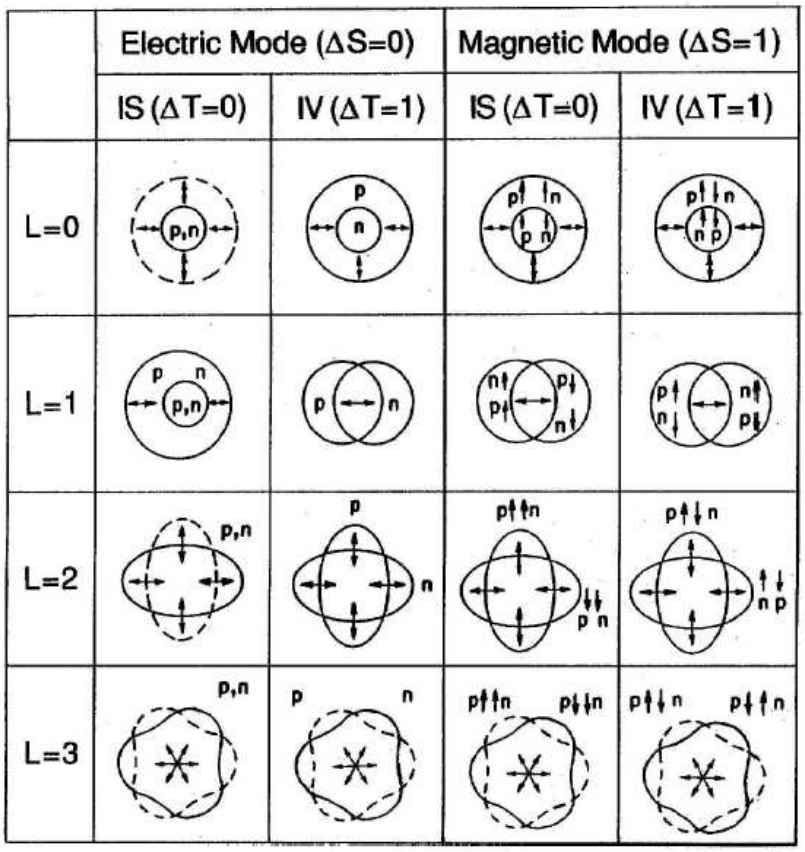

Figure 2.1: Schematic representation of various collective modes taken from Ref. [Ito05].

2.1.2 Microscopic picture

Microscopically, one can describe giant resonances as a coherent superposition of particle-hole excitations resulting from the application of a one-body operator on the ground state of the nucleus [Har01]:

$$|\Psi_{GR}^{\lambda,\sigma,\tau}\rangle = O^{\lambda,\sigma,\tau}|\Psi_{g.s.}\rangle, \tag{2.1}$$

where the parameter λ represents the multipolarity of the resonance and τ and σ represent the isospin structure and spin of the particular resonance in question, respectively. By way of example, in the case of electric isoscalar transitions one may use the operator [Har01]:

$$O_{\mu}^{\lambda,0,0} = \sum_{i=1}^{A} r_i^{\lambda} Y_{\lambda\mu}(\Omega_i), \quad \lambda \geq 2 \tag{2.2}$$

where the summation runs over all nucleons i. In order to gain an insight into the qualitative features of giant resonances, a schematic shell-model picture as illustrated in Fig. 2.2 is informative. Well known features of this model are the alternating parity of the single-particle wave functions in subsequent shells N, N+1, N+2, N+3 ... and the energy difference $\Delta E = \Delta N \times 1\hbar\omega = \Delta N \times 41A^{-1/3}$ MeV. The operator $O_{\mu}^{\lambda,0,0}$ can only induce transitions with $\Delta N \leq \lambda$ while, because of parity conservation, odd λ transitions require $\Delta N = 1, 3, \ldots$ and even λ transitions require $\Delta N = 0, 2, \ldots$ This results in the simple scheme shown in Fig. 2.2 and given in Table 2.1 [Har01].

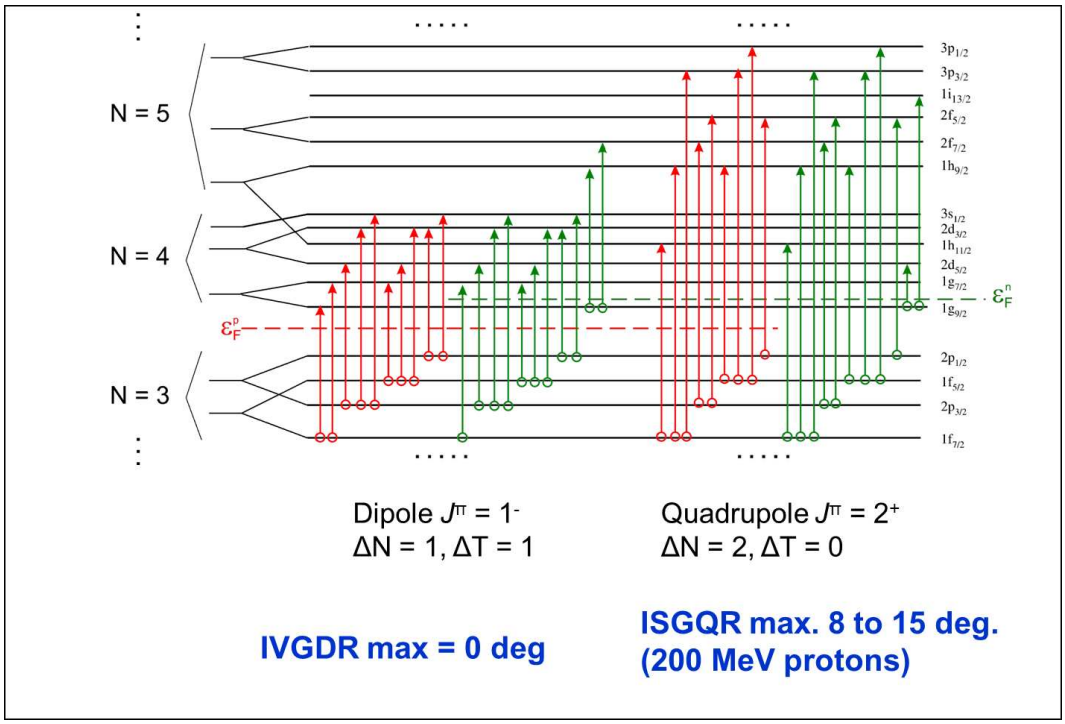

Figure 2.2: Schematic picture of $E1$ and $E2$ single-particle transitions between shell-model states in ^{90}Zr [She04]. Proton (red arrows with open cicles) and neutron (green arrows with open circles) $1p$-$1h$ transitions from and to corresponding energy levels below and above the Fermi level ε_{F}, which contribute coherently to a given collective mode, are shown.

Table 2.1: Multipole excitations as particle-hole excitations across major shells [Har01].

Monopole	$\lambda = 0$	$(0\hbar\omega)$	–	$(2\hbar\omega)$	–	–
Dipole	$\lambda = 1$	–	$(1\hbar\omega)$	–	–	–
Quadrupole	$\lambda = 2$	$(0\hbar\omega)$	–	$(2\hbar\omega)$	–	–
Octupole	$\lambda = 3$	–	$(1\hbar\omega)$	–	$(3\hbar\omega)$	–
Hexadecapole	$\lambda = 4$	$(0\hbar\omega)$	–	$(2\hbar\omega)$	–	$(4\hbar\omega)$

2.2 Damping of giant resonances

One of the basic problems in the study of the giant resonances is the understanding of how their widths and damping in microscopic theories could be interpreted. The first approximation of the width Γ of the resonance is defined by

$$\Gamma = \Delta\Gamma + \Gamma^{\uparrow} + \Gamma^{\downarrow}, \tag{2.3}$$

where it consists of three contributions: a fragmentation of the initial one-particle one-hole ($1p$-$1h$) excitations called Landau damping ($\Delta\Gamma$), direct particle emission from the ($1p$-$1h$) excitations expressed by an escape width $\Gamma^{\uparrow}$, and coupling to the more complex two-particle two-hole ($2p$-$2h$) and many particle-many hole (np-nh) states leading to a spreading width $\Gamma^{\downarrow}$ due to internal mixing [Goe82] (see Fig. 2.3).

The spreading width concept is given by the doorway model for the decay of giant resonances. Detailed discussion of this concept is given in the following subsection.

2.2.1 Doorway-state picture of giant resonances

Past studies have widely described internal mixing as a process that happens *via* a hierarchy of couplings towards more and more complex degrees-of-freedom in the nucleus, starting from the $2p$-$2h$ and ending with the np-nh states of the compound nucleus. In 1963, Block and Feshbach [Blo63] introduced the doorway concept which they found to dominate the damping of giant resonances in heavy nuclei. The concept was later generally formulated by Feshbach [Fes64, Fes74].

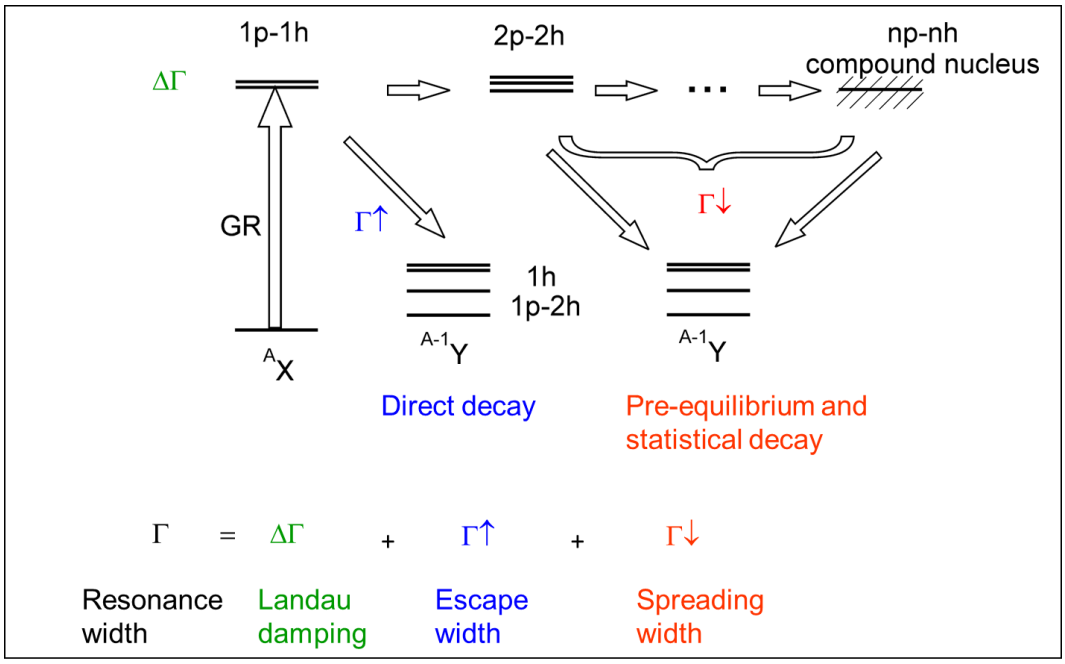

Figure 2.3: Schematic representation of the width of the collective $1p$-$1h$ state into a direct component $\Gamma^{\uparrow}$ and a spreading component $\Gamma^{\downarrow}$ of a giant resonance [Har01].

The schematic representation of the damping of giant resonances within a doorway picture is depicted in Fig. 2.4. An infinite spectrum of eigenvalues $\mathbf{F}^{+}|0\rangle$ is produced after the application of an external field at a time $t = 0$ thereby exciting the nucleus from its ground state $|0\rangle$.

Initially, a mean field is settled down in the system by the time of $t = 10^{-24} - 10^{-23}$ s, thus enabling the selection of only few dominant frequencies in the nuclear response, which correspond to energies of the doorway states. Though these particular states, described by the Random Phase Approximation (RPA), do not have any width, the fragmentation of strength by a few MeV might become visible if the number of such doorways is increased. This is expected to be significant only for light nuclei. On the next level, these doorway states couple through residual two-body interaction to the more complicated $2p$-$2h$ states, hence, acquiring an additional width. Most of these $2p$-$2h$ configurations are background states (shown as dotted lines in Fig. 2.4), the coupling to which is weak and stochastic. Included within such a background

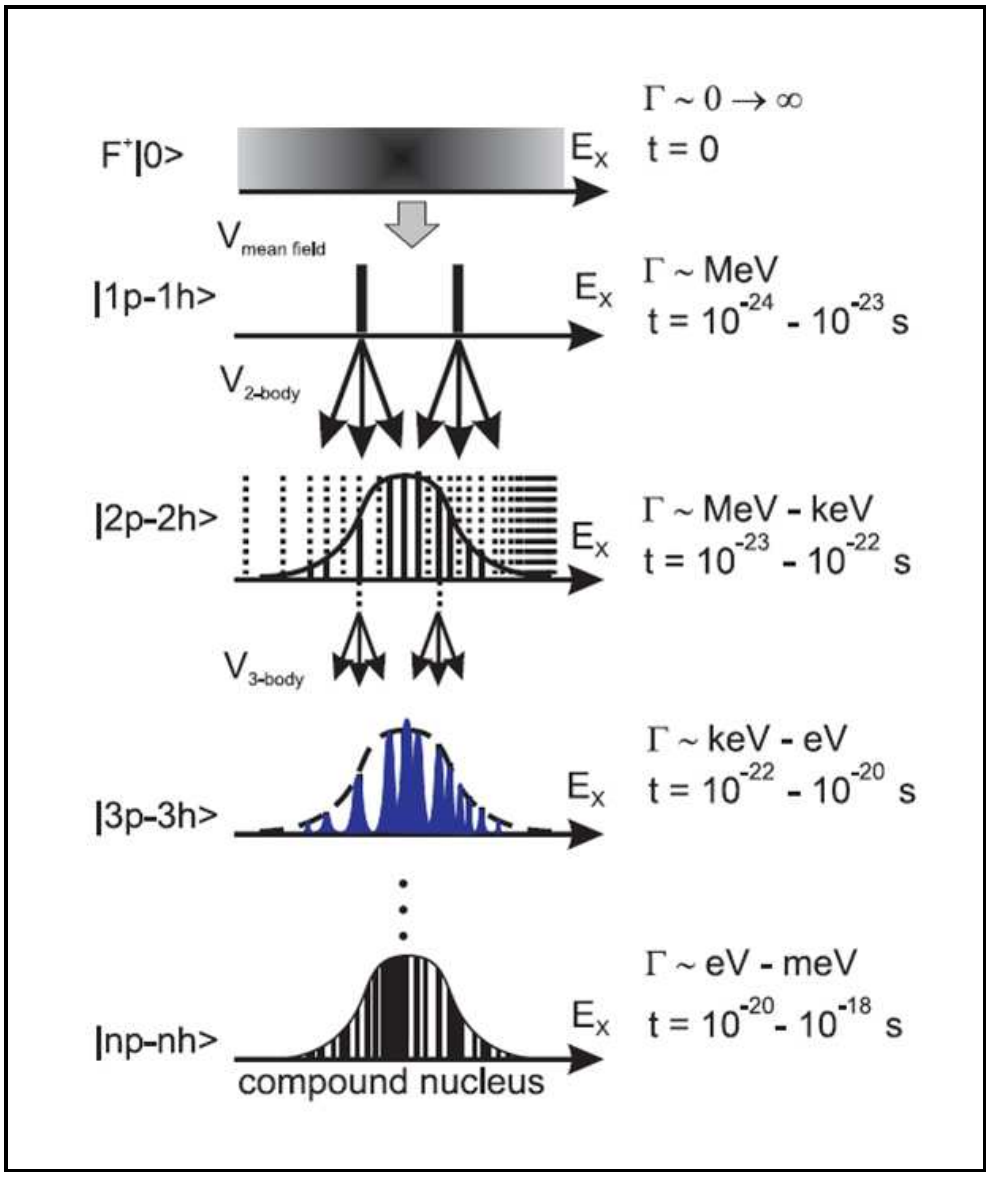

Figure 2.4: Damping of giant resonances. A hierarchy of lifetimes and energy scales in the decay of giant resonances as a result of different processes [She05].

are a few collective $2p$-$2h$ states, the coupling to which is much stronger (solid lines at the $2p$-$2h$ level in Fig. 2.4).

Experiments have confirmed the existence of fine structure in nuclear response as these states are partially overlapping. On this level, the energy scales from several MeV down to hundreds of keV are expected to be observed. Many of these $2p$-$2h$ states can in turn act as doorways and couple through residual interaction to even

more complex configurations. This chain of couplings can be extended down to the level of compound nucleus, where the energy is already equally distributed over all available degrees-of-freedom. This could take $t = 10^{-18}$ s except in the event that such a system undegoes a subsequent decay *via* a photon or particle emission, a process known as statistical decay.

Actually, the width associated with the coupling to $3p$-$3h$ and more complicated states, and eventually to the totally mixed states describing the compound nucleus, does not differ substantially from the spreading produced by the doorway coupling to $2p$-$2h$, since the increase of the density of complex states is compensated for by the decrease of the coupling matrix elements. The effect of this coupling is reflected in a smoothly varying strength function. In fact, a particle decay out of the system might occur at any step of this hierarchy. Consequently, one can distinguish between different types of decay processes, as shown in Fig. 2.3.

2.3 Scattering formalism

The time-independent Schrödinger equation [Gri04] gives a good description of a particle scattered from a potential $V(r)$:

$$(H - E)\psi(k, r) = 0, \tag{2.4}$$

where H is the Hamiltonian and can be expressed as:

$$H = H_0 + V. \tag{2.5}$$

Therefore, by substituting Eq. (2.5) into Eq. (2.4), it follows that:

$$(H_0 + V - E)\psi(k, r) = 0. \tag{2.6}$$

From Eq. (2.5) the hamiltonian H_0 describes the unperturbed motion of the system, and V describes the interaction, which disappears for sufficiently large separation of the interacting particles of the system. Here, E represents the energy in the centre-of-mass system and the wave-function ψ represents the particle. This typical solution needs to have a boundary condition whose total wave-function must have an asymptotic behaviour for the incoming plane wave and the outgoing spherical wave,

$$\psi(k,r) \rightarrow \phi + f(\theta)\frac{e^{ikr}}{r}, \tag{2.7}$$

where r gives the relative distance between the particles in the entrance channel, the wave vector is given by k, ϕ is a plane wave and $f(\theta)$ is the scattering amplitude which is related to the differential cross-sections by

$$\frac{d\sigma}{d\Omega}(\theta) = |f(\theta)|^2. \tag{2.8}$$

Equation (2.4) can be expressed in integral form and in such a particular case, its eigenfunctions ψ are given by the Lippmann-Schwinger equation:

$$\Psi^{\pm} = \Phi + G_0^{\pm} V \Psi^{\pm}, \tag{2.9}$$

or using Dirac notation

$$|\psi^{\pm}\rangle = |\phi\rangle + G_0^{\pm} V |\psi\rangle, \tag{2.10}$$

where the G_0 is the Green's function of the unperturbed equation

$$G_0^{\pm} = \frac{1}{E - H_0 \pm i\varepsilon}. \tag{2.11}$$

Substituting Eq. (2.11) into Eq. (2.9), one gets [Sat83]:

$$\Psi^{\pm} = \Phi + \frac{1}{E - H_0 \pm i\varepsilon} V \Psi^{\pm} = \Phi + (E - H_0 \pm i\varepsilon)^{-1} V \Psi^{\pm}. \tag{2.12}$$

The Lippmann-Schwinger equation has two solutions. Firstly, it is the plane wave and the outgoing scattered wave usually given by "+" sign and secondly, a plane wave and the ingoing scattered wave denoted by "−" sign. The T transition operator can be defined using the Green's function operator G_0 as

$$T^{\pm} = V + VG_0^{\pm}T^{\pm}, \tag{2.13}$$

with the transition matrix element

$$T_{fi} = \langle\phi|T^{+}|\phi\rangle = \langle\phi|V|\psi^{+}\rangle, \tag{2.14}$$

where i and f represent the initial and final scattering wave functions respectively. The state vector $|\psi^{\pm}\rangle$ in Eq. (2.10) and the T matrix operator in Eq. (2.13) can be expressed as a series expansion in V. Their iterated forms are given by

$$|\psi^{\pm}\rangle = |\phi\rangle + G_0^{\pm}V|\phi\rangle + G_0^{\pm}VG_0^{\pm}V|\phi\rangle + ... \tag{2.15}$$

and

$$T^{\pm} = V + VG_0^{\pm}T^{\pm} + VG_0^{\pm}VG_0^{\pm}V + ..., \tag{2.16}$$

respectively. One can approximate the two series by taking only the first n terms into account, which is known as the Born approximation to n^{th} order. In the second series G_0^{th} propagates the particle from scattering to scattering point. By considering only the first n terms into account, one limits the nuclear reaction to an n-step scattering process. In conclusion, one can relate the matrix element T_{fi} defined in Eq. (2.14) to the scattering amplitude by the expression:

$$f(\theta) = \frac{\mu}{2\pi\hbar^2}T_{fi} \tag{2.17}$$

with μ being the reduced mass of the system.

2.3.1 Distorted waves and optical potential

According to Bauwens *et al.* [Bau00], Coulomb interaction plays a role in excitation of 1^- states observed in the past (p,p′) studies. A distorted-wave Born approximation (DWBA) calculation employing the code DWBA07 [Ray07] suggests that angular distributions of transitions to both 1^+ and Coulomb-excited 1^- states have a maximum at 0°, therefore making it a significant tool in calculating transition amplitudes. Besides the optical model, the computer code DWBA07 also includes a fully microscopic non-local optical model obtained with the description of the target by its occupation numbers and with the two-body interaction for the initial and final distorted waves. Two approaches can be used in the description of distorted waves. One approach involves the expansion of the scattering matrix T_{fi} in a basis of distorted wave-functions Ψ defined by the Lippman-Schwinger equation given by Eq. (2.12).

In the first approach, a local representation of the potential, the optical potential $U_0(\vec{r})$, can be obtained by folding the interaction with the ground state density $\rho_0(\vec{r}_N)$ of the nucleus

$$U_0(\vec{r}) = \int \rho_0(\vec{r}_N) V_0(\vec{r} - \vec{r}_N) d^3 r_N. \tag{2.18}$$

The other alternative method involves the application of a phenomenological optical potential, which is commonly determined by a fit to elastic scattering data. The interaction potential U consists of two parts namely, the Coulomb and nuclear potential parts.

The complex nuclear potential is given by [Kra88]:

$$U(r) = V(r) + iW(r), \tag{2.19}$$

where $V(r)$ is the real part of the central potential which describes the elastic scattering and is responsible for the distortion of the incoming and outgoing waves and $W(r)$ is the imaginary part of the central potential and responsible for absorption of flux into non-elastic scattering channels, and hence contains the residual interaction. In analogy with optics the real part of the potential describes the scattering in the dispersive medium, while the imaginary part corresponds to the absorption. The nuclear potential is complex due to its short-range attractive interaction and represents the many-body interaction between colliding nuclei. Furthermore, this nuclear potential also has some terms describing the spin-orbit coupling and isospin dependence. A physically realistic phenomenological potential utilised is of the Woods-Saxon type. The standard form of the optical potential used in the calculation of the distorted waves is parameterised as:

$$\begin{aligned} U(r) = V_{\mathrm{C}}(r) - V f_{\mathrm{o}}(r, R_{\mathrm{o}}, a_{\mathrm{o}}) - iW(f_{\mathrm{w}}(r, R_{\mathrm{w}}, a_{\mathrm{w}}) \\ + 4W_d a_{\mathrm{w}} \frac{d}{dr} f_{\mathrm{w}}(r, R_{\mathrm{w}}, a_{\mathrm{w}}) \\ + \frac{2}{r}\left[V_{\mathrm{so}} \frac{d}{dr} f_{\mathrm{vso}}(r, R_{\mathrm{vso}}, a_{\mathrm{vso}})\right] \\ + \frac{2}{r}\left[iW_{\mathrm{so}} \frac{d}{dr} f_{\mathrm{wso}}(r, R_{\mathrm{wso}}, a_{\mathrm{wso}})\right] \vec{L}.\vec{\sigma}. \end{aligned} \tag{2.20}$$

The Coulomb potential V_{C}(r) is that from a uniformly charged sphere of radius $r_{\mathrm{oC}}A^{1/3}$. The quantities V_{so} and W_{so} are the corresponding real and imaginary strengths of the spin-orbit potential, W_{d} represents the imaginary surface potential and $\vec{L}$ and $\vec{\sigma}$ represent the orbital and spin angular momentum of the incident nucleon, respectively. The radial-form factors of Woods-Saxon type (geometry f) in Eq. (2.20) can be expressed as

$$f(r, R_x, a_x) = \frac{1}{1 + exp\left[(r - R_x)/a_x\right]} \tag{2.21}$$

with $R_x = r_{ox}A^{1/3}$ and a_x the corresponding diffuseness parameter.

Excitation of the IVGDR by inelastic scattering of protons at intermediate energies is strongly dependent on the scattering angle. In order to identify suitable scattering angles at which measurements of excitation-energy spectra should be taken, calculations can be made for inelastic scattering within the DWBA07 code [Ray07]. By way of example, Fig. 2.5 shows the results for ^{58}Ni nucleus for an $L = 1$ transfer together with other multipoles excited. It should be noted that in the present experiment, measurements were taken for the inclusive scattering angular range of $\theta_{\mathrm{Lab}} = 0^{\circ}$ – 1.91°. As in previous studies of the IVGDR [Pol11], contributions to an underlying background from higher-order multipoles are expected to be present. On the other hand, the calculations from the DWBA07 code can also be used to perform Multipole Decomposition Analysis (MDA).

The MDA is mainly performed to determine the deviation between calculated and experimentally obtained cross-sections at most forward scattering angles (e.g. $\theta_{\mathrm{Lab}} < 2^{\circ}$) which are commonly due to the Coulomb-nuclear interference and contributions from unresolved transitions with higher multipolarities.

2.4 Charged-particle induced reactions

Nuclei contain protons and are charged with the charge of $+Ze$. There is a long-range repulsive force between the interacting nuclei due to their charges:

$$\vec{F} = \frac{1}{4\pi\varepsilon_0}\frac{Z_{\mathrm{P}}Z_{\mathrm{T}}e^2}{r^2}\frac{\vec{r}}{r} \tag{2.22}$$

Since the force is repulsive the trajectories are hyperbolic. If the projectile energy is not sufficient to bring two nuclei to a distance smaller than the range of nuclear interactions, the only result of the collision is either elastic scattering (Rutherford) or inelastic scattering (Coulomb excitation). For Rutherford scattering both projectile and target emerge from the collision in their respective ground states. In Coulomb

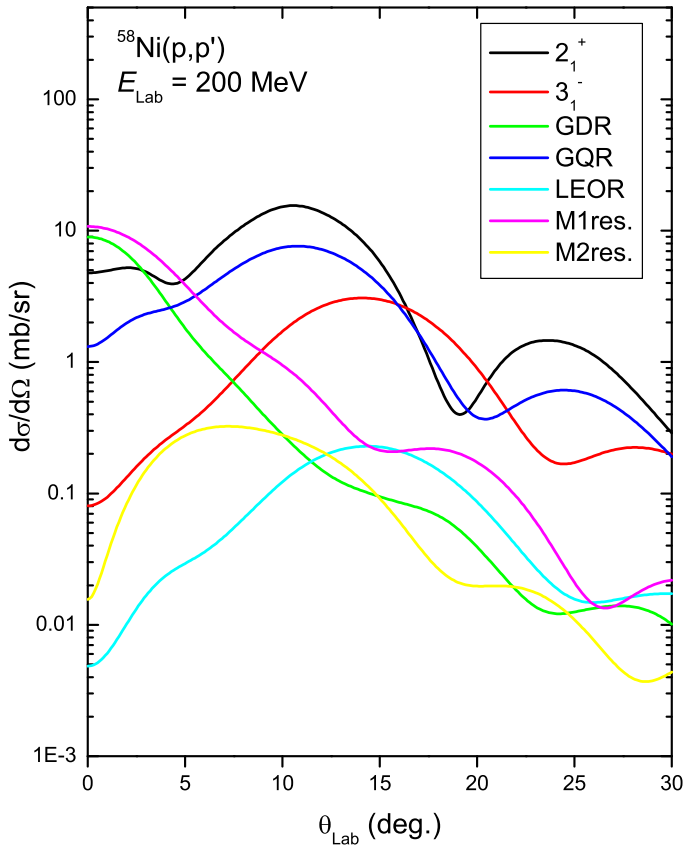

Figure 2.5: Angular distributions for DWBA07 inelastic proton scattering on ^{58}Ni for GDR, GQR, $M1$ resonance, $M2$ resonance and Low energy Octupole resonance (LEOR) at $E_{\mathrm{p}} = 200$ MeV. There are also results for the 2_1^+ and 3_1^- states.

excitation either the target or the projectile or both emerge in an excited state.

2.4.1 Rutherford approach

In the semiclassical approach of the Coulomb excitation process, the projectile can be considered as a point-like charged particle moving along a hyperbolic orbit in the repulsive Coulomb field of a target nucleus. The projectile's trajectory along the orbit is shown in Fig. 2.6.

At low incident energies, the projectile is assumed to follow a Rutherfordian path, while at high incident energies, the projectile is assumed to move along a straight-line trajectory. For the Rutherford scattering scenario, the impact parameter is expressed as:

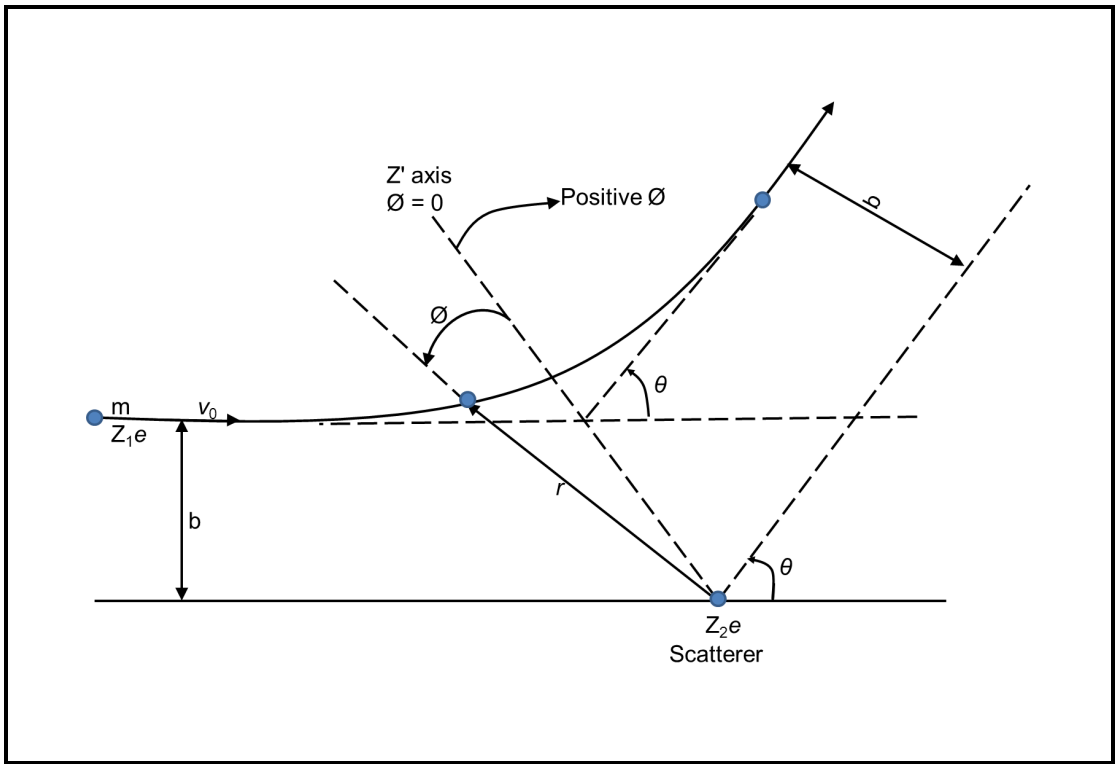

Figure 2.6: Schematic view of the momentum change. Trajectories are symmetric with respect to angle ϕ.

$$
\begin{aligned}
b &= \frac{Z_{\mathrm{P}} Z_{\mathrm{T}} e^2}{4\pi\varepsilon_0} \frac{1}{p v_0} \frac{1}{\tan(\theta/2)} \\
&= \frac{Z_{\mathrm{P}} Z_{\mathrm{T}} e^2}{4\pi\varepsilon_0} \frac{1}{2K} \frac{1}{\tan(\theta/2)}
\end{aligned}
\tag{2.23}
$$

with K being the initial kinetic energy for the projectile. Equation (2.23) defines the relationship between the impact parameter (b) and the scattering angle (θ).

Moreover, by assuming a head-on collision the distance of the closest approach d_0 can be calculated from the conservation of energy:

$$
K = \frac{Z_{\mathrm{P}} Z_{\mathrm{T}} e^2}{4\pi\varepsilon_0} \frac{1}{d_0} \tag{2.24}
$$

$$
d_0 = \frac{Z_{\mathrm{P}} Z_{\mathrm{T}} e^2}{4\pi\varepsilon_0} \frac{1}{K}. \tag{2.25}
$$

As a result, the relation between the impact parameter and the scattering angle then simplifies with the use of the distance of the closest approach parameter:

$$b = \frac{d_0}{2}\frac{1}{\tan(\theta/2)}. \tag{2.26}$$

Finally, the previously related equations lead us to the Rutherford scattering formula given by

$$\begin{aligned} \frac{d\sigma}{d\Omega} &= \left(\frac{d_0}{4}\right)^2 \frac{1}{\sin^4(\theta/2)} \\ &= \left(\frac{Z_{\mathrm{P}} Z_{\mathrm{T}} e^2}{4\pi\varepsilon_0}\frac{1}{4K}\right)^2 \frac{1}{\sin^4(\theta/2)}. \end{aligned} \tag{2.27}$$

2.4.2 Coulomb excitation

An effective technique to investigate dipole transition strength over a large excitation-energy range in nuclei is Coulomb excitation in relativistic heavy-ion scattering [Ald75], where the cross-sections are related to multipole matrix elements that characterise the γ-decay of excited nuclear states. The simplest way to describe the reaction mechanism in relativistic collisions is provided by the equivalent photon method, originally developed by Fermi [Fer24] and later on improved by Weizsäcker [Wei34] and Williams [Wil34], (commonly known as the Weizsäcker-Williams method).

Since Coulomb excitation is a process in which a charged particle transmits energy to the nucleus through the electromagnetic field, it can happen at a much lower energy than that necessary for the particle to overcome the Coulomb barrier. The nuclear force is, in this way, excluded in the process. At very high incident energies the nuclear cross-sections for the Coulomb excitation of giant resonances exceed the nuclear geometrical cross-sections. Since these resonances decay mostly through particle emission or fission, this indicates that Coulomb excitation of giant resonances is a very important process to be considered in relativistic heavy-ion collisions and

fragmentation processes, especially in heavy-ion colliders. At intermediate energies ($E_{\mathrm{Lab}} \gtrsim 100$ MeV/nucleon) the cross-sections are also large and this offers good possibilities to establish and study the properties of the IVGDR and ISGQR. For other modes, the cross-sections are too small.

2.4.3 Fermi's method

In 1924, Fermi used a non-relativistic approach to explain the process of electromagnetic excitation due to a moving charge [Fer24], as illustrated in Fig. 2.7. In his approach, the target nucleus, with charge $Z_{\mathrm{T}}e$, is assumed to be stationary, while the projectile moves along a linear trajectory, with a non-relativistic velocity $\vec{v}$. It should be noted that the role of the target and of the projectile can be exchanged, i.e. one can consider the case of internal excitation of the projectile by the electromagnetic field of the target, and *vice-versa*. The geometry of the process can be reduced to two dimensions, onto a plane defined by the trajectory of the projectile and by the centre of the target. The origin of the time scale is positioned at the turning point of the projectile, i.e. when the projectile is at the distance of closest approach at the time $t = 0$, or impact parameter b, with respect to the centre of the target. The electric field $\vec{E}$ generated by the target nucleus can be described by the expression:

$$\vec{E}(\vec{r}) = \frac{Z_{\mathrm{T}}e}{\|\vec{r}\|^2}\vec{u_{\mathrm{r}}} = \frac{Z_{\mathrm{T}}e}{\|\vec{r}\|^3}\vec{r}, \tag{2.28}$$

where Z_{T} is the charge number of the target nucleus, e is the unit charge, and $\vec{u_{\mathrm{r}}}$ is the unit vector of $\vec{r}$. According to the inverse kinematics geometry of Fig. 2.7, one can parameterise the position vector $\vec{r}$ in the following way:

$$\vec{r} = \begin{pmatrix} vt \\ \\ b \end{pmatrix}, \quad \|\vec{r}\| = \sqrt{b^2 + v^2t^2}. \tag{2.29}$$

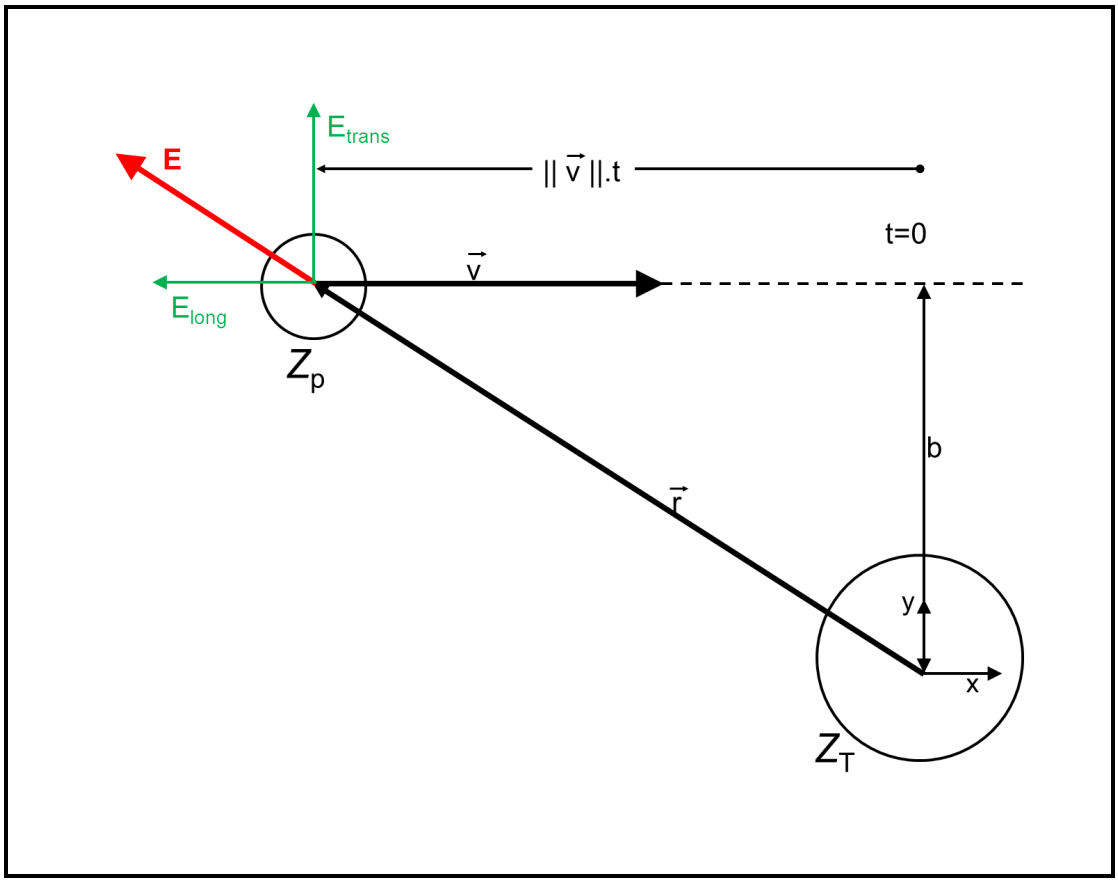

Figure 2.7: Schematic view of the geometry of heavy-ion-induced electromagnetic excitation.

The longitudinal and radial electric fields can be described using Eqs. (2.28) and (2.29):

$$E_{\parallel}(t) = \frac{Z_{\mathrm{T}} e v t}{(b^2 + v^2 t^2)^{3/2}}, \tag{2.30}$$

$$E_{\perp}(t) = \frac{Z_{\mathrm{T}} e b}{(b^2 + v^2 t^2)^{3/2}}. \tag{2.31}$$

The primary aim of this approach is to attribute an energy distribution to a given interaction with the parameter set $\{Z_{\mathrm{T}}, v, b\}$. Therefore, the electric fields in Eqs. (2.30) and (2.31) must first be transformed from the time to the frequency domain *via* a Fourier transformation. The following Fourier series will describe the electric

fields in Eqs. (2.30) and (2.31):

$$E_{\parallel}(t) = \sum_n a_{\mathrm{n}} \sin\left(\frac{2\pi n}{T}t\right), \tag{2.32}$$

$$E_{\perp}(t) = \sum_n b_{\mathrm{n}} \cos\left(\frac{2\pi n}{T}t\right), \tag{2.33}$$

where T is the period of the function. The Fourier coefficients can be calculated with:

$$a_{\mathrm{n}} = \frac{2}{T}\int_{-0.5T}^{0.5T} E_{\parallel}(t)\sin\left(\frac{2\pi n}{T}t\right)dt = \frac{2Z_{\mathrm{T}}ev}{T}\int_{-0.5T}^{0.5T}\frac{t\sin\left(\frac{2\pi n}{T}t\right)}{(b^2+v^2t^2)^{3/2}}dt, \tag{2.34}$$

$$b_{\mathrm{n}} = \frac{2}{T}\int_{-0.5T}^{0.5T} E_{\perp}(t)\cos\left(\frac{2\pi n}{T}t\right)dt = \frac{2Z_{\mathrm{T}}eb}{T}\int_{-0.5T}^{0.5T}\frac{\cos\left(\frac{2\pi n}{T}t\right)}{(b^2+v^2t^2)^{3/2}}dt. \tag{2.35}$$

Using these expressions, Eqs. (2.32) and (2.33) represent the electric fields of light waves, which can be described by the corresponding frequency spectrum [Jac99]:

$$\frac{dI(\nu,b)}{d\nu} = \frac{c}{2\pi} \mid E(\nu,b) \mid^2 . \tag{2.36}$$

By defining the frequency as $\nu = n/T$ in Eqs. (2.34) and (2.35) and by expanding the period of the function to $\pm\,\infty$, the spectrum of the combined longitudinal and transverse electric fields is described by:

$$\begin{aligned}\frac{dI(\nu,b)}{d\nu} = {} & \frac{cZ_{\mathrm{T}}^2e^2}{2\pi}b^2\left(\int_{-\infty}^{\infty}\frac{\cos[2\pi\nu t]}{(b^2+v^2t^2)^{3/2}}dt\right)^2 \\ & + \frac{cZ_{\mathrm{T}}^2e^2}{2\pi}v^2\left(\int_{-\infty}^{\infty}\frac{\cos[2\pi\nu t]}{(b^2+v^2t^2)^{3/2}}dt\right)^2 .\end{aligned} \tag{2.37}$$

The solutions of the two integrals in Eq. (2.38) are modified Bessel functions of the second kind, simplifying the intensity expression to:

$$\frac{dI(\nu,b)}{d\nu} = \frac{8\pi Z_{\mathrm{T}}^2e^2\nu^2}{v^2}\left(K_0^2\left(\frac{2\pi\nu b}{v}\right)^2 + K_1^2\left(\frac{2\pi\nu b}{v}\right)\right), \tag{2.38}$$

where K_0 and K_1 are modified Bessel functions of the second kind of order zero and one, respectively. In his approach, Fermi shows the derivation of the frequency or energy spectrum based on a time-varying electric field.

2.4.4 Weizsäcker-Williams method

In 1934, Weizsäcker and Williams developed independently the equivalent photon method under relativistic conditions. While still in inverse kinematics (see Fig. 2.7), the electric fields of Eqs. (2.30) and (2.31) must be modified [Har01, Jac99, Ber86]:

$$E_{\parallel}(t) = \frac{Z_{\mathrm{T}} e \gamma v t}{(b^2 + \gamma^2 v^2 t^2)^{3/2}}, \tag{2.39}$$

$$E_{\perp}(t) = \frac{Z_{\mathrm{T}} e \gamma b}{(b^2 + \gamma v^2 t^2)^{3/2}}, \tag{2.40}$$

where γ is the relativistic Lorentz factor given by $\gamma = (1 - v^2/c^2)^{-1/2}$.

For completeness, the magnetic fields generated by the motion of the charge are:

$$B_{\parallel}(t) = 0, \tag{2.41}$$

$$B_{\perp}(t) = \beta B_{\perp}(t). \tag{2.42}$$

Previous studies [Har01, Ber09] have shown that an increase in the velocity of the projectile makes the transverse electric field narrower due to the reduction in interaction time. Consequently, a narrow time distribution produces a wide frequency distribution after a Fourier transformation, hence higher projectile velocities yield frequency spectra that reach out to higher values. Since the frequency distribution decreases asymptotically on the high-frequency side, a maximum excitation energy cannot be defined. The so-called adiabaticity parameter ξ is defined as the ratio of the collision time to the excitation time. For the excitation to occur, ξ should be less that unity. Otherwise, the duration of the collision is prolonged, and the interaction becomes adiabatic, i.e. without any energy transfer. The adiabaticity

parameter is given by [Ber85]:

$$\xi = \frac{\omega b}{\gamma v} = \frac{\epsilon b}{\hbar \gamma \beta c}, \tag{2.43}$$

where ϵ is the excitation energy and b is the impact parameter. Based on this definition, the maximum excitation energy can be estimated if $\xi = 1$ and if $b = b_{\min}$:

$$\epsilon_{\max} = \frac{\hbar \gamma \beta c}{b_{\min}}. \tag{2.44}$$

For the quantitative understanding of the frequency spectrum, a Fourier transformation similar to expressions (2.32) and (2.33) is applied on Eqs. (2.39) and (2.40) to generate a frequency spectrum of the two perpendicular electric fields according to Eq. (2.36) [Jac99]:

$$\frac{dI_{\parallel}(\omega, b)}{d\omega} = \frac{Z_{\mathrm{T}} e^2}{\pi^2 c} \left(\frac{c}{v}\right)^2 \frac{1}{b^2} \xi_b^2 K_1(\xi_b), \tag{2.45}$$

$$\frac{dI_{\perp}(\omega, b)}{d\omega} = \frac{Z_{\mathrm{T}} e^2}{\pi^2 c} \left(\frac{c}{v}\right)^2 \frac{1}{b^2} \frac{1}{\gamma^2} \xi_b^2 K_1(\xi_b), \tag{2.46}$$

with $I(\omega, b)$ being the intensity of the virtual radiation, $\omega = 2\pi\nu$ and $\xi_b = \omega \mathrm{b}/\gamma \mathrm{v}$. Both intensity components of Eqs. (2.45) and (2.46) must be added together in order to describe the interaction felt by the projectile nucleus. Each value of b will generate a different spectrum. Since the impact parameter cannot be measured, the spectrum will be integrated over all possible impact parameter values [Jac99,Ben89]:

$$\frac{dI(\omega)}{d\omega} = 2\pi \int_{b_{\min}}^{\infty} \left(\frac{dI_{\parallel}}{\omega}(\omega, b) + \frac{dI_{\perp}}{\omega}(\omega, b) \right) b \, db \tag{2.47}$$

$$= \frac{2 Z_{\mathrm{T}}^2 e^2}{\pi c} \left(\frac{c}{v}\right)^2 \left(\xi K_0(\xi) K_1(\xi) - \frac{v^2}{2c^2} \xi^2 \left[K_1^2(\xi) - K_0^2(\xi) \right] \right) \tag{2.48}$$

with the adiabaticity parameter $\xi = \omega b_{\min}/\gamma v$. Based on Eqs. (2.47) and (2.48), the quantity $N(\hbar\omega)$ can be interpreted as the "virtual quanta" calculated:

$$\frac{dI(\omega)}{d\omega} d\omega = \hbar\omega N(\hbar\omega) d(\hbar\omega). \tag{2.49}$$

One of the most important features of the Weizsäcker-Williams method is the link between the virtual photon spectrum and the electromagnetic excitation cross-section *via* Eq. (2.49):

$$\sigma_C = \int N(\hbar\omega)\sigma_\gamma(\hbar\omega)d(\hbar\omega) \tag{2.50}$$

$$= \int \frac{1}{\hbar\omega}\frac{dI(\omega)}{\omega}\sigma_\gamma(\omega)d(\omega), \tag{2.51}$$

where σ_C is the Coulomb cross-section, σ_γ is the photo cross-section and the integral runs over all the frequency spectrum of the virtual radiation.

Although the approach presented above provides the description of the virtual photon field for the set of electric fields in Eqs. (2.39) and (2.40), it cannot be used directly for the understanding of the various giant resonance modes. The reduced transition rates for electromagnetic processes B($\sigma\lambda$, $I_i \rightarrow I_f$), provide the strength of a transition based on the transition operator. The calculation of the photo-absorption cross-section from the reduced transition rate for a given giant resonance ($\pi\lambda$)-mode is given [Ber85, Ber99]:

$$\sigma_\gamma^\pi\lambda(\epsilon) = \frac{(2\pi)^3(\lambda+1)}{\lambda\left[(2\lambda+1)!!\right]^2}\sum_f \rho_f(\epsilon)k^{2\lambda-1}B(\pi\lambda, I_i \rightarrow I_f), \tag{2.52}$$

where $\rho_f(\epsilon)$ is the density of final states as a function of excitation energy, and $k = \omega/\mathrm{c}$. The total photo-absorption cross-section is then simply the sum of all ($\pi\lambda$)-modes:

$$\sigma_\gamma(\epsilon) = \sum_{\pi\lambda}\sigma_\gamma^{\pi\lambda}(\epsilon). \tag{2.53}$$

In order to obtain the Coulomb excitation cross-section according to Eqs. (2.50) and (2.51), the total number of virtual quanta $N_{\pi\lambda}(\epsilon)$ for each ($\pi\lambda$)-mode must be calculated.

This is attained by using a Liénard-Wiechert potential to describe the electromagnetic fields [Ber86, Ber99, Ale89, Win79], which are later expanded by a Taylor series around the centre of the projectile nucleus. The first and second terms of the Taylor series give rise to the $E1$ and $M1$ contributions, as well as a portion of the $E2$ contribution. For the full $E2$ excitation amplitude, the third term of the Taylor series is also required. The electromagnetic fields are expanded into multipole components using spherical harmonics and are then converted into multipole potentials. The excitation amplitudes can then be calculated *via* first-order perturbation theory, using the multipole potential as the perturbation. This yields a result comparable to the Fourier-transformed electric fields of Eqs. (2.45) and (2.46), with the main difference being that this approach generates separate amplitudes for the various $\pi\lambda$ modes. After the removal of the dependence on the impact parameter by integration, total virtual photon numbers for the major modes ($E1$, $E2$ and $M1$) are given analytically by the following equations [Ber09]:

$$N_{E1}(\epsilon) = \frac{2}{\pi} Z_{\mathrm{T}}^2 e^2 \alpha \left(\frac{c}{v}\right)^2 \left(\xi K_0(\xi) K_1(\xi) - \frac{v^2 \xi^2}{2c^2}\left[K_1^2(\xi) - K_0^2(\xi)\right]\right), \quad (2.54)$$

$$N_{E2}(\epsilon) = \frac{2}{\pi} Z_{\mathrm{T}}^2 e^2 \alpha \left(\frac{c}{v}\right)^4 \left\{2\left[1 - \frac{v^2}{c^2}\right] K_1^2(\xi) + \xi\left[1 - \frac{v^2}{2c^2}\right]^2 K_0(\xi) K_1(\xi) \right. \quad (2.55)$$
$$\left. + \frac{\xi^2 v^4}{2c^4}\left[K_1^2(\xi) - K_0^2(\xi)\right] + \xi^2\left[2 - \frac{v^2}{c^2}\right]^2 K_1^2(\xi)\right\},$$

$$N_{M1}(\epsilon) = \frac{2}{\pi} Z_{\mathrm{T}}^2 e^2 \alpha \frac{\xi^2}{b^2}\left(\xi K_0(\xi) K_1(\xi) - \frac{\xi^2}{2}\left[K_1^2(\xi) - K_0^2(\xi)\right]\right). \quad (2.56)$$

These equations are true only in the case of the inverse kinematics, but on the other hand, if one considers a normal case where the projectile is the one incident on the target nucleus then the given equations are modified to [Ber09]:

$$N_{E1}(\epsilon) = \frac{2}{\pi} Z_{\rm P}^2 \alpha \left(\frac{c}{v}\right)^2 \left(\xi K_0(\xi) K_1(\xi) - \frac{v^2 \xi^2}{2c^2}\left[K_1^2(\xi) - K_0^2(\xi)\right]\right), \quad (2.57)$$

$$N_{E2}(\epsilon) = \frac{2}{\pi} Z_{\rm P}^2 \alpha \left(\frac{c}{v}\right)^4 \left\{2\left[1 - \frac{v^2}{c^2}\right] K_1^2(\xi) + \xi \left[1 - \frac{v^2}{2c^2}\right]^2 K_0(\xi) K_1(\xi) \right. \quad (2.58)$$
$$\left. + \frac{\xi^2 v^4}{2c^4}\left[K_1^2(\xi) - K_0^2(\xi)\right] + \xi^2 \left[2 - \frac{v^2}{c^2}\right]^2 K_1^2(\xi)\right\},$$

$$N_{M1}(\epsilon) = \frac{2}{\pi} Z_{\rm P}^2 \alpha \frac{\xi^2}{R^2} \left(\xi K_0(\xi) K_1(\xi) - \frac{\xi^2}{2}\left[K_1^2(\xi) - K_0^2(\xi)\right]\right), \quad (2.59)$$

where $Z_{\rm p}$ is the projectile charge number, c is the speed of light, v is the velocity of the projectile, $K_{0,1}$ are modified Bessel functions and $\xi = \omega R/\gamma v$, where ω is the angular frequency given by $\omega = \epsilon/\hbar = E_{\rm f} - E_{\rm i}/\hbar$ and the fine structure constant $\alpha = e^2/\hbar c$. It should be noted that R is the low cut-off impact parameter for virtual photon production below which nuclear effects become important and can be expressed as:

$$R = r_0 \left[A_{\rm P}^{1/3} + A_{\rm T}^{1/3}\right] + R_{\rm sep}, \quad (2.60)$$

where $R_{\rm sep} = 2.61$ fm represents the separation distance between the projectile and target nuclear surfaces. By way of example, virtual $E1$ gamma production is shown in Fig. 2.8 where it can be seen that the production rate falls off dramatically as the γ-ray energy increases.

2.5 Microscopic models for the calculation of dipole strength distributions

The application of theoretical models in nuclear physics is a vital input in trying to explain the origin and nature of the fine structure of the characteristic energy scales found in experiments. A vast number of theoretical microscopical calculations have

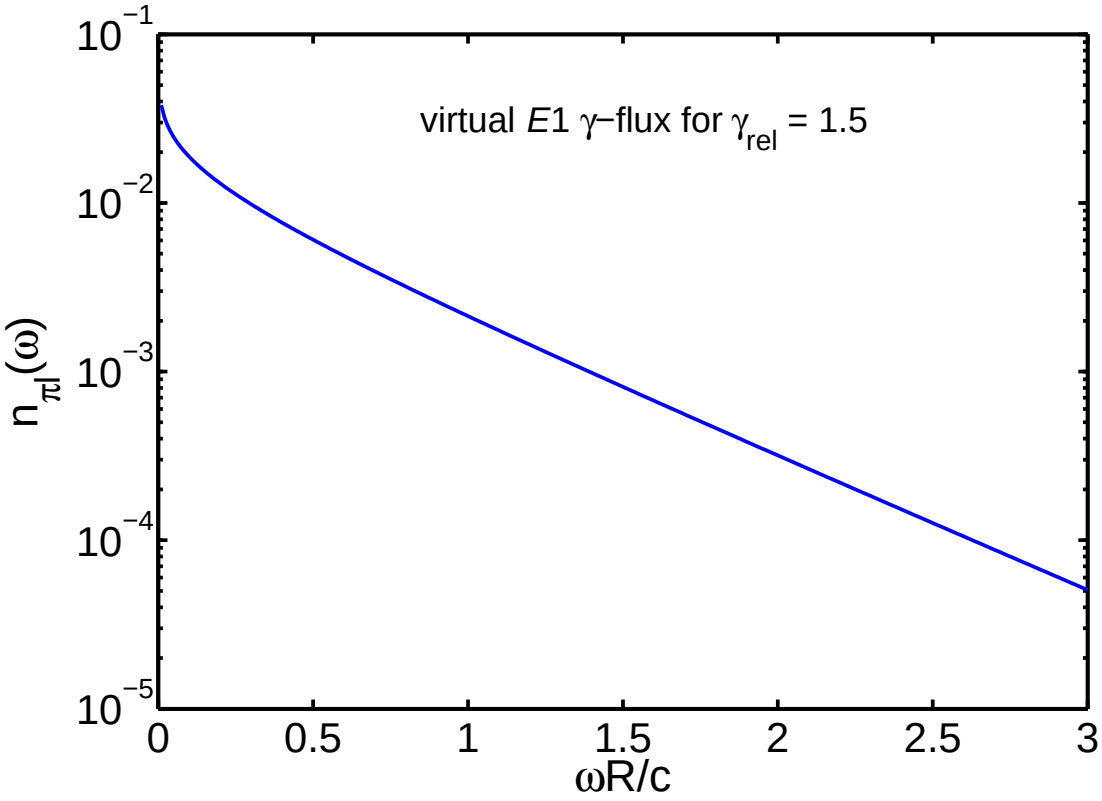

Figure 2.8: Equivalent photon number per unit projectile charge, for $E1$ radiation, and as a function of the dimensionless quantity ωR/c. The ratio of the projectile energy to its rest energy is given by γ ($c = 1$).

been utilised with the aim to understand the origin of fine structure and damping mechanisms in medium and heavy mass nuclei. The list of such models include the Extended Theory of Finite Fermi Systems (ETFFS) [Kam97], the Quasi-particle Phonon Model (QPM) [Sol92], the Extended Time Dependent Hartree-Fock (ETDHF) model [Lac01], the Random Phase Approximation (RPA) [Bro64] and Second Random Phase Approximation (SRPA) [Dro86]. Models pertinent to the present investigation are discussed below.

2.5.1 Quasi-particle Phonon Model (QPM)

In order to reveal the physical nature of the giant resonances one needs theoretical predictions obtained in the framework of models which consider couplings to

complex degrees-of-freedom. In this work the Quasi-particle Phonon Model (QPM) [Sol92, Ber99] is used, which has proved to be very successful tool in the microscopic description of collective modes in medium and heavy mass nuclei [Rei02, Rye02]. This model has the following two advantages: through the diagonalisation of the model Hamiltonian, one can eliminate the need to treat large configuration spaces *via* a specific truncation scheme based on the properties of a coupling hierarchy. It also allows for the possibility to separate different contributions to the damping in the nuclear response, thus the model can offer a further insight into the physical nature of the observed fine structure and characteristic energy scales.

In the QPM approach, $1p$-$1h$ excitations are projected on a space of one-phonon states, whose properties (excitation energies and internal fermionic structure) are obtained from solving quasi-particle RPA equations [Sol92]. When the phonon basis is constructed, the wave function of excited states are written as a combination of interacting one- and multi-phonon configurations [Pon99]. The latter are obtained by coupling one-phonon configurations. The QPM requires a basis truncation when actual calculations are made. This reduction is performed following two decisive features: firstly, very complex N-phonon configurations are neglected. In reality, the most complex configurations included in the wave function of low-lying states are of 3-phonon nature. Secondly, only configurations with an excitation energy below an arbitrary threshold are accounted for. The truncation process follows from the fact that, the density of complex configurations is rather low below the particle threshold and the influence of truncated configurations at high excitation energies on the properties of low-lying states is very weak. Following from the previous statement, one can consider QPM calculations as rather realistic from the point of view of the basis completeness at low excitation energies. A more detailed description of the QPM theory will now be introduced, because the in-depth analysis presented in chapter 4 will be based on these results.

In the QPM nuclear excitations are described by the creation of phonons made up from particle-hole pairs. Due to pairing correlations, the occupation probability for a state j is not exactly one or zero. These states are denoted as quasi-particle (qp) states. Since $1p$-$1h$ pairs couple to an integer transfer of the quantum numbers, one can describe the transition as a creation of a quasi-boson, the so-called phonon. Note, however, that the term phonon is not reserved for collective states only, but applies to transitions with rather pure $1p$-$1h$ character as well. The model can account not only for 1-phonon transitions, but also for multi-phonon excitations.

A characteristic feature of the QPM is a step-by-step diagonalisation of the Hamiltonian of the system. The model Hamiltonian is first introduced on the basis of nucleons moving in the mean field and interacting with one another by means of a residual interaction

$$\boldsymbol{H} = \boldsymbol{H}_{\text{s.p.}} + \boldsymbol{H}_{\text{pair}} + \boldsymbol{H}_{\text{r.i.}}. \tag{2.61}$$

The first term in Eq. (2.61) corresponds to the average field for protons (p) and neutrons (n). It can be expressed in terms of operators for creation $\mathbf{a}^{+}_{jm\tau}$ and annihilation $\mathbf{a}_{jm\tau}$ of particles on the level of the average field with quantum numbers $j \equiv [n, l, j]$ and m in the form

$$\boldsymbol{H}_{\text{s.p.}} = \sum_{\tau}^{n,p} \sum_{j,m} E_{j\tau} \mathbf{a}^{+}_{jm\tau} \mathbf{a}_{jm\tau}, \tag{2.62}$$

where E_j is the energy of the single-particle level degenerated in spherical nuclei with respect to the magnetic quantum number m, and $\tau = -1(+1)$ refers to neutrons (protons).

The second term of Eq. (2.61) represents the residual interaction, responsible for pairing in non-magic nuclei. It is described by monopole pairing with a fixed matrix

element $G_\tau^{(0)}$ which is treated as a parameter to be adjusted to experimental pairing energies

$$\boldsymbol{H}_{\rm pair} = \sum_{\tau}^{n,p} G_\tau^{(0)} \sum_{jj'} \sqrt{(2j+1)(2j'+1)} [\mathbf{a}^+_{jm\tau}\mathbf{a}^+_{j-m\tau}]_{00} [\mathbf{a}_{j'-m\tau}\mathbf{a}_{j'm\tau}]_{00}, \qquad (2.63)$$

with

$$[\mathbf{a}^+_{jm\tau}\mathbf{a}^+_{j'm'\tau}]_{\lambda\mu} = \sum_{m,m'} C^{\lambda\mu}_{jmj'm'} \mathbf{a}^+_{jm\tau}\mathbf{a}^+_{j'm'\tau}, \qquad (2.64)$$

where $C^{\lambda\mu}_{jmj'm'}$ are Clebsch-Gordan coefficients. The pairing term gives a non-zero contribution for open proton or neutron systems in the case of semi-magic nuclei. Since the QPM is preferably applied in medium and heavy nuclei with filling of different subshells of neutrons and protons, the neutron-proton monopole pairing is usually neglected.

The third term of Eq. (2.61) characterises the residual interaction $\boldsymbol{H}_{\rm r.i.}$. It is taken in a separable form in order to allow for multipole decomposition. Its part in the particle-hole channel can be expressed as

$$\boldsymbol{H}^{(p-h)}_{\rm r.i.} = \sum_{\lambda\mu} \sum_{\tau\rho}^{\pm 1} ((1-p)\kappa_0^\lambda + \rho\kappa_1^\lambda) \boldsymbol{M}^+_{\lambda\mu}(\tau) \boldsymbol{M}_{\lambda\mu}(\tau\rho), \qquad (2.65)$$

where $\kappa^\lambda_{0(1)}$ are the coupling constants, which determine the strength of isoscalar (isovector) residual interaction and $\rho = 0(1)$ for isoscalar (isovector) transitions. The multipole operator $\boldsymbol{M}^+_{\lambda\mu(\tau)}$ is given by

$$\boldsymbol{M}^+_{\lambda\mu}(\tau) = \sum_{j,m,j',m'} < jm\tau | i^\lambda f^\tau_\lambda(r)\, \boldsymbol{Y}_{\lambda\mu}(\Omega) | j'm'\tau > \mathbf{a}^+_{jm\tau}\mathbf{a}_{j'm'\tau} \qquad (2.66)$$

for natural parity states and for unnatural-parity states by

$$\boldsymbol{M}^{+}_{\lambda\mu}(\tau) = \sum_{j,m,m',lm1} < jm\tau|i^l f^{\tau}_{l}(r)[\sigma.\boldsymbol{Y}_{lm1}(\Omega)]_{\lambda\mu}|j'm'\tau > \mathbf{a}^{+}_{jm\tau}\mathbf{a}_{j'm'\tau}. \qquad (2.67)$$

The function $f^{\tau}_{\lambda}(r)$ is a radial form factor which is taken either in form r^{λ} or as a derivative of the central part of the average field $f^{\tau}_{\lambda}(r) = \mathrm{d}U^{\tau}(r)/dr$.

The solution of the Schrödinger equation is obtained by means of iterative (step-by-step) diagonalisation of the model Hamiltonian given by Eq. (2.61). The first two terms are diagonalised at the beginning. For this purpose, the Bogoliubov canonical transformation from particle creation (annihilation) operators to quasi-particle creation (annihilation) operators is applied

$$\mathbf{a}^{+}_{jm\tau} = u_j\alpha^{+}_{jm\tau} + (-1)^{j-m}v_j\alpha_{j-m\tau}. \qquad (2.68)$$

The values u^2_j and v^2_j correspond to occupation probabilities for particles and holes in the shell j. The ground state of even-even nuclei is considered as quasi-particle vacuum $\alpha_{jm\tau}|\rangle_q \equiv 0$. The energy of the ground state is then minimised

$$\delta\left\{\langle|\boldsymbol{H}_{\mathrm{s.p.}} + \boldsymbol{H}_{\mathrm{pair}}|\rangle_q + \sum_j \mu_j(u^2_j + v^2_j - 1)\right\} = 0, \qquad (2.69)$$

where μ_j represents the Lagrange coefficients. The resulting well-known BCS equations can be solved to provide the correlation functions $C_\tau = G^{(0)}_\tau \sum_j u_j v_j$ and chemical potentials λ_τ for neutron and proton systems. The coefficients of the Bogoliubov transformation can be calculated from these values according to

$$v^2_j = \frac{1}{2}\left(1 - \frac{E_{j\tau} - \lambda_\tau}{\epsilon_{j\tau}}\right), u^2_j = 1 - v^2_j, \qquad (2.70)$$

where $\epsilon_{j\tau}$ is the quasi-particle energy

$$\epsilon_{j\tau} = \sqrt{C_\tau^2 + [E_{j\tau} - \lambda_\tau]^2}. \tag{2.71}$$

Having diagonalised the first two terms of the model Hamiltonian, one can write

$$\boldsymbol{H}_{\text{s.p.}} + \boldsymbol{H}_{\text{pair}} = \sum_{\tau}^{n,p} \sum_{j,m} \epsilon_{j\tau} \alpha^+_{jm\tau} \alpha_{jm\tau}. \tag{2.72}$$

Since the ground state is determined as a quasi-particle vacuum, the simplest excited states in the nucleus are two quasi-particle states $\alpha^+_{jm\tau}\alpha^+_{j'm'\tau}|\rangle_q$ which correspond to particle-hole transitions if monopole pairing vanishes. For collective transitions the process can also be described as creation of a phonon. Moreover, one may map into the space of quasi-boson operators and introduce the following phonon operator for multipolarity λ and projection μ

$$\boldsymbol{Q}^+_{\lambda\mu i} = \frac{1}{2} \sum_{\tau}^{n,p} \sum_{jj'} \psi^{\lambda i}_{jj'\tau} [\alpha^+_{j\tau}\alpha^+_{j'\tau}]_{\lambda\mu} - (-1)^{\lambda-\mu} \phi^{\lambda i}_{jj'\tau} [\alpha_{j'\tau}\alpha_{j\tau}]_{\lambda-\mu}. \tag{2.73}$$

The total number of different phonons for a given λ should be equal to the sum of neutron and proton two quasi-particle states coupled to the same angular momentum. An index i, so-called root quantum number, is used to number these phonons. The phonons $\boldsymbol{Q}^+_{\lambda\mu i}$ in Eq. (2.73) are made up only from proton-proton and neutron-neutron two quasi-particle congurations $[\alpha^+_{j\tau}\alpha^+_{j'\tau}]_{\lambda\mu}$. The coefficients $\psi^{\lambda i}_{jj'\tau}$ and $\phi^{\lambda i}_{jj'\tau}$ can be obtained by diagonalisation of the Hamiltonian in the space of one-phonon states $\boldsymbol{Q}^+_{\lambda\mu i}|\rangle_{ph}$ using the variation procedure

$$\delta \left\{ \langle| \boldsymbol{Q}_{\lambda\mu i} \boldsymbol{H} \boldsymbol{Q}^+_{\lambda\mu i}|\rangle_{ph} - \left(\frac{\omega_{\lambda i}}{2}\right) \left[\sum_{jj'} (\psi^{\lambda i}_{jj'\tau})^2 - (\phi^{\lambda i}_{jj'\tau})^2 - 2 \right] \right\} = 0, \tag{2.74}$$

where $\omega_{\lambda i}$ is the energy of the i-th phonon. This procedure yields the well-known RPA equations, whose solutions for each multipolarity λ^π give the spectrum of one-phonon excitations $\omega_{\lambda i}$.

For realistic calculations, the average field for neutrons and protons is approximated by a phenomenological Woods-Saxon potential with parameters from [Pon79]

$$U^{\tau}(r) = \frac{V_0^{\tau}}{1 + e^{(r-R_0^{\tau})/a_0^{\tau}}} - \frac{\hbar^2}{\mu^2 c^2} \frac{1}{r} \frac{d}{dr} \left(\frac{V_{ls}^{\tau}}{1 + e^{(r-R_{ls}^{\tau})/a_{ls}^{\tau}}} \mathbf{l}.\mathbf{s} \right) + V_{\text{Coul}}(r) \tag{2.75}$$

including a central, a spin-orbit and a Coulomb term, respectively.

The present work deals with Giant Resonances (GRs). GRs are characterised by many $1p$-$1h$ amplitudes which basically contribute in phase to wave functions of phonons in the resonance region and therefore describe a collective motion of the nucleus. Complex configurations, e.g. two-phonon states, are not so important for the description of global properties of the GDR such as the energy-weighted sum rule or the centroid energy. However, it is necessary to take them into account in order to explain the experimentally observed strength fragmentation, i.e. the fine structure of the giant resonance. After solving the RPA equations the diagonalised model Hamiltonian in the space of one-phonon states can be rewritten in terms of the phonon operators

$$\boldsymbol{H} = \sum_{\lambda\mu i} \omega_{\lambda i} \boldsymbol{Q}^{+}_{\lambda\mu i} \boldsymbol{Q}_{\lambda\mu i} + \boldsymbol{H}_{\text{int.}}, \tag{2.76}$$

where $\boldsymbol{H}_{\text{int.}}$ contains the remaining part of the residual interaction, which cannot be projected onto the space of the phonon operators. One can expand it in an infinite sum of even-number phonon operators. By keeping only the first term of the expansion, i.e. only two-phonon operators, one can obtain the non-diagonal terms of the model Hamiltonian $\boldsymbol{H}_{\text{int.}}$ in the space of phonon operators in the form

$$\boldsymbol{H}_{\text{int}} = \sum_{\substack{\lambda\mu i \\ \lambda_1\mu_1 i_1 \\ \lambda_2\mu_2 i_2}} U^{\lambda_1 i_1}_{\lambda_2 i_2}(\lambda i) \boldsymbol{Q}^{+}_{\lambda\mu i} [\boldsymbol{Q}_{\lambda_1\mu_1 i_1} \boldsymbol{Q}_{\lambda_2\mu_2 i_2}]_{\lambda\mu} + h.c., \tag{2.77}$$

where the matrix elements of the interaction between one- and two-phonon configurations $U^{\lambda_1 i_1}_{\lambda_2 i_2}(\lambda i) = \langle \boldsymbol{Q}_{\lambda\mu i} | \boldsymbol{H} | \boldsymbol{Q}^+_{\lambda_1\mu i_1} \boldsymbol{Q}^+_{\lambda_2\mu i_2}]_\lambda \rangle$ can be calculated by making use of the internal fermion structure, i.e. from the amplitudes $\psi^{\lambda_1 i_1}_{jj'}$,$\phi^{\lambda_1 i_1}_{jj'}$, $\phi^{\lambda_2 i_2}_{jj'}$, $\psi^{\lambda_2 i_2}_{jj'}$, and $\psi^{\lambda i}_{jj'}$, $\phi^{\lambda i}_{jj'}$.

Accordingly, the wave function of excited states with angular momentum λ and projection μ in even-even nuclei is written as a composition of one-phonon, two-, and three-phonon configurations:

$$|\Psi\rangle_{\lambda\mu} = \Big\{ \sum_i R_i \boldsymbol{Q}^+_{\lambda\mu i} + \sum_{\substack{\lambda_1\mu_1 i_1 \\ \lambda_2\mu_2 i_2}} P^{\lambda_1 i_1}_{\lambda_2 i_2} [\boldsymbol{Q}^+_{\lambda_1\mu_1 i_1} \boldsymbol{Q}^+_{\lambda_2\mu_2 i_2}]_{\lambda\mu} + \sum_{\substack{\lambda_1\mu_1 i_1 \\ \lambda_2\mu_2 i_2 \\ \lambda_3\mu_3 i_3}} T^{\lambda_1 i_1 \lambda_2 i_2}_{\lambda_3 i_3} [\boldsymbol{Q}^+_{\lambda_1\mu_1 i_1} \boldsymbol{Q}^+_{\lambda_2\mu_2 i_2} \boldsymbol{Q}^+_{\lambda_3\mu_3 i_3}]_{\lambda\mu} \Big\} |\rangle_{ph}. \quad (2.78)$$

The coefficients R_i, $P^{\lambda 1 i_1}_{\lambda_2 i_2}$ and $T^{\lambda_1 i_1 \lambda_2 i_2}_{\lambda_3 i_3}$, together with eigenenergies of the states Eq. (2.78), are calculated from the diagonalisation of the Hamiltonian Eq. (2.76) in the space of the states Eq. (2.78).

The density of complex (two- and three-phonon) configurations increases very rapidly with excitation energy. For this reason, the QPM calculations of the GDR in the present study have been performed on the basis of the interacting one- and two-phonon configurations only. The two-phonon configurations were made up from phonons of the multipolarity from $1^\pm$ to $9^\pm$. They were cut about 4 – 5 MeV above the centroid energy of the GDR. As a result of this truncation of complex configurations, the calculation underestimated the total width of the GDR. The single-particle basis in QPM calculations is rather complete and includes all mean-field levels from $1s_{1/2}$ to quasi-bound levels in the continuum. For this reason, no effective charges are needed as in e.g. shell-model calculations. The effective charges for the GDR are $e_N = -Z/A$ and $e_Z = N/A$ to exclude the centre-of-mass motion.

2.5.2 Equation of Motion Phonon Method (EMPM)

Initially a Hamiltonian, H, was used

$$H = H_0 + V. \tag{2.79}$$

In the coupled j - j scheme the one- and two-body pieces assume the second quantised form

$$H_0 = \sum_r [r]^{1/2} \epsilon_r (a_r^\dagger \times b_r)^0, \tag{2.80}$$

$$V = -\frac{1}{4} \sum_{rsqt}^{\Gamma} [\Gamma]^{1/2} V_{rsqt}^{\Gamma} [(a_r^\dagger \times a_s^\dagger)^\Gamma \times (b_q \times b_t)^\Gamma]^0, \tag{2.81}$$

where

$$\begin{aligned} V_{rsqt}^{\Gamma} &= \langle (q \times t)^\Gamma | V | (r \times s)^\Gamma \rangle \\ &- (-)^{r+s-\Gamma} \langle (q \times t)^\Gamma | V | (s \times r)^\Gamma \rangle. \end{aligned} \tag{2.82}$$

Following the notation of French [Fre65] and putting $b_r = (-)^{j_r+m_r} a_{j_r-m_r}$ and $[\Gamma] = 2\Gamma + 1 = (2J_\Gamma + 1)$.

The two-body potential Eq. (2.81) can be written in the recoupled form

$$V = \frac{1}{4} \sum_{rsqt\sigma} [\sigma]^{1/2} F_{rsqt}^{\sigma} [(a_r^\dagger \times b_s)^\sigma \times (a_q^\dagger \times b_t)^\sigma]^0, \tag{2.83}$$

where

$$F_{rsqt}^{\sigma} = \sum_{\Gamma} [\Gamma] (-)^{r+t-\sigma-\Gamma} W(rsqt; \sigma\Gamma) V_{rsqt}^{\Gamma} \tag{2.84}$$

and $W(rsqt;\sigma\Gamma)$ are Racah coefficients.

The primary aim of this method is to generate a basis of n-phonon states $|n;\beta\rangle$ so composed

$$|n;\beta\rangle = \sum_{\lambda\alpha} C^{\beta}_{\lambda\alpha} \left\{ O^{\dagger}_{\lambda} \times |n-1,\alpha\rangle \right\}^{\beta}, \tag{2.85}$$

where the TDA particle-hole (ph) phonon operator

$$O^{\dagger}_{\lambda} = \sum_{ph} c^{\lambda}_{ph} (a^{\dagger}_{p} \times b_{h})^{\lambda} \tag{2.86}$$

acts on the $(n-1)$-phonon states $|n-1,\alpha\rangle$.

The process commences with writing the equations of motion

$$\langle n,\beta| \left\{ [H, O^{\dagger}_{\lambda}] \times |n-1,\alpha\rangle \right\}^{\beta} = (E_{\beta} - E_{\alpha}) \langle n,\beta| \left\{ O^{\dagger}_{\lambda} \times |n-1,\alpha\rangle \right\}^{\beta}. \tag{2.87}$$

Using the Wigner-Eckart theorem one obtains

$$\langle n,\beta \| [H, O^{\dagger}_{\lambda}] \| n-1,\alpha\rangle = (E_{\beta} - E_{\alpha}) \langle n,\beta \| O^{\dagger}_{\lambda} \| n-1,\alpha\rangle. \tag{2.88}$$

Through the expansion of the commutator and subsequently inverting Eq. (2.86) to express the ph operators present in the expansion in terms of the phonon operators $O^{\dagger}_{\lambda}$, one gets [Bia12a]

$$\sum_{\lambda'\gamma} \mathcal{A}^{\beta}(\lambda\alpha, \lambda'\gamma) X^{\beta}_{\lambda'\gamma} = E_{\beta} X^{\beta}_{\lambda\alpha}, \tag{2.89}$$

where

$$X^{\beta}_{\lambda\alpha} = \langle n,\beta \| O^{\dagger}_{\lambda} \| n-1,\alpha\rangle. \tag{2.90}$$

The above amplitudes are connected to the expansion coefficients $C^{\beta}_{\lambda\alpha}$ of the states $|n;\beta\rangle$ [Eq. (2.85)] by

$$X^{\beta}_{\lambda\alpha} = \sum_{\lambda'\alpha'} \mathcal{D}^{\beta}(\lambda\alpha, \lambda'\alpha') C^{\beta}_{\lambda'\alpha'}, \tag{2.91}$$

where

$$\mathcal{D}^{\beta}(\alpha\lambda; \alpha'\lambda') = [\langle n-1, \alpha'| \times O_{\lambda'}]_{\beta} [O^{\dagger}_{\lambda} \times |n-1'\alpha\rangle]_{\beta} \tag{2.92}$$

is the metric matrix.

The matrix $\mathcal{A}$ is expressed as:

$$\mathcal{A}^{\beta}(\lambda\alpha, \lambda'\gamma) = (E_{\lambda} + E_{\alpha})\delta_{\lambda\lambda'}\delta_{\alpha\gamma} + \sum_{\sigma} W(\beta\lambda'\alpha\sigma; \gamma\lambda)\mathcal{V}^{\sigma}_{\lambda\alpha,\lambda'\gamma}. \tag{2.93}$$

The phonon-phonon potential is defined by

$$\mathcal{V}^{\sigma}_{\lambda\alpha;\lambda'\gamma} = \sum_{rs} \mathcal{V}^{\sigma}_{\lambda\lambda'}(rs)\rho^{(n)}_{\alpha\gamma}([r \times s]^{\sigma}), \tag{2.94}$$

where

$$\mathcal{V}^{\sigma}_{\lambda\lambda'}(rs) = \sum_{tq} \rho_{\lambda\lambda'}([q \times t]^{\sigma}) F^{\sigma}_{qtrs} \tag{2.95}$$

and

$$\begin{aligned} \rho_{\lambda\lambda'}([r \times s]^{\sigma}) &= \langle \lambda' \| (a^{\dagger}_{r} \times b_{s})^{\sigma} \| \lambda \rangle \\ &= [\lambda\lambda'\sigma]^{1/2} \sum_{t} c^{\lambda}_{ts} c^{\lambda'}_{tr} W(\lambda' t\sigma s; r\lambda). \end{aligned} \tag{2.96}$$

Here it implies $t = p$ when $(rs) = (hh')$ and $t = h$ when $(rs) = (pp')$.

The n-phonon density matrix is written as [Bia12b]:

$$\rho^{(n)}_{\alpha\alpha'}([r \times s]^{\sigma} = \langle n;\alpha' \| [a^{\dagger}_{r} \times b_{s}]^{\sigma} \| n;\alpha\rangle \cdot \tag{2.97}$$

In [Bia12a], the formal analogy of the structure of the phonon matrix $\mathcal{A}^{\beta}(\lambda\alpha,\lambda'\alpha')$ with the form of the TDA matrix $\mathcal{A}^{\lambda}(ph;p'h')$ was noted. Formally, the former is deduced from the latter by replacing the ph energies with the sum of phonon energies and the ph interaction with a phonon-phonon interaction.

The subsequent step involves expressing the $X^{\beta}_{\lambda\alpha}$ amplitudes in terms of the coefficients $C^{\beta}_{\lambda\alpha}$. The outcome yields the generalised eigenvalue equation

$$\mathcal{H}C = (\mathcal{A}\mathcal{D})C = EC \tag{2.98}$$

or, more explicitly,

$$\begin{aligned} \sum_{\lambda'\alpha'} \mathcal{H}^{\beta}(\lambda\alpha,\lambda'\alpha')C^{\beta}_{\lambda'\alpha'} &= \sum_{\lambda'\alpha'} (A\mathcal{D})^{\beta}(\lambda\alpha,\lambda'\alpha')C^{\beta}_{\lambda'\alpha'} \\ &= E_{\beta} \sum_{\lambda'\alpha'} \mathcal{D}^{\beta}(\lambda\alpha,\lambda'\alpha')C^{\beta}_{\lambda'\alpha'}. \end{aligned} \tag{2.99}$$

Recursive formulas hold for all quantities and consequently, the eigenvalue Eq. (2.100) can be solved iteratively once the TDA phonons are generated.

The procedure outlined in [And07, And08] describes the removal of the redundant states on the basis of the Cholesky decomposition method. In this method a basis of linear independent states $O^{\dagger}_{\lambda}|n-1;\alpha\rangle$ is selected and the physical subspace of the correct dimensions $N_n < N_r$ is spanned, hence, enabling one to construct a $N_n \times N_n$ nonsingular matrix D_n. By left multiplication in the N_n-dimensional subspace one obtains from Eq. (2.98)

$$[\mathcal{D}_n^{-1}(\mathcal{A}\mathcal{D})]C = EC. \tag{2.100}$$

Only the coefficients $C^{(\beta)}_{\lambda\alpha}$ of the N_n-dimensional physical subspace can be determined by this equation. The remaining redudant $N_r - N_n$ coefficients are undetermined and as a result can be safely equatted to zero. The eigenvalue problem is thereby solved exactly. A set of orthonormal multiphonon states $|0\rangle, |1,\lambda\rangle, ...|n,\alpha\rangle...$ is therefore, generated.

In such a basis, the resulting Hamiltonian takes a simple form and can be easily diagonalised to yield eigenfunctions of the form

$$|\Psi_\nu\rangle = \sum_{n\alpha} C^{(\nu)}_\alpha |n;\alpha\rangle. \tag{2.101}$$

The above formula holds also for the ground state which, therefore, is explicitly correlated. The eigenstates obtained may be used to compare the transition amplitudes. In the coupled scheme, the one-body operator is defined by [Bia12b]:

$$\mathcal{M}(\lambda) = \frac{1}{[\lambda]^{1/2}} \sum_{rs} \langle r\|\mathcal{M}_\lambda\|s\rangle [a^\dagger_r \times a_s]^\lambda. \tag{2.102}$$

The reduced transition transition amplitudes are expressed as

$$\langle \Psi_{\nu_f J_f}\|\mathcal{M}(\lambda)\|\Psi_{\nu_i J_i}\rangle = \sum_{(n_i\alpha)(n_f\beta)} C^{(\nu_i)}_\alpha C^{(\nu_f)}_\beta \langle n_f, _f\, \|\mathcal{M}(\lambda)\|n_i,\alpha J_i\rangle, \tag{2.103}$$

where the matrix elements of $\mathcal{M}(\lambda)$ between multiphonon states are

$$\begin{aligned}
\langle n_f;\beta J_f\|\mathcal{M}(\lambda)\|n_i;\alpha J_i\rangle &= [\lambda]^{-1/2}[\delta_{n_f n_i} \sum_{rs} \langle r\|\mathcal{M}_\lambda\|s\rangle \rho^{(n_i)}_{\alpha\beta}([r\times s]^\lambda) \\
&+ \delta_{n_f(n_i+1)} \sum_x \mathcal{M}[0 \longrightarrow (x\lambda)] X^\beta_{(x\lambda)\alpha} \\
&+ \delta_{n_f(n_i-1)} (-)^{J_f - J_i} \sum_x \mathcal{M}[0 \longrightarrow (x\lambda)] X^\alpha_{(x\lambda)\beta}].
\end{aligned} \tag{2.104}$$

The first is a scattering term where states with the same number of phonons are coupled through the single-particle transition matrix elements, $\langle s|\mathcal{M}_\lambda|r\rangle$, weighted

by the particle or hole density matrices. the other two terms contain the TDA transition amplitudes

$$\begin{aligned} \mathcal{M}[0 \longrightarrow (x\lambda)] &= \langle x\lambda \| \mathcal{M}(\lambda) \| 0 \rangle \\ &= \sum_{ph} c_{ph}^{(x\lambda)} \langle p \| \mathcal{M}_\lambda \| h \rangle. \end{aligned} \tag{2.105}$$

2.6 Extraction of characteristic energy scales

Characteristic energy scales extracted from different nuclei across the periodic table are important tools in studying the various damping mechanisms which take place in atomic nuclei. A detailed description of the plethora of techniques that were suggested for extracting these energy scales can be found in Ref. [She08] for more detailed discussion. Amongst all the approaches, Fourier analysis has had extraordinary success in many different scientific fields. It has been used in time-sequence data sets in order to determine dominant periodicities from the power spectrum extracted. However, its disadvantage is that of failure to identify some scales in specific regions of the energy spectrum that will be analysed. As a result wavelet analysis was found to be a very promising tool in the detailed study of energy scales due to its ability to extract both position and localisation of multi-scale structures simultaneously.

2.6.1 Fourier Transform

The Fast Fourier Transform (FFT) is a mathematical transformation whose strength strongly depends on its flexibility to relate with some very important pairs of physical variables, namely time and frequency. In that context, it is possible to transform the results as a function of energy and express them either as a function of frequency or as a function of wavelength (1/frequency) in the corresponding energy units. It should be mentioned that the signals to be analysed should be periodic [Mor94]. Despite its functionality, the Fourier transform has several limitations:

1. The technique can not accurately represent functions that have non-periodic components that are localised in time or space,

2. It is based on the assumption that the signal is periodic and of infinite length, and

3. The FFT technique is unable to provide any information about the time dependence of a signal, in the case of stationary signal and, therefore, fails to give a time evolution of the frequency pattern.

2.6.1.1 Discrete Fourier Transform

Given an input data sequence of length N, the Discrete Fourier Transform (DFT) is mathematically defined as:

$$X(k) = \sum_{n=1}^{N} x(n) exp(-2\pi i)(k-1)\left(\frac{n-1}{N}\right), \qquad 1 \leq k \leq N, \qquad (2.106)$$

where function, $X(k)$ represents the Fourier coefficients or harmonics. The functions $x(n)$ and $X(k)$ are complex sequencies and are known as time-domain and frequency-domain data, respectively.

2.6.1.2 Power spectrum

A Fourier transformation that is performed on a time series yields a complex vector. In addition, a Fourier transform of the form $\hat{f}(k)$ on a function $f(x)$ of quantity x can be related to the corresponding Fourier power spectrum $P_f(k)$ as [Mat07]:

$$P_f(k) = |\hat{f}(k)\hat{f}^*(k)|, \qquad (2.107)$$

up to some normalisation of the spectrum. The absolute value of the complex vector is given by the parameter P which is known as the power. Here, (1/frequency) gives the wavelength from an energy spectrum, therefore, allowing the production of a power spectrum against characteristic energy scales in units of energy (keV or MeV).

2.6.2 Wavelet transform analysis

Wavelet transform is more flexible and particularly useful for the analysis of transients, aperiodicity and other non-stationary signal features. It is classified into two classes: Continuous Wavelet Transform (CWT) and Discrete Wavelet Transform (DWT). The two wavelet transforms have one common use, they can be utilised in the representation of continuous position spectra. In general, CWT can be applied over every possible scale and translation while on the other hand the DWT is applicable only on specific subset of scale and translation values or representation grid. Wavelets are powerful statistical tools which can be used in a wide range of areas namely, signal processing, data compression, smoothing and image denoising, fingerprint verification, speech recognition, etc.

2.6.2.1 Some advantages of the Wavelet Transform Theory

The following advantages can be identified for Wavelet Transform Theory:

- Wavelets offer a simultaneous localisation in time and frequency domain,
- By using fast wavelet transform, it is computationally very fast,
- Wavelets have the great advantage of being able to separate the fine details in a signal. Very small wavelets can be used to isolate very fine details in a signal, while very large wavelets can identify coarse details, and
- A wavelet transform can be used to decompose a signal into component wavelets.

2.6.2.2 Theory of wavelet analysis

A wavelet can be defined as an oscillation that decays quickly and expressed as [Gro84]:

$$\psi_{b,c}(t) = \frac{1}{\sqrt{|b|}}\psi\left(\frac{t-c}{b}\right),\ b, c \in R, b \neq 0. \tag{2.108}$$

The parameter b represents the scaling (dilation) of the wavelet, and measures the degree of compression, c is the location (translation) parameter which determines the time location of the wavelet and $\psi(t)$ is the basis function of a wavelet. A wavelet function, $\psi(t)$ will have n vanishing moments when it satisfies the following expression [Mal92]:

$$k^{th}\text{moment} : m_{\mathrm{k}} = \int_{-\infty}^{\infty} t^{\mathrm{k}}\psi(t)\mathrm{d}t = 0 \tag{2.109}$$

where the parameter m_{k} denotes the moment. This wavelet function with n vanishing moments is normally referred to as orthogonal to polynomial of degree $n-1$, hence it can be used to suppress polynomial of degree $n-1$ through convolution. Moreover, a wavelet function with n vanishing moments can be written as the nth-order differentiation of a function $\theta(t)$ [Mal98]:

$$\psi(t) = (-1)^n \frac{d^n\theta(t)}{dt^n}, \tag{2.110}$$

where $\theta(t)$ is a function with fast decay and whose integral is a non-zero constant.

If the wavelet function has n vanishing moments, the wavelet transform would be [Mal98]:

$$Wf(b,c) = f^*\psi_b(c) = f^*\left(b^n\frac{d^n\theta_b}{dt^n}\right)(c) = b^n\frac{d^n}{dt^n}(f^*\theta_b)(c), \tag{2.111}$$

where * denotes the operator of convolution, and $\psi_b(t) = \frac{1}{b}\psi\left(\frac{t}{b}\right)$ and $\theta_b(t) = \frac{1}{b}\theta\left(\frac{t}{b}\right)$. Therefore, one can get the nth-order derivative calculation of an analytical signal *via* one wavelet transform by using a wavelet function with n vanishing moments.

A large number of wavelets have been used recently and it has been shown that these wavelets are of great help in unraveling some of the important properties of atomic nuclei. The studies on wavelet transforms have revealed that the commonly used

wavelet functions were suitable in smoothing and differentiation processes. On the other hand, the number of vanishing moments (n) of a wavelet is a direct indicator of the order of the derivative that a specific wavelet will determine. It should be noted that the amount of smoothing is determined by the choice of the wavelet and its associated width. Figure 2.9 gives some examples of functions that have been widely used in wavelet analysis.

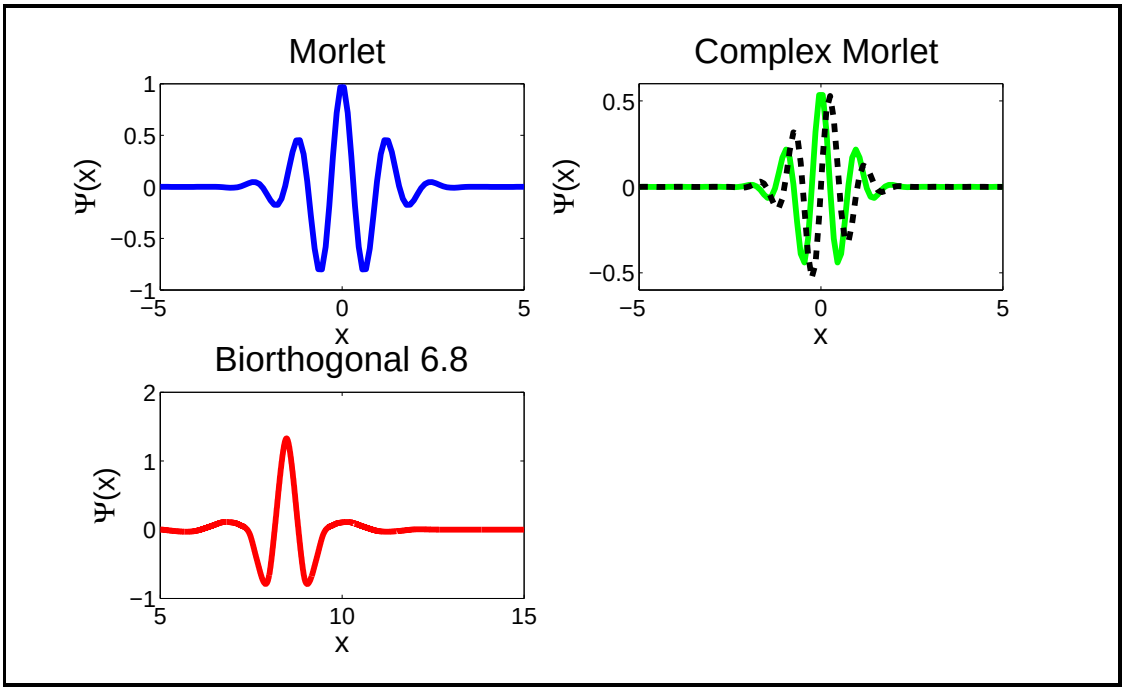

Figure 2.9: Illustration of the principles of wavelet analysis and wavelet families. Real (k= 5, see Eq. (2.114)) and complex Morlet ($f_c = 1$, $f_b = 1$, see Eq. (2.115)) wavelets are the products of cosine and Gaussian functions. The real and the imaginary parts of the complex Morlet are shown in solid and dashed lines respectively. The Biorthogonal 6.8 wavelet has an antisymmetrical shape but no analytical expression.

2.6.2.3 Continuous Wavelet Transform (CWT)

Continuous wavelets are more desirable and useful when high temporal and spectral resolution and/or phase information is required. The results from CWT are fairly clear and easy to interpret. However, its computational strength depends on the complexity of the problem i.e. huge arrays of the wavelet coefficients may need a significant strength of computational power. Its major disadvantage is that only an

approximate reconstruction of the signal from the obtained wavelet coefficients can be perfomed. Here, the Continuous Wavelet Transform can be defined as the sum over all time ($-\infty$ to $+\infty$) of the signal multiplied by a scaled, shifted version of the wavelet function:

$$C(b,c) = \int S(t)\frac{1}{\sqrt{b}}\psi\left(\frac{t-c}{b}\right)dt, \tag{2.112}$$

where b is the scale (dilation parameter) and c is the position (translation parameter) and are equivalent to δE and E_{x}, respectively, in the analysis of energy scale. The parameter $S(t)$ is the signal to be transformed. By folding the original energy spectrum $\sigma(E)$ with a chosen wavelet function ψ, one can generate the coefficients using the following equation:

$$C(E_{\mathrm{x}},\delta E) = \frac{1}{\sqrt{\delta E}}\int \sigma(E)\psi\left(\frac{E_{\mathrm{x}}-E}{\delta E}\right)dE. \tag{2.113}$$

The parameters E_{x} and δE represent the excitation energy and bin size, respectively and these can be varied continuously or in discrete steps j, where $E = 2j$, $j = 1$, 2, 3, . . . , and $E_{\mathrm{x}} = \delta E$. The choice of wavelet is made based on its mathematical properties among which are moments, compact support and the regularity of a signal [Mat07]. However, complex wavelets have been found to be very effective in producing a complex CWT analysis, since one can examine the phase of the result.

The Real Morlet wavelet was originally introduced by Jean Morlet in 1982 and it comes from utilising a periodic wave and subsequently localising the periodic wave with a Gaussian (Bell-shaped) envelope. It can be expressed as [Mor82]:

$$\Psi(x) = \frac{1}{\pi^{1/4}}e^{-\frac{x^2}{2}}cos(ikx). \tag{2.114}$$

The parameter k weighs the resolution in scales *versus* the resolution in localisation. In order to satisfy the admissibility conditions $k \leq 5$ must be fulfilled [Mat07].

Furthermore, the complex Morlet wavelet [Teo98] takes the form

$$\Psi(x) = \frac{1}{\sqrt{\pi f_b}} e^{2i\pi f_c x} e^{-\frac{x^2}{f_b}}, \tag{2.115}$$

where f_{b} is the wavelet bandwidth parameter and f_{c} is the wavelet centre frequency.

2.6.2.4 Discrete Wavelet Transform (DWT)

The Discrete Wavelet Transform (DWT) in comparison with CWT has been shown to be a better method in representing data in areas such as compression and filtering. It can be performed quickly and can produce a very sparse representation of large amounts of data, conserving at the same time the characteristic features. Another important aspect of DWT is its configuration in powers of 2. However, the DWT has the following short comings:

1. The scale resolution is limited since one needs to increase the bandwidth of the filter by a factor of two at each new scale,

2. It does not possess translational invariance, i.e. the results will depend on the selected interval and how this interval is divided into separate subregions, and

3. It can be performed only with some specific wavelets from which an orthogonal basis of functions can be constructed.

From Eq. (2.112), if b and c assume only discrete values then we have

$$\delta E_k = 2^k \Delta \tag{2.116}$$

and

$$E_{xk} = k.\delta E_k,\ k = 1, 2, ..., \tag{2.117}$$

where Δ is the bin size of the data and k specifies the number of significant sinusoidal oscillations within a Gaussian window.

The DWT can be used in the analysis or decomposition of signals and images. On the other hand, the decomposed components can be assembled back into the original signal without loss of information and this is known as either reconstruction or synthesis. The DWT separates (filters) the data down into a sequence of approximations (A_i) and details (D_i) through the use of low-pass and high-pass filters (see Ref. [She08] for more details). The mathematical process that effects the synthesis is termed the inverse discrete wavelet transform. This process is iteratively repeated to yield a multi-level decomposition (see Fig. 2.10) and is applicable for the present use in determining the background required in the extraction of level densities. Furthermore, the application of the DWT uses the property of vanishing moments fulfilled by many wavelet functions; namely

$$\int E^n \psi(E) dE = 0,\ n = 0, 1, ...m. \tag{2.118}$$

When Eq. 2.118 holds, any non-resonant background in the spectrum, whether of physical or experimental nature, does not contribute to the wavelet coefficients as long as it can be approximated by a polynomial function of order m. In the present analysis the biortogonal family of mother wavelets BIOR$Nr.Nd$ was used, where Nr indicates the nth vanishing moment with a polynomial function of order $n-1$, while Nd represents the level of decomposition [Mat07].

2.7 Extraction of level densities

Level densities are essential in describing the fundamental quantities in nuclei which are defined as complex quantum mechanical systems. Through the statistical model of nuclear reactions, these fundamental quantities (nuclear level densities) have a strong influence on the results of calculations and evaluations. Such is the case for reaction cross-sections required in a number of applications namely in astrophysical

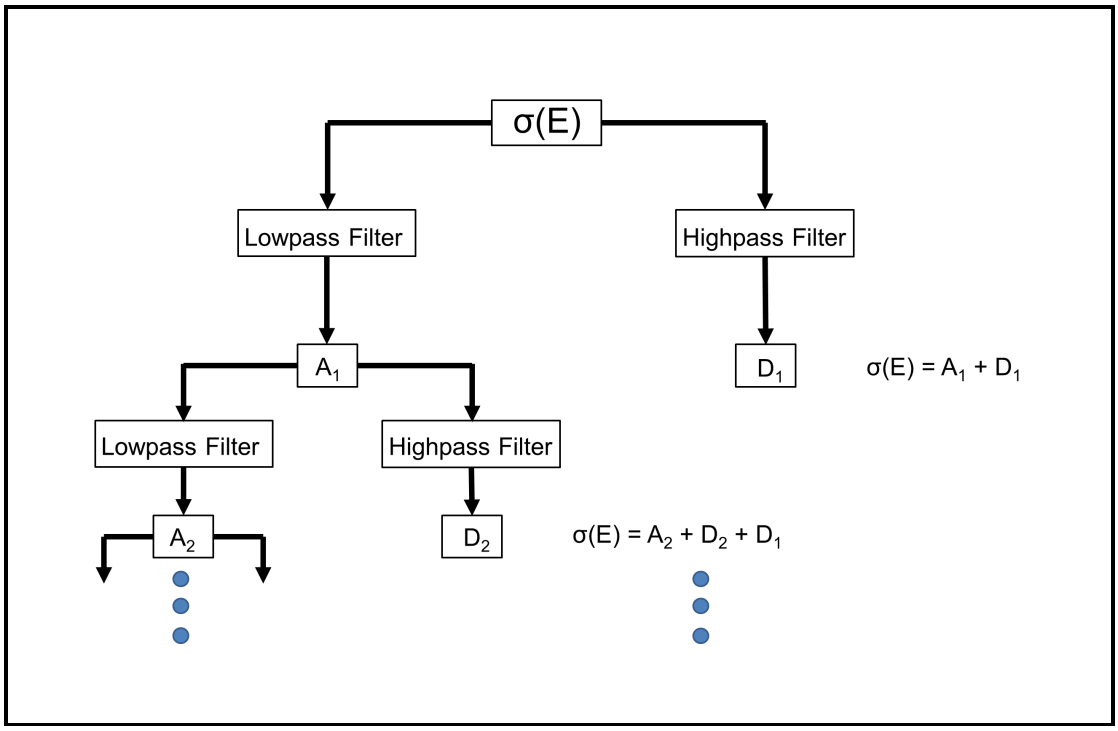

Figure 2.10: Decomposition of the original signal $\sigma(E)$ into approximations and details obtained by using the discrete wavelet transform.

calculations to determine thermonuclear rates for nucleosynthesis [Ripl06] and in fission and fusion reactor design [Bha83]. Studies from the past work have revealed that the constraints associated with satisfying both the accuracy and concise reflection of basic features of the level density behaviour can not be easily resolved at excitation energies above particle thresholds in a given nucleus. In that context, the fluctuation analysis which is a model-independent way for extracting experimental nuclear level densities is presented.

The fluctuation analysis technique has been successfully adopted in the analysis of giant resonance data [Kal05, Kal07] where spin- and parity-resolved level densities were extracted in the region of the Gamow-Teller (GT) resonances and magnetic quadrupole resonances, respectively. Moreover, one can test the theoretical models of giant resonance excitation due to the possibility of parity dependence of level densities extracted in the excitation-energy region of giant resonances in light nuclei.

The interplay between giant resonances and the contribution of the background, instrumental and continuum has been a problem in many nuclear physics experiments. In this particular analysis, the backgrounds due to the experimental uncertainties and contributions from other multipolarity giant resonances are subtracted in the excitation-energy region of interest. The shape of the background was determined in a model-independent way using the Discrete Wavelet Transform (DWT) analysis technique. The method of background subtraction is discussed fully in Sect. 4.7.2.

2.7.1 Level density models

Besides their fundamental importance in nuclear structure, nuclear level densities are the basic input parameters in nuclear reaction theory. Calculations of neutron- and proton-capture reaction rates in nuclear astrophysics require knowledge of the level densities. The high level density of nuclear states at higher excitation energies makes it difficult to identify individual states, therefore, the need for level density determination in this region of excitation energy is also of paramount importance. Furthermore, these nuclear level densities also play a vital role in inferring nuclear thermodynamic properties. Thermodynamic quantities can be employed in the investigation of the phase transition phenomena in nuclei. In the early 1930's, Bethe led some of the pioneering theoretical work whose development resulted in the Fermi Gas model [Bet37]. In his work Bethe described the nucleus as a gas of non-interacting fermions moving freely in equally spaced single-particle orbits. The level density was determined by calculating the entropy from Fermi statistics. The analytical form of the Fermi Gas model has found its application nowadays in experimental data. In the model, the density of states is the number of excited states per unit energy [Won90]. The density of states, ρ, according to the Fermi Gas model can be expressed as

$$\rho(E) = \frac{1}{12a^{1/4}E^{5/4}} exp\left(2\sqrt{aE}\right), \tag{2.119}$$

where E represents the excitation energy and a is the level density parameter. This density of states quantity (ρ) can be used in determining the rate of reactions occuring in a given energy region and to approximate the probability of finding a state at a given energy.

As a result of these assumptions, the nuclear partition function is written as a product of the individual partition functions of constituent nucleons. Then the level density is obtained by the inverse Laplace transform of the partition function. The Bethe formula predicts an exponential increase in the number of levels with excitation energy and atomic mass. This is qualitatively consistent with the experimental data. However, due to the independent-particle and equidistant-level assumptions, this formula does not take into account, e.g., odd-even and collective effects. Therefore, in order to reproduce the experimentally observed level spacings, various phenomenological modifications to Bethe's original expression were proposed, in particular to take into account shell and pairing effects. The so-called popularly used Back Shifted Fermi Gas (BSFG) model which uses a simpler approach was proposed later [Gad68, Hui69, Von69]. The BSFG model consists of a two-parameter description in which both the ground state energy correction, Δ, and the level density parameter, a, were fitted to the experimental data. This model is given by [Von69]:

$$\rho(E) = \frac{1}{12a^{1/4}(E-\Delta)^{5/4}} exp\left(2\sqrt{a(E-\Delta)}\right), \tag{2.120}$$

where both a and Δ are considered as free parameters. This model was observed to satisfactorily describe the level density values in light nuclei over the whole range of excitation energy [Dil73, Kat70, Lu72]. For that mass range, the ground state position is back-shifted by an amount of 1 – 3 MeV in order to obtain good fits to the experimental data.

Later, the development of powerful computational and theoretical methods used in calculating the level densities has led to the introduction of the two microscopic models *viz* Hartree Fock-Bogoliubov (HFB) plus Combinatorial model [Hil06] and the Hartree Fock-Bardeen-Cooper-Schrieffer (HF-BCS) model [Dem01]. The most recent developed microscopic model, the HFB plus Combinatorial [Kon08] consists of rotational and vibrational degrees-of-freedom coupled together with a combinatorial model for the occupation of single-particle states. This led to the introduction of a connection between the phenomenological level density approaches and a normalisation factor to the microscopic calculations. The calculations make a coherent use of nuclear structure properties determined within the deformed Skyrme Hartree-Fock-Bogoliubov framework. A remarkable feature of this approach is its ability to provide not only the energy and spin dependence of the level density, but also the parity dependence as well as the partial particle-hole level density that cannot be extracted in any satisfactory way from the statistical approach. To add to the list of level density models, the Shell-Model Monte Carlo (SMMC) calculations [Alh07] is another microscopic model capable of providing spin-dependent level density information of the measured nuclei.

2.7.1.1 Back-Shifted Fermi Gas (BSFG) model

This model has been successfully applied in the extraction of neutron resonance densities and low-lying states. The level density, ρ, described in terms of excitation energy E_{x} and spin J is given by [Rau97, Egi05]:

$$\rho(E_{\mathrm{x}}, J) = \frac{1}{2} F\left(E_{\mathrm{x}}, J\right) \rho\left(E_{\mathrm{x}}\right) \tag{2.121}$$

with

$$\rho(E_{\mathrm{x}}) = \frac{1}{\sqrt{2\pi\sigma}} \frac{\sqrt{\pi}}{12 a^{1/4}} exp \frac{\left(2\sqrt{a(E_{\mathrm{x}} - \delta)}\right)}{(E_{\mathrm{x}} - \delta)^{5/4}} \tag{2.122}$$

and

$$F(E_{\mathrm{x}}, J) = \frac{2J+1}{2\sigma^2} exp\left(\frac{-J(J+1)}{2\sigma^2}\right), \tag{2.123}$$

where

- $\sigma^2 = \frac{\Theta_{rigid}}{\hbar^2}\sqrt{\frac{(E_{\mathrm{x}}-\delta)}{a}}$ = spin cutoff parameter,
- $\Theta_{\mathrm{rigid}} = M_{\mathrm{exp}} A R^2$,
- δ = the back-shift energy,
- $\mathrm{R} = r_{\mathrm{o}} A^{1/3}$ = the nuclear radius,
- M_{exp} = the experimental mass of the nucleus,
- a = the level density parameter, and
- A = the nuclear mass.

The pairing gap Δ is from differences in the binding energies of neighbouring nuclei, hence the back-shift is calculated by setting

$$\delta(Z,N) = \frac{1}{2}\left(\Delta_{\mathrm{n}}(Z,N) + \Delta_{\mathrm{p}}(Z,N)\right), \tag{2.124}$$

where $\Delta_{\mathrm{n}}(Z,\ N)$ and $\Delta_{\mathrm{p}}(Z,\ N)$ are neutron- and proton-separation energy, respectively. Also, the energy-dependent level density parameter, a, can be expressed as

$$a(E_{\mathrm{x}}, Z, N) = a(A)\left(1 + C(Z,N)\frac{f(E_{\mathrm{x}}-\delta)}{E_{\mathrm{x}}-\delta}\right), \tag{2.125}$$

where $\mathrm{C} = \delta - \Delta$ represents the microscopic energy correction, and

$$a(A) = \alpha A + \beta A^{2/3} \tag{2.126}$$

$$f(E_{\rm x}-\delta) = 1 - exp\left(-\gamma(E_{\rm x}-\delta)\right)\cdot \tag{2.127}$$

The values for the parameter α, β and γ are determined by a fit to experimental s-wave neutron resonance spacings of 272 nuclei at the neutron-separation energy in Ref. [Rau97] and are given as $\alpha = 0.1337$, $\beta = -0.06571$ and $\gamma = 0.04884$.

The cumulative number of levels as a function of excitation energy ($E_{\rm x}$) can be expressed as

$$N_0(E_{\rm x}, J) = \int_0^{E_{\rm x}} \rho(E, J)dE. \tag{2.128}$$

Similarly, a relation for the mean level spacing $\langle D\rangle$ in the energy interval $[E_{\rm x}^a,\ E_{\rm x}^b]$ is given by the following:

$$\langle D\rangle = \frac{E_{\rm x}^b - E_{\rm x}^a}{N_o(E_{\rm x}^b, J) - N_o(E_{\rm x}^a, J)}. \tag{2.129}$$

2.7.1.2 Hartree-Fock-Bogoliubov (HFB) model

This is one of the microscopic nuclear models used to compute level densities. The microscopic HFB plus Combinatorial model [Hil06] computes particle-hole level densities as a function of energy, spin and parity, taking the collective behaviour of nuclei into consideration. The recent HFB calculations within the Skyrme framework are performed using an effective interaction adjusted for nuclear masses and nuclear matter properties. This microscopic approach is based on a consistent use of the shell effects, pairing correlations, deformation effects and collective excitations in both spherical and deformed nuclei. Results from this calculation have been found to be comparable with those of the BSFG calculations. In order to characterise the BSK13 force, one would need the following essential ingredients *viz* the energy per nucleon, $a_{\rm v}$, at equilibrium in symmetric nuclear matter, the corresponding density $\rho_{\rm o}$, the isoscalar and isovector effective masses and the symmetry coefficient. Moreover,

through the use of available online tables of known excitation energies [astro-ulb], one can deduce the spin- and parity-depedent level densities even for $N \backsimeq Z$ nuclei at higher excitation energies.

2.7.2 Fluctuation analysis

In order to determine the level densities in excited nuclei, fluctuation analysis is found useful especially in regions of overlapping levels. It was originally proposed as a technique to study nuclear experiments like β-delayed particle emission spectra [Jon76] and was later adopted to electron scattering experiments [Mul83] and it can be used in general for high energy-resolution spectra for nuclear reactions [Han90]. The motivation for carrying out this work is to acquire information on level densities in the excitation-energy regions other than those close to the ground state (done by counting) or near the particle thresholds. Such data are generally scarce, in particular for specific J^{π} values. Level densities of a number of nuclei in the mass range $A = 20 - 60$ have been derived from cross-sections at excitation energies around 20 MeV [Bha83] through fluctuation analysis. In this present work, the autocorrelation function from the fluctuation analysis [Han79] is used as a key tool to obtain a measure of the cross-section fluctuations with respect to a stationary mean value. The basic ideas and the assumptions behind the method are discussed below.

2.7.2.1 Conditions of applicability

In an energy region where the mean level spacing ($\langle D \rangle$) is smaller than the experimental energy-resolution (ΔE) one has to distinguish between two possible cases:

- $\langle \Gamma \rangle / \langle D \rangle \leq 1$, i.e. the mean level width $\langle \Gamma \rangle$ is smaller than the average distance between levels $\langle D \rangle$ and fluctuations emanate from the high density of non-resolved states and their incoherent overlap and

- $\langle\Gamma\rangle/\langle D\rangle > 1$, i.e the mean level width $\langle\Gamma\rangle$ is greater than average distance between levels $\langle D\rangle$, hence leading to the so-called Ericson fluctuations which are due to the coherent overlapping of the states [Eri60].

In principle, it is possible to utilise the method even in the Ericson regime, but the statistics have to be extremely high in this case [Rei00], therefore, in practice one is usually limited to the first case where $\langle\Gamma\rangle/\langle D\rangle \leq 1$. The application of the fluctuation analysis is based on the following two assumptions.

Firstly, in a highly excited nucleus with strong fluctuation configuration mixing of levels with the same spin and parity, the probability for a certain spacing between adjacent states according to the Wigner distribution is defined as [Wig65]:

$$P_{\mathrm{W}}(s) = \frac{\pi s}{2} exp\left(-\frac{\pi s^2}{4}\right), \tag{2.130}$$

where

$$s = \frac{D}{\langle D\rangle} \tag{2.131}$$

and $\langle D\rangle$ is the mean value of the resonance spacing D. This distribution has a maximum around the mean value and shows so-called repulsion, i.e. a suppression at small distances between adjacent levels. Secondly, the ground state decay widths or transition strengths obey a Porter-Thomas distribution given by [Por65]:

$$P_{\mathrm{PT}}(s) = \frac{1}{\sqrt{2\pi s}} exp\left(-\frac{s}{2}\right), \tag{2.132}$$

where

$$s = \frac{\Gamma}{\langle\Gamma\rangle} \tag{2.133}$$

and $\langle\Gamma\rangle$ is the mean value of the level width Γ. This equation predicts that weak transitions are more likely. Wigner and Porter-Thomas distributions have been applied in the estimations of mean widths and resonance spacings explained in the calculation of nuclear reaction data [Ripl06]. The two assumptions were adopted from random matrix theory (RMT) [Guh98] and based on the observation that they provide a good description of nuclear excitations in the vicinity of the neutron-separation energy [Haq82].

2.7.2.2 Methodology

The basic steps taken in the application of fluctuation analysis are briefly discussed in this subsection. Firstly, one has to subtract the background from the measured experimental (p,p$'$) spectrum in the excitation-energy region under investigation. After background subtraction, the spectrum contains the information on the nuclear excitation fluctuations. Secondly, the background subtracted spectrum is smoothed using a Gaussian function whose width, σ, is smaller than the experimental energy-resolution (ΔE) so as to eliminate contributions arising from finite statistics. The new spectrum is referred to as $g(E_{\mathrm{x}})$ hereafter. In order to remove the gross structures in the resonance the measured spectrum is also folded with a Gaussian function with a width, $\sigma_{>}$ larger than the experimental energy-resolution. The resulting spectrum is called $g_{>}(E_{\mathrm{x}})$ later. This particular spectrum defines the mean about which the original points fluctuate.

Dividing $g(E_{\mathrm{x}})$ by $g_{>}(E_{\mathrm{x}})$ allows the elimination of the long range correlations in the spectrum and this ratio yields a dimensionless stationary spectrum. This stationary spectrum fluctuates around unity and can be defined as:

$$\langle d(E_{\mathrm{x}})\rangle = \left\langle \frac{g(E_{\mathrm{x}})}{g_{>}(E_{\mathrm{x}})} \right\rangle = 1. \tag{2.134}$$

The left- and right-angle brackets in Eq. (2.134) indicate averaging over the excitation-

energy range where the level spacing is to be extracted.

The local intensity fluctuations in this stationary spectrum can be expressed in terms of an autocorrelation function

$$C(\epsilon) = \frac{\langle d(E_{\rm x}).d(E_{\rm x}+\epsilon)\rangle}{\langle d(E_{\rm x})\rangle.\langle d(E_{\rm x}+\epsilon)\rangle}, \tag{2.135}$$

where ϵ is the energy increment at excitation energy, $E_{\rm x}$ and is a measure of spectral fluctuations with respect to a local mean value. The value $(C(\epsilon)-1)$ is known as the variance, since

$$C(\epsilon=0)-1 = \frac{\langle d^2(E_{\rm x})\rangle - \langle d(E_{\rm x})\rangle^2}{\langle d(E_{\rm x})\rangle^2}. \tag{2.136}$$

This experimental autocorrelation function can be approximated by the following expression [Jon76]

$$\begin{aligned} C(\epsilon) = 1 + \frac{\alpha\langle D\rangle}{2\sigma\sqrt{\pi}} &\left\{ exp\left(-\frac{\epsilon^2}{4\sigma^2}\right) + \frac{1}{y} exp\left(-\frac{\epsilon^2}{4\sigma^2 y^2}\right)\right\} \\ &\times \left\{ -\sqrt{\frac{8}{1+y^2}} exp\left(-\frac{\epsilon^2}{4\sigma^2(1+y^2)}\right)\right\}. \end{aligned} \tag{2.137}$$

The above expression can be re-arranged and reduced to the form:

$$C(\epsilon) - 1 = \frac{\alpha\langle D\rangle}{2\sigma\sqrt{\pi}} \times f(\epsilon,\sigma), \tag{2.138}$$

where

$$y = \frac{\sigma_>}{\sigma}, \tag{2.139}$$

where the function $f(\epsilon,\sigma)$ is normalised such that $f(\epsilon=0)=1$. It is important to note that the most stable result were achieved by setting $\sigma \backsimeq \frac{1}{2}\Delta E$ and $\sigma_> = (2.5$ – $3.5)\sigma$ and this finding is in agreement with results of [Neu97]. The quantity α is

the sum of the normalised variances of the assumed spacing and transition width distributions, and is given by

$$\alpha = \alpha_{\mathrm{W}} + \alpha_{\mathrm{PT}} = 2.0 + 0.273. \tag{2.140}$$

This is true only if states of the same spin and parity, J^{π}, are present in the spectrum, in this case 1^{-} states. Thus, one either assumes this condition experimentally utilising the selectivity of specific reactions or it has to be corrected for. The mean level spacing $\langle D \rangle$ is proportional to the variance of $d(E_{\mathrm{x}})$ and can be extracted from the value $C(\epsilon = 0) - 1$. The nuclear level density can be determined from the mean level spacing as $\rho(E) = 1/\langle D \rangle$. Uncertainties in the extracted values of $\langle D \rangle$ may arise from the following sources: statistical errors, inaccuracies in defining the backgrounds, the widths of the smoothing functions, the ranges of the energy intervals, etc.

Chapter 3

Experimental equipment, techniques and procedures

Introduction

Past studies have shown that the spectroscopy of charged particles provides a potentially rich source of nuclear structure information, and extensive studies have been performed with electrons and protons as probes. The introduction of magnetic spectrometers in nuclear structure studies brought tremendous improvement in the analysis of nuclear reaction products, due to their high resolution capabilities. Spectroscopy with magnetic spectrometers has been seen to offer several advantages compared to other detection techniques such as detection based on gas ionisation, detection based on semiconductors or detection based on scintillation. Among these advantages is the strong selection of the reaction products based on their mass over charge ratio which results in the reduction of the background. This enables the detection of the reaction products at very forward scattering angles with magnetic spectrometers.

High energy-resolution measurements of inelastic proton scattering at zero degrees have presented a very difficult experimental challenge, due to the very small magnetic rigidity difference between the incident and scattered particles. Consequently, these measurements are known to be extremely sensitive to beam halo and background from scattered protons since the beam exits the spectrometer very close to the position of the focal plane detectors. Historically, zero degrees (p,p$'$) measurements at medium beam energies with reasonably low background have been successfully carried out only at 2 research institutes namely the Research Centre for Nuclear Physics (RCNP) in Osaka, Japan and the Indiana University Cyclotron Facility (IUCF) in Bloomington, Indiana, USA. However, such measurements can now also be carried out at the iThemba Laboratory for Accelerator Based Sciences (iThemba LABS) in Cape Town, South Africa [Nev11]. The considerable improvements in the stability of cyclotrons in the recent years due to the availability of efficient diagnostic tools such as the use of non-destructive diagnostic beam position monitors [Die05] and equipment for beam phase measurements [Con06], have enabled the measurements of high energy-resolution zero-degrees experimental data at iThemba LABS. Moreover, in the work presented here, two main techniques were implemented *viz* the faint-beam method and lateral dispersion matching [Fuj02b]. The latter allows the beam properties to be matched with dispersion properties of the magnetic spectrometer while the former is a unique method that uses copper meshes prior to the injection cyclotron to reduce the beam intensity by orders of magnitude without changing the beam profile. In this way the spectrometer can be used to directly observe the beam in the focal plane without damaging the detector system. This allows one to ascertain the level of dispersion matching between the beam and spectrometer.

This chapter contains a description of the experimental setup, experimental techniques, data acquisition and the experimental procedure necessary for measurements of zero degree inelastic proton scattering.

3.1 The iThemba LABS accelerator complex

The first operational circular accelerator was proposed in 1930 [Law30] by Ernest Orlando Lawrence at the University of California, Berkeley. In a simple cyclotron, the charged particles circulate in a strong magnetic field and are accelerated by electric fields in one or more gaps. After having passed a gap, the particles move inside an electrode and are screened from the electric field. When the particles exit from the screened area and enter the next gap, the phase of the time-varying voltage has changed by 180° so that the particles are again accelerated. The process is repetitive. After many turns of acceleration, resulting in an outward spiral trajectory, the particles reach the boundaries of the strong magnetic field. Here, the field is shaped so that the beam of circulating particles can emerge and be formed into an external beam.

At iThemba LABS, a national facility situated at Faure, near Cape Town, South Africa, cyclotrons produce the fast moving charged particles that are used in physics research, radioisotope production and radiotherapy. Protons, alpha particles as well as heavy ions such as oxygen, chlorine, krypton and xenon are accelerated at iThemba LABS for various purposes.

For experiments such as the one described in this thesis a proton beam produced by the MINIMAFIOS ECR ion source is injected into the K[1] = 8 MeV Solid Pole injector Cyclotron (SPC2) and pre-accelerated to the energy required by the K = 200 MeV Separated Sector Cyclotron. The accelerated beam is sent to the SSC through the K and J beamlines where it is accelerated to the desired energy of 200 MeV. The beam is then transported *via* a high-resolution double monochromator system consisting of the X, P1, P2 and S beamlines to the scattering chamber of the K600 magnetic spectrometer (see Fig. 3.1).

[1] where K is the energy constant for a magnetic device given by $K = (mE)/q^2$, where m is the mass of the particle (amu), q is its charge (C) and E is its kinetic energy (MeV).

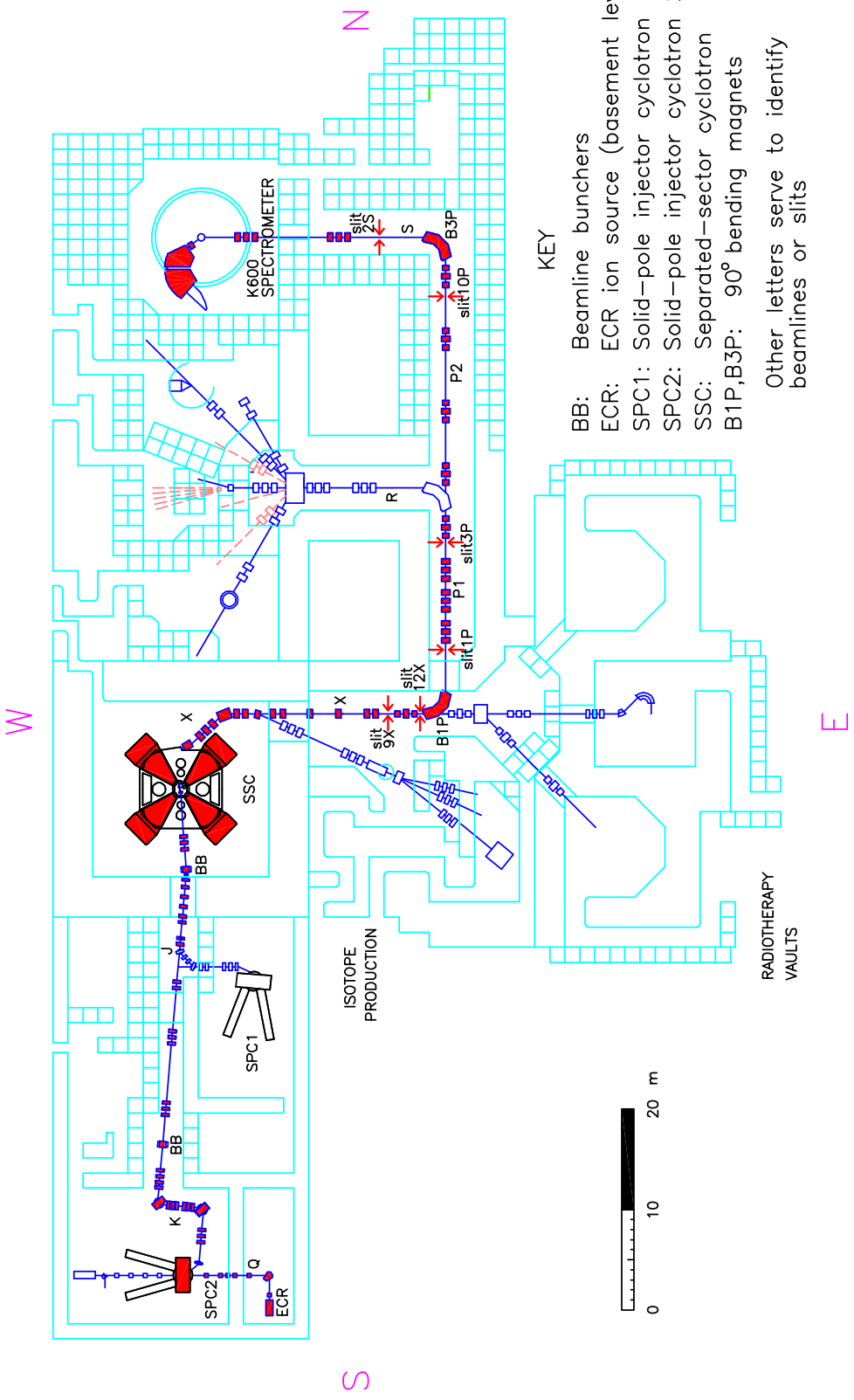

Figure 3.1: A schematic overview of the cyclotron facility at iThemba LABS.

3.1.1 The second solid-pole injector cyclotron (SPC2): K = 8 MeV

This cyclotron illustrated in Fig. 3.2, uses an external ion source (the MINIMAFIOS Electron Cyclotron Resonance ion source (ECR)) to produce and pre-accelerate heavy as well as light ion beams, which are injected axially into it. It has two sector magnets with two dees and an extraction radius of 0.476 m. Its magnetic field can be adjusted with six trim-coils, two harmonic coils and two cone coils in order to achieve the smallest width (FWHM) for the incident beam.

3.1.2 The separated-sector cyclotron (SSC): K = 200 MeV

This cyclotron has four sector magnets with sector angle of 34°. The sector angle of 34° is chosen with the aim to avoid the $\nu_z = 1$ resonance, for the 200 MeV proton beam near extraction, and the $\nu_x + 2\nu_z = 4$ inherent resonance. The resonance lines, $\nu_z = 1$ and $\nu_x + 2\nu_z = 4$ tend to cause beam loss along the beamline or severe deterioration of the beam quality at the extraction end. One should note that, an increase in the sector angle (e.g. to 36°) will cause the resonance line for the acceleration of 200 MeV protons in Fig. 3.3 to move downwards and will be very close to the $\nu_z = 1$ resonance line (This resonance line is not shown on the graph but lies on the horizontal axis of graph 3.3) and if the sector angle is lowered (e.g. to 32°) the resonance line for the acceleration of 200 MeV protons will move very close to the $\nu_x + 2\nu_z = 4$ resonance. Both these two resonances will be very harmful to the beam and will cause the beam to blow up. The $\nu_z = 1$ resonance will blow up the beam in the vertical direction and the $\nu_x + 2\nu_z = 4$ will blow up the beam in the horizontal and vertical plane. If the beam is accelerated for a long time close to these resonance lines a large part of the beam will be lost inside the machine and the quality of the beam that is extracted out of the cyclotron will be very poor [Con92]. Vacuum chambers are mounted in the pole gaps and between the magnet sectors.

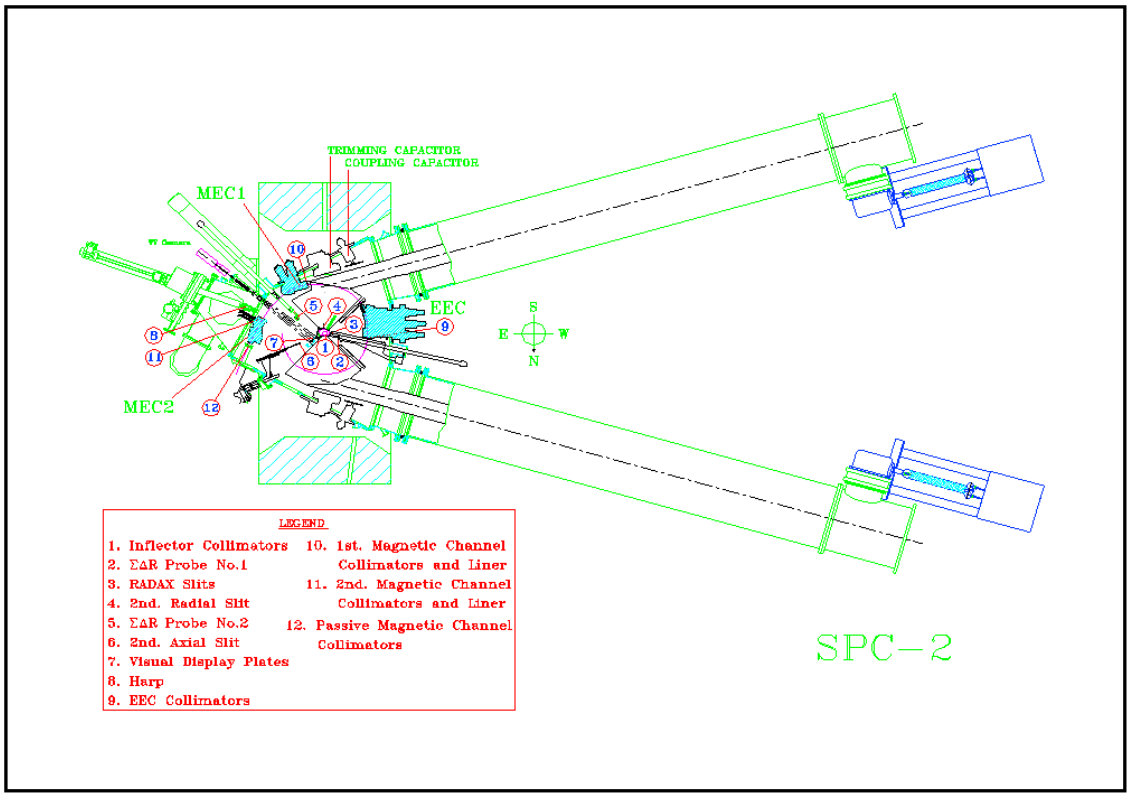

Figure 3.2: A schematic overview of the SPC2 cyclotron.

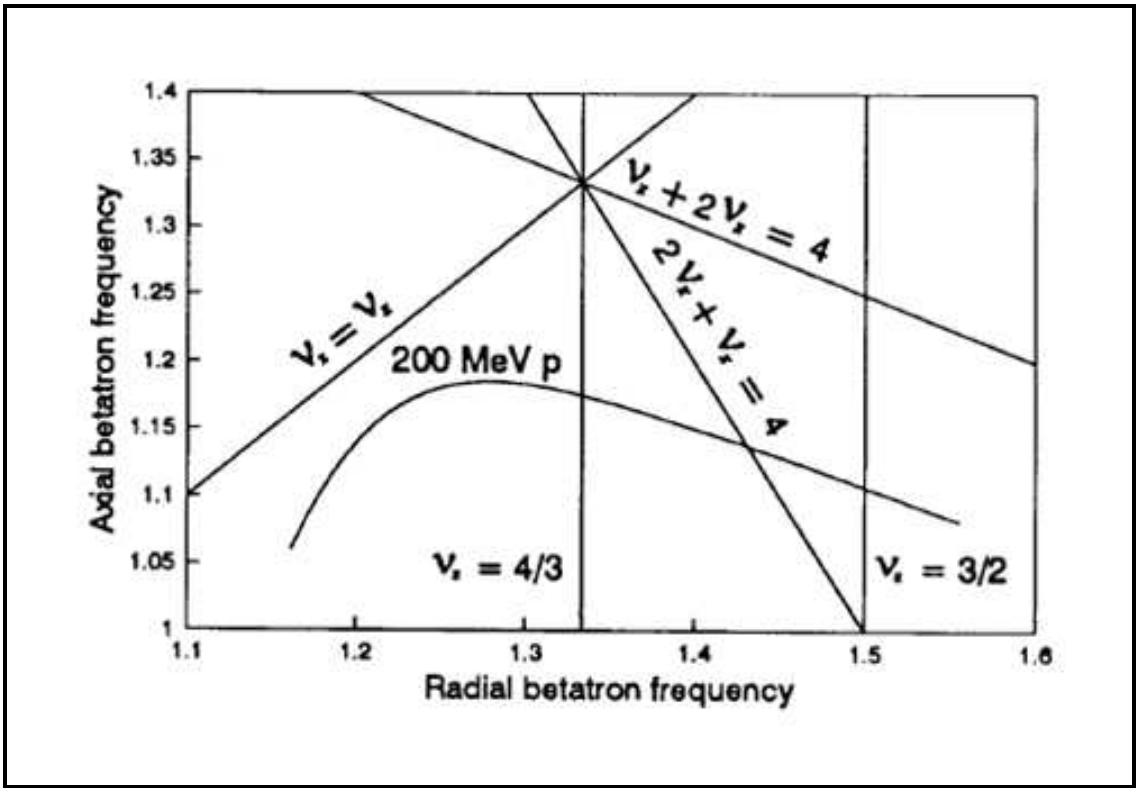

Figure 3.3: The resonance lines of importance for a 200 MeV proton beam in the SSC [Con92].

The rf system of the SSC consists two vertical half-wave ($\lambda/2$) resonators which can be tuned over the frequency range of 6 to 26 MHz. The SSC has a diameter of 13.2 m and a height of 7 m. Each of its four magnets weighs 1400 tons and are positioned to an accuracy of 0.1 mm. The first SSC beams for nuclear physics research were extracted in 1986. During 1987 facilities for the production of radioisotopes with a 100 μA, 66 MeV proton beam were commissioned. In the same year the gantry for neutron therapy was tested with a 30 μA, 66 MeV proton beam. The beamline for proton therapy was completed early in 1993. An overview of the cyclotron facility at the iThemba LABS is illustrated in Fig. 3.1.

3.1.3 General beam setup

In the present work a high quality beam is a major requirement, hence, it should have a low energy spread and a small radial emittance. To achieve such a beam a single turn extraction from the SPC2 and the SSC must be achieved. Extra care should also be taken to maximise beam transmission, thus creating a significant reduction in potential sources of beam halo, since maximising beam transmission means a smaller number of re-scattering sources. Further ensuring a small horizontal beam size at the object point is a necessary condition for high energy-resolution in the spectrometer focal plane [Fuj02b].

3.2 K600 magnetic spectrometer

The iThemba LABS K600 magnetic spectrometer (see Fig. 3.4) is a quadrupole dipole dipole (QDD)-type horizontal-bending, focusing magnetic spectrometer for protons and other light ions of intermediate energy. According to the 1992 National Accelerator Centre (NAC) Annual Report [NAC92] (iThemba LABS was formerly known as NAC), the K600 magnetic spectrometer was first commissioned in October 1991. The design of the K600 magnetic spectrometer at the iThemba LABS follows that of the K600 magnetic spectrometer (now decommissioned) at the Indiana

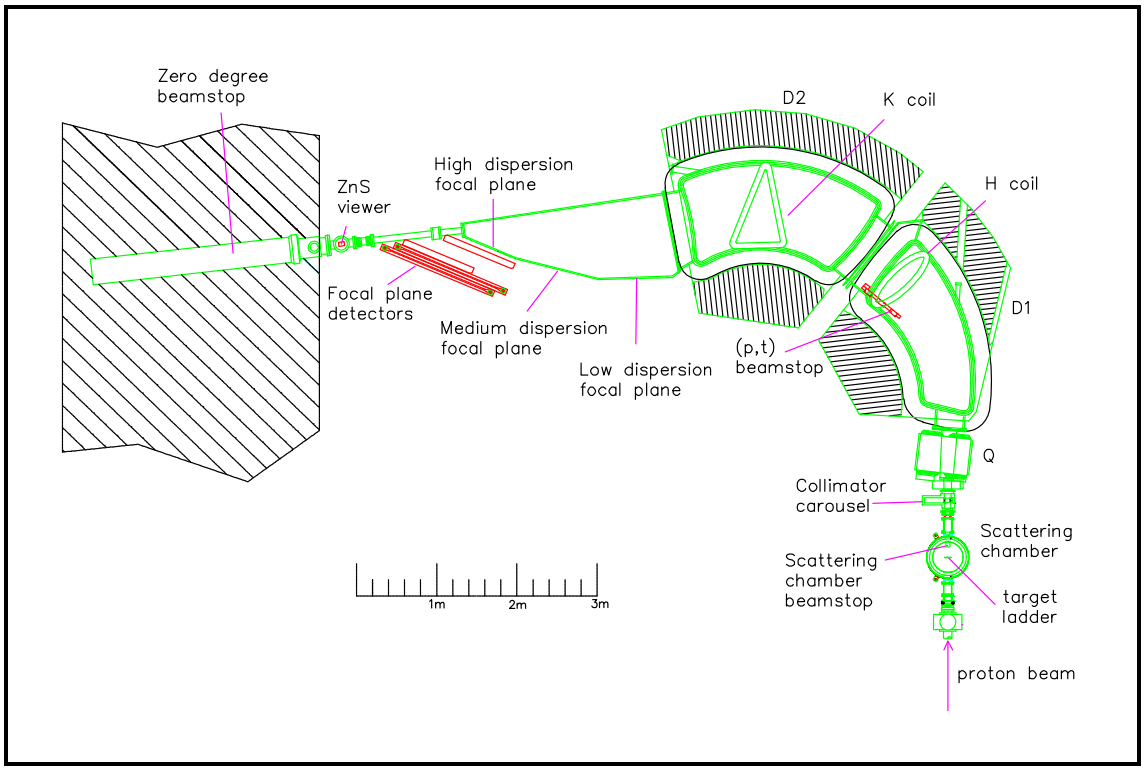

Figure 3.4: The K600 magnetic spectrometer at iThemba LABS shown here in the zero degree mode.

University Cyclotron Facility [Fos89]. It can be operated in three modes: low, medium and high dispersion, which refers to the size of dispersion achieved, as well as the position of the focal plane detectors. In the present experiment, the spectrometer was used in the high dispersion mode for a 200 MeV incident proton beam, covering an excitation-energy region 8 MeV $\leq E_{\mathrm{x}} \leq$ 25 MeV. The work reported here was the first at iThemba LABS to utilise the high dispersion focal plane coupled with the zero degree mode. This focal plane was chosen for good separation of the beam from the lowest measurable excitation energy E_{x}, consequently enabling the access to lower excitation energies than would be possible with the other focal planes in the zero degree mode.

The general properties of the K600 magnetic spectrometer, and those specifically associated with the high dispersion focal plane, are listed in Table 3.1 and Table 3.2 respectively.

Table 3.1: General technical specifications of the K600 magnetic spectrometer.

Element	Value
Nominal bend radius	2.1 m
Nominal bend angle	115°
Maximum dipole field	1.64 Tesla
Maximum magnetic rigidity	3.60 Tm
Distance: target to back of collimator	735.5 mm
Maximum diameter collimator	55 mm
Resolving power, P/δP (with 0.6 mm object width)	28000
Maximum solid angle $\Delta\theta\Delta\phi$	4.39 msr
Maximum vertical acceptance $\Delta\theta$	$\pm$ 37.4 mrad or $\pm$ 2.14°

Table 3.2: Ion optical properties of the high dispersion focal plane of the K600 magnetic spectrometer for a dipole field ratio of 1.49.

Element	Value
Momentum dispersion $(x \mid \frac{\Delta p}{p})$	-10.9 cm/%
Energy dispersion for 200 MeV proton setting	31 keV/mm
Momentum range, P_{max}/P_{min}	1.048
Horizontal magnification at P_{max}	-0.74
Vertical magnification at P_{max}	-7.05
Tilting angle of focal plane w.r.t central ray	32.2°

The quadrupole magnet (Q) at the entrance of the spectrometer is used for vertical focusing at the focal plane. The two horizontally-bending dipole magnets (D1 and D2) each has a pole-face current winding coil, the so-called K and H correction coils. The K-coil (in D2) is a quadrupole focusing element, used to adjust for first-order kinematic variations of momentum with the horizontal scattering angle $(x \mid \theta)$. The H-coil (in D1) is a hexapole focusing element to correct for second-order $(x \mid \theta^2)$ aberrations. The terms $(x \mid \theta)$ and $(x \mid \theta^2)$ represent the sensitivity of the focal plane position ($x_{\rm fp}$) to the scattering angle ($\theta_{\rm scat}$) of the reaction products, as is used in Ref. [Eng81].

The proton beam from the accelerator enters a 524 mm diameter scattering chamber which contains, at its centre, a target ladder (capable of holding six targets) as well

as a turntable on which a small Faraday cup or detectors can be mounted. In the case of measurements at small angles an internal Faraday cup, made of brass, can be used as a beamdump, while for larger angles (greater than 21°) one can use an external beamdump. For zero degrees measurements, the beam is transported through the zero-degree beamline to the zero-degree beamstop embedded in the concrete wall of the experimental area. The inelastically scattered protons which are scattered off the target are collimated by one of the collimators installed in a carousel located in front of the quadrupole magnet, thereby defining the solid angle acceptance of the spectrometer. The particles are then focused on the focal plane of the spectrometer, where a position sensitive detector system is positioned.

3.3 Focal plane detector system

The focal plane detector package consists of two vertical drift chambers (VDCs) and a pair of rectangular plastic scintillation detectors behind the VDCs. Technical details of the detectors are summarised in Table 3.3 and Table 3.4. The original vertical drift chambers available at iThemba LABS only have good horizontal position determination capabilities, but very limited vertical position determination capabilities. Another characteristic of these detectors is that they were designed for the medium dispersion focal plane, and have a lot of non-position sensitive material at both ends of the detector. This means that when they are used in the zero degree mode, where one wants to position the detector as close as possible to the zero degree beamline to be able to measure at as low as possible excitation energy (E_{x}), these detectors would have a significant dead region before the first active signal wire. For these reasons new detectors were designed and built.

In order to achieve better background suppression and subtraction at zero degrees, good vertical position detection is required. Vertical position sensitivity is also necessary to accurately determine the effective scattering angle at zero degrees.

Table 3.3: Technical specifications of the new UX Vertical Drift Chamber.

Wire conguration	vertical and 50°
Horizontal VDC acceptance	78 cm
Vertical VDC acceptance	10 cm
Signal wire	20 μm gold plated tungsten
Guard wire	50 μm gold plated tungsten
Cathode planes	20 μm Al foil
Number of signal wires	198 and 143
Number of guard wires	199(+2) and 144(+2)
Cathode-anode spacing	8 mm
Signal wire spacing	4 mm
Guard wire spacing	4 mm
Gas mixture	90% Ar10% CO_2
Entrance and exit windows	25 μm mylar
Pre-amplifier	Technoland PMT-005
Typical guard wire voltage	~ -500 V
Typical cathode plane voltage	~ -3800 V

Table 3.4: Technical specifications of the focal plane scintillators.

Paddles	
Scintillating material	Bicron BC-408
Scintillator dimensions	48×4×0.5(or 0.25) inch^3
Lightguide	Saint Gobain Crystals 90° adiabatic twisted pair
PMT	Hamamatsu R329-02 with a Hamamatsu E934 base
Typical PMT voltage for 200 MeV protons	~ -1700 V for $\frac{1}{2}$ inch
	~ -1900 V for $\frac{1}{4}$ inch
Max PMT voltage	2700 V

For these reasons the new VDCs have a U-wire plane as well as an X-wire plane as shown in Fig. 3.5. The X signal and guard/field shaping-wires are aligned perpendicularly to the scattering plane while the U signal and guard-wires are tilted at an angle of 50° with respect to the scattering plane. The U wire-plane has 143 gold-plated tungsten signal-wires, 20 μm in diameter and 144 field-shaping wires made of 50 μm diameter gold-plated tungsten, spaced 4 mm apart. On the other hand, the X wire-plane comprises of 198 gold-plated tungsten signal-wires, each with a diameter of 20 μm and 199 field-shaping wires made of 50 μm diameter gold-plated

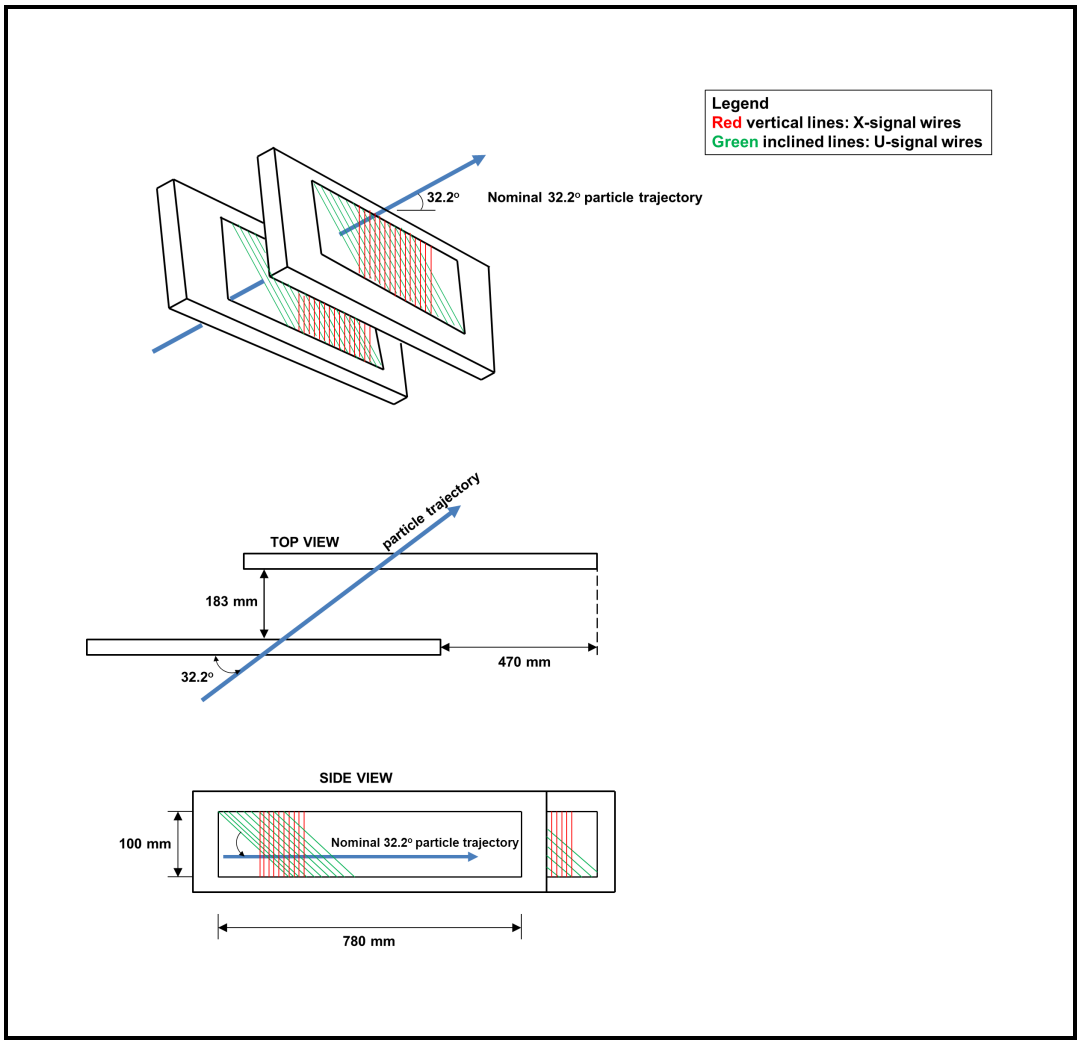

Figure 3.5: A schematic diagram of the K600 focal plane detector system.

tungsten, spaced 4 mm apart. Tungsten is used as the base material for the signal-wires because of its high tensile strength, whereas gold is used as a conductive plating due to its high resistance to corrosion and high work function (which reduces the secondary emission at the conductive surface). To the field-shaping wires, a voltage of ~ -500 V is applied. A 20 μm thick aluminum foil is used to make each of the three cathode planes that sandwich the wire planes. The cathode planes are spaced 16 mm apart, resulting in 8 mm spacing between the signal-wire and cathode planes. Typically a negative high voltage of -3700 V is applied to these planes in order to allow effective detection of protons [Nev11]. To isolate the interior of the vertical drift chamber from the atmosphere, two Mylar planes, each 25 μm thick are utilised.

This choice of material prevents fast diffusion of moisture from the experimental area to the inside of the VDCs, thus preventing leakage current and sparking in the detector. A gas mixture of 90% Ar and 10% CO_2 is used as the ionisation medium in the volume between the two Mylar planes. This particular choice of gas was selected for the following reasons: (i) its non-flammable, (ii) it is cheap and (iii) poses no possibility of polymerisation effects which can endanger the long term properties of the drift chambers compared to a Ar-isobutane gas mixture (which is also flammable and expensive). Each signal-wire and guard-wire is soldered onto a single (417 mm $\times$ 936 mm) printed circuit board. The entire VDC is then sealed. This prevents contaminants such as oxygen from entering into the sense-wire region of the wire chambers.

Sixteen-channel Technoland P-TM 005 preamp/discriminator cards [TechNo] are used to pre-amplify and discriminate the signals before they are sent to CAEN V1190A time-to-digital converters (TDCs) [TDC] via sixteen-channel twisted pair ribbon cables.

Installed behind the VDCs are two ΔE–ΔE type plastic scintillation detectors, 1/2" and 1/4" thick respectively. The signals from the four photo-multiplier tubes (PMTs), mounted at the two ends of each plastic scintillator, are sent to a CAEN V792NC charge-to-digital converter (QDC) [QDC]. The coincidence signals from these photo-multiplier tubes are used for particle identification and the generation of fast timing signals which provide trigger signals for the Data Acquisition (DAQ) system.

3.4 Data acquisition system and electronics

The Data Acqusition (DAQ) system comprises electronics in the NIM standard that is used to generate the trigger signal, as well as electronics according to the VME

standard used to digitise the time-of-flight (TOF) and VDC drift time measurements, the measurement of accumulated charge in the paddles, as well as to accumulate scaler signals. The following VME hardware modules were used: two CAEN V820 scaler modules, one CAEN V792 QDC and seven CAEN V1190A TDCs. Each TDC channel has a time-resolution of 100 ps. The trigger signal was formed by the coincidence of the two plastic scintillators, since they are considered to have 100% efficiency for detecting the high energy charged particles. A diagram of the trigger electronics in shown in Fig. 3.6.

MIDAS software [Rit93] was used to process data digitised by the VME electronics. It is a data acquisition package written in C++ under the General Programming License (GPL), and is widely used in nuclear and particle physics experiments. The software package has a library that can be used for data transport between different computers and programs, and a set of programs for data logging and system management. Its valuable features include a fast online database, on which experimental configuration information can be stored, and a web interface, that makes the experiment remotely controllable. A slow control system is integrated (although not implemented for this experiment) which can be used to control high voltages and measure things such as temperatures. Although the system is independent of any specific hardware, it is mostly used in VME, FASTBUS and CAMAC systems. Online as well as offline analysis of the data was carried out using the combination of ROOT [Bru95] and MIDAS.

3.5 Dispersion matching

The energy-resolution one can achieve with a magnetic spectrometer system depends upon several factors. The three main factors are:

- the angular kinematic broadening,

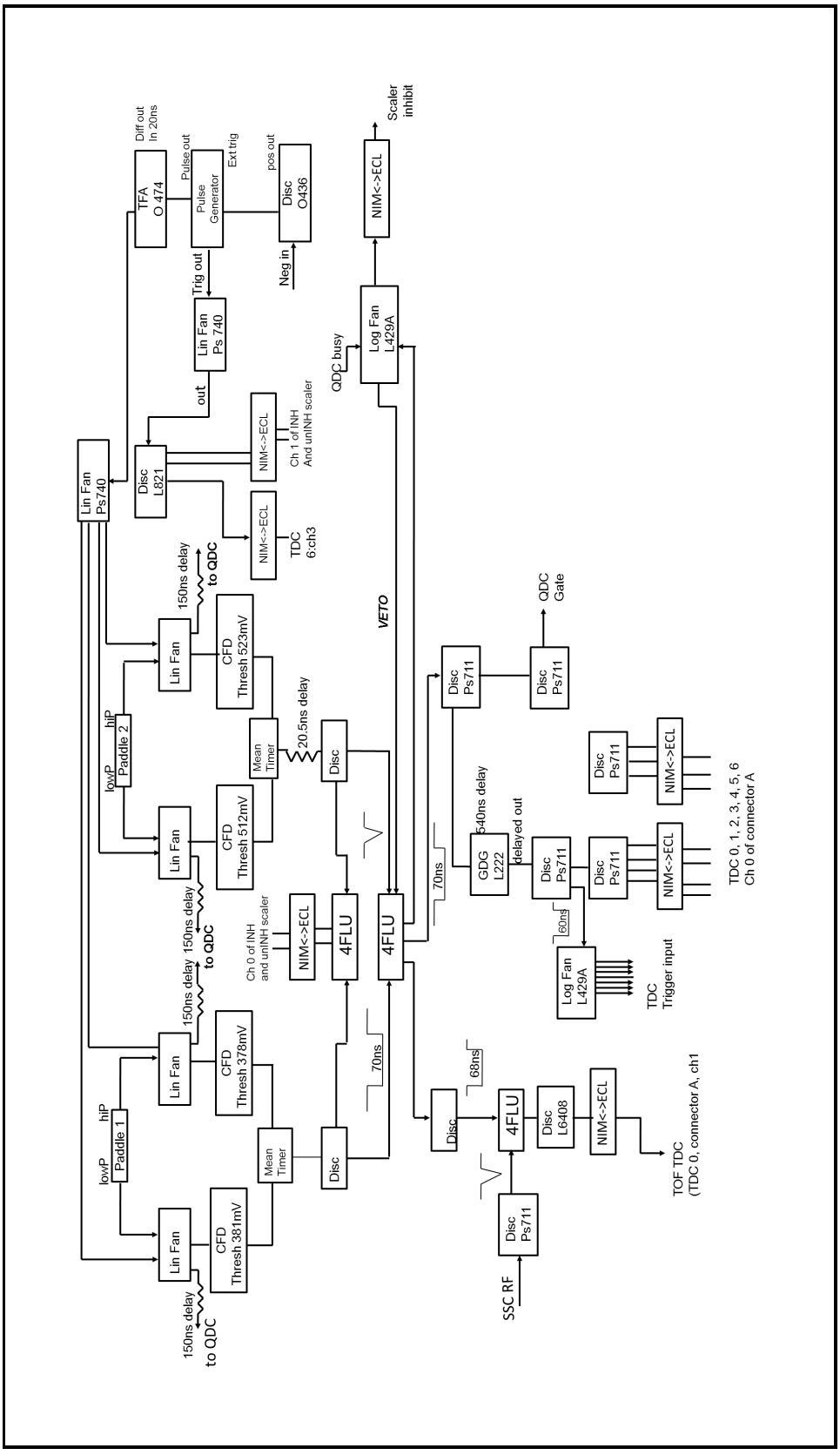

Figure 3.6: A schematic diagram of the K600 trigger electronics.

- target thickness, and
- energy spread in incident beam.

Angular kinematic broadening owes its importance to the finite solid angle acceptance of the spectrometer. It can be corrected by using the K and H coils, and if needed, by offline lineshape correction. The influence of target thickness effects on energy-resolution is as a result of energy losses and straggling in the target foil, which spread the energy distribution of the scattered particle. It is eliminated by using thin enough targets (about a few mg/cm^2). Energy spread in the incident beam can be overcomed by the method of dispersion matching.

As the beam momentum (energy) delivered by an accelerator increases, the momentum (energy) spread of the beam usually increases. Large momentum spread Δp in the beam can severely limit the resolution of the energy spectrum measured with a magnetic spectrometer. In order to use the full potential of a high resolution magnetic spectrometer, thus to derive a good quality spectrum from the measurements in the focal plane detectors, the characteristics of the beam should be matched to the requirements of the magnetic spectrometer by a proper adjustment of the beamline optics. The techniques of matching beam properties to the specific spectrometer focusing conditions enable the compensation of line broadening effects which are usually caused by the beam momentum spread. This is critically important for an experiment such as the one presented here, where the highest possible energy-resolution is aimed for.

The concept of dispersion matching can be explained as follows. An achromatic beam is set up in such a way that the position and angle of protons on the target are independent of the momentum of the incident proton, or $(x \mid \delta p/p) = 0$ and $(\theta \mid \delta p/p) = 0$ [Eng81]. Therefore, in the achromatic mode, the position and the angle of scattered rays at the focal plane depend on the initial beam energy spread,

thereby limiting the experimental energy-resolution. To overcome this problem a dispersion matched beam should spatially separate the protons according to their momentum such that the higher momentum particles will travel a longer distance through the spectrometer than smaller momentum paricles, hence, effectively achieving achromatic focus in the K600 focal plane [Fuj00, Fuj02b]. The concept of lateral dispersion matching is schematically shown in Fig. 3.7.

3.5.1 Faint beam technique

The faint beam technique is used to optimise the beam dispersion matching conditions. It involves the use of beam attenuation copper meshes to reduce the number of protons in the beam by a factor of up to 10^6 without changing the beam profile or ion-optical characteristics of the beam [Fuj02b]. It is especially useful in the case of zero-degree measurements. At finite angles one can do dispersion matching by looking at the ground state of some suitable nucleus. But with the K600 magnetic spectrometer connected to the zero-degree beamdump one can only look, in principle, at excitation energies (E_{x}) of 7 MeV or higher. As a result, in order to perform dispersion matching on some excited state, the process may be exceedingly slow due to the low countrate. But with the use of the faint beam, one can safely observe the beam directly in the focal plane detectors of the magnetic spectrometer. This enables one to achieve lateral dispersion matching of the beam to the magnetic spectrometer.

At iThemba LABS faint beam is available only when injector cyclotron 2 (SPC2) is in use because SPC2 can accommodate an external ion source, compared to Solid Pole injector Cyclotron 1 (SPC1) which only has an internal ion source. The attenuation meshes have very tiny holes and can reduce the beam from the ion source going to SPC2 by a factor of 10^2, 10^4 or 10^6. By scaling the five spectrometer magnetic elements appropriately in order to allow the proton beam to pass through the focal

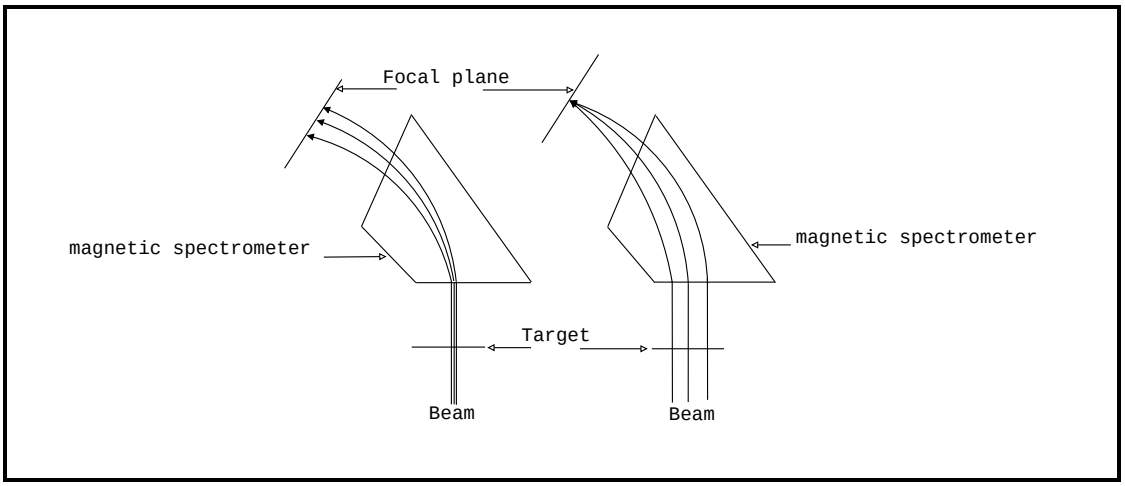

Figure 3.7: Schematic ion trajectories under achromatic (left) and lateral dispersion matching (right) conditions.

plane detectors, a direct measurement of the degree of dispersion matching can be achieved. The beamline elements are then optimised in order to minimise the size of the beam image in the ($x_{\rm fp}$,$\theta_{\rm fp}$) scatter-plots, as shown in Figs. 3.8 and 3.9.

3.6 Experimental procedure

During the experiment, the target nuclei were bombarded with a proton beam at an incident beam energy of 200 MeV over a period of four weekends. Useful data were acquired on three of the weekends. A beam current of $\sim$ 1 nA was used. This limitation in the beam intensity was due to the fact that a high quality beam was desired and $\sim$ 1 nA represented the maximum beam intensity that had a small energy spread, small emittance and little halo.

3.6.1 Targets

Typical self-supporting targets of areal densities, 0.8 – 2.5 mg/cm^2 were used (see Table 3.5). The aim was to obtain the best possible energy-resolution and sufficiently high counting statistics, allowing the fine structure characteristics and $E1$ strength distributions of the IVGDR to be clearly observed. In the present work, a good

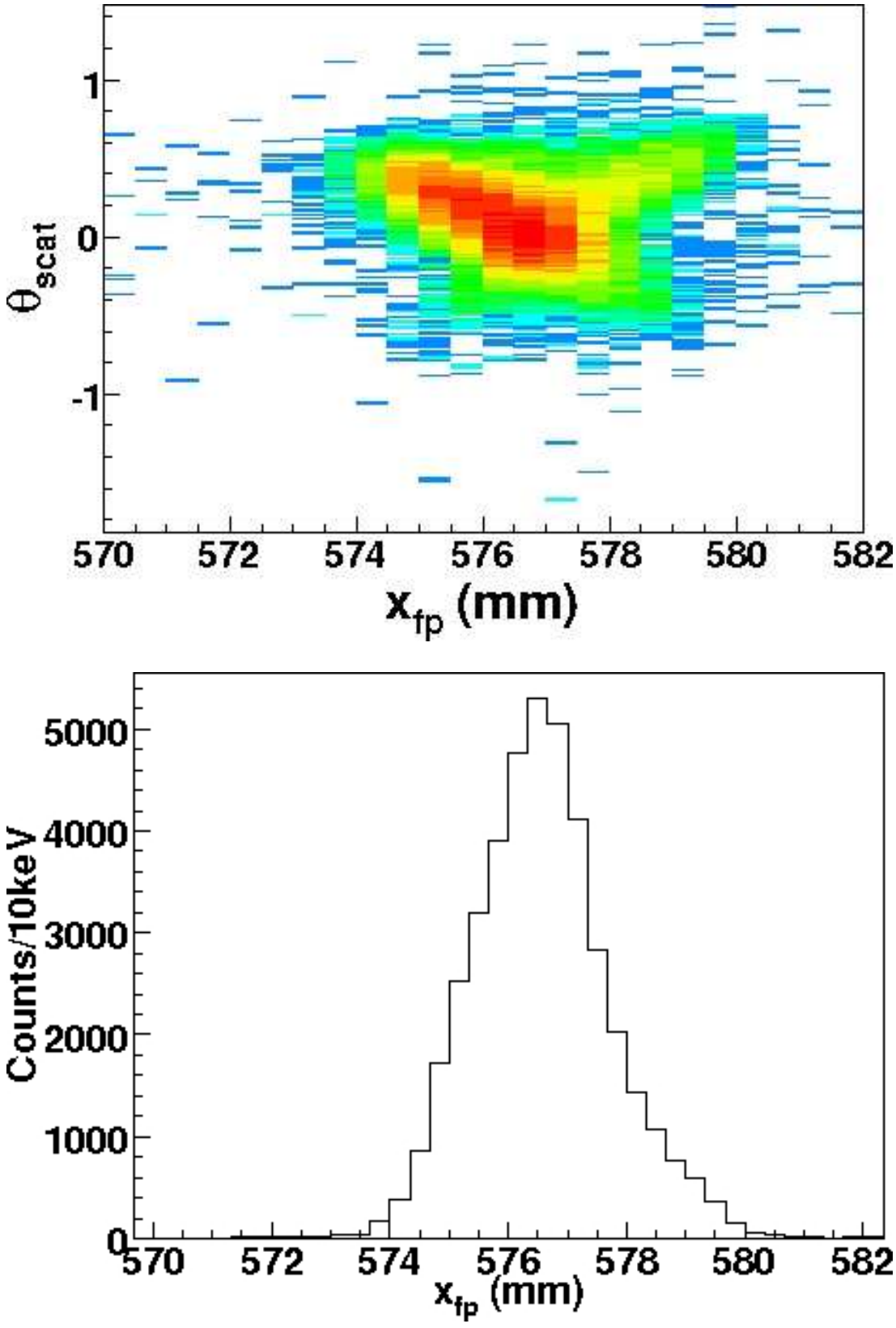

Figure 3.8: *Top panel*: A two-dimensional histogram of the faint beam showing the horizontal scattering angle against the horizontal focal plane position before optimisation. *Bottom panel*: A one-dimensional projection illustrating the horizontal focal plane position of the faint beam (FWHM = 65 keV).

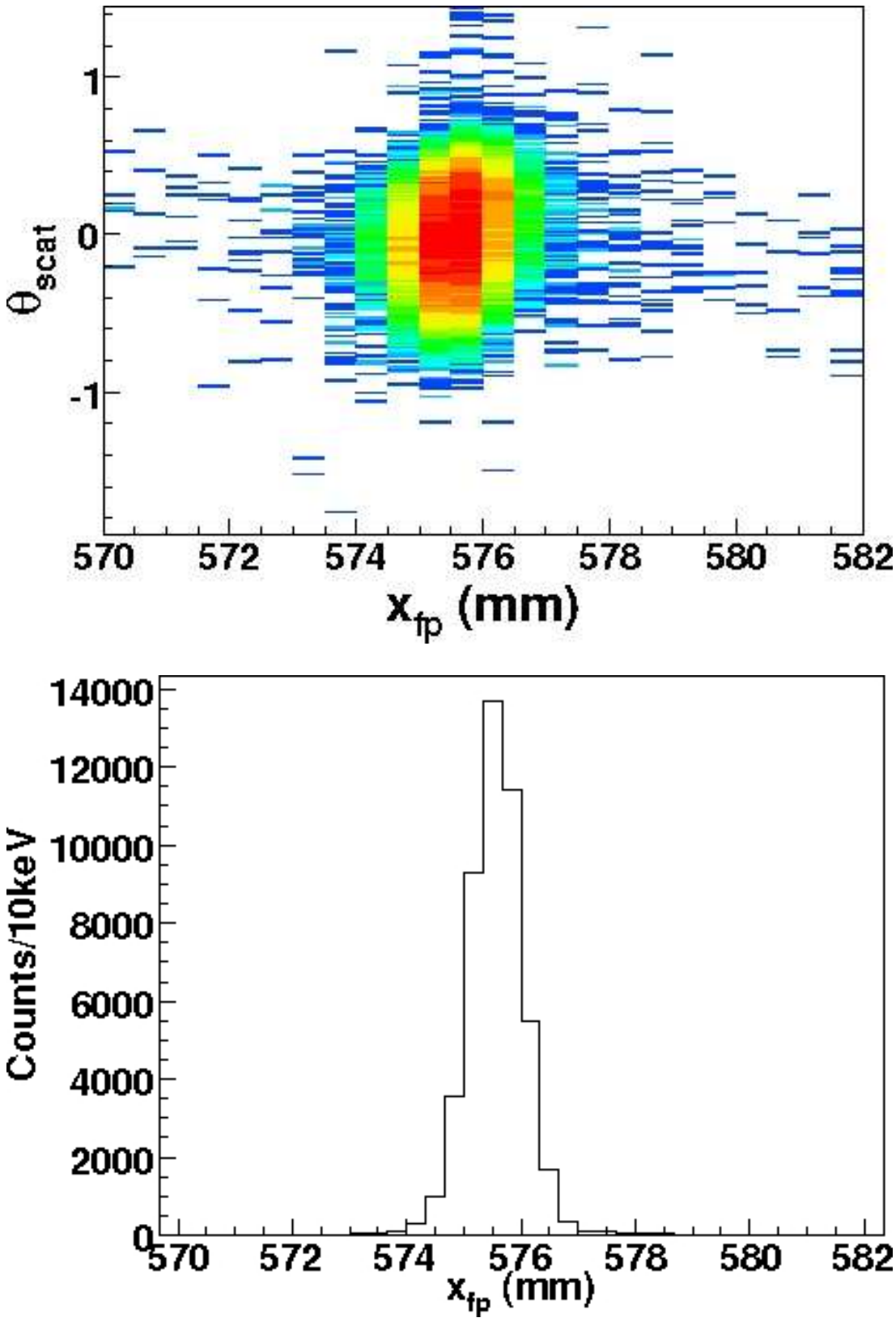

Figure 3.9: *Top panel*: An improved two-dimensional histogram of the faint beam showing the horizontal scattering angle against the horizontal focal plane position after optimisation. *Bottom panel*: A one-dimensional projection illustrating the horizontal focal plane position of the faint beam (FWHM = 29 keV).

Table 3.5: A summary of the targets used during the present experiment.

Target	Z	N	Areal density
^{208}Pb	82	126	2.10 ± 0.02 mg/cm^2
^{58}Ni	28	30	2.50 ± 0.02 mg/cm^2
^{56}Fe	26	30	1.43 ± 0.02 mg/cm^2
^{nat}Ca	20	20	1.08 ± 0.02 mg/cm^2
^{27}Al	13	14	0.82 ± 0.02 mg/cm^2

energy-resolution value of $\Delta E \simeq 42$ keV (FWHM) could be achieved in the case of ^{56}Fe. A systematic study over a wide mass range (^{27}Al to ^{208}Pb) was done in order to determine the structure of the low-lying $E1$ strength and also to observe how the giant dipole resonance (GDR) centroid energy varies across the Periodic Table. Two of the targets were manufactured specifically for this experiment, with the other three available from previous experiments. The preparations to manufacture the targets ^{56}Fe and ^{nat}Ca were as follows:

- The ^{56}Fe target was prepared using a method that involved melting a metal powder with an e-gun, under high vacuum, to yield a metal bead. This was followed by rolling the metal bead to a thin film using a mechanical rolling mill.

- The ^{nat}Ca target was prepared with the vacuum deposition evaporation method [Khe10], using 99.0% pure calcium metal pieces supplied by Aldrich (Milwaukee, USA). In order to prevent oxidation the evaporator was vented with argon (Ar) gas prior to and after deposition. Calcium metal pieces were first loaded into a tantalum boat and then melted using resistive heating at a working pressure of 10^{-5} mbar.

Isotopically, ^{nat}Ca contains 96.941% of ^{40}Ca. In between data runs a ^{12}C target of

thickness of 1.00 mg/cm^2 was used for calibration purposes and an empty target frame was employed for beam tuning and to monitor beam halo, which comprised mainly of secondary particles originating from the scattering of the beam from beamline components.

3.6.2 K600 fields

The main experiment began with a field setting procedure to set values of the electric currents for the quadrupole and two dipoles magnets of the K600 magnetic spectrometer according to the values obtained from the computer programme SPEXCIT. The currents in the quadrupole and dipoles magnets were determined by an interpolation of the actual experimentally measured field maps in the K600 magnetic spectrometer as contained in the code SPEXCIT [Cor92]. All magnets were set according to a pre-determined hysteresis curve or a degaussing cycle to ensure that correct and reproducible field values were obtained for each set point. The main requirement was to set the field in such a way that the beam would be cleanly transported through the K600 magnetic spectrometer to the zero-degree beamdump. The ratio of the magnetic fields of the two dipole magnets, $R = B(\mathrm{D1})/B(\mathrm{D2}) = 1.49$, as used for the high-dispersion mode differs from the original designed value of $R = 1.33$ [Nev11]. The dipole ratio of $R = 1.49$ allows better separation of the beam from low-lying states, thus implying access to smaller excitation energies because of its added advantage of increasing the dispersion from the design value of -9.8 cm/% (for $R = 1.33$) to -10.9 cm/%. The lowest E_{x} accessible is limited by how close the position sensitive part of the detectors can be from the beamline (see Section 3.3 for details). The momentum range that can be observed is limited by the P_{max}/P_{min} range indicated in Table 3.2.

3.6.3 Beam viewers

In order to achieve optimum beam transport and alignment through the spectrometer, three ZnS beam-viewers in the K600 magnetic spectrometer vault were used. The first one, which was located just after the last quadrupole in the S-line (QS6) is a ZnS mesh commonly known as the wire-mesh viewer, shown in Fig. 3.10. The second viewer, a solid ZnS screen, is the standard beam-viewer and is placed at the target position (see Fig. 3.11). The last viewer, shown in Fig 3.12, is also a solid ZnS screen and is located in the zero-degree beamline just before the zero-degree beamdump.

3.6.4 White tune

A white tune is a process whereby the whole focal plane is illuminated uniformly. By illuminating the focal plane in this way, one is able to check for the dead and/or misaligned preamp or TDC channels associated with wires in the VDCs. The K600 magnetic specrometer was placed at 7° (which was the maximum angle that could be reached when the detectors were positioned in the high dispersion focal plane) and data for a white tune were acquired. In the present work, a white tune spectrum was taken at a proton energy setting for the K600 of 165 MeV with a ^{12}C target and 49 mm diameter entrance collimator.

3.6.5 Zero degree beam optimisation

(1) The K600 magnetic spectrometer was placed at 0° and the beampipe that connected the K600 magnetic spectrometer to the zero-degree beamdump in the concrete wall was installed.

(2) Extra care was taken in order to transport the beam to the zero-degree beam dump, through the K600 magnetic specrometer, using the zero-degree viewer and with all detectors switched off.

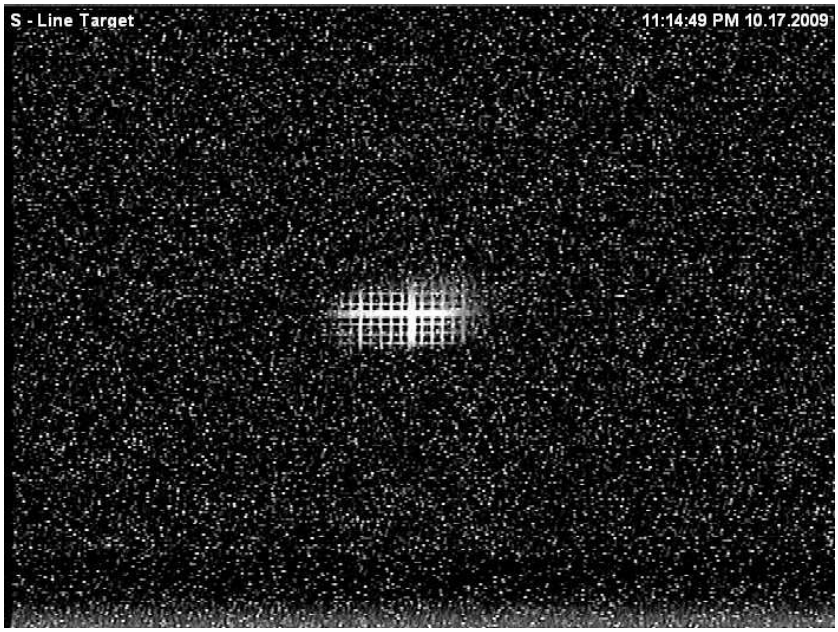

Figure 3.10: The wire-mesh viewer shown in the in-beam position. The viewer is positioned 45° with respect to the beam. The beam direction is from left to right. Each small square represents 1 mm^2.



Figure 3.11: The target viewer shown in the in-beam position.



Figure 3.12: The zero degree viewer shown in the in-beam position. The viewer is positioned 45° with respect to the beam. The beam can be seen as the faint parallelogram in the center.

(3) The next step was to ensure low background with only the scintillator detectors on. Once halo was low enough, the VDCs were switched on in order to look at the effect of the K and H coils so as to correct kinematic effects.

(4) The faint beam meshes were put in position and the K600 magnetic spectrometer field was changed so that the beam would pass through the central part of the focal plane. This was done in order to optimise the energy-resolution of the faint beam. Initially, one aims to adjust the beam elements closest to the beamline and work towards the SSC. Quadrupoles Q6S and Q5S were particularly effective. The next effective element to tune was Q21P. The resolution was optimised to 29.1 keV. In the process, Q21P was increased to almost the same level as Q19P.

(5) The K600 magnetic spectrometer field was changed back to its original setting to enable beam transport to the zero-degree beamdump. Halo was optimised with a dispersion matched beam to ensure a countrate of < 100Hz at 1nA.

(6) A ^{12}C target was used to determine the energy-resolution and calibration of the focal plane. In the event that the energy-resolution was not good enough, steps 4

and 5 were iteratively repeated, until the required energy-resolution was achieved.

During the experiment, data were acquired for a period of one hour intervals (trigger rate $\sim$ 100 – 250 Hz depending on the target), followed by a background measurement with an empty target frame, after which the next data run was started. Background from beam halo was monitored by Bergoz Beam Loss Monitors (BLM) mounted at five strategic positions along the beamline. A Bergoz BLM consists of two PIN-photodiodes mounted face-to-face to detect charged particles. It has an active area of 7.34 mm^2 and can tolerate a maximum countrate of about 10 MHz. Information from these BLMs was of utmost importance to the beam operators since it helped them in diagnosing the source of halo seen in the focal plane detectors.

The ray tracing program TRACK [VRA] was used with a D1/D2 current ratio of 1.49 to determine not only the angle of the beamdump position but also the first settings of the spectrometer magnets required to deliver the beam into the beamdump (see Fig. 3.13). This dipole ratio also ensures a shift of the elastic scattering cone away from a potential re-scattering source at the high momentum side of the downstream exit flange of dipole magnet D2 (see right panel of Fig. 3.13). Once stable beam conditions were achieved, the only adjustments that were made to optimise halo were downstream of slit 9X, namely the optimisation of halo slits in the P and S-line (position and size). In order to maintain dispersion matching conditions between the beamline and the magnetic spectrometer the only adjustments made were upstream of slit 9X namely the phase and voltage of the AX, K-line and J-line bunchers as well as the phase and voltage of the SSC so as to compensate for drifts in the magnetic field of the SSC. This helped to ensure that the beamline and the magnetic spectrometer stay properly dispersion matched.

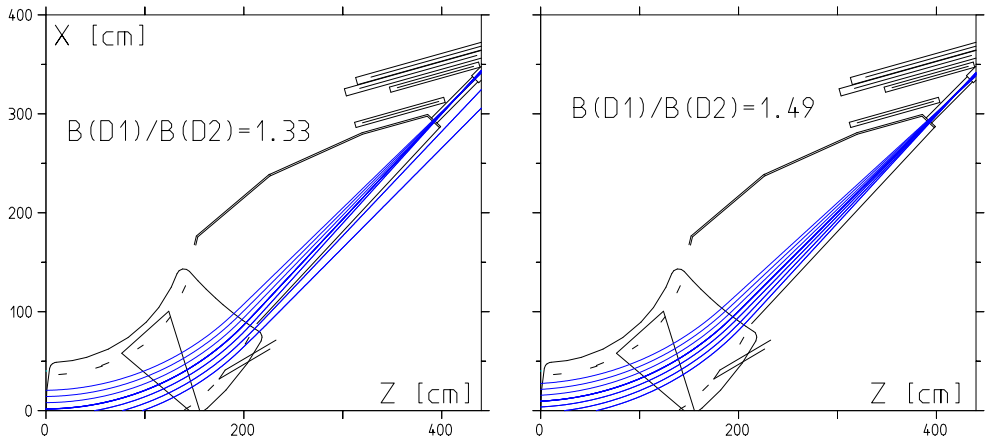

Figure 3.13: TRACK ray-tracing results for elastically scattered protons (for $E_{\mathrm{p}} = 200$ MeV) with an angular acceptance of $\pm$ 1.91° for the two dipole ratios $R = 1.33$ and $R = 1.49$. One should note that in the case of $R = 1.33$, the two rays shown outside of the focal-plane vacuum chamber represent particles that will re-scatter from the dipole D2 exit flange and vacuum chamber wall.

3.7 Data extraction

Raw data in the form of event files created by the MIDAS Data Acquisition system can be analysed offline. Offline data analysis was performed with a C++ code developed at iThemba LABS. This code translates the raw MIDAS files into ROOT files and was written specially for the new focal plane detector package of the K600 magnetic spectrometer. The code, f-plane.c, populates histogram and TTree data structures for ROOT. Subroutines are defined for, amongst other things, associating a wire number with a TDC channel number, and calculating the horizontal and vertical positions of particles at the focal plane. In the initialisation routine, the histograms and ROOT relational database structures, called TTrees, are defined for the variables that are most important for the data analysis. In the event routine, the histograms and TTree structures are filled with experimental data that satisfy the necessary requirements to be considered a good event.

3.7.1 Methods of particle identification

Particle identification is a way of obtaining the particle's identity through the use of the information it leaves as the particle passes through a detector system. The position of the particle in the focal plane of the magnetic spectrometer provides information on its magnetic rigidity. Magnetic rigidity can be described as a measure of the ratio of the momentum of the particle divided by its charge, thus a higher momentum particle, or one with a smaller charge, will have a higher resistance to deflection by a magnetic field. It is defined non-relativistically by:

$$m\frac{v^2}{\rho} = qvB \rightarrow B\rho = \frac{mv}{q} = \frac{p}{q}, \tag{3.1}$$

where B is the magnetic field of the spectrometer, ρ is the radius of curvature of the particle through the spectrometer, p is the particle's momentum, and q is its charge.

The process of particle identification relies on the combination of knowledge of the position of the particle in the focal plane, its energy loss in the plastic scintillators, as well as the particle's time-of-flight (TOF) measurement. The TOF is measured as the relative time elapsed between a coincident paddle signal and the radio-frequency signal from the SSC. This gives an indication of the time-of-flight between the target and the focal plane. The absolute value can be calculated using:

$$\mathrm{TOF} = \frac{d}{v} = \frac{d}{\left(\sqrt{1 - \left(\frac{M}{E_{\mathrm{total}}}\right)^2}\, c\right)}, \tag{3.2}$$

where d is the distance travelled by the particle, v is its relativistically calculated velocity and $M = m\mathrm{c}^2$ represents its rest mass energy. Here, E_{total} is the total energy given by $E_{\mathrm{total}} = M + E_{\mathrm{kinetic}}$.

From TRACK [VRA] we know that the range for the distance travelled in the K600

magnetic spectrometer from the target to the focal plane varies between 8.78 – 9.38 m (valid for a 200 incident MeV proton beam and protons observed in the high dispersion focal plane in the zero degree mode). Typically the distance of 8.78 m is covered by 174 MeV protons, and the distance of 9.38 m is covered by 192 MeV protons. From this, one can calculate the time-of-flight range to be between 54.5 ns and 56.1 ns.

The energy loss and TOF character of events caused purely by beam halo is shown in the top panel of Fig. 3.14. From the bottom panel of Fig. 3.14, it is clear that the majority of the background due to beam halo can be distinguished from protons scattered from a target. It was found that the best way to properly select the particles of interest in the plot of the scintillator pulse height *versus* TOF was to first select the proper events in a plot of TOF *versus* the focal plane position (x_{fp}).

This is shown in the top panel of Fig. 3.15. Once a proper software cut is applied the resulting two-dimensional histogram of the scintillator pulse height *versus* TOF, shown in the bottom panel of Fig. 3.15, allows for an even better identification of good events.

In the ΔE–ΔE technique, one relies on the fact that the energy loss of a charged particle passing through a material is described by the Bethe-Bloch approximation, which states that the energy loss (ΔE) is proportional to the square of the particle's atomic number divided by the square of its velocity [Kno79]. The principal operation of this technique is that a given particle loses a different fraction of its energy in the first and second ΔE detectors depending on its energy and identity resulting in the ΔE–ΔE plot showing different patterns for different types of charged particle.

The two-dimensional curve illustrated by the top ΔE–ΔE plot of Fig. 3.16 shows a typical backbend structure when very low energy protons are stopped in the second

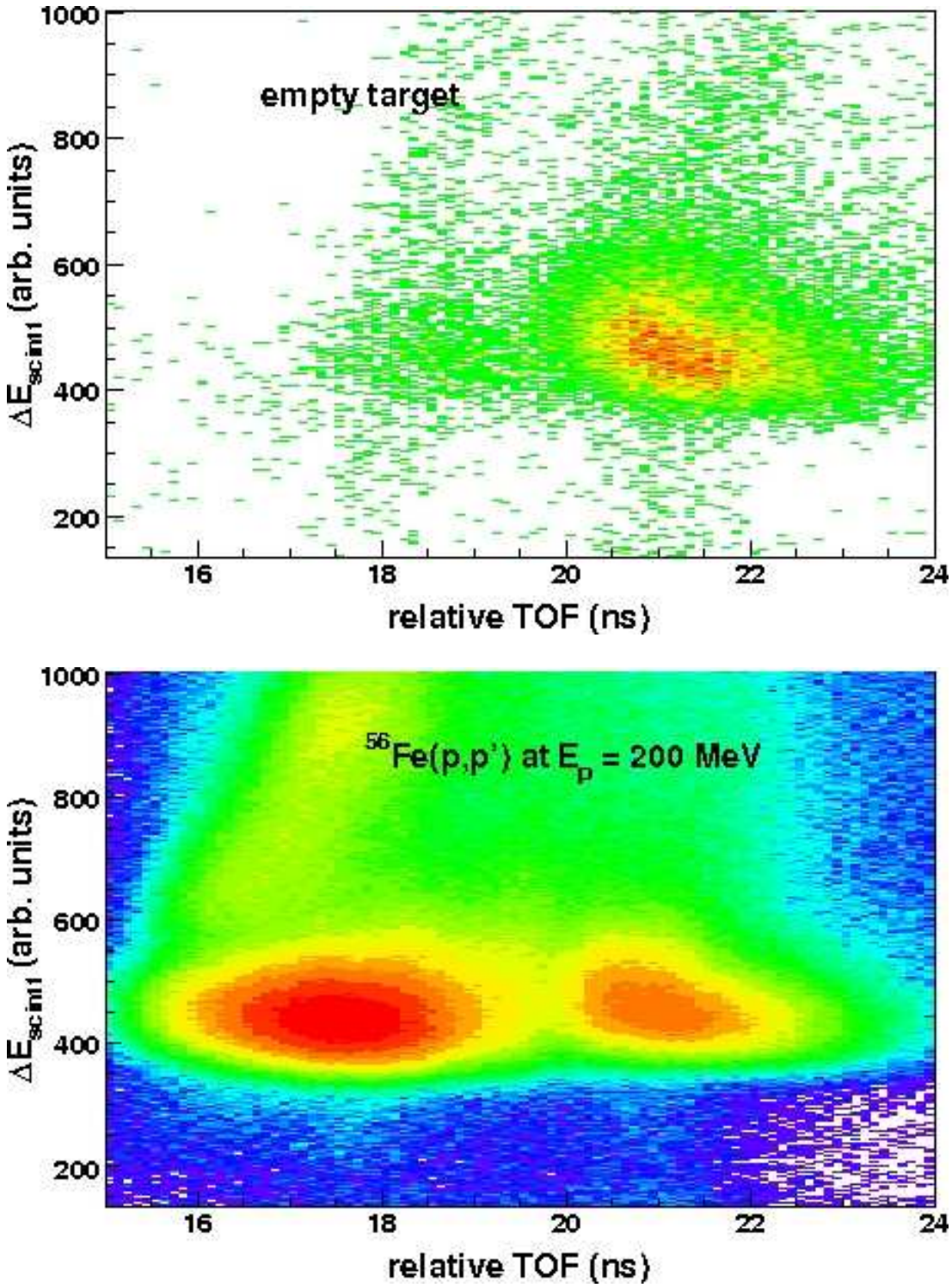

Figure 3.14: *Top panel*: A two-dimensional histogram showing the locus of the pulse height of the first scintillator *versus* TOF caused by beam halo. *Bottom panel*: A two-dimensional histogram illustrating the pulse height of the first scintillator *versus* TOF for the ^{56}Fe target. The right locus represents beam halo events, and the left locus represents the protons scattered from the target.

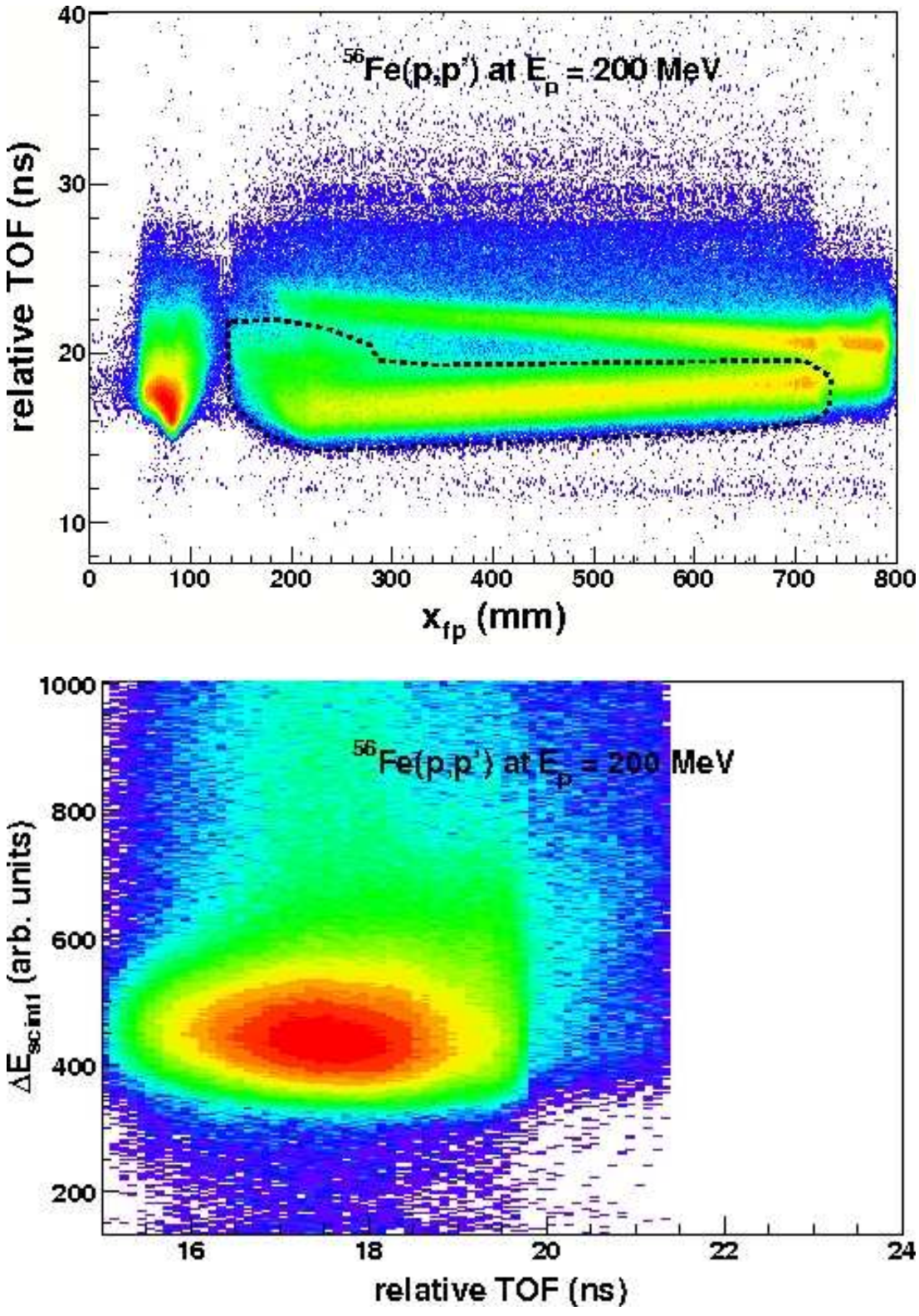

Figure 3.15: *Top panel*: A two-dimensional histogram of TOF *versus* the horizontal focal position ($x_{\rm fp}$) showing loci for the inelastically scattered protons (gated part) and beam halo (ungated part). *Bottom panel*: A two-dimensional histogram of the pulse height of the first scintillator *versus* TOF for events selected by the gated region in the top panel.

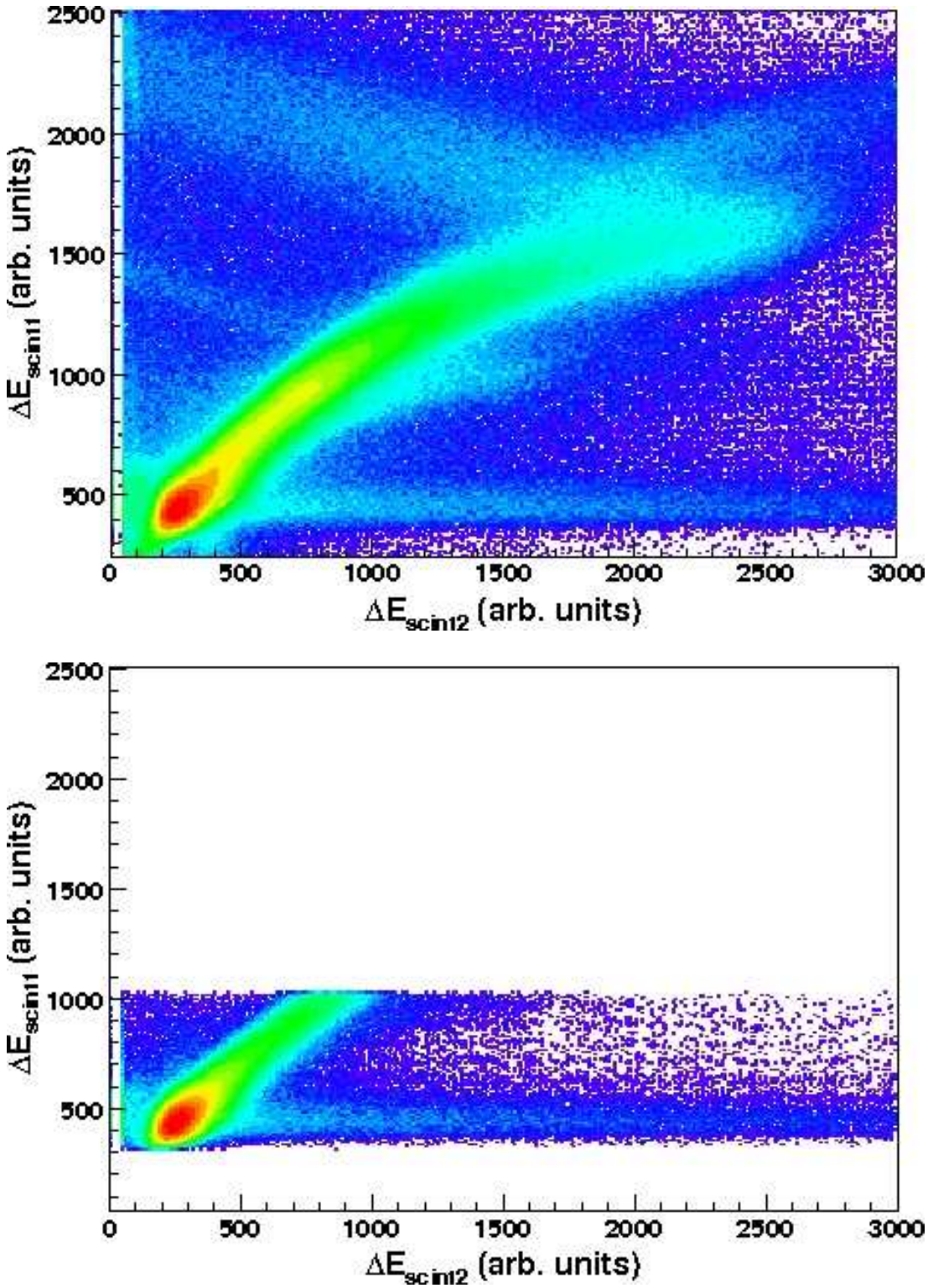

Figure 3.16: *Top panel*: First scintillator pulse height *versus* second scintillator pulse height for all events, without any cut. *Bottom panel*: A typical two-dimensional particle identification (PID) plot that is obtained after applying both the TOF *versus* horizontal focal plane position ($x_{\rm fp}$) and first scintillator pulse height *versus* TOF cuts.

scintillator detector. These protons can therefore have a kinetic energy of $E_{\mathrm{p}} \leq 35.3$ MeV. The bottom ΔE–ΔE figure of Fig. 3.16 represents all the valid events after TOF cuts.

3.7.2 VDC operation

In order to accurately determine the focal plane co-ordinates for all valid VDC events, drift time and wire position information for these events are used. The drift distance of the particle is then determined by using the drift times, which are measured from the point of primary ionisation to the point where avalanching occurs in each cell, together with the known average drift velocity. Thus the distance from the signal-wire to the position where the particle initially passes through the drift cell is determined. The application of a high voltage to the HV planes creates an electric field that causes the drift of electrons towards the anode signal-wire plane. The created electric field is constant, except for the regions in close proximity to the signal-wires and it ensures a linear time-to-position relationship over the drift region.

Therefore, in order to determine the focal plane co-ordinates for all valid VDC events, the drift distance and wire position information for the signal-wires situated around the wire that has the minimum drift time is utilised. A valid VDC event is defined in Sect. 3.7.4 and an example of a plot of drift cell characteristics for valid VDC event is shown in Fig. 3.17.

3.7.2.1 Look Up Table (LUT)

In order to determine accurate position information of the particles passing through the focal plane, the drift time characteristics of the detector must be known. Knowing the characteristic drift time distribution $\frac{dN}{dt}$, one can obtain the distance (y) from the signal wire to the position where the particle passed through a specific drift cell in the detector (VDC), hence the drift distance of the electrons.

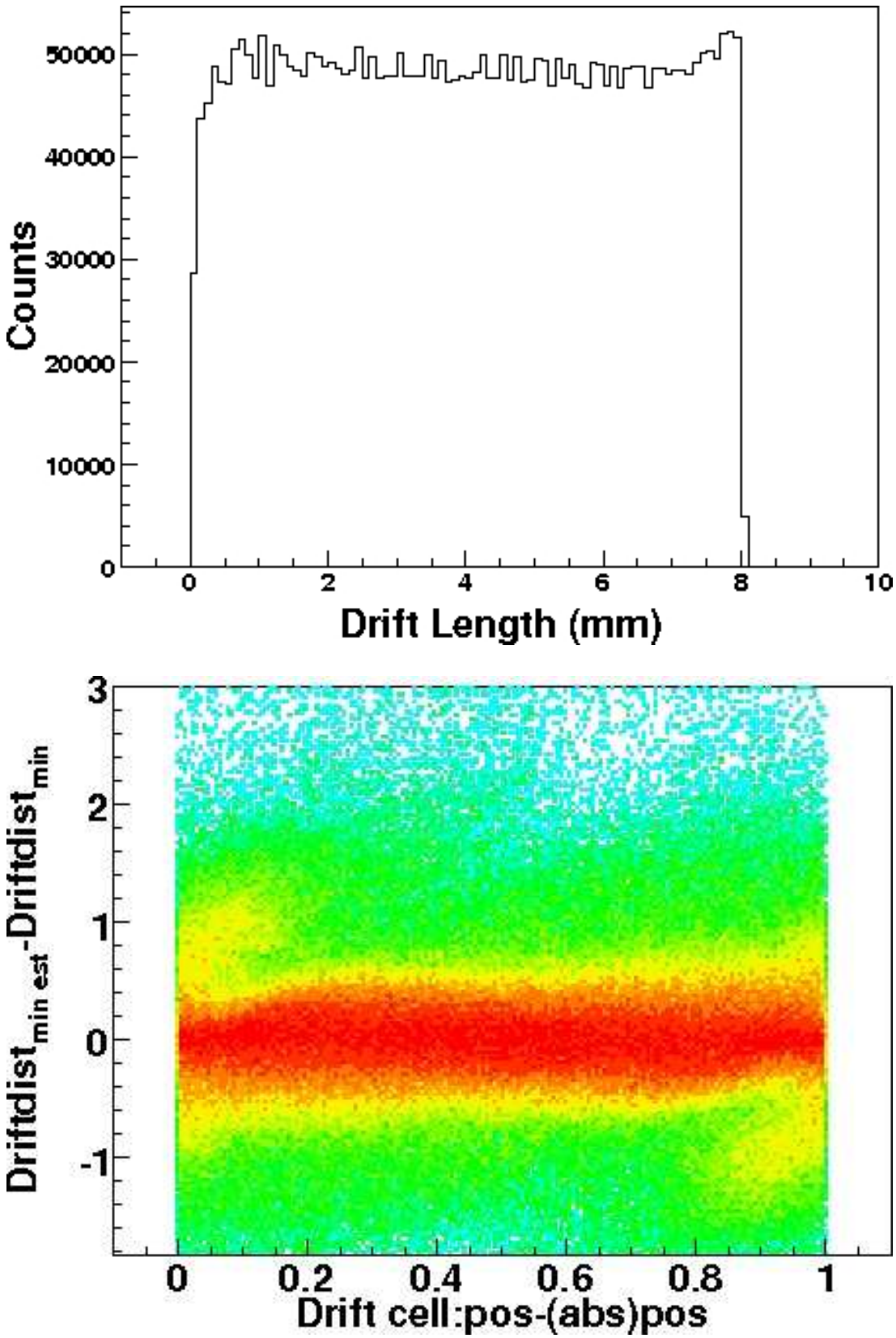

Figure 3.17: *Top panel*: An example of a one-dimensional histogram showing good drift length characteristics for all the wires of the horizontal focal plane position ($x_{\rm fp}$) wireplane. *Bottom panel*: A two dimensional spectrum that can be obtained for a good LUT and valid VDC events.

This drift distance for each signal wire is calculated as

$$y(t) = \left(\frac{dN}{dy}\right)^{-1} \int_{t_0}^{t} \left(\frac{dN}{dt'}\right) dt', \tag{3.3}$$

where

- t_0 is the particle's arrival time in the drift cell,
- t is the time at which the pulse appears at the anode [Ber77], and
- $\frac{dN}{dy}$ is a measure of the spatial distribution of events in the drift cell, obtainable from wire position information.

For one to obtain a characteristic drift time distribution, the focal plane is uniformly illuminated with particles and the average timing response of all the signal wires is measured. This generates the "white spectrum". This distribution of drift times ($\frac{dN}{dt}$) will be proportional to the drift velocity (ω(t)) and it follows that:

$$y(t) = \int_{t_0}^{t} \left(\frac{dN}{dt'}\right) dt' \propto \int_{t_0}^{t} \omega(t')dt' \tag{3.4}$$

A lookup table (LUT) can be generated by using Eq. (3.4) and the drift time distribution acquired through the above white spectrum. A lookup table is used for mapping of the drift times to their corresponding drift distances. A lookup table should be obtained for each specific experiment, as it may depend on the high voltage, the gas mixture, the energy of the particles that cause the ionisation and the physical condition of the chamber.

3.7.3 Position resolution

In the case of the U plane, one must take into account the fact that the wires are inclined at 50° with respect to the horizontal in order to obtain horizontal (x) and vertical (y) focal plane position information.

Once the particles' focal plane positions are determined, a raytrace subroutine is used to track the path of the inelastically scattered particles. To do this, the raytrace subroutine uses an interpolation procedure. The position accuracy, σ_{x}, from a single drift cell [Ber77] of a drift chamber, is defined as a factor that contributes to the overall position resolution that can be achieved with the magnetic spectrometer. This quantity can also be used to determine the angle accuracy, σ_θ, which can be achieved with the VDC. The slope of the trajectory shown in Fig. 3.18 can be calculated in a number of ways. One way in which this can be done is to use the drift distances associated with two adjacent wires, say wires g and h. In this case the trajectory slope, S, is given by:

$$S_{g,h} = \frac{d_{\mathrm{h}} - d_{\mathrm{g}}}{\text{wire seperation}}, \tag{3.5}$$

The quantity, d represents the drift distance. One can also determine the slope using the drift distances associated with for example wires k and l. Since the slope should be constant, i.e. the track should be at a constant angle on both sides of the wire plane, the differences

$$D = \left(\frac{d_{\mathrm{h}} - d_{\mathrm{g}}}{\text{wire seperation}} - \frac{d_{\mathrm{l}} - d_{\mathrm{k}}}{\text{wire seperation}} \right), \tag{3.6}$$

should be equal to zero. The variables $d_{\mathrm{h,g,l,k}}$ denote the drift distances of wires, h, g, l, k respectively. In reality, however, because of statistical fluctuations, a distribution centred around zero can be attained [New96]. If one denotes the standard deviation of this distribution by σ_{D} and then applies the general law of error propagation to Eq. (3.6) (with covariances assumed to be zero) one gets:

$$\Delta \mathrm{D}^2 = \Delta d_{\mathrm{h}}^2 + \Delta d_{\mathrm{g}}^2 + \Delta d_{\mathrm{l}}^2 + \Delta d_{\mathrm{k}}^2. \tag{3.7}$$

Again, if each Δd appearing in Eq. (3.7) is replaced by its standard deviation, and

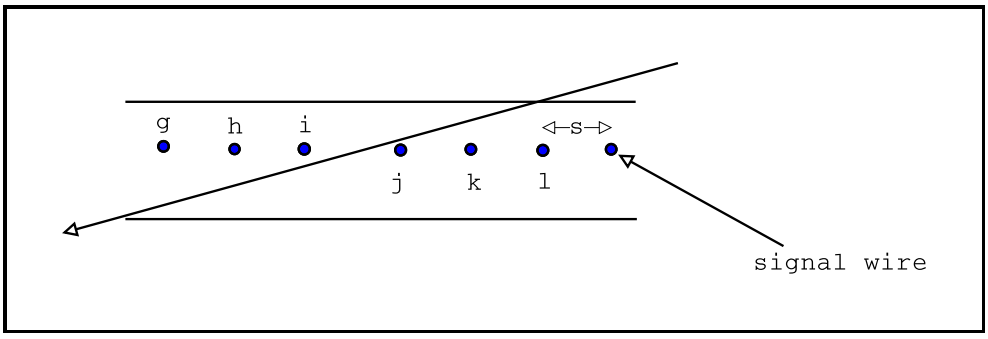

Figure 3.18: Schematic representation of a trajectory associated with a charged particle intersecting the VDC resulting in a six-wire event [New96].

assuming that

$$\Delta d_{\mathrm{h}} = \Delta d_{\mathrm{g}} = \Delta d_{\mathrm{l}} = \Delta d_{\mathrm{k}} = \sigma_{\mathrm{c}}, \tag{3.8}$$

then σ_{D} is related to the standard deviation of the drift distance, σ_{c}, by [Ber77]

$$\sigma_{\mathrm{D}} = 2\sigma_{\mathrm{c}}\cdot \tag{3.9}$$

The standard deviation of the drift distance can also be referred to as the "intrinsic cell accuracy". The intrinsic position resolution of the drift chamber is calculated as:

$$FWHM_{\mathrm{pos}} = \sigma_{\mathrm{x}} = \frac{\sigma_{\mathrm{c}}}{\sqrt{\mathrm{n}}}, \tag{3.10}$$

where n is the number of wires used to determine the position [Ber77].

3.7.4 VDC efficiency

The efficiency, ε, of the VDC is a direct reflection of its ability to detect charged particles in the focal plane and gives excellent information on the gas quality and functioning of the pre-amplifier cards. It is defined as the product of the geometric

efficiency ($\varepsilon_{\rm g}$) and the intrinsic efficiency ($\varepsilon_{\rm i}$) parameters [Leo87]:

$$\varepsilon = \varepsilon_g \cdot \varepsilon_i. \tag{3.11}$$

The intrinsic efficiency can be calculated as:

$$\varepsilon_i = \frac{N_{\rm accepted}}{N_{\rm tot}}, \tag{3.12}$$

where $N_{\rm tot}$ denotes the total number of protons seen in the scintillator. The quantity $N_{\rm accepted}$ denotes the number of *valid* events recorded. The criteria for good events are given below:

(a) TOF and scintillator (paddle) signal should be within gated regions,

(b) Number of hit wires should be between 3 and 6,

(c) reduced chi squared (χ^2) should be less than 1, and

(d) drift time should be within the gated region.

3.7.5 Background subtraction procedure

Background subtraction was performed by utilising differences in the characteristics of different types of events in the vertical focal plane position ($y_{\rm fp}$) *versus* horizontal focal plane position ($x_{\rm fp}$). This was because the energy loss and TOF characteristics of the target related background could not be clearly separated from those of the protons of interest by the application of standard particle identification (PID) techniques. For this reason the spectrometer was operated in vertical focus mode to allow for effective background subtraction. In this ion-optical mode the protons of interest, also known as *physics events* were focused around the vertical focal plane postion ($y_{\rm fp} = 0$), while the target related background and beam halo events were evenly distributed in the vertical direction.

A two-dimensional scatterplot that shows the ($x_{\rm fp}$, $y_{\rm fp}$) distribution of events for

inelastic proton scattering of ^{56}Fe at $E_{\mathrm{p}} = 200$ MeV is shown in Fig. 3.19. It is assumed that the shape of the background underneath the central region around $y_{\mathrm{fp}} = 0$ can be approximated by the two Δy regions on either side. By making each Δy region half the size of the central Δy region, one is able to effectively estimate the background contributions below the central Δy region. In Fig. 3.20, the resultant spectrum after subtracting the sum of the two Δy regions (blue spectrum in Fig. 3.19) from the focal plane position spectrum representing all selected events (black spectrum in Fig. 3.19) is shown.

3.7.6 Horizontal angle calibration

Angle calibration is performed for the following reasons: (i) to be able to transform horizontal focal plane angle (θ_{fp}) to horizontal scattering angle (θ_{scat}) to enable line-shape corrections based on θ_{scat} and (ii) to determine both the vertical (ϕ_{scat}) and horizontal scattering (θ_{scat}) angles, which will allow proper angle cuts to be made. However, we could not run with a good off-focus mode in this experiment, therefore no good y_{fp} and thus θ_{scat} calibration was achieved. This then makes it impossible to present our results in smaller angular distributions, even though we have a good horizontal scattering angle calibration.

In order to reconstruct the horizontal scattering angle (θ_{scat}) from the measured focal plane angle (θ_{fp}), proton inelastic scattering measurements at finite angles were performed using a pepper-pot collimator shown in Fig. 3.21 and in Fig. 3.22 an example of a corresponding plot for the focal plane angle calibration is illustrated. The pepper-pot collimator was positioned at 735.5 mm downstream from the target in the normal collimator position. The data from the pepper-pot will help in making horizontal angle calibration for the $\pm$ 1.91° acceptance.

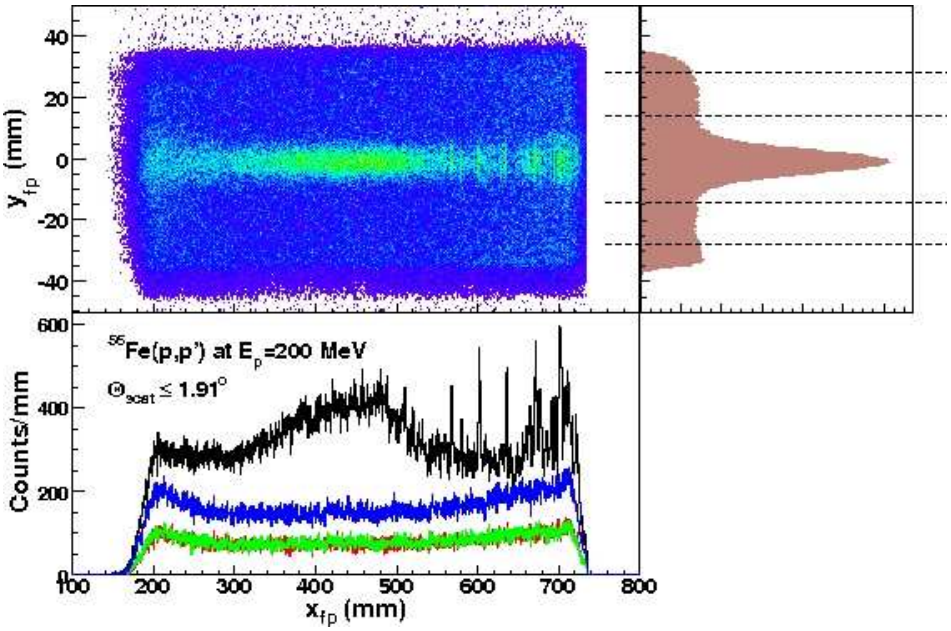

Figure 3.19: *Top panel*: A two-dimensional scatterplot in which the central region represents both physics and background events whereas the two outer Δy sections represent only background events. *Right panel*: Projection of the events onto $y_{\rm fp}$. *Bottom panel*: The red spectrum represents the background of the upper Δy section and the green spectrum represents the background of the lower Δy section as indicated in the top panel. The black spectrum represents the focal plane position spectrum for all selected events in the central Δy region. The blue spectrum represents the background that results from the sum of the two outer Δy sections.

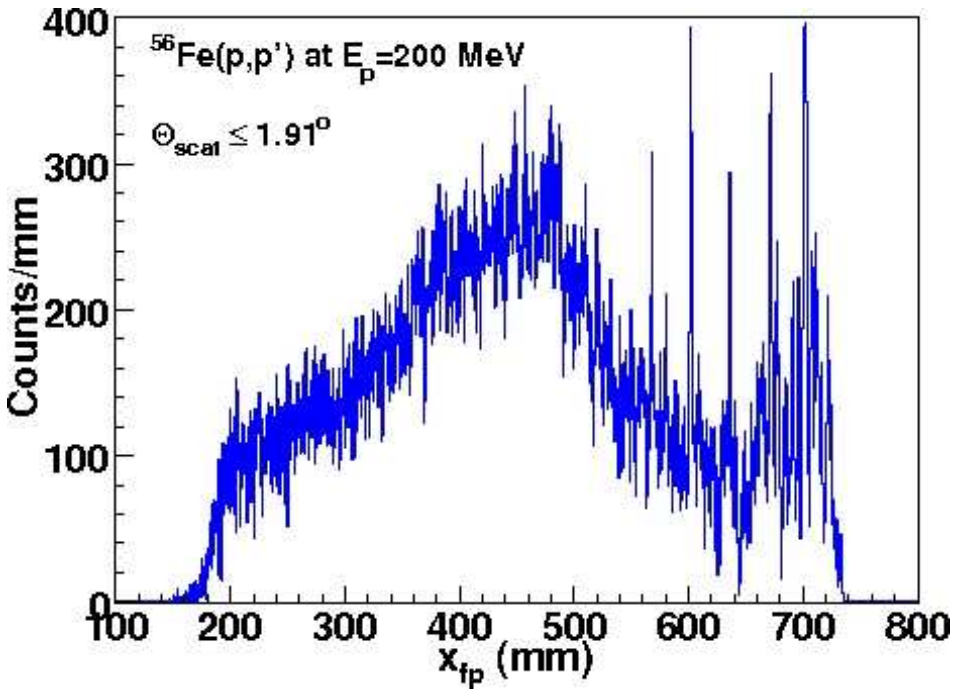

Figure 3.20: The resultant background subtracted spectrum after subtracting the blue spectrum from the black spectrum as shown in Fig. 3.19.



Figure 3.21: The pepper-pot collimator. This collimator has the following properties: its first hole from the middle on the x-axis/y-axis is at 0.819° (14.3 mrad), the second is at 1.679° (29.3 mrad) and the third is at 2.251° (39.3 mrad). The holes span 0.41° (7.15 mrad), except for the smaller hole which spans $\sim$ 0.20° (3.57 mrad). The smaller hole, achieved by adding an insert, is not shown.

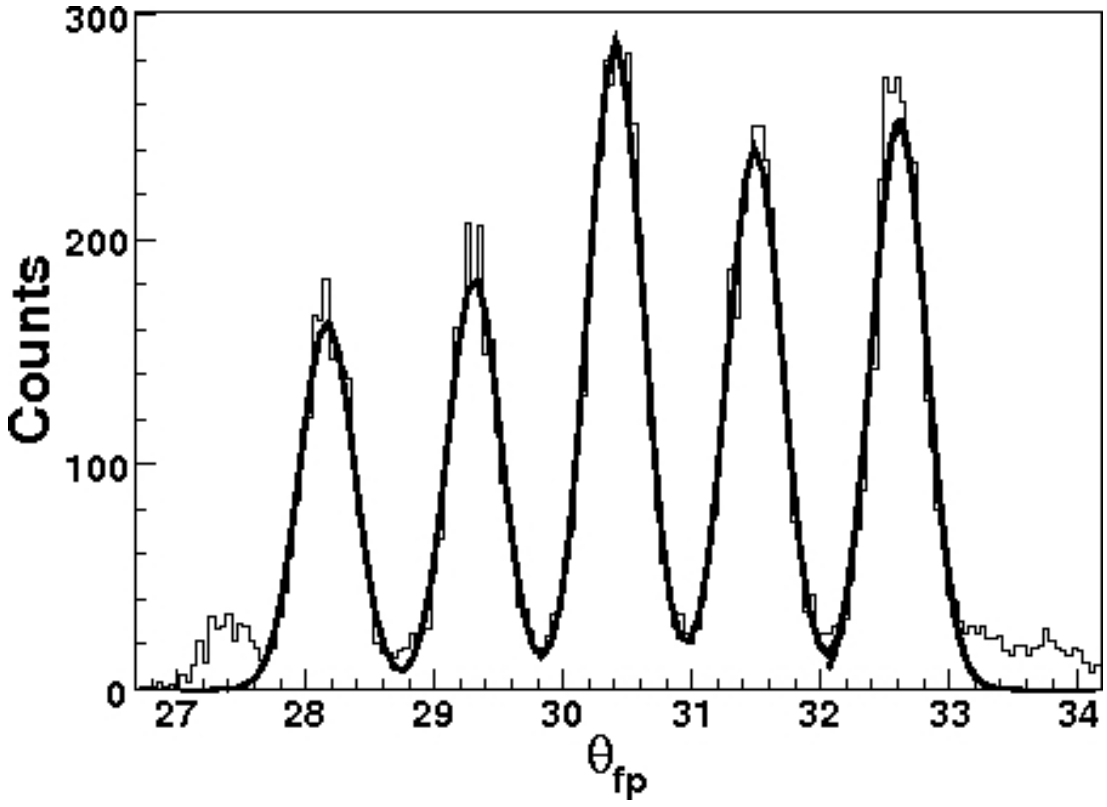

Figure 3.22: Focal plane angle ($\theta_{\rm fp}$) pepperpot spectrum with Gaussian fitted on the observed peaks.

A summary of the procedure used to obtain the pepperpot spectrum is as follows: with the K600 magnetic spectrometer positioned at 7°, the K600 magnetic spectrometer fields with the same ratios as those used in the actual 0° measurement were used. In other words, all the magnetic elements (2 dipoles, quadrupole and K and H coils) were scaled so that their relative ratios were the same as those used in the 0° measurement. The elements were scaled a number of times with the aim to get the elastic peak at several different focal plane positions, so that one can map out the angle calibration for the whole focal plane. The final calibration can be written as:

$$\begin{aligned} \theta_{\rm scat} &= (-0.68927 - 9.71781 \times 10^{-5} x_{\rm fp})\theta_{\rm fp} \\ &+ (23.9306 - 0.00154353 x_{\rm fp}). \end{aligned} \tag{3.13}$$

3.7.7 Lineshape correction

Owing to the kinematics of the reactions, particles emerging from the target at the same excitation energy of the residual nucleus but at different reaction angles have different momenta. This, together with the optical aberrations, can influence the resolution if the angular acceptance is large enough. Experimentally the K and H coils were employed to minimise these effects. Lineshape correction is, therefore, done to correct for the remaining effects. Figure 3.23 shows the effects of kinematics and aberrations on the energy spectra of the present experiment. In order to achieve the best possible energy-resolution for our measured (p,p′) excitation-energy spectra we performed software corrections to compensate for these effects. These software corrections were achieved by ensuring that the slanted vertical lines which correspond to discrete nuclear states in the scattering angle ($\theta_{\rm scat}$) *versus* horizontal focal plane position ($x_{\rm fp}$) histogram were corrected to be vertically straight.

Offline lineshape correction was achieved by adding a value that is sensitive to $\theta_{\rm scat}$

to the original $x_{\rm fp}$ value until the curvatures were removed. This can require an equation up to the fourth-order polynomial function of $\theta_{\rm scat}$:

$$x_{\rm fpcorr} = x_{\rm fp} - C_1\theta_{\rm scat} - C_2\theta^2_{\rm scat} - C_3\theta^3_{\rm scat} - C_4\theta^4_{\rm scat}. \quad (3.14)$$

It also can be possible that the constants C_1 – C_4 are sensitive to the horizontal focal plane position ($x_{\rm fp}$), such that:

$$C_{\rm i} = a_{0\rm i} + a_{1\rm i}x_{\rm fp} + a_{2\rm i}x^2_{\rm fp} \quad (3.15)$$

The two figures, Fig. 3.23 and Fig. 3.24 show the same spectrum before and after corrections. The straight vertical lines corresponding to discrete states that can be clearly seen. The energy-resolution (FWHM) was dramatically improved from 80 keV before lineshape correction to 47 keV after lineshape correction. An example of one of the equations that was utilised is as follows:

$$x_{\rm fpcorr} = x_{\rm fp} - (-0.3)\theta_{\rm scat} - (+0.005)\theta^2_{\rm scat} - (+0.002)\theta^3_{\rm scat} - (-0.01)\theta^4_{\rm scat} \quad (3.16)$$

3.7.8 Energy calibration

Peak centroids were extracted from the position spectra of the ^{12}C(p,p$'$), $^{\rm nat}$Ca(p,p$'$) and ^{58}Ni(p,p$'$) nuclei reaction *via* a Gaussian peak fitting procedure. The position of each peak identified in the horizontal focal plane position ($x_{\rm fp}$) spectrum was associated with its corresponding nuclear excited state. The corresponding momenta for each nuclear excited state was calculated. Calibration curves of momentum (p) *versus* focal plane position ($x_{\rm fp}$) were established *via* the least squares fitting procedure followed by the conversion of the proton energy ($E_{\rm p}$) to the excitation energy ($E_{\rm x}$). Four strong discrete peaks were used for the calibration *viz*: ^{12}C (12.710 MeV and 15.110 MeV, both 1^+ states), $^{\rm nat}$Ca (10.3188 MeV, 1^+ state) and ^{58}Ni (10.660 MeV, 1^+ state).

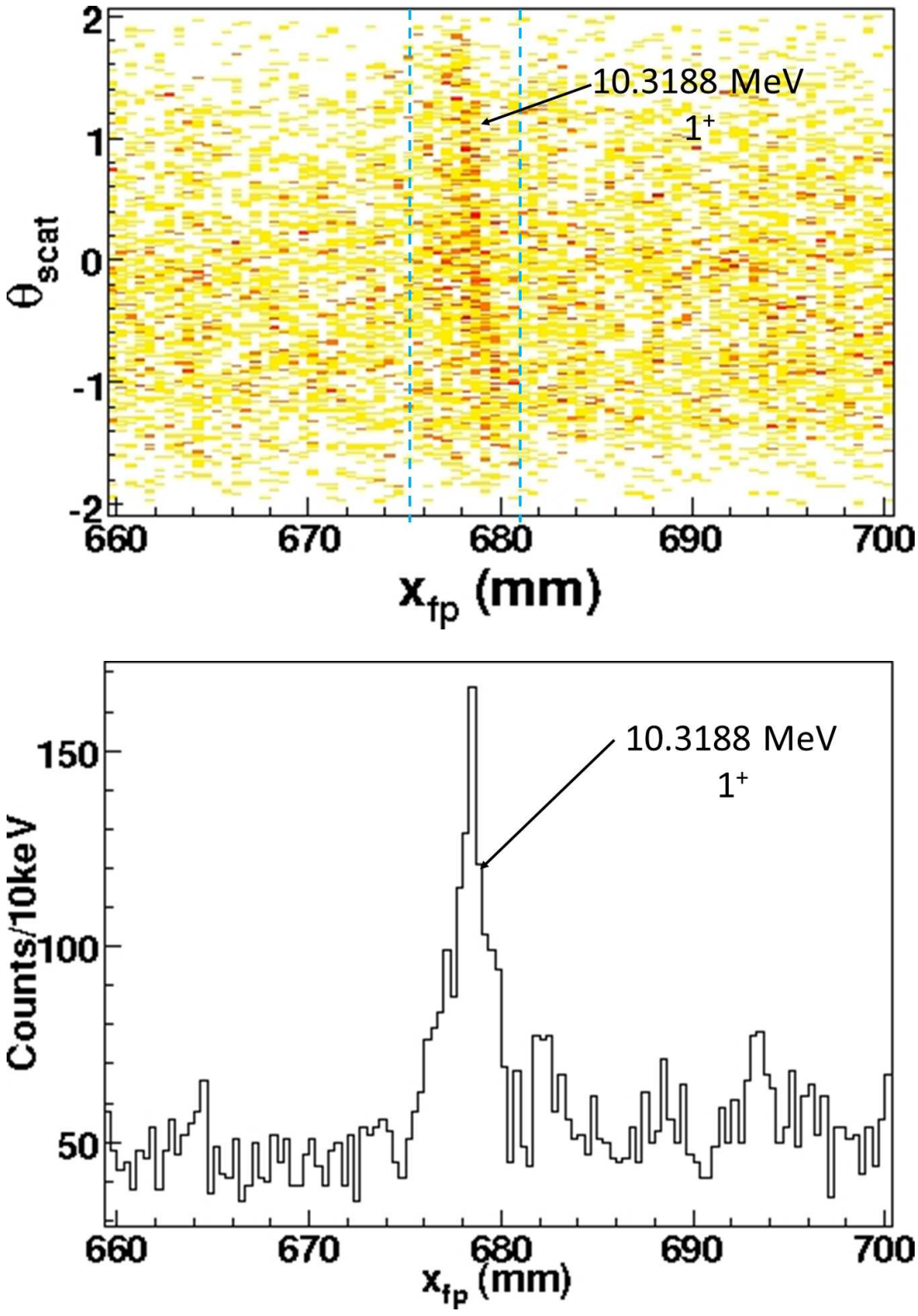

Figure 3.23: *Top panel*: Two-dimensional histogram of $\theta_{\rm scat}$ *versus* $x_{\rm fp}$ for $^{\rm nat}$Ca without lineshape correction. *Bottom panel*: Corresponding horizontal focal position ($x_{\rm fp}$) spectrum before lineshape correction.

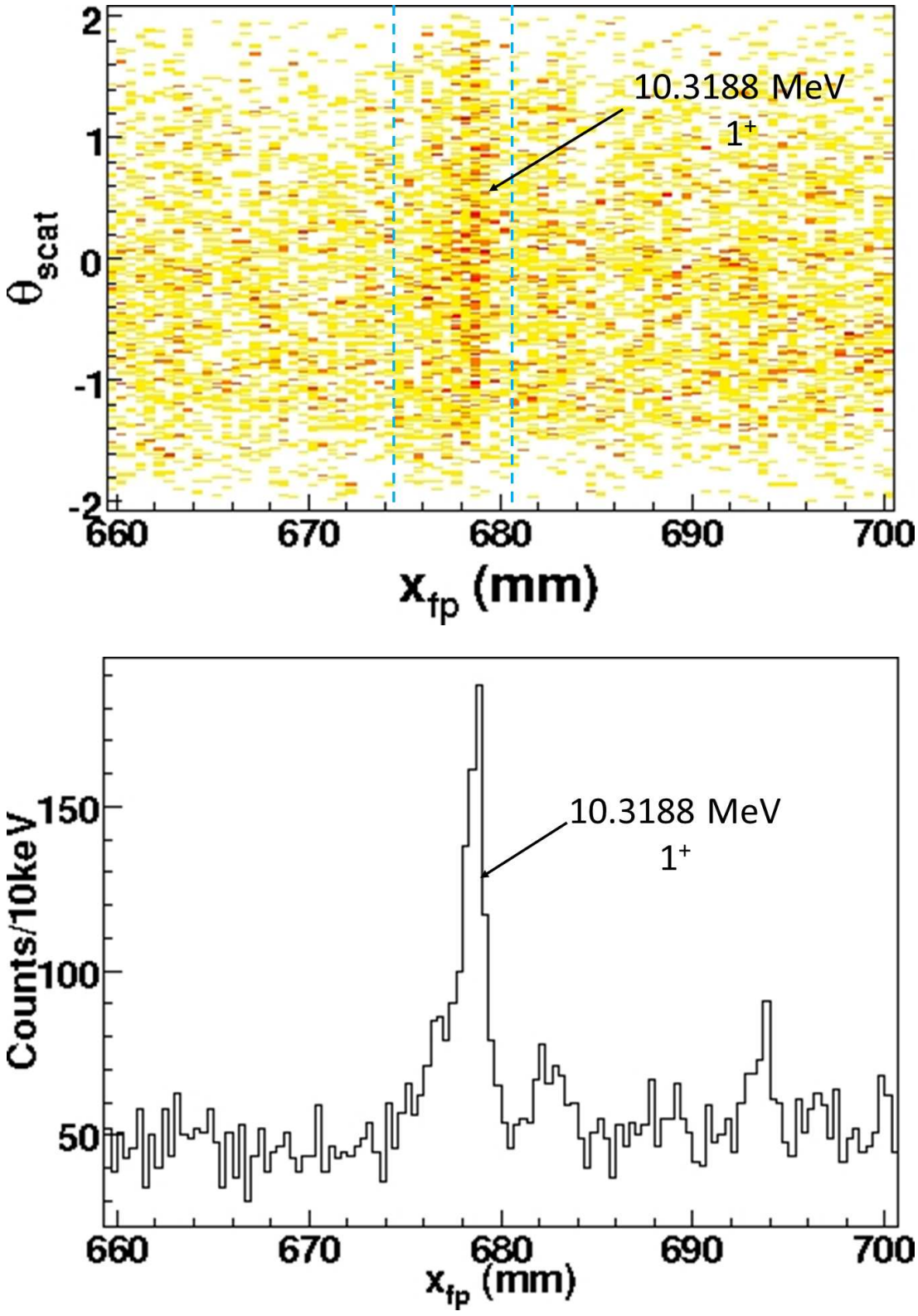

Figure 3.24: *Top panel*: Two-dimensional histogram of $\theta_{\rm scat}$ *versus* $x_{\rm fp}$ for $^{\rm nat}$Ca with lineshape correction. The abberations of $x_{\rm fp}$ for the $\theta_{\rm scat}$ are corrected by software and the excited state has been straightened. *Bottom panel*: Corresponding horizontal focal plane position spectrum after lineshape correction.

An example of a calibration curve for momentum utilising a second-order polynomial function is shown in Fig. 3.25 and the calibration parameters of the different weekends are listed in Table 3.6.

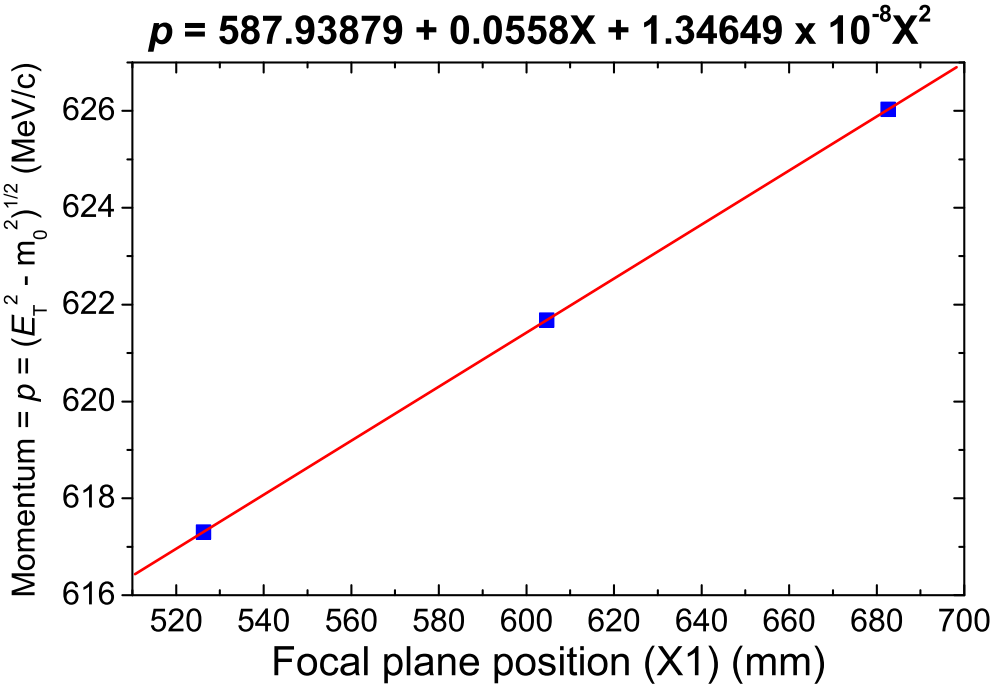

Figure 3.25: Momentum calibration curve for the K600 focal plane Weekend 3.

Table 3.6: Momentum calibration curves for the 3 different weekends.

Calibration Equation	Weekend
$p = 597.48327 + 0.02583X + 2.57364 \times 10^{-5}X^2$	2
$p = 587.93879 + 0.05580X + 1.34649 \times 10^{-8}X^2$	3
$p = 588.80055 + 0.05404X + 1.22054 \times 10^{-6}X^2$	4

3.8 Experimental cross-sections

The experimental double-differential cross-section of the inelastic proton scattering in units of mb·sr^{-1}MeV^{-1} can be written as

$$\frac{d^2\sigma}{d\Omega dE} = \frac{N_c}{N_0 \cdot \rho \cdot D \cdot \varepsilon \cdot \Delta\Omega \cdot \Delta E} \times 10^{27}, \tag{3.17}$$

where

- N_c is the corrected number of counts in an energy bin,
- N_0 is the total number of incident protons on the target,
- ρ is the number of target nuclei per unit area (in mb^{-1}),
- D is an electronic dead time correction factor,
- $\Delta\Omega$ is the solid angle of the K600 in sr,
- ΔE is energy bin size (in MeV), and
- ε is the K600 VDC efficiency, calculated as the product of individual VDC efficiencies.

The number of incident protons is calculated by

$$N_0 = \frac{CII \cdot R \cdot 10^{-12}}{e}, \tag{3.18}$$

where

- CII is the scaler read-out of the current integrator,
- R is the selected range (in nA) of the current integrator which represents 1000 counts per seconds for a full scale current read-out, and
- e is the proton electric charge (in Coulomb).

The number of target nuclei per unit area ρ was calculated from

$$\rho = \frac{\lambda \cdot N_A}{A} \tag{3.19}$$

where

- λ is the target thickness (g/cm^2),
- N_A is Avogadro's number, and
- A is mass number of the nucleus in question.

3.8.1 Error analysis

The final results for the different double-differential cross-sections of a specific target data sets from different weekends were combined using the method of weighted mean [Leo87], where the final value for the observable x_i is calculated by

$$\overline{x} = \frac{\sum\limits_i \frac{x_i}{(\delta x_i)^2}}{\sum\limits_j \frac{1}{(\delta x_j)^2}} \tag{3.20}$$

and the associated error δx_i is given by

$$\delta \overline{x}_i = \frac{1}{\sum\limits_j \frac{1}{(\delta x_j)^2}}. \tag{3.21}$$

3.8.1.1 Statistical errors

The statistical error for the double-differential cross-section is expressed as

$$\delta \left(\frac{d^2\sigma}{d\Omega dE} \right) = \frac{10^{27} \cdot \sqrt{N_c}}{N_o \cdot \rho \cdot D \cdot \Delta\Omega \cdot \Delta E \cdot \varepsilon}. \tag{3.22}$$

3.8.1.2 Systematic errors

These type of errors affect the accuracy of a measurement. They are biased (one-sided) errors, because, in the absence of other types of errors, repeated measurements yield results that differ from the true or accepted value by the same amount. The accuracy of measurements subject to systematic errors cannot be improved by repeating those measurements. Systematic errors are extremely difficult to analyse using statistical analysis, therefore, making them very difficult to detect, but once detected can be reduced only by refining the measurement method or technique.

In this present work sources of systematic errors may arise from inaccurate thicknesses of the target nuclei, inaccurate identification of the particles, inacurrate K600 solid angle, inaccurate reading of the current integrator values, etc.

The systematic error in the measured cross-section values is mainly due to the uncertainty in the target nucleus thickness which is estimated to be less than 11% for all the targets.

Chapter 4

Results, analysis and discussion

4.1 Introduction

In this chapter the experimental results will be presented and compared to theoretical predictions. Section 4.2 gives an overview of the measured experimental data which is followed by a description in Sect. 4.3 of the background subtraction procedure. Section 4.4 presents results of the comparison between the present data converted to equivalent photo-absorption cross-sections and earlier measurements using real photons and thus serves as a test case for the experimental method. An in-depth discussion of the results of the Quasi-particle Phonon Model (QPM) for the Isovector Giant Dipole Resonance (IVGDR) is given in Sect. 4.5, and in Sect. 4.5.1 a comparison between the electric dipole response in the experimental results against theoretical results is presented. In Sect. 4.6 the extraction of characteristic energy scales in the excitation-energy region of the IVGDR in the nuclei under investigation using the wavelet analysis technique is discussed for the experimental results, the microscopic QPM and EMPM calculations. Finally, details of the extraction of experimental level densities of $J^{\pi} = 1^{-}$ states for the target nuclei investigated and their comparisons with theoretical model predictions are discussed in Sect. 4.7.

4.2 Overview of the measured experimental data

Figure 4.1 presents the experimentally measured (p,p′) excitation-energy spectra for the target nuclei ^{208}Pb, ^{58}Ni, ^{56}Fe, ^{nat}Ca and ^{27}Al. The experimental energy-resolutions for ^{208}Pb, ^{58}Ni, ^{56}Fe, ^{nat}Ca were 45 keV, 52 keV, 42 keV and 47 keV (FWHMs), respectively. Inelastically scattered protons were measured in a broad excitation-energy region of $E_x = 8 - 25$ MeV. For all the targets except ^{208}Pb, one can clearly identify discrete low-lying states mostly below the corresponding neutron threshold, S_n. The neutron and proton thresholds for the target nuclei are summarised in Table 4.1. In the giant resonance region of the energy spectrum for each target nucleus (^{208}Pb – ^{27}Al) a prominent feature due to the Coulomb excitation of the GDR is observed. At the maximum of the IVGDR, $E_x \approx 14$ MeV for ^{208}Pb moving up to $E_x \approx 20$ MeV for the lighter nuclei, the fine structure is well pronounced and each of the excitation-energy spectra displays very different specific details within the IVGDR region.

Experimental double-differential cross-sections were determined for each target, these cross-sections were calculated using Eq. (3.17), and are shown in Fig. 4.2.

Table 4.1: Neutron and proton thresholds for the 5 target nuclei.

Nucleus	Neutron threshold, S_n (MeV)	Proton threshold, S_p(MeV)
^{208}Pb	7.368	8.005
^{58}Ni	12.216	8.172
^{56}Fe	11.197	10.184
^{40}Ca	15.635	8.328
^{27}Al	13.058	8.271

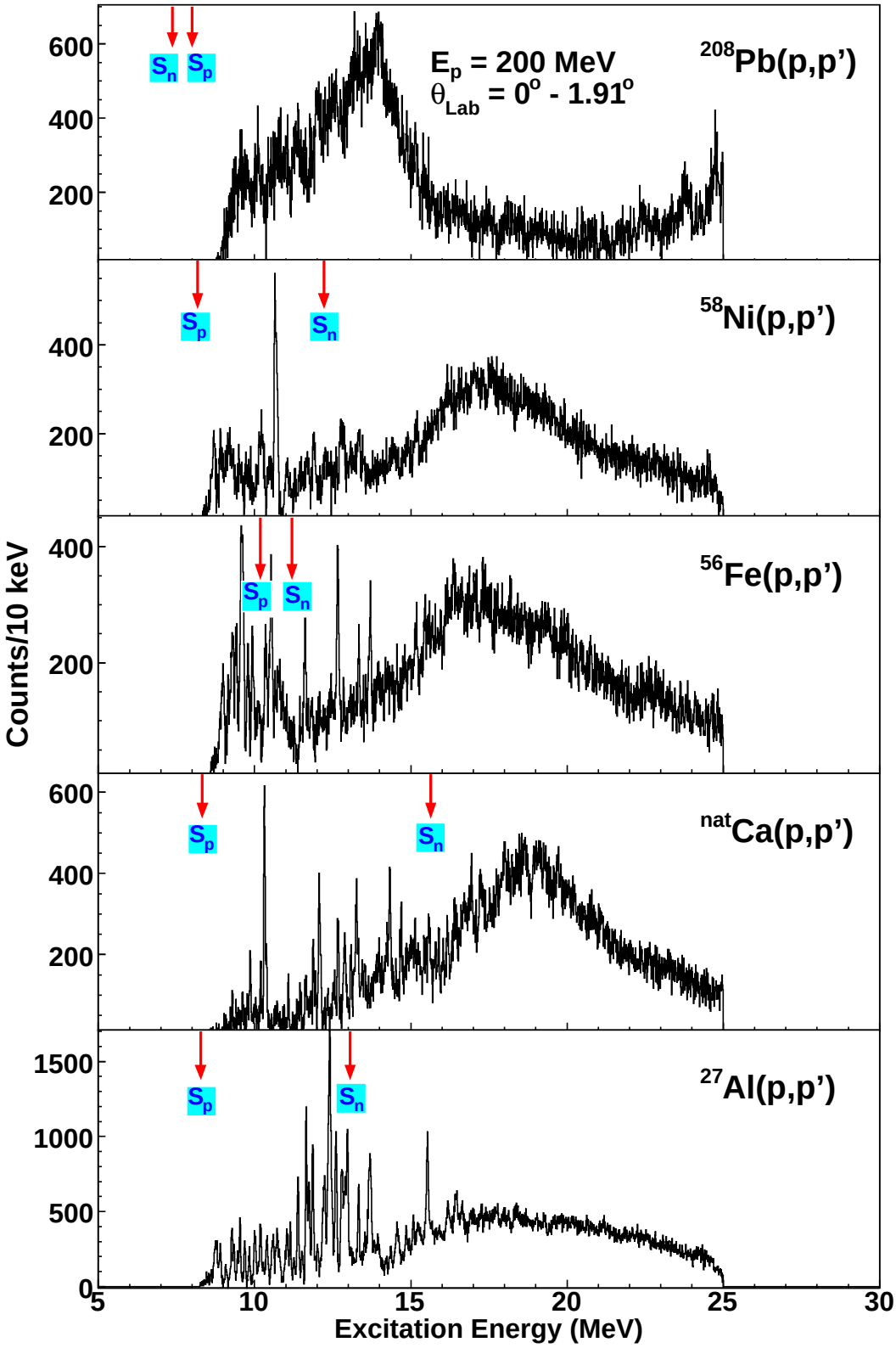

Figure 4.1: Experimentally measured excitation-energy spectra for ^{208}Pb(p,p′), ^{58}Ni(p,p′), ^{56}Fe(p,p′), ^{nat}Ca(p,p′) and ^{27}Al(p,p′) at $E_p = 200$ MeV and small scattering angles, $\theta_{Lab} = 0° - 1.91°$.

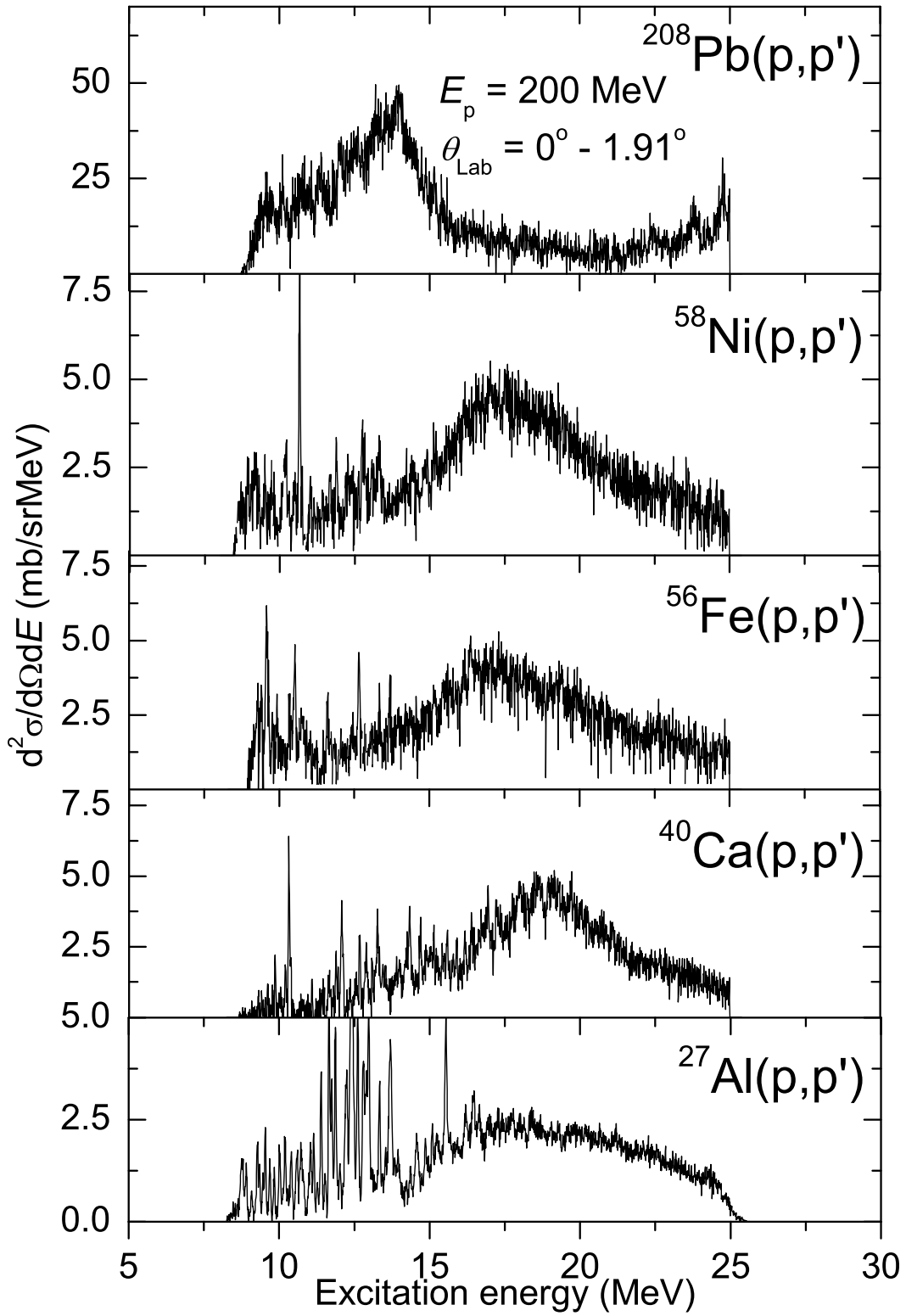

Figure 4.2: Experimental double-differential cross-sections for ^{208}Pb(p,p′), ^{58}Ni(p,p′), ^{56}Fe(p,p′), ^{40}Ca(p,p′) and ^{27}Al(p,p′) at $E_{\rm p} = 200$ MeV and small scattering angles, $\theta_{\rm Lab} = 0^\circ - 1.91^\circ$.

4.3 Background subtraction in the region of the isovector giant dipole resonance

Although inelastic proton scattering excites preferentially the dipole mode, the Isoscalar Giant Quadrupole Resonance (ISGQR) and the Isovector Giant Quadrupole Resonance (IVGQR) are also excited in this reaction [Boh75]. In an attempt to reliably isolate the dipole resonance, contributions that need to be subtracted from the data include (i) the ISGQR with a well documented resonance energy given by $E_{\mathrm{ISGQR}} = 63A^{-1/3}$ MeV [Har01] placing it underneath the IVGDR and (ii) the empirically obtained phenomenological background situated at higher excitation energies. In order to determine efficiently these background contributions, some assumptions need to be made about their shapes and magnitudes. The contributions from the ISGQR and phenomenological backgrounds are calculated by assuming a Lorentzian shape given by Eq. (1.3). The ISGQR component from DWBA calculations occupies a fraction of the cross-section that agrees very well with a calculation assuming exhaustion of the energy-weighted sum rule (EWSR) for giant quadrupole resonances (GQR) [Har01]. On the other hand, the phenomenological background is assumed to describe the behaviour of the differential cross-section at higher excitation energies and incorporates all unknown contributions from other multipolarities, IVGQR and quasi-free scattering. This background component occupies the excitation-energy region from 20.5 MeV and beyond. From DWBA calculations, its fraction of cross-section makes a good agreement with a calculation that assumes exhaustion of the EWSR [Pol11]. In the test case of ^{208}Pb, this phenomenological background was assumed to originate from the well documented IVGQR component located around $E_{\mathrm{IVGQR}} = 130A^{-1/3}$ MeV, exhausting 50 – 100% of the appropriate sum rule and has a width of 5 – 10 MeV [Har01]. The background subtraction steps followed on the present ^{208}Pb nucleus agreed very well with the recent work of Poltoratska *et al.* [Pol11]. Typical excitation-energy spectra illustrating the background subtraction procedure are shown in Figs. 4.3 – 4.7.

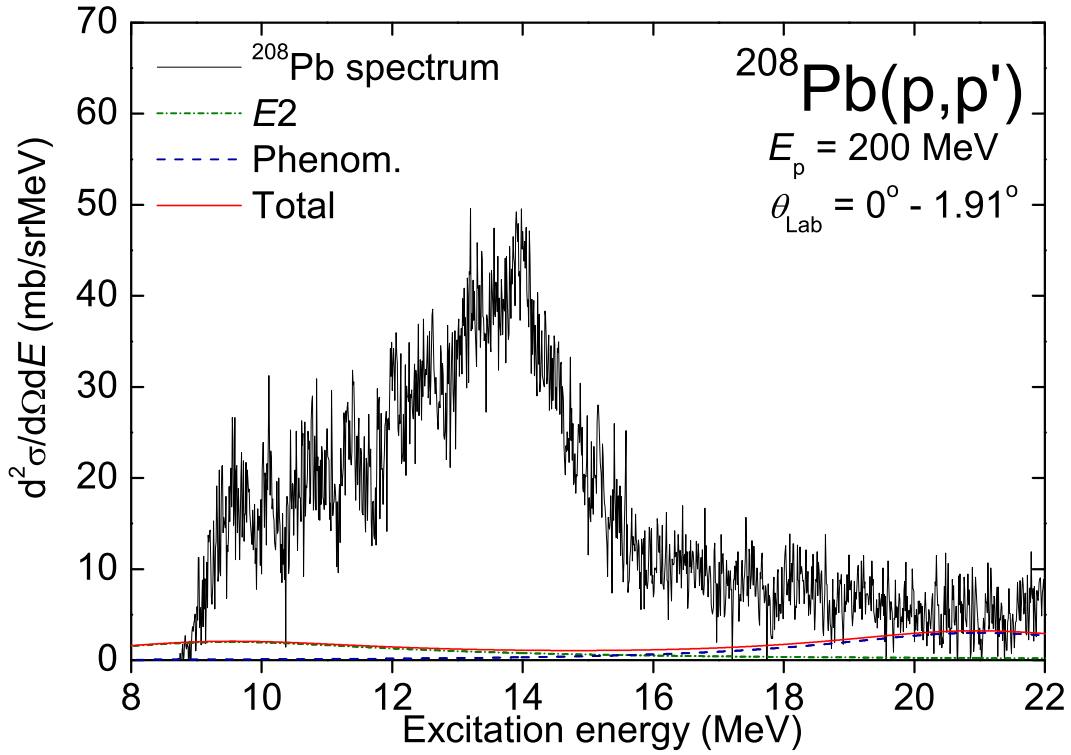

Figure 4.3: Estimated contributions to the excitation-energy spectrum of ^{208}Pb in the GDR region by $E2$ cross-sections and a phenomenological background. **Colour:** The green dash-dotted curve corresponds to the $E2$ contribution, while the blue dashed one shows the phenomenological background. The red continuous curve illustrates the sum of these contributions.

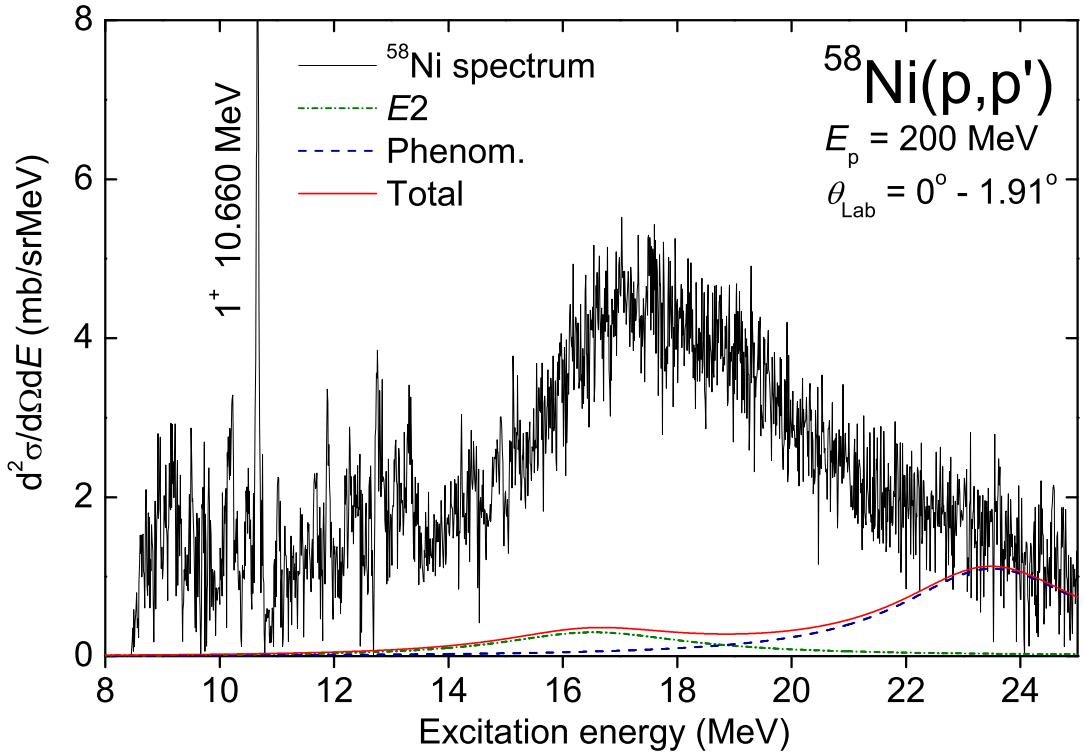

Figure 4.4: Estimated contributions to the excitation-energy spectrum of ^{58}Ni in the GDR region by $E2$ cross-sections and a phenomenological background. Here the 10.660 MeV magnetic dipole ($M1$) state also reported in Ref. [Fuj07] is very prominent.

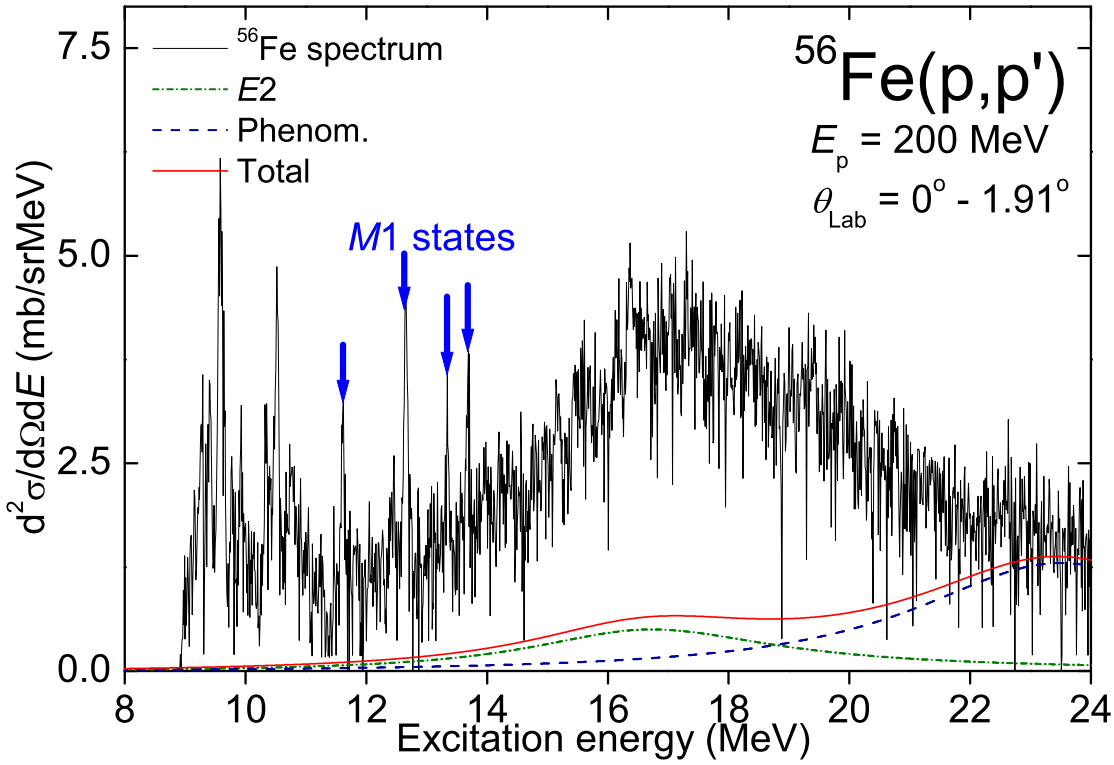

Figure 4.5: Estimated contributions to the excitation-energy spectrum of ^{56}Fe in the GDR region by $E2$ cross-sections and a phenomenological background. Candidates of $M1$ states are indicated by vertical arrows [Nag10].

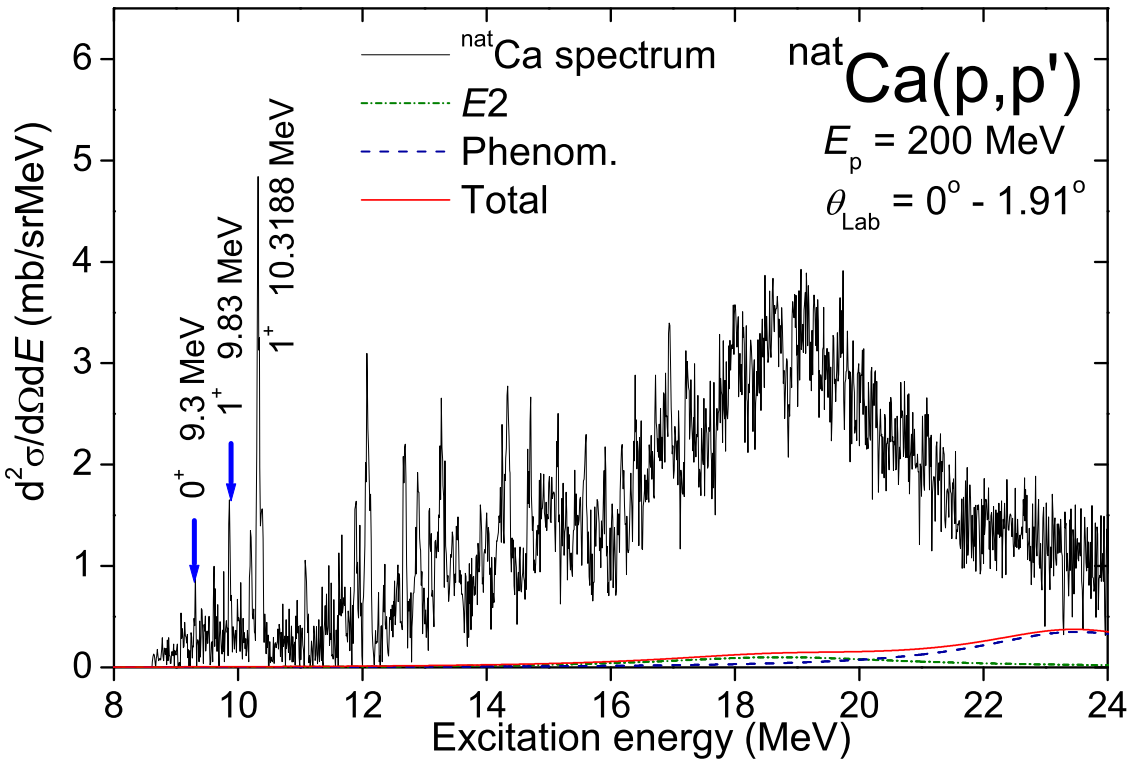

Figure 4.6: Estimated contributions to the excitation-energy spectrum of ^{nat}Ca in the GDR region by $E2$ cross-sections and a phenomenological background. Here the well-known 10.3188 MeV $M1$ state in ^{40}Ca reported in [Ana81], the 0^+ state at 9.304 MeV and 1^+ state at 9.83 MeV in ^{40}Ca are indicated also.

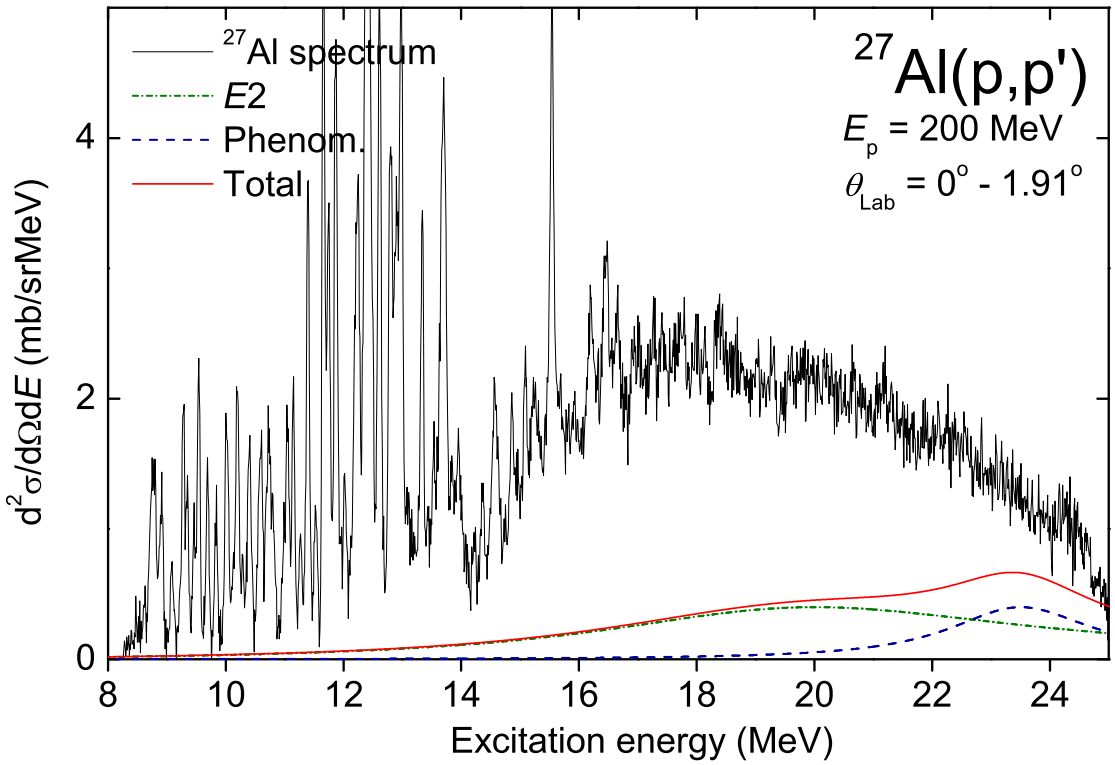

Figure 4.7: Estimated contributions to the excitation-energy spectrum of ^{27}Al in the GDR region by $E2$ cross-sections and a phenomenological background.

After the subtraction of the summed background denoted by the red continuous line, the background free spectrum is then divided by the virtual gamma function and rebinned to the energy bin-size of the published total photo-absorption data to which it will be compared with. The same procedure is applied to the other target nuclei as well.

4.4 Photo-excitation and decay of the IVGDR

Here, the experimental measured results are converted to the equivalent photo-absorption spectra and are then compared with previously published total photo-absorption data. The conversion of the measured (p,p′) excitation-energy spectra to equivalent photo-absorption data (labelled as (p,p$'_{\gamma corr}$)) was done after background subtraction described in Sect. 4.3. The virtual $E1$ γ-production rate was determined using Eqs. (2.57) and (2.60) (see Sect. 2.4.4). It is, however, necessary to determine the lower cut-off impact parameter $b_{\min}$ and as a starting point the results of Fig. 5

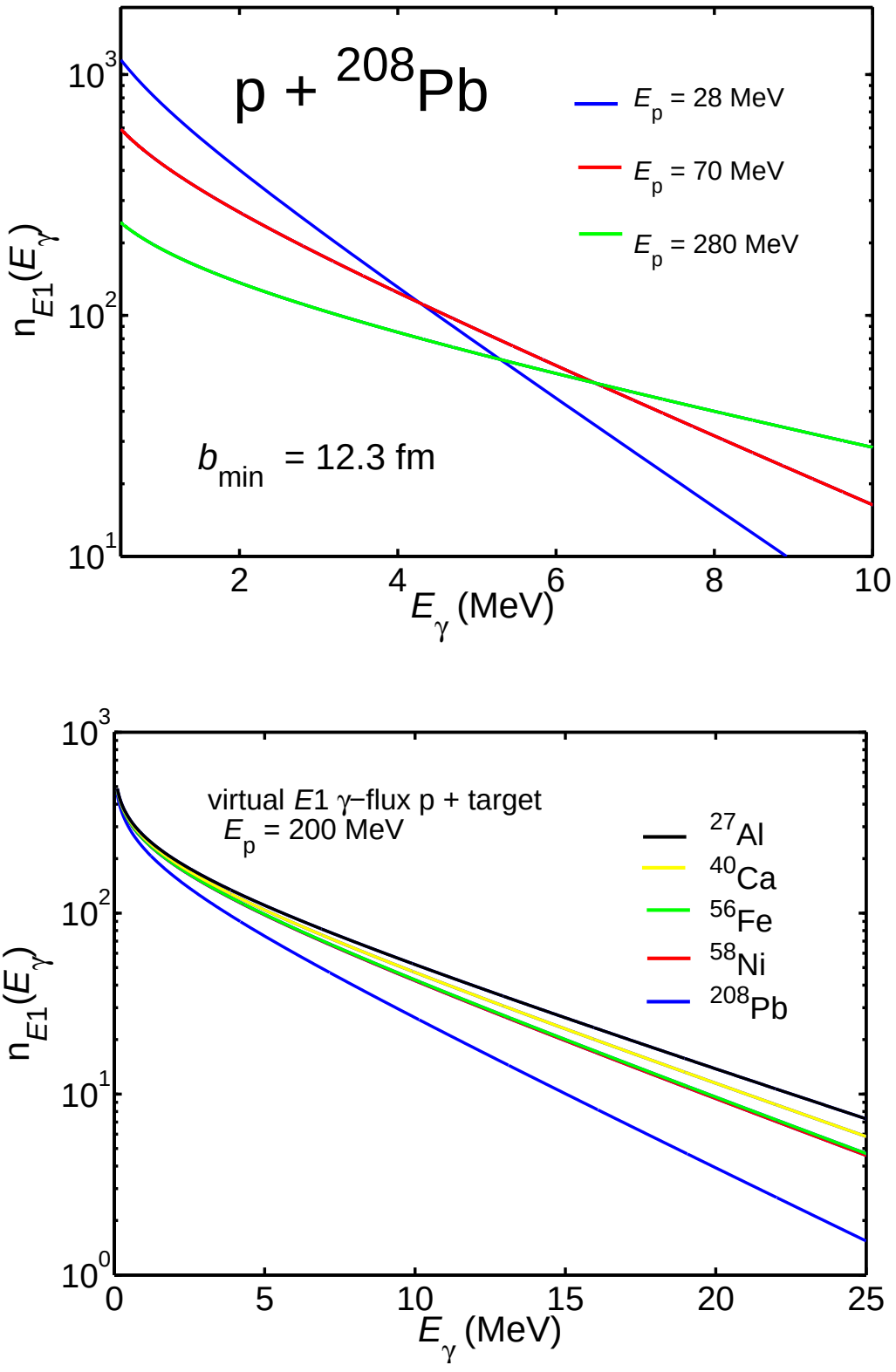

Figure 4.8: *Top panel*: Total number of virtual photons for the $E1$ multipolarity, created by a proton passing by a lead target at impact parameters $b_{\min} = 12.3$ fm and larger (i.e. integrated over impact parameters), for three typical bombarding energies [Ber09]. *Bottom panel*: Total number of virtual photons for the $E1$ multipolarity, as created by a proton passing by the experimental targets at an incident energy of $E_{\rm p} = 200$ MeV (see text).

in Ref. [Ber09], shown at the top of Fig. 4.8, were reproduced. Here, for p +^{208}Pb at various incident energies a value of $b_{\min}$ = 12.3 fm was used. Following the prescription of Eq. (2.60), R_{sep} was determined to be 2.61 fm using a radius r_0 = 1.4 fm. These values were then consistently applied to the other target nuclei to determine $E1$ production rate of virtual photons with a proton beam of 200 MeV as a function of γ-energy for the different target nuclei used in this study and the results are shown in the bottom part of Fig. 4.8.

4.4.1 Equivalent photon method

In order to compare the previously published total photo-absorption data with the present measured data, there is need to convert the measured (p,p′) excitation-energy data into equivalent photo-absorption data (p,p$'_{\gamma\text{corr}}$). According to the equivalent photon method, the excitation of the target nucleus can be described as the absorption of equivalent photons whose spectrum is determined by the Fourier transform of the time-dependent electromagnetic field generated by the projectile [Jac75] (see Sect. 2.4.4). The method is used to calculate the equivalent photon numbers or the $E1$ multipolarity of the virtual radiation and after dividing the background-subtracted measured spectrum by the virtual gamma function, the final step involves normalising the equivalent photo-absorption spectrum to the available published absolute cross-sections of the total photo-absorption data (see Sect. 4.5.1 and the corresponding (p,p$'_{\gamma\text{corr}}$) spectra). The following normalisation factors were used: ^{27}Al(22), ^{40}Ca(25), ^{56}Fe(21), ^{58}Ni(16) and ^{208}Pb(20). To scale up the resulting (p,p$'_{\gamma\text{corr}}$) cross-sections to the corresponding total photo-absorption cross-sections and within the uncertainities of determining experimental absolute (p,p$'_{\gamma\text{corr}}$) cross-sections the factor can be seen to be constant at 20 $\pm$ 5. This results from the limited solid angle measurement used experimentally.

As a starting point, the top part of Fig. 4.9 shows the results of a previous study for

^{208}Pb(p,p$'$) at $E_{\rm p}$ = 295 MeV [Pol11] where there is clearly an excellent correspondence between ^{208}Pb(p,p$'_{\gamma{\rm corr}}$) spectrum and the total photo-absorption data (for the sake of inter comparison all of the figures for this section are placed at the end). The bottom part of Fig. 4.9 displays a comparison between the present, normalised, equivalent photo-absorption cross-section energy spectrum and the published total photo-absorption data on ^{208}Pb [Var03]. Inspecting Fig. 4.9, one can see that the two data sets (previous ^{208}Pb(p,p$'_{\gamma{\rm corr}}$) at 295 MeV and present ^{208}Pb(p,p$'_{\gamma{\rm corr}}$) at 200 MeV) demonstrate a remarkable agreement suggesting that the purely semi-classical calculation given by Eq. (2.57) is able to reproduce the available published total photo-absorption measurement on ^{208}Pb. In addition, because of the excellent agreement between the published photo-nuclear data and the equivalent photo-absorption spectra for other nuclei studied namely ^{58}Ni [Ish02a], ^{56}Fe [Bor00], ^{40}Ca [Ero03] and ^{27}Al [Ahr75], one can justify the use of semi-classical method (see Figs 4.10, 4.11, 4.12 and 4.13, respectively). Therefore, our equivalent photo-absorption cross-section data support the conclusions on the presence of the IVGDR in ^{208}Pb, ^{58} Ni, ^{56}Fe, ^{40}Ca and ^{27}Al, obtained from studying the photo-nuclear data. Unfortunately, no plot of total photo-absorption data in comparison with the present equivalent photo-absorption ^{56}Fe energy spectrum is shown due to the unavailablity of (γ,ABS) data in the literature. From the figures presented in this section, it is clear that ^{208}Pb nucleus has the lowest neutron- and-proton separation energies compared to the other relatively low mass nuclei. This is consistent with the Liquid Drop Model of the nucleus as a balance between the attractive short-range nuclear force (volume) and long-range Coulomb repulsion terms, resulting in less tightly-bound heavy nuclei. The nucleus ^{40}Ca is seen as having the highest neutron-separation energy, being a doubly magic nucleus with its valence shells completely filled, hence requiring more energy to remove a single neutron. On the other hand, ^{56}Fe nucleus is seen to have the largest proton-separation energy, being linked to it having the largest binding energy per nucleon, hence more energy will be required to remove the tightly bound proton.

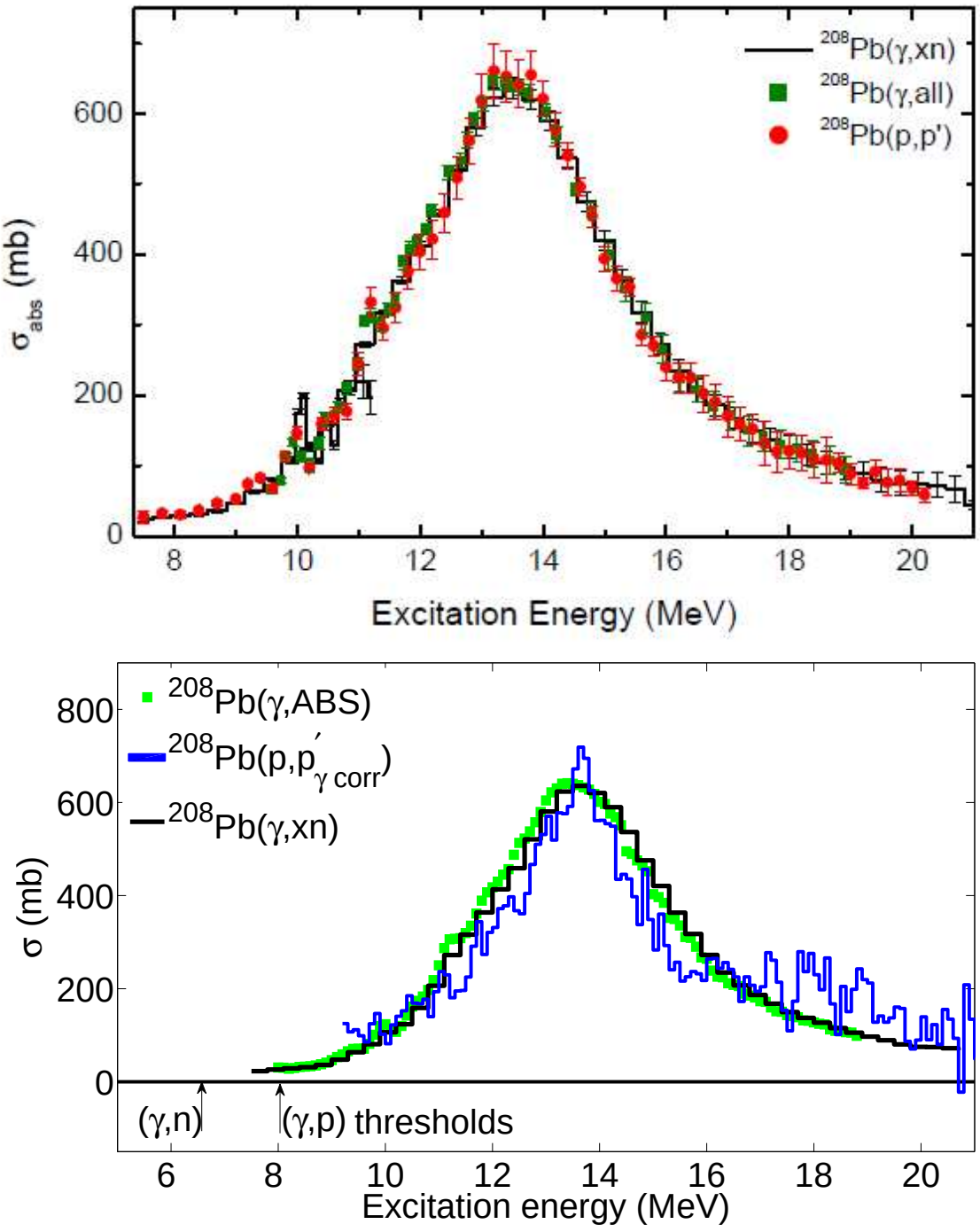

Figure 4.9: *Top panel*: Total photo-absorption cross-sections for the previous ^{208}Pb nucleus in the GDR region. The red circles denote $\sigma_{\rm abs}$ obtained in the work at $E_{\rm p}$ = 295 MeV [Pol11], green squares represent the (γ,all) data from [Sch88] and black histogram represents the (γ,xn) data from [Vey70,Bel82]. *Bottom panel*: The blue histogram denotes the total photo-absorption cross-section ($\sigma(\mathrm{p,p'_{\gamma corr}})$) obtained in the present work at $E_{\rm p}$ = 200 MeV, green squares represent the σ(γ,ABS) data from [Var03], and black histogram represents the σ(γ,xn) data from [Vey70, Bel82].

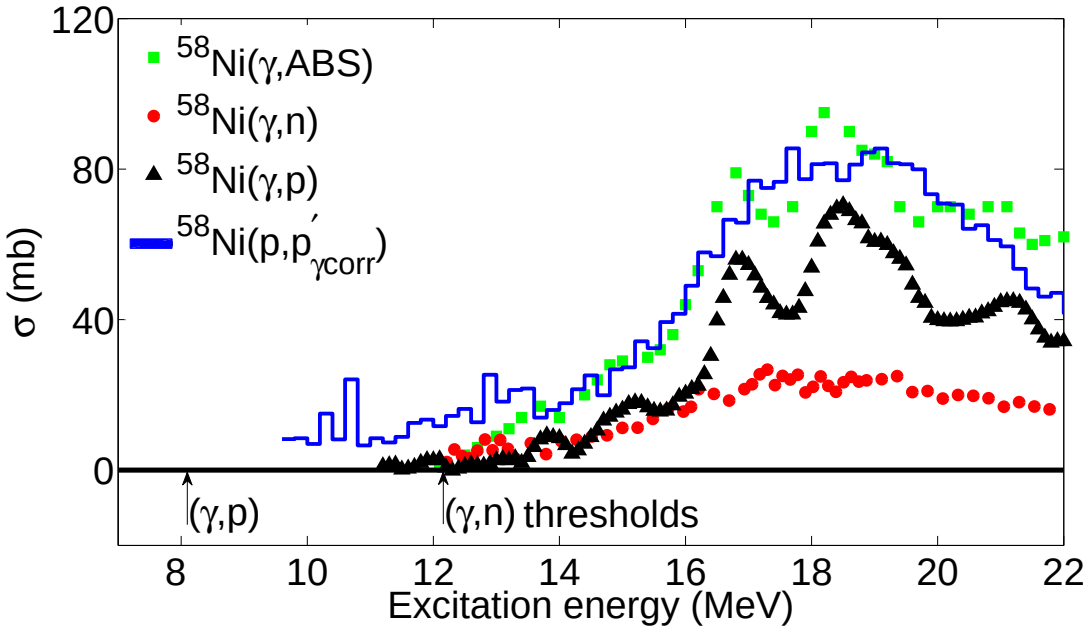

Figure 4.10: The blue histogram denotes the total photo-absorption cross-section ($\sigma(\mathrm{p},\mathrm{p}'_{\gamma\mathrm{corr}})$) obtained in the present work at E_p = 200 MeV, green squares represent the $\sigma(\gamma$,ABS) data from [Ish02a], red circles denote $\sigma(\gamma$,n) from [Ful74] and black triangles represent $\sigma(\gamma$,p) data from [Ish70].

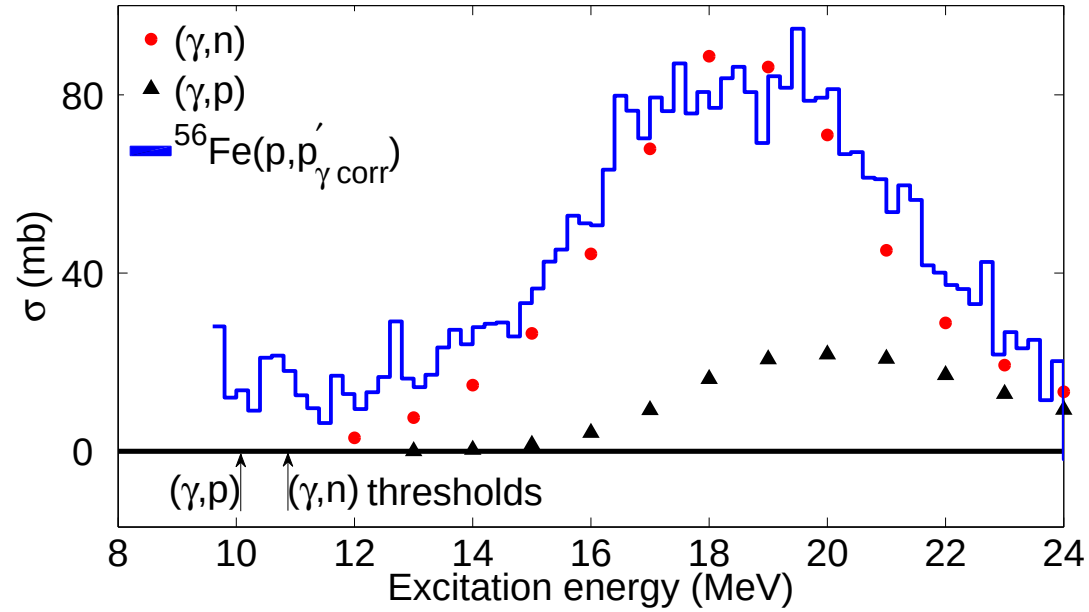

Figure 4.11: The blue histogram denotes the total photo-absorption cross-section ($\sigma(\mathrm{p},\mathrm{p}'_{\gamma\mathrm{corr}})$) obtained in the present work at E_p = 200 MeV, red circles denote $\sigma(\gamma$,n) from [Bor00] and black triangles represent $\sigma(\gamma$,p) from [Bor00].

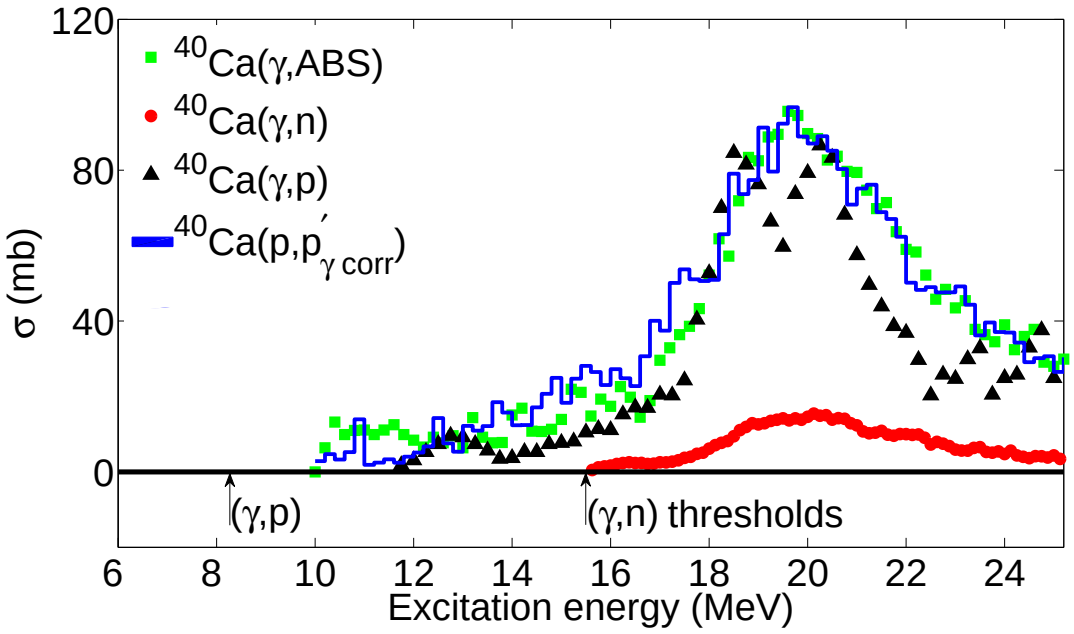

Figure 4.12: The blue histogram denotes the total photo-absorption cross-section ($\sigma(\mathrm{p,p'_{\gamma corr}})$) obtained in the present work at E_p = 200 MeV, green squares represent the $\sigma(\gamma$,ABS) data from [Ero03], red circles denote $\sigma(\gamma$,n) from [Gor67a] and black triangles represent $\sigma(\gamma$,p) from [Gor67b].

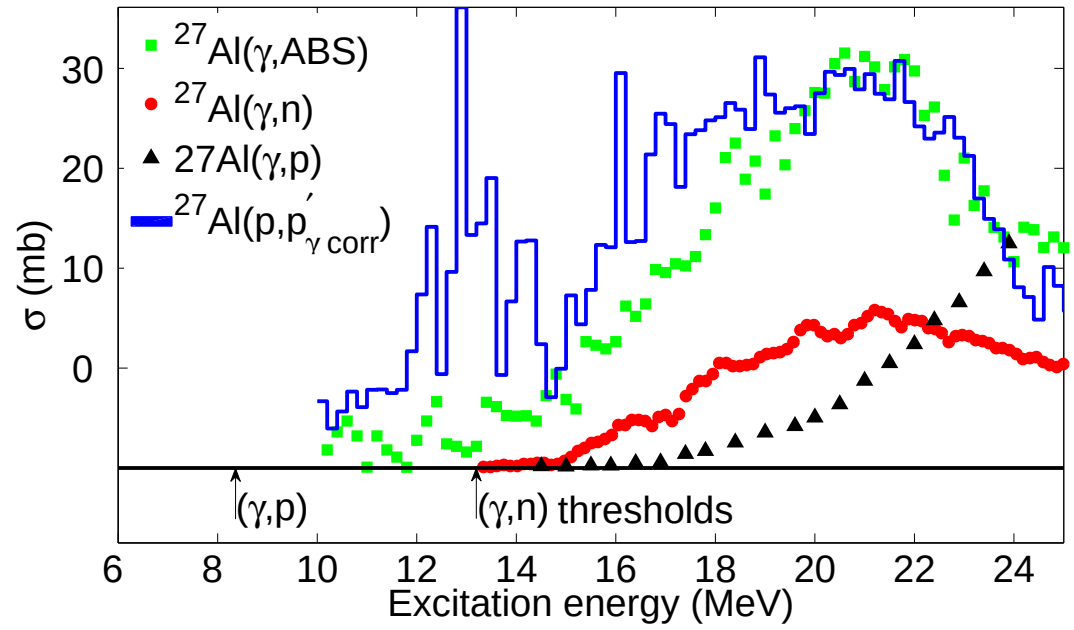

Figure 4.13: The blue histogram denotes the total photo-absorption cross-section ($\sigma(\mathrm{p,p'_{\gamma corr}})$) obtained in the present work at E_p = 200 MeV, green squares represent the $\sigma(\gamma$,ABS) data from [Ahr75], red circles denote $\sigma(\gamma$,n) from [Vey74] and black triangles represent $\sigma(\gamma$,p) from [Sho62].

4.5 QPM $E1$ strength function for ^{208}Pb, ^{58}Ni, ^{56}Fe and ^{40}Ca

Prior to performing the analysis on the fine structure of the GDR, a comparison is made between the experimental results and the global distributions of the $E1$ strengths obtained in the QPM. Information extracted from the energy scales present in the excitation-energy spectra of giant resonances is significant in distinguishing which mechanisms are dominant for the decay processes. However, there is still no clear explanation on the interpretation of the fine structure scales observed. As a result, the presence of advanced sophisticated microscopic models such as the QPM plays a crucial role in addressing the fine structure interpretation. For a physical interpretation of the obtained experimental results, one should compare them with the microscopic predictions for the strength functions of the collective mode being investigated.

The calculated B($E1$) strength distribution in ^{208}Pb, smoothed with the experimental energy-resolution of 45 keV (FWHM) is shown in Fig. 4.14. Here, a resonance feature centered at $E_{\rm x} \approx 14$ MeV is observed and the strength distribution shows considerable fine structure. The calculated strength distributions smoothed with the experimental energy-resolutions 52 keV, 42 keV and 47 keV (FWHMs) for ^{58}Ni, ^{56}Fe and ^{40}Ca, respectively, are also shown. From this plot, one can clearly visualise that the broad bumps corresponding to GDRs have been observed in the excitation-energy region 17 – 19 MeV for ^{58}Ni and around 17 – 20 MeV for ^{56}Fe nucleus. Moreover, for ^{40}Ca nucleus, the prominent isovector giant dipole resonance (IVGDR), situated around $E_{\rm x} \approx 17$ – 20 MeV with pronounced fine structure, is observed. The features of Fig. 4.14 reproduce reasonably well the resonance regions as observed in the experimental results displayed in Fig. 4.1. Figure 4.14 provides sufficient evidence that fine structure exists in the theoretical QPM predictions and presages the expectation of fine structure in the experimentally measured excitation-

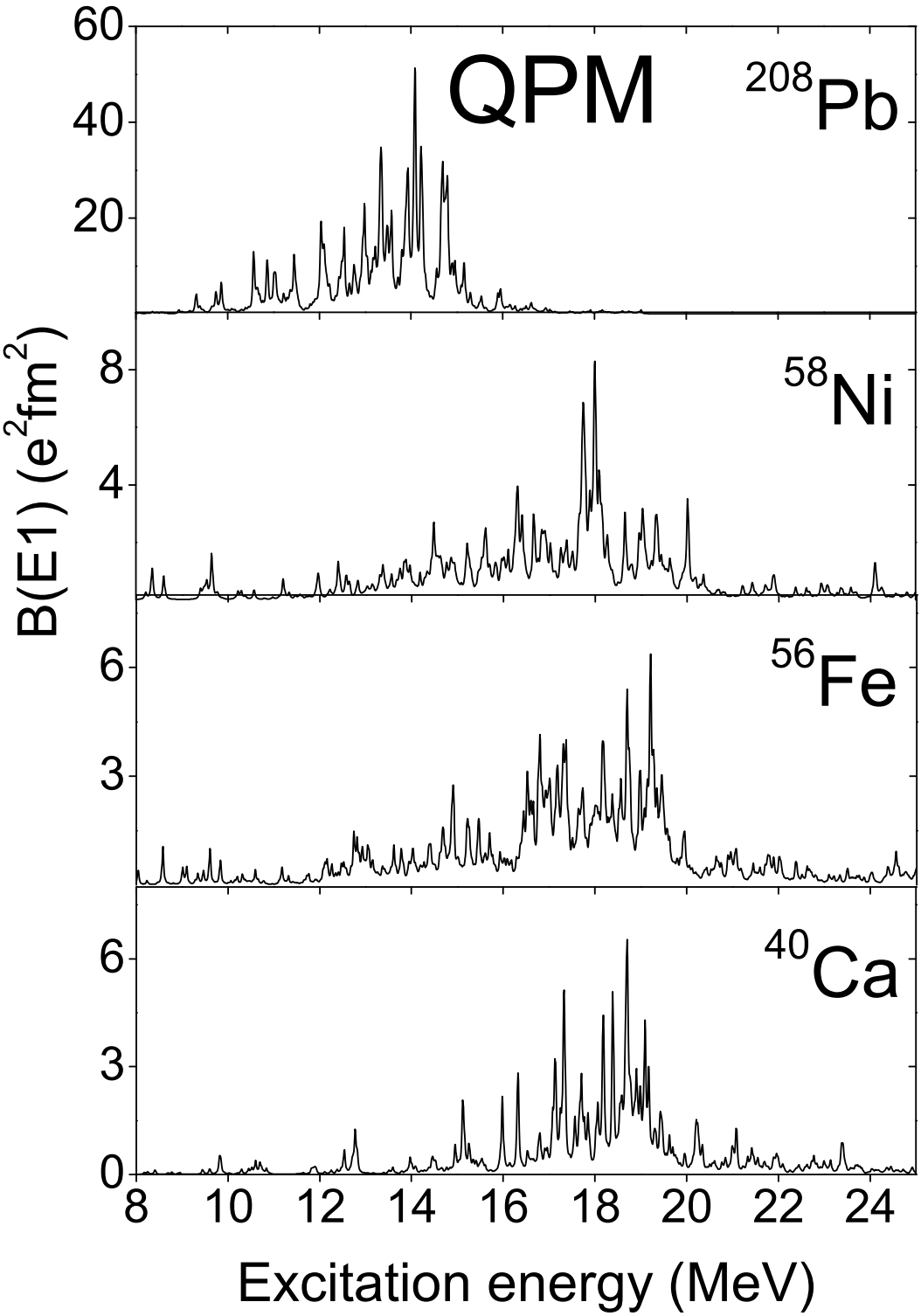

Figure 4.14: QPM $E1$ strength distributions for the target nuclei after being folded with the corresponding experimental energy-resolutions.

energy spectra.

No QPM calculations were perfomed for ^{27}Al nucleus, the reason being that it is an odd mass nucleus and is too light, resulting in QPM calculations being extremely difficult to perform since the mean field is calculated from the harmonic oscillator instead of the commonly used Woods-Saxon potential.

The density of complex (2- and 3-phonon) configurations increases very rapidly with excitation energy. For this reason, the QPM calculations of the GDR in the present study have been performed on the basis of the interacting one- and two-phonon configurations only. From QPM results including 2-phonon states, one can conclude that Landau damping is the most important mechanism leading to strength fragmentation.

4.5.1 $E1$ response: experiment *versus* theory

The microscopic calculations of the QPM are compared to the measured (p,p′) excitation-energy spectra and the equivalent photo-absorption spectra as shown in Figs. 4.15 – 4.18. In general, by inspecting all the comparison plots, it is clear that the GDR total width is somewhat underpredicted by the theoretical calculations. This is not surprising because the calculations were performed in one- and two-phonon basis, i.e. only the first stage of the doorway damping is accounted for leading to underestimation of the total width of the GDR. The measured (p,p′) excitation-energy spectra (top panels) failed to reproduce the resonance centroid energies, while the equivalent photo-absorption spectra (middle panels) accurately reproduced the centroid energies and QPM calculations (bottom panels) slightly underpredicted them. This originates from the photo-absorption cross-section being proportional to B($E1$)E_{x}, i.e. due to the energy dependence of the virtual photon numbers, its centroid energy is a few hundred keV above that of B($E1$) distribution.

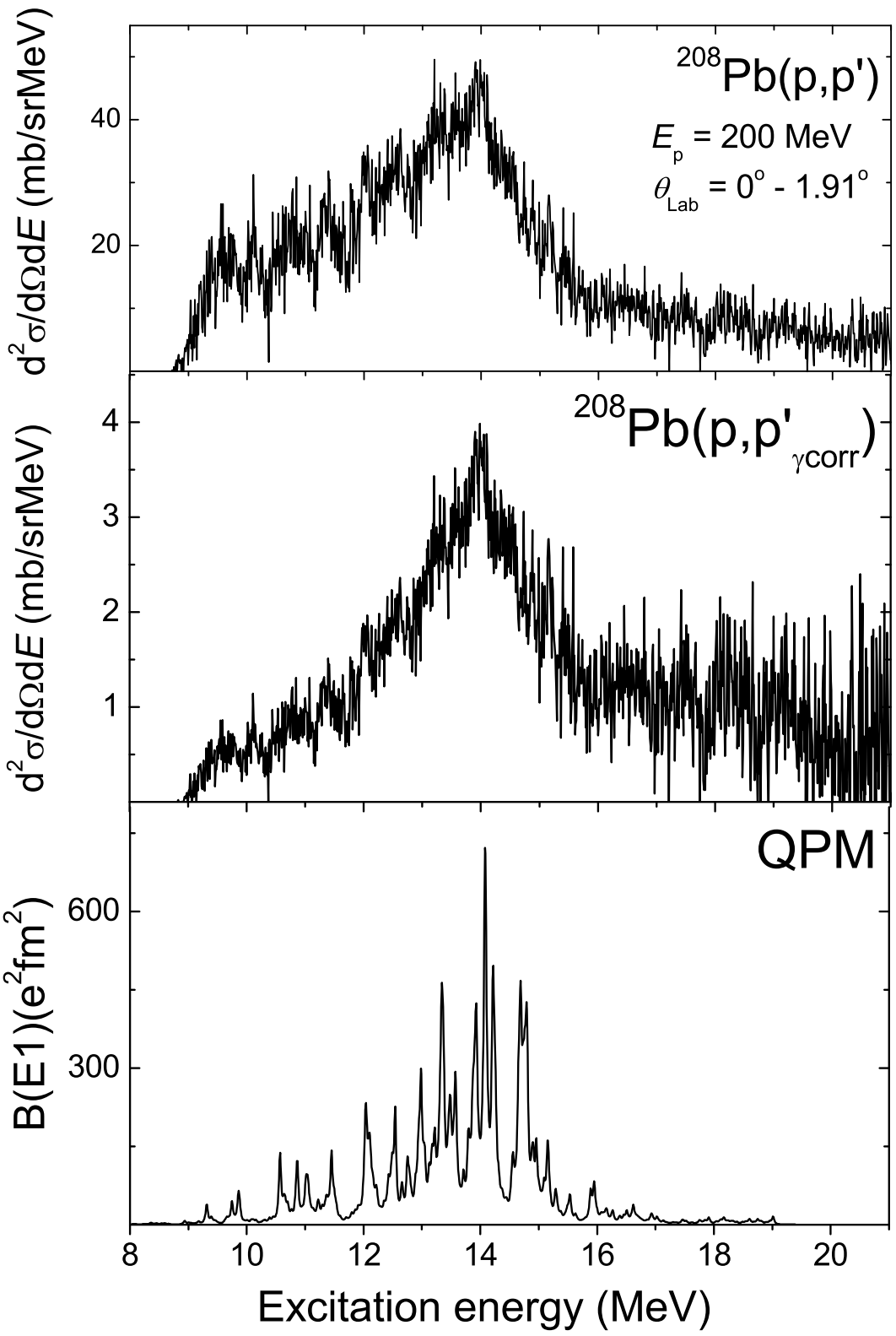

Figure 4.15: *Top panel*: $E1$ response in experimental ^{208}Pb(p,p′) spectrum between 8 MeV and 21 MeV. *Middle panel*: $E1$ response in ^{208}Pb(p,p′$_{\gamma corr}$) spectrum between 8 MeV and 21 MeV. *Bottom panel*: QPM theoretical calculations for ^{208}Pb nucleus.

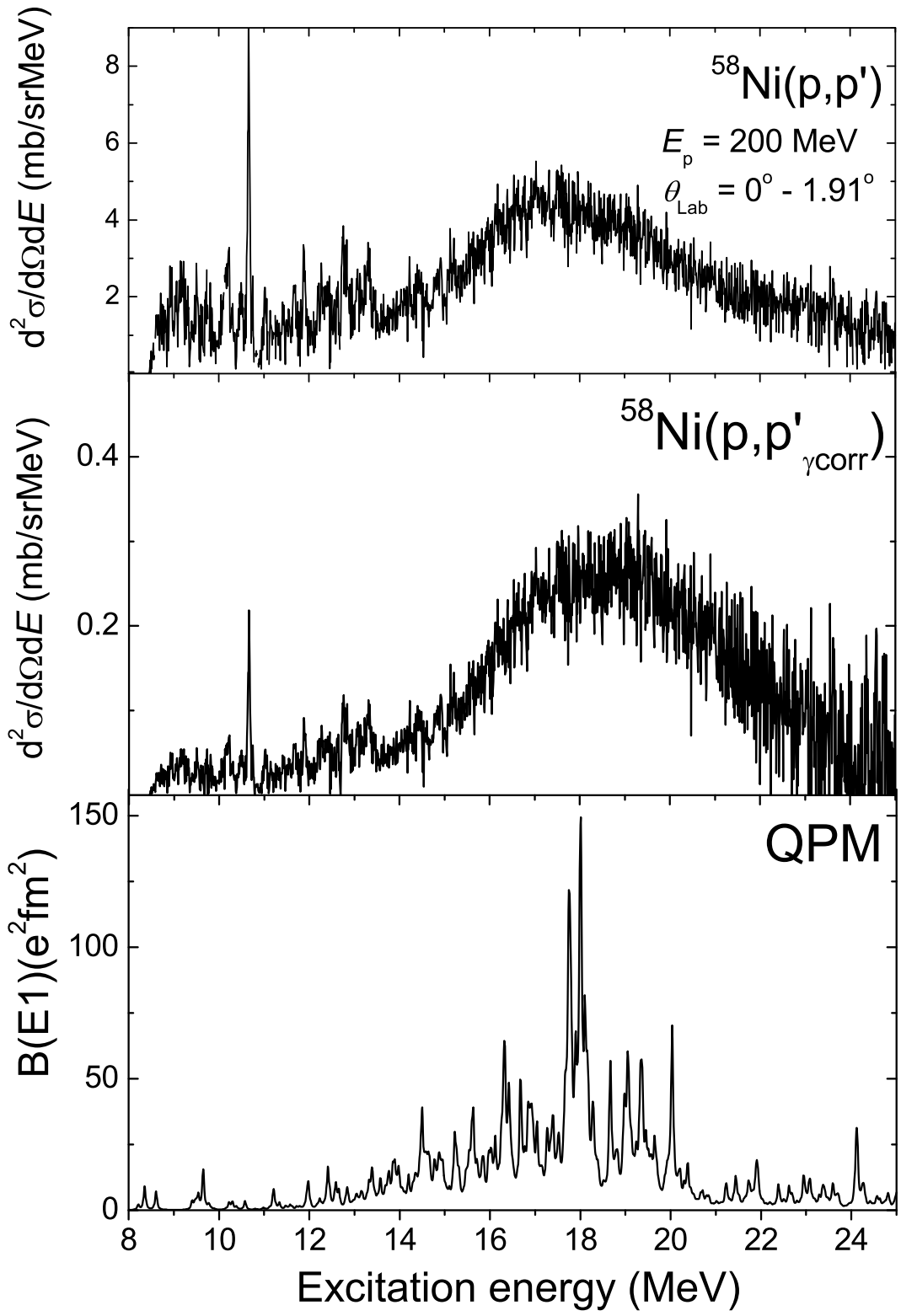

Figure 4.16: *Top panel*: $E1$ response in experimental ^{58}Ni(p,p′) spectrum between 8 MeV and 25 MeV. *Middle panel*: $E1$ response in ^{58}Ni(p,p$'_{\gamma corr}$) spectrum between 8 MeV and 25 MeV. *Bottom panel*: QPM theoretical calculations for ^{58}Ni nucleus.

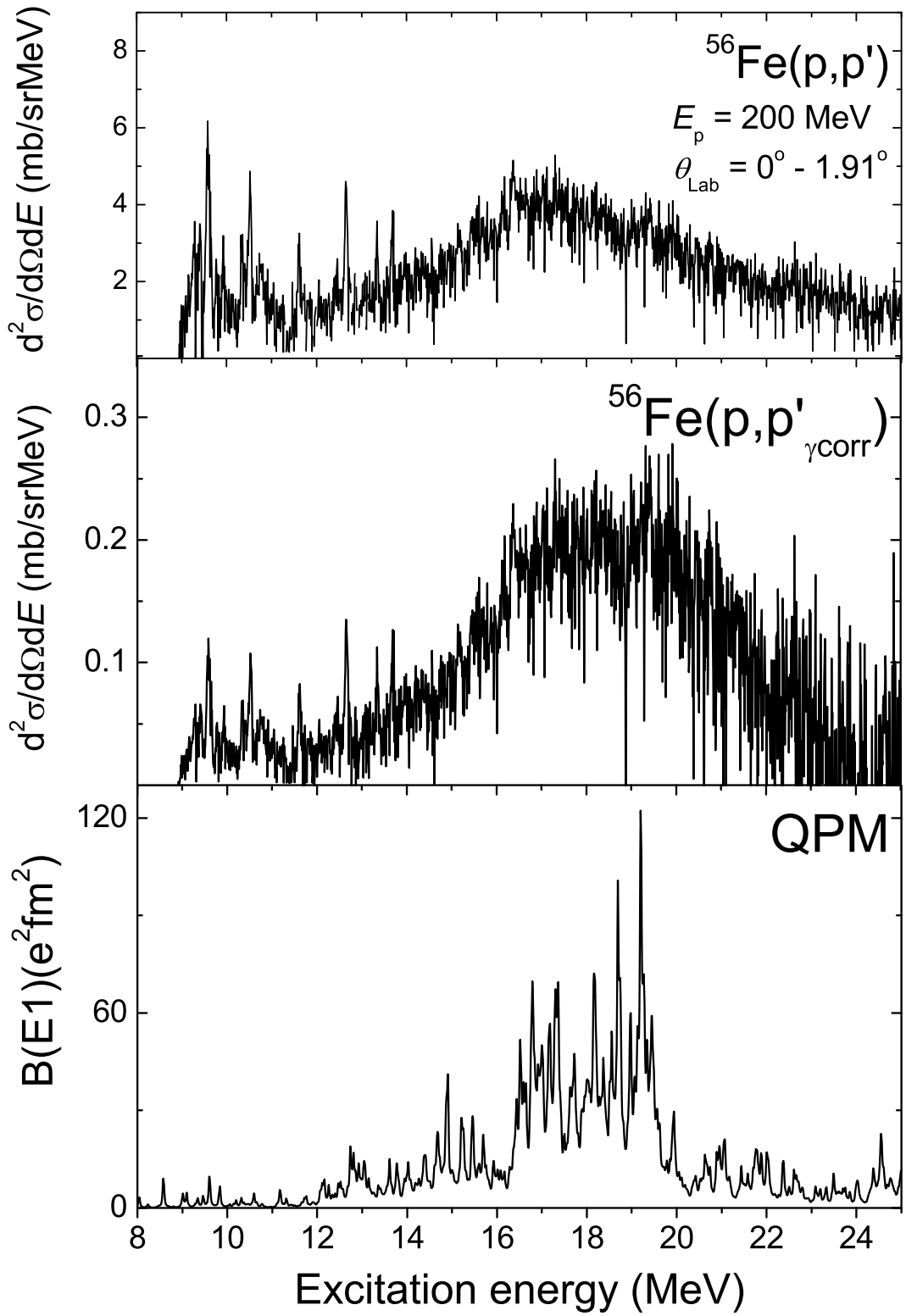

Figure 4.17: *Top panel*: $E1$ response in experimental ^{56}Fe(p,p′) spectrum between 8 MeV and 25 MeV. *Middle panel*: $E1$ response in ^{56}Fe(p,p$'_{\gamma corr}$) spectrum between 8 MeV and 25 MeV. *Bottom panel*: QPM theoretical calculations for ^{56}Fe nucleus.

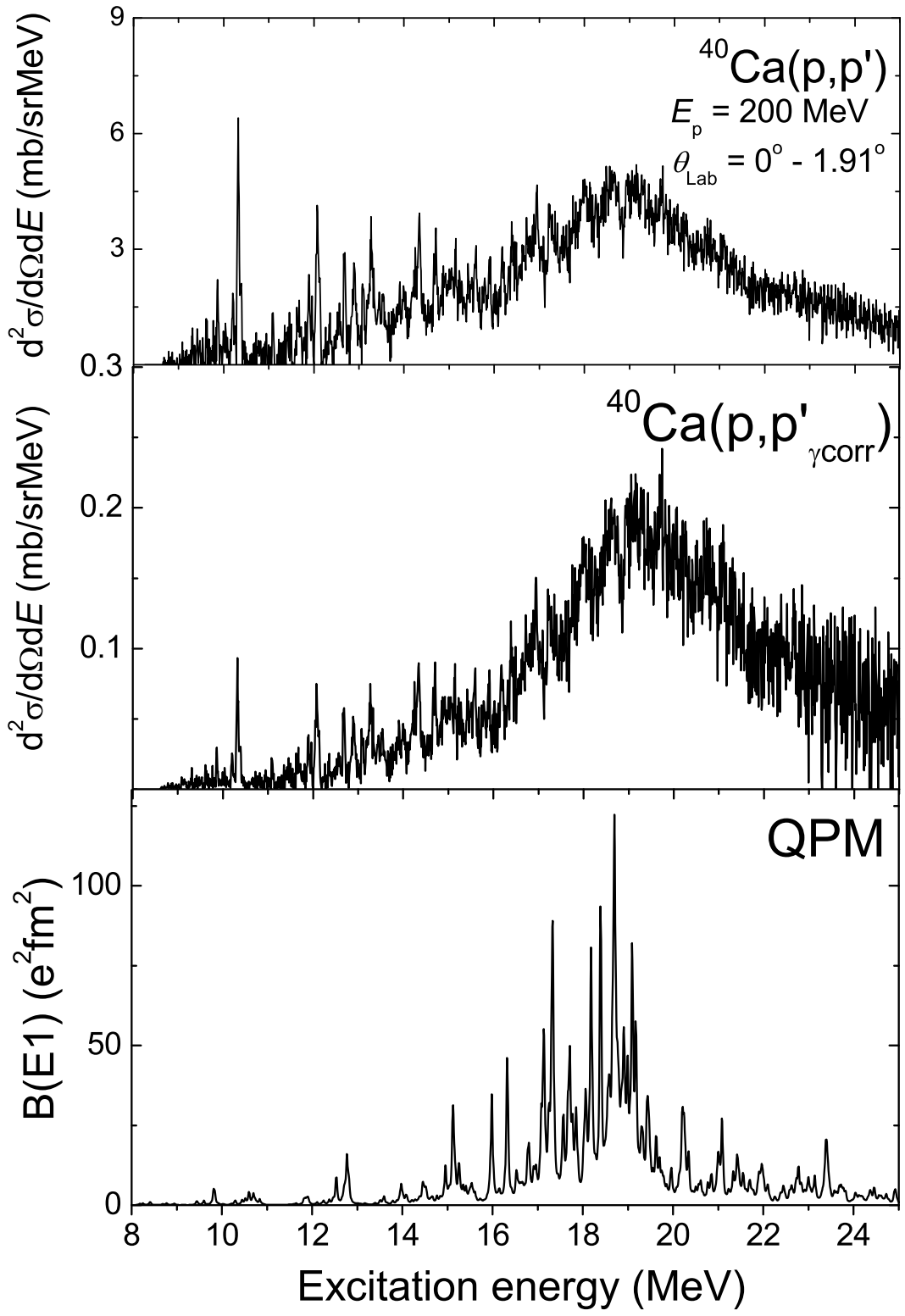

Figure 4.18: *Top panel*: $E1$ response in experimental ^{40}Ca(p,p′) spectrum between 8 MeV and 25 MeV. *Middle panel*: $E1$ response in ^{40}Ca(p,p$'_{\gamma corr}$) spectrum between 8 MeV and 25 MeV. *Bottom panel*: QPM theoretical calculations for ^{40}Ca nucleus.

4.6 Characteristic energy scales: experimental *versus* theoretical

The application of the wavelet analysis technique provides a more detailed insight into and quantitative measure of the observed structures in the IVGDR region. One of the primary aims of this work is to extract characteristic energy scales from the excitation-energy region of the IVGDR, comparing the energy scales obtained from experiment with those from theoretical model predictions.

In order to perform wavelet analysis on the data, the Matlab software [Mat07] is used. More details of this technique are given in Sect. 2.6.2. The choice of the Mother wavelet plays an important role in this type of analysis. In order to achieve an optimum representation of the signal σ using wavelet transformation, one has to select a function ψ which resembles the properties and features of the studied signal. The better the correspondence between the shape of ψ and σ is, the larger is the wavelet coefficient. A maximum of the wavelet coefficients at certain value δE indicates a correlation in the signal at the given scale, often called *characteristic scale*. As a result, this choice of Mother wavelet should have a direct link with the type of spectrum being fitted.

The Morlet or complex Morlet Mother wavelet is favoured in studies of fine structure phenomena because of its ability to give the smallest time-bandwidth product [Lag92]. In the present analysis the complex Morlet Mother wavelet was chosen since extracted energy scales are directly comparable to the equivalent natural Fourier scale.

The Continuous Wavelet Transform (CWT) was applied to the region in the equivalent photo-absorption spectrum corresponding to the maximum of the IVGDR using the complex Morlet Mother wavelet. The equivalent photo-absorption spectra

better represent the IVGDR in terms of position and width after the background from other multipoles and quasi-free scattering has been subtracted from the measured (p,p′) excitation-energy spectra. As such, characteristic energy scales from the microscopic QPM calculations can be compared to energy scales from equivalent photo-absorption spectra. Moreover, in the case of ^{208}Pb, scales were also extracted from the EMPM calculations and compared *against* QPM scales within the same excitation-energy range.

In Figs. 4.19 – 4.24 the excitation-energy spectra (top-right panels) and corresponding wavelet transforms (middle- and bottom-right panels) are plotted for ^{208}Pb, ^{58}Ni, ^{56}Fe, ^{40}Ca and ^{27}Al. The middle-right panels display the scale region up to 5 MeV while the bottom-right panels (up to 2.0 MeV) show the same results but with a reduced wavelet scale range to emphasise the presence of characteristic energy scales in the fine structure. The shading intensity of each point on these plot corresponds to the magnitude of the wavelet coefficients. Blue colour indicate regions of smallest values of the wavelet coefficients, while red regions represent maximum values of wavelet coefficients. In order to obtain a quantitative measure for the characteristic energy scales that correspond to the maxima of the absolute values of the wavelet coefficients, power spectra (square root of the sum of the squares of the complex coefficients) are plotted (bottom-left panels). Specific characteristic energy scales which are clearly visible or pronounced in the power spectra are indicated by full arrows. Weak characteristic energy scales or less visible scales are shown by dashed arrows.

A summary of the extracted characteristic energy scales is given in Table 4.2. The table gives 4 categories of energy scales: *Identical scales* between "theory" and "experiment" are shown in bold, *pronounced scales* have horizontal lines over them, *weak scales* are not in bold and have no horizontal lines, and scales representing the *total widths of GDRs* are in green colour with horizontal lines under them.

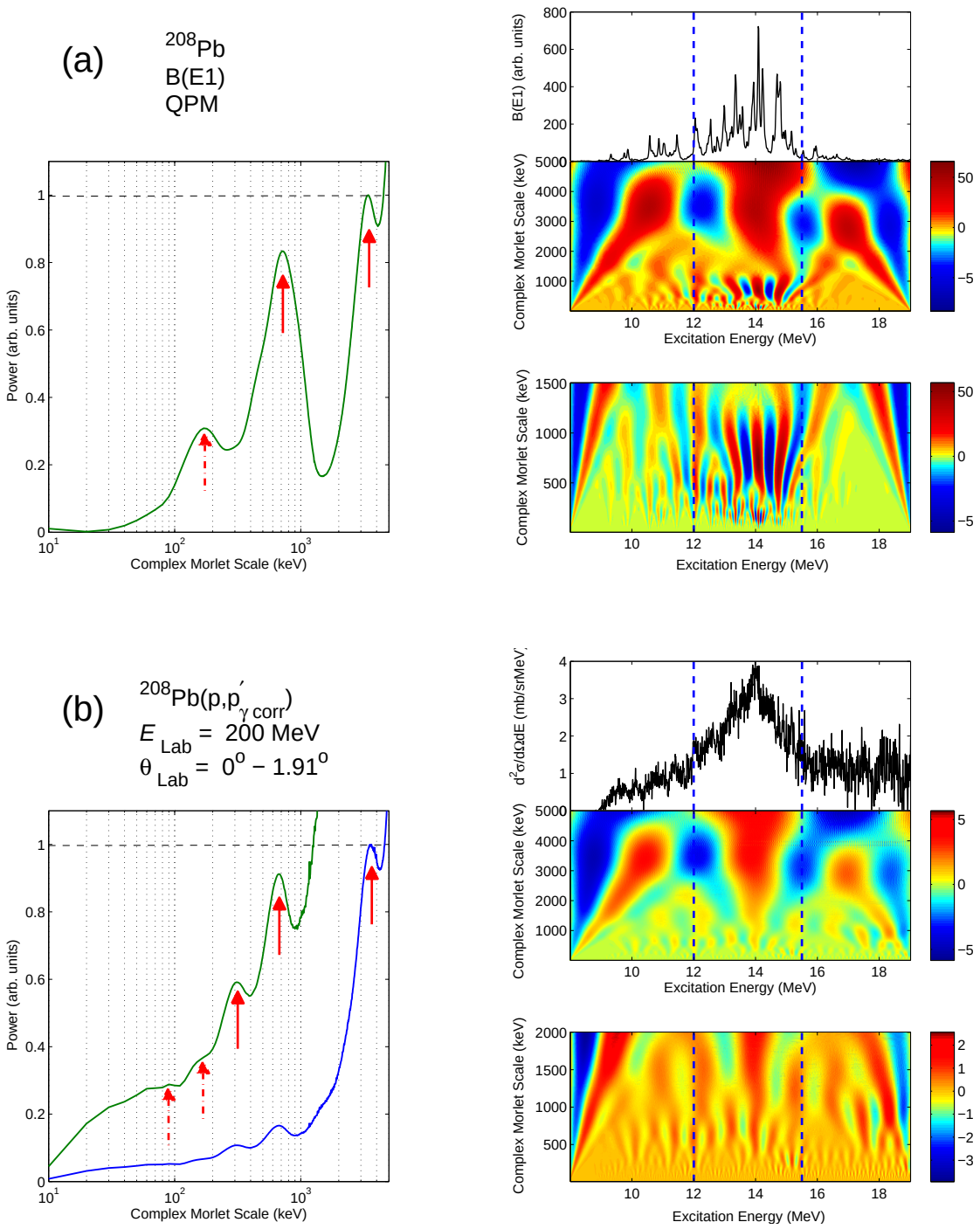

Figure 4.19: *Top panel*: CWT analysis of the IVGDR strength distribution from QPM calculations of ^{208}Pb. The power spectrum on the left represents the region 12 $\leq E_{\rm x} \leq$ 15.5 MeV. *Bottom panel*: CWT analysis of the excitation-energy spectrum of the ^{208}Pb(p,p$'_{\gamma{\rm corr}}$). The power spectrum on the left corresponds to the IVGDR measured and the same region is used in the top part of the figure. **Colour**: The green line in the power spectrum indicates the same characteristic energy scales shown by the blue line but only that they been scaled up by a certain enhancement factor to make them visible and the same applies for all the other nuclei. It should be noted that the scales for the total widths of the GDRs in the table 4.2 are not shown in the other plotted figures except for ^{208}Pb because the scale axis is limited to 5 MeV for better visibility of low-lying wavelet coefficients.

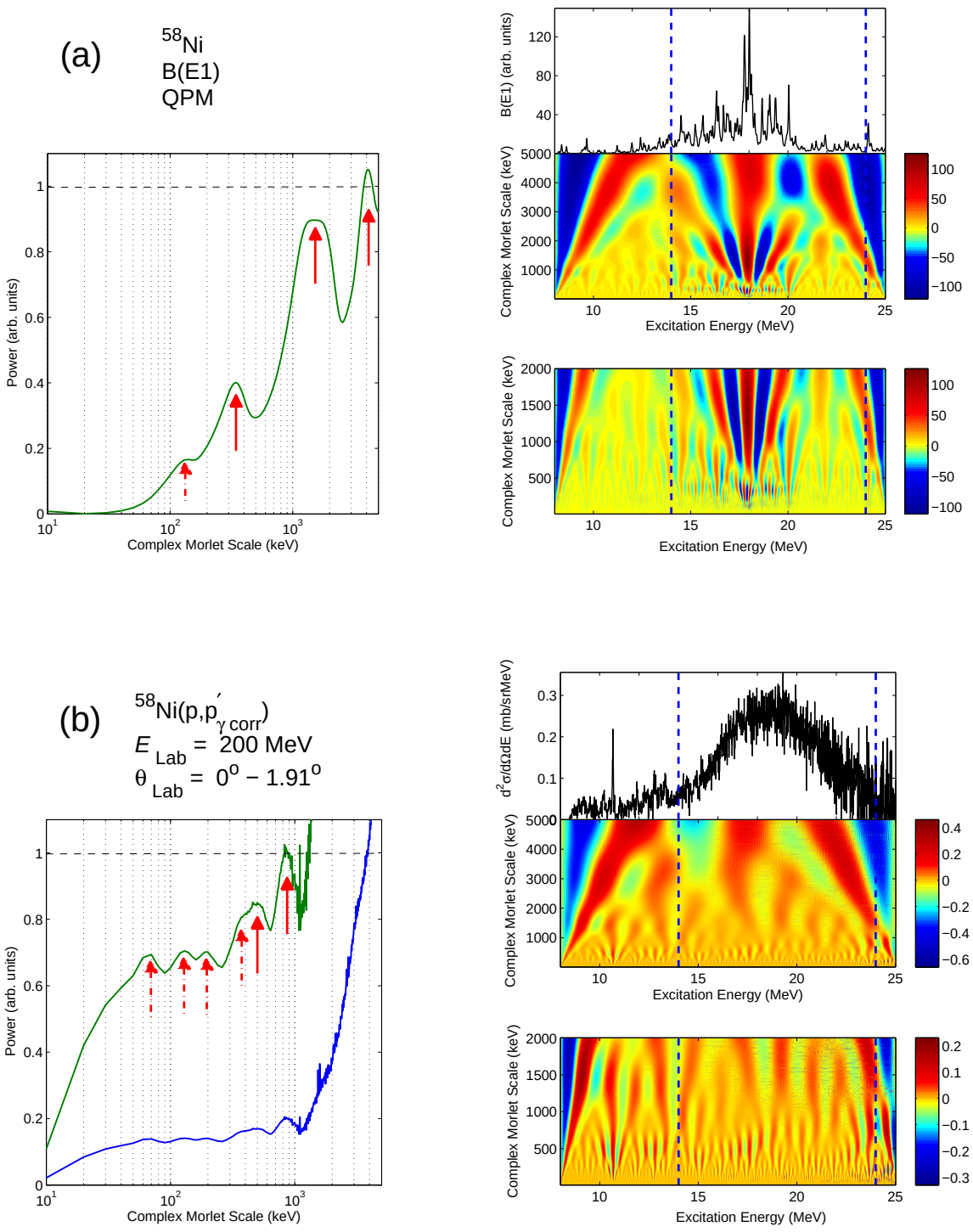

Figure 4.20: *Top panel*: CWT analysis of the IVGDR strength distribution from QPM calculations of ^{58}Ni. The power spectrum on the left represents the region $14 \leq E_{\mathrm{x}} \leq 24$ MeV. *Bottom panel*: CWT analysis of the excitation-energy spectrum of the ^{58}Ni(p,p$'_{\gamma\mathrm{corr}}$). The power spectrum on the left corresponds to the IVGDR measured and the same region is used in the top part of the figure.

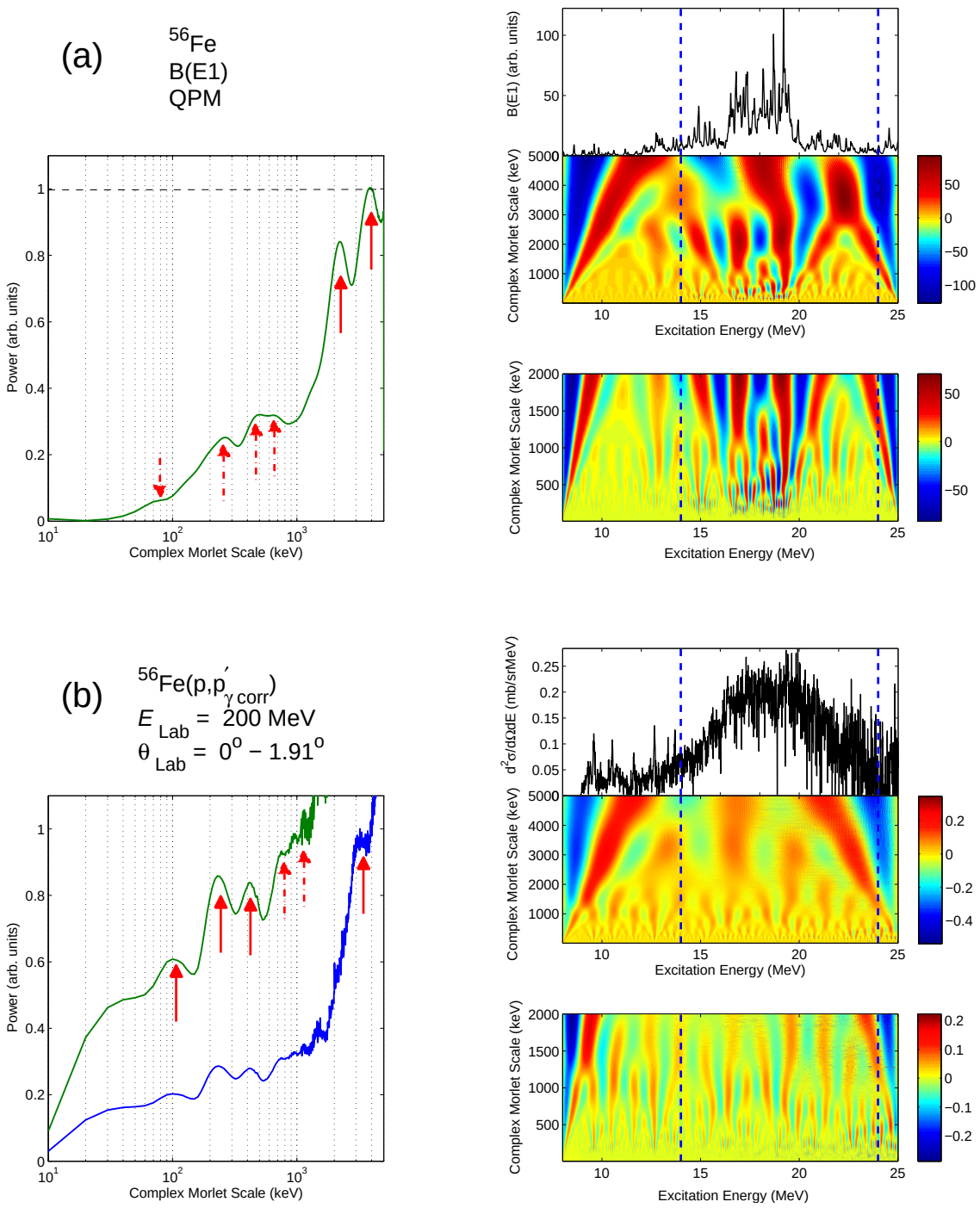

Figure 4.21: *Top panel*: CWT analysis of the IVGDR strength distribution from QPM calculations of ^{56}Fe. The power spectrum on the left represents the region $14 \leq E_{\mathrm{x}} \leq 24$ MeV. *Bottom panel*: CWT analysis of the excitation-energy spectrum of the ^{56}Fe(p,p$'_{\gamma\mathrm{corr}}$). The power spectrum on the left corresponds to the IVGDR measured and the same region is used in the top part of the figure.

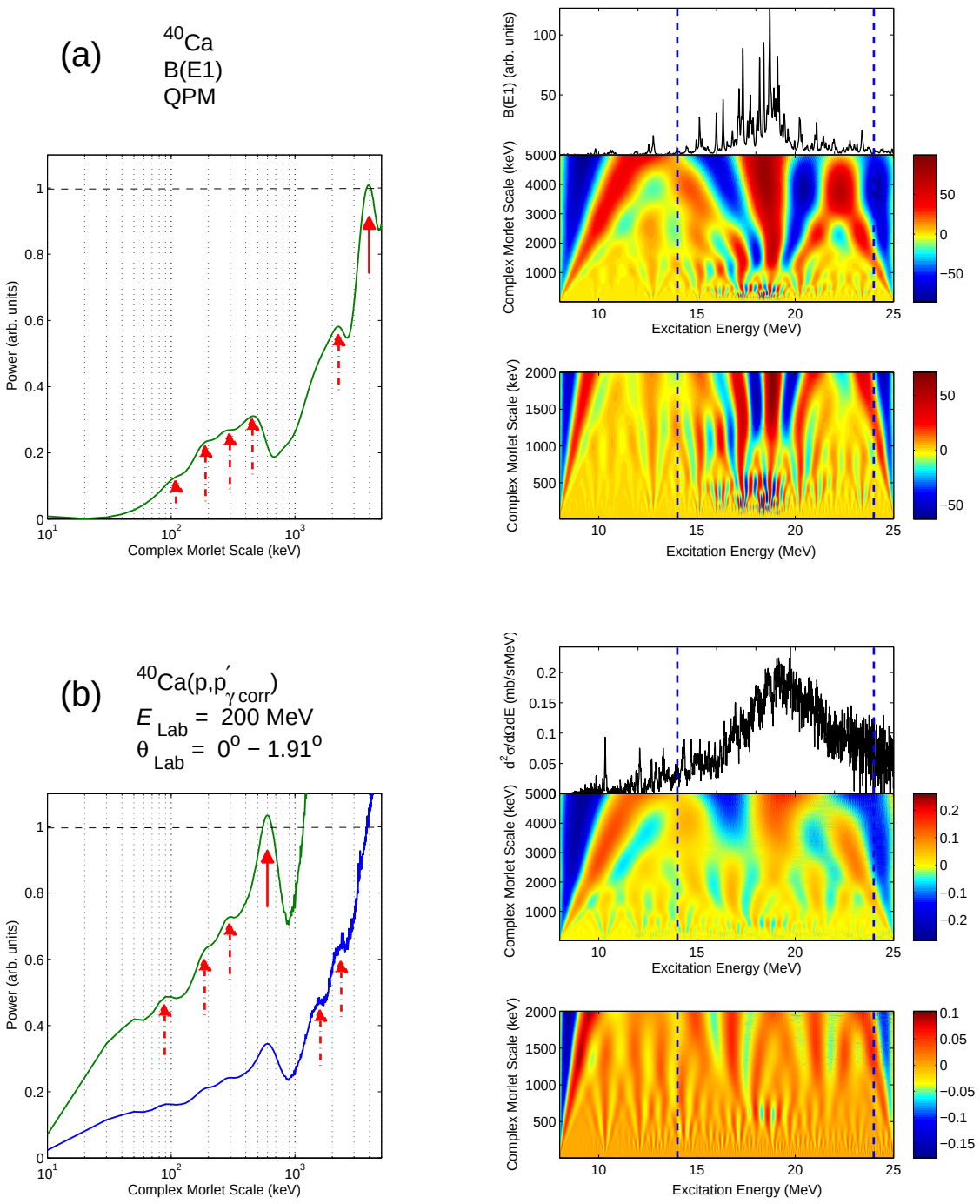

Figure 4.22: *Top panel*: CWT analysis of the IVGDR strength distribution from QPM calculations of ^{40}Ca. The power spectrum on the left represents the region $14 \leq E_{\rm x} \leq 24$ MeV. *Bottom panel*: CWT analysis of the excitation-energy spectrum of the ^{40}Ca(p,p$'_{\gamma{\rm corr}}$). The power spectrum on the left corresponds to the IVGDR measured and the same region is used in the top part of the figure.

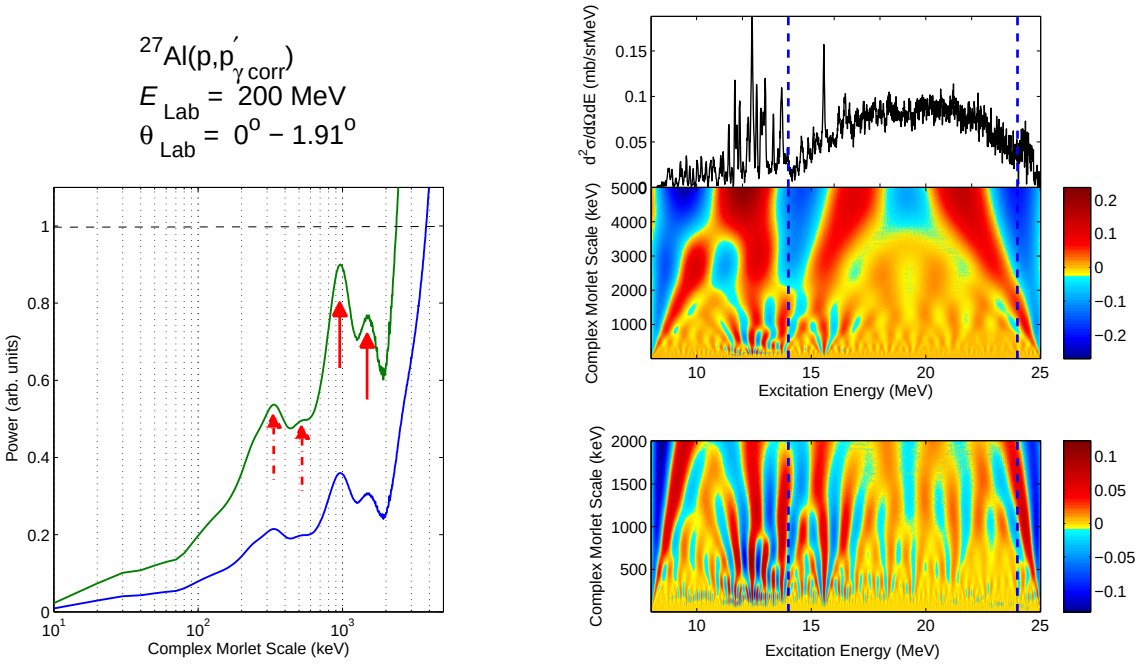

Figure 4.23: CWT analysis of the excitation-energy spectrum of the ^{27}Al(p,p$'_{\gamma corr}$). The power spectrum on the left represents the region $14 \leq E_x \leq 24$ MeV.

Table 4.2: Characteristic energy scales of the GDR in ^{208}Pb, ^{58}Ni, ^{56}Fe, ^{40}Ca and ^{27}Al extracted from the wavelet analysis of equivalent photo-absorption results and QPM calculations. Bold energy scales represent identical scales between "theory" and "experiment", energy scales with horizontal lines over them represent clearly identifiable scales (e.g. $\overline{abc}$), weak scales are not in bold and have no horizontal lines and finally, the energy scales representing the total widths of GDRs are shown in green colour with horizontal lines under them (e.g. $\underline{abc}$).

Nucleus	Scale	**Class I** $\Delta E < 300$ keV	**Class II** $300 \leq \Delta E \leq 1000$ keV	**Class III** $\Delta E \geq 1000$ keV
^{208}Pb	(p,p$'_{\gamma corr}$)	90 **170**	$\overline{310}$ $\overline{\mathbf{700}}$	$\underline{3600}$
	QPM	**170**	$\overline{\mathbf{700}}$	$\overline{3450}$
^{58}Ni	(p,p$'_{\gamma corr}$)	70 **130** 200	**350** $\overline{490}$ $\overline{850}$	$\underline{7150}$
	QPM	**130**	$\overline{\mathbf{350}}$	$\overline{1540}$ $\overline{4130}$
^{56}Fe	(p,p$'_{\gamma corr}$)	$\overline{110}$ $\overline{\mathbf{250}}$	$\overline{\mathbf{440}}$ 790 940	1170 $\overline{3230}$ $\underline{7240}$
	QPM	80 **250**	**440** 680	$\overline{2210}$ $\overline{3990}$
^{40}Ca	(p,p$'_{\gamma corr}$)	90 **190**	**300** $\overline{610}$	1560 2410 $\underline{7470}$
	QPM	110 **190**	**300** 470	2290 $\overline{4010}$
^{27}Al	(p,p$'_{\gamma corr}$)	–	340 530 $\overline{980}$	$\overline{1500}$ $\underline{7600}$

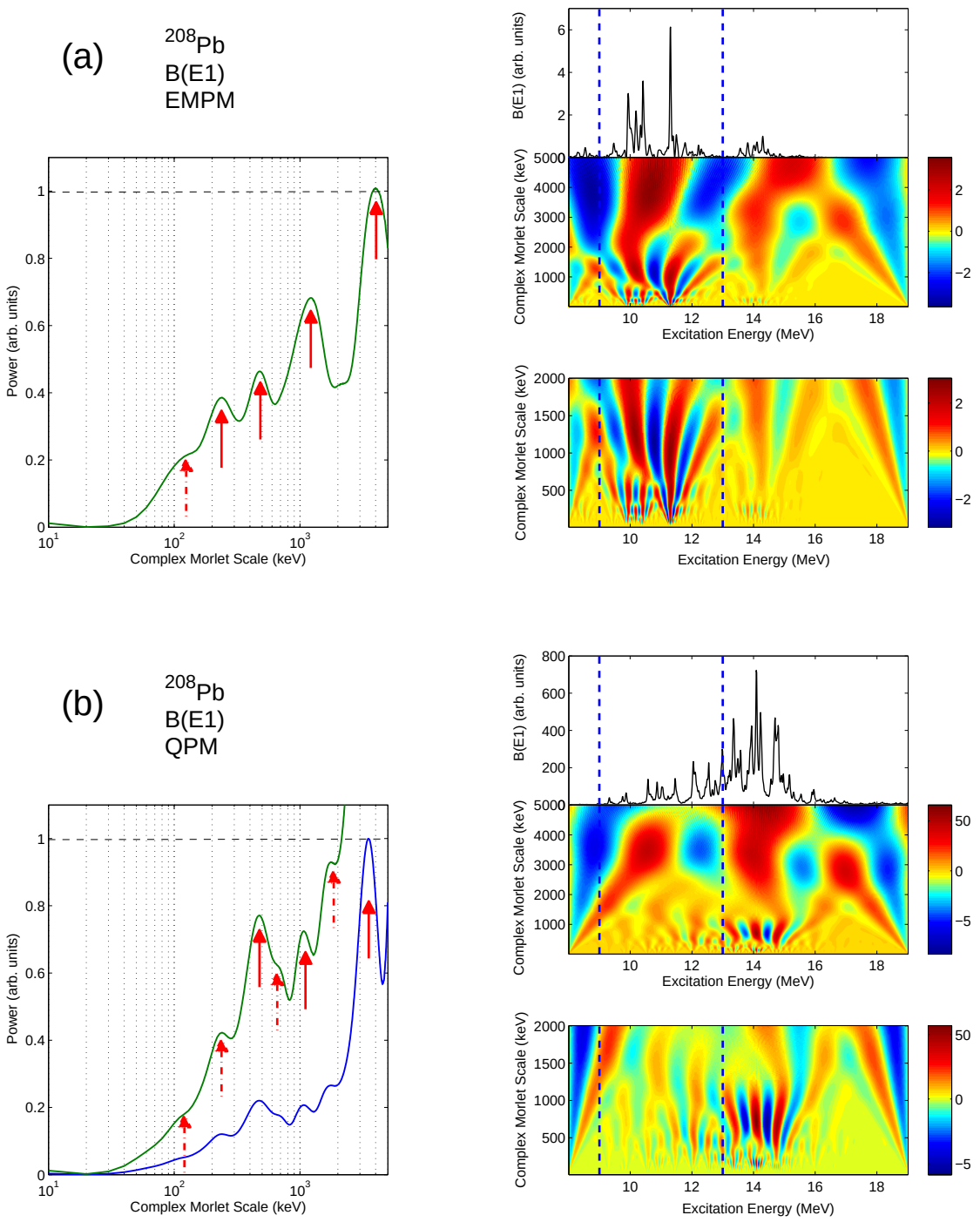

Figure 4.24: *Top panel*: CWT analysis of the IVGDR strength distribution from EMPM calculations of ^{208}Pb. The power spectrum on the left represents the region $9 \leq E_{\mathrm{x}} \leq 13$ MeV. *Bottom panel*: CWT analysis of the IVGDR strength distribution from QPM calculations of ^{208}Pb. The power spectrum on the left corresponds to the IVGDR measured and the same region is used in the top part of the figure.

A comparison between EMPM energy scales and QPM energy scales gave the following energy scales: **120**, $\overline{\mathbf{240}}$, $\overline{\mathbf{490}}$, $\overline{1230}$, and $\overline{4070}$ keV (EMPM energy scales) and **120**, **240**, $\overline{\mathbf{490}}$, 690, $\overline{1120}$, 1760, and $\overline{3510}$ keV (QPM energy scales). Here, it is interesting to note that identical energy scales appear in the lower more pronounced excitation-energy region, $E_{\mathrm{x}} = 9 - 13$ MeV for ^{208}Pb EMPM model and the QPM model (see Fig. 4.24).

4.6.1 RPA discussion

While the quantitative results of various theoretical models differ significantly, the success in reproducing at least the qualitative features of the characteristic energy scales motivates attempts to extract their under-lying physical nature from the model predictions. Within the RPA model, where only $1p$-$1h$ transitions are treated, the GDR strength is concentrated in just a few states. Furthermore, the extraction of information on the dominant damping mechanism can be achieved through CWT analysis of the QPM calculations including only 1-phonon transitions.

The strength distributions calculated with QPM and RPA methods are plotted in Figs. 4.25 – 4.28 together with the equivalent photo-absorption spectra. The left panels of the figures show the response functions while the right panels depict the resulting wavelet power distributions from wavelet analysis. The RPA response function results for ^{208}Pb – ^{40}Ca show that all the nuclei contain more than four states, such that the response functions show fine structures already on the RPA levels. Accordingly, the wavelet analysis of the RPA results is able to detect characteristic energy scales, beyond trivial scale-folding widths of the experimental energy-resolutions, included for the comparison with experiment. The deduced RPA results are reasonably similar to the QPM results including 2-phonon states, confirming that Landau damping is the most important mechanism leading to the formation of fine structure and related characteristic energy scales, found in the experimental spectra.

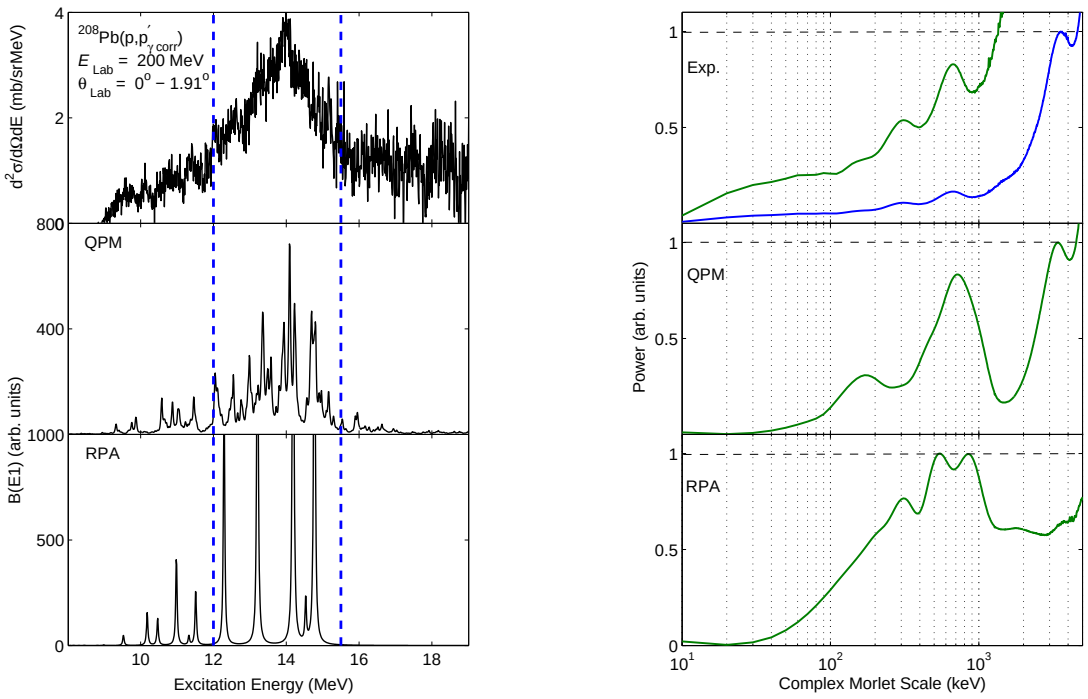

Figure 4.25: ^{208}Pb equivalent photo-absorption spectrum together with the power spectrum from the CWT analysis in comparison with QPM and RPA predictions.

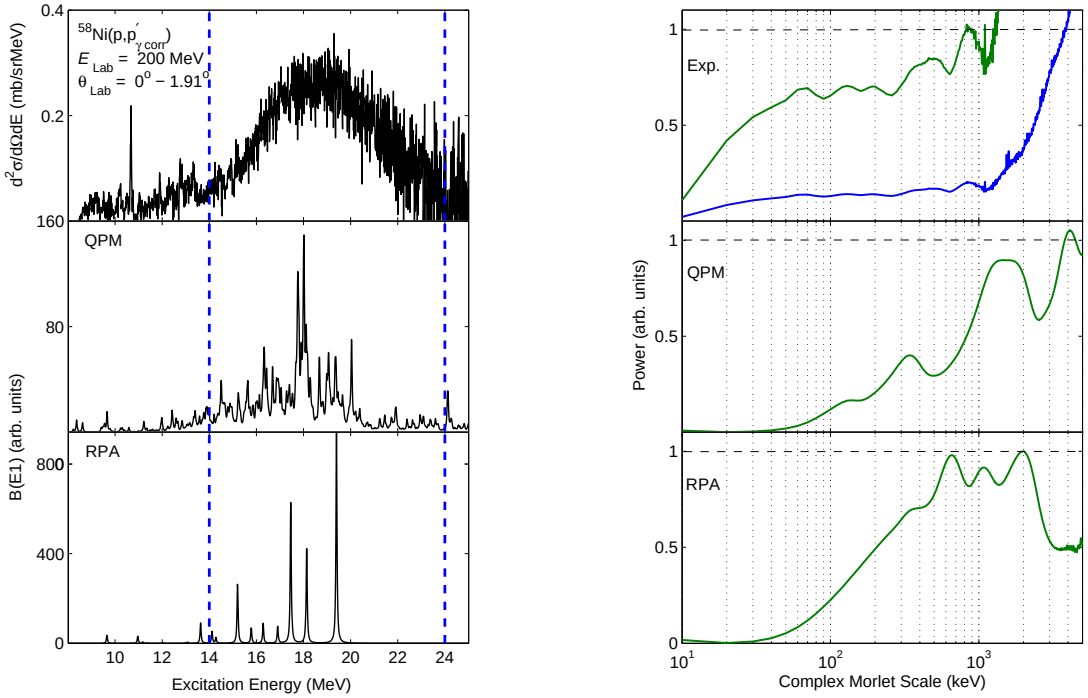

Figure 4.26: ^{58}Ni equivalent photo-absorption spectrum together with the power spectrum from the CWT analysis in comparison with QPM and RPA predictions.

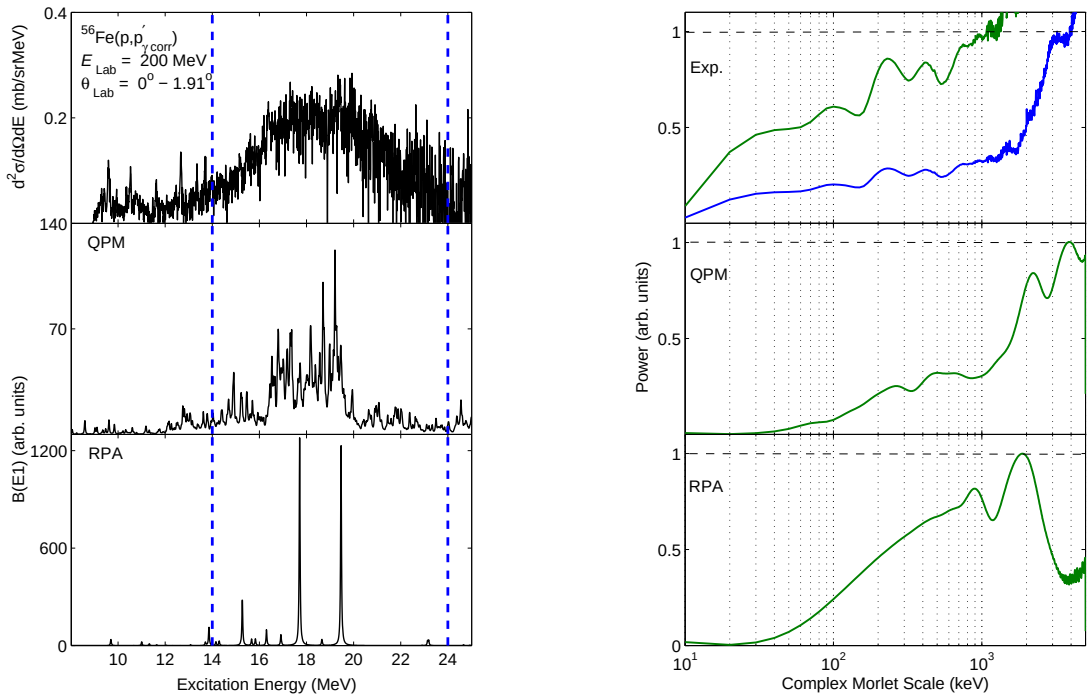

Figure 4.27: ^{56}Fe equivalent photo-absorption spectrum together with the power spectrum from the CWT analysis in comparison with QPM and RPA predictions.

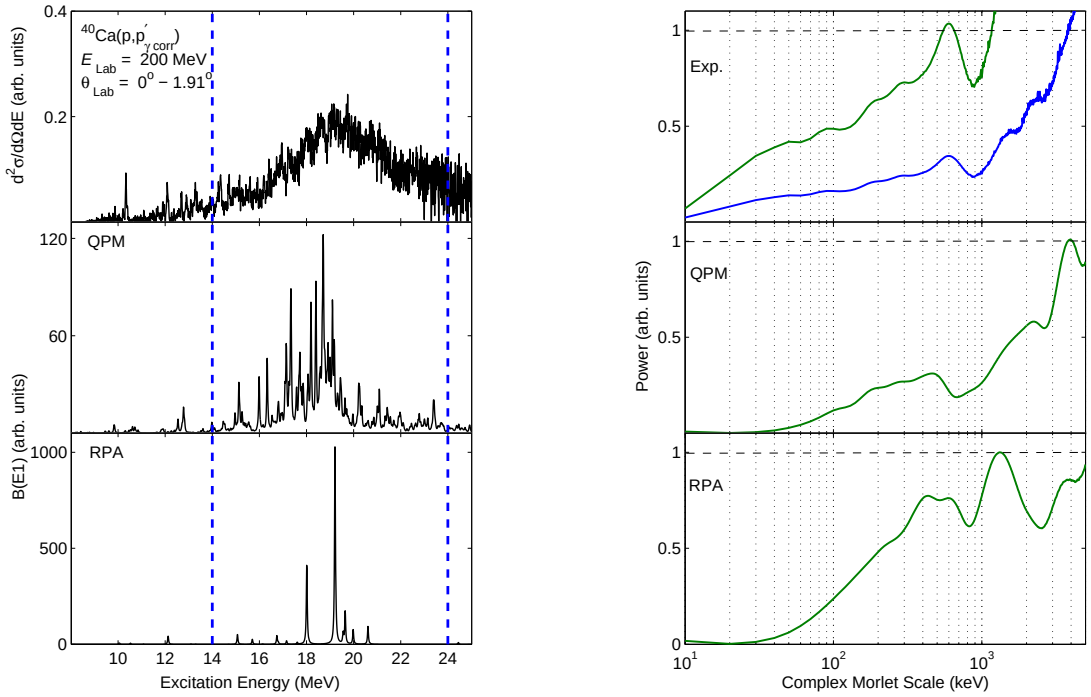

Figure 4.28: ^{40}Ca equivalent photo-absorption spectrum together with the power spectrum from the CWT analysis in comparison with QPM and RPA predictions.

4.7 Extraction of the level densities

The level densities of $J^{\pi} = 1^{-}$ states in ^{208}Pb, ^{58}Ni, ^{56}Fe and ^{40}Ca nuclei were extracted by means a fluctuation analysis technique in the excitation-energy interval, $E_{\mathrm{x}} = 8$ – 20 MeV. The extracted experimental level densities were then compared with different parameterisations of the Back Shifted Fermi Gas (BSFG) model [Rau97, Egi05], the microscopic calculations performed in the framework of the Hartree Fock-Bogoliubov (HFB) model [Hil06], and the Hartree Fock-BCS approach [Dem01].

4.7.1 Fluctuation analysis technique

Basic research on nuclear level densities has been concerned with a number of phenomenological and microscopic models, their validation by comparison with measurements and the extraction of level density parameters from experimental data.

A detailed description of the fluctuation analysis method used for the extraction of level densities was presented in Sect. 2.7.2. Referring back to Eq. (2.138), the autocorrelation function value $(C(\epsilon) - 1)$ at $\epsilon = 0$, is proportional to the mean level spacing $\langle D \rangle$, therefore, leading to direct extraction of $\langle D \rangle$ once the value of the autocorrelation function is known. The extraction process can be done using either one of the following two possible approaches:

- the determination of the background in order to extract the mean level spacing from the experimental autocorrelation function by using Eq. (2.138).
- by making an assumption that defines the level density, e.g. calculating the level density by theoretical model means, so as to allow direct background determination by varying its shape in a way that the experimental value $(C(\epsilon = 0) - 1)$ becomes equal to the theoretical value.

For this particular work, level densities were extracted by using the first approach.

The majority of instrumental background was removed using software cuts during data analysis which allows the remaining background contributions to be accounted for using the model-independent Discrete Wavelet Transform (DWT), in the region of IVGDR.

4.7.2 DWT decomposition and background determination

The DWT decomposition analysis was applied to the experimental measured data in the region of the IVGDR. In the analysis, the background can be described by a smooth and well approximated polynomial function of low order. This allows to take advantage of the vanishing moments of wavelets in which the Biorthogonal 6.8 wavelet family (see Table 4.3) is chosen. This choice of wavelet family has suitable vanishing moments when applied to the form of background present in this analysis [Dau94]. Furthermore, a function having sufficient number of moments will allow all non-resonant components to be found in the approximations (A_{i}), while details (D_{i}) give the information on the fluctuations. Consequently, at some stage of the decomposition the approximation corresponds to the background and does not carry information on the fine structure anymore. This stage of decomposition depends on such parameters like the bin size or the total width of the resonance.

As an example, we consider the excitation-energy spectrum of ^{208}Pb(p,p$'$) which was decomposed into approximations (A_{i}) and details (D_{i}) as shown in Fig. 4.29. The global shape of the IVGDR region is given by $A9$ so that the next approximation corresponds to the background which carries no fine structure information. As a result, background $A10$ is chosen since it is considered to be a non-resonant contribution to the spectrum. Finally, a fluctuation analysis is performed after subtracting the $A10$ background from the excitation-energy spectrum of each target nucleus.

4.7.3 Extraction of 1^- level densities

Following on from the DWT analysis described above, the upper part of Fig. 4.30 displays the experimental measured example of ^{208}Pb(p,p′) excitation-energy spectrum with the assumed DWT background. The fluctuation analysis of Sect. 2.7.2 then requires the smoothed spectra $g(E_x)$ and $g_>(E_x)$, displayed superimposed on each other, the stationary spectrum $d(E_x)$ and in the bottom part of Fig. 4.30 the autocorrelation function for the experimental measured data.

The extraction of the mean level spacing $\langle D \rangle$ makes use of the experimental $(C(\epsilon = 0)-1)$ value which is inserted into Eq. (2.138) with the values of the other parameters listed in Table 4.3. Moreover, the resulting mean level spacing $\langle D \rangle$ and level density ρ are defined by

$$\langle D \rangle = (C(\epsilon = 0) - 1) \times \text{Constant}, \tag{4.1}$$

$$\rho = 1/\langle D \rangle. \tag{4.2}$$

The level density in each energy bin is calculated using Eq. (4.2) as the reciprocal of the mean level spacing. The same approach for the extraction of 1^- level densities in the target nuclei (^{208}Pb – ^{40}Ca) was applied. Using Eq. (4.1), the following expressions to determine the mean level spacing were used for the different target nuclei:

$$\langle D \rangle_{\mathbf{Pb}} = (C(\epsilon = 0) - 1) \times 0.073589, \tag{4.3}$$

$$\langle D \rangle_{\mathbf{Ni}} = (C(\epsilon = 0) - 1) \times 0.089954, \tag{4.4}$$

$$\langle D \rangle_{\mathbf{Fe}} = (C(\epsilon = 0) - 1) \times 0.070416, \tag{4.5}$$

$$\langle D \rangle_{\mathbf{Ca}} = (C(\epsilon = 0) - 1) \times 0.080486. \tag{4.6}$$

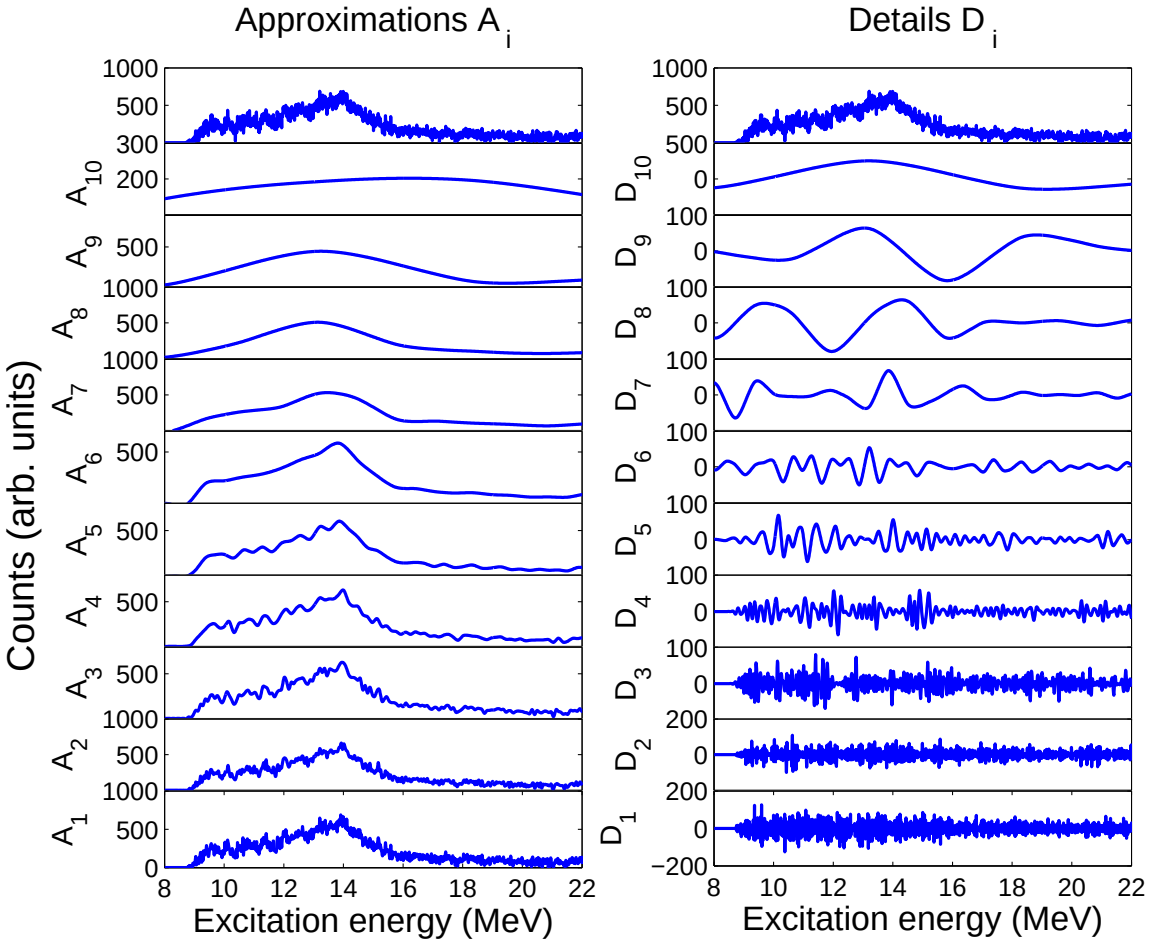

Figure 4.29: Decomposition of the ^{208}Pb(p,p′) excitation-energy spectrum with the DWT analysis into approximations A_i and details D_i. The approximation $A9$ describes the total width of the GDR, thus $A10$ can be adopted as background shape.

Table 4.3: List of parameters utilised in the level density extraction of $J^\pi = 1^-$ states.

Nucleus	α-value	Expt energy-resolution (ΔE)	Background Type
^{208}Pb	2.273	45 keV	Bior 6.8
^{58}Ni	2.273	52 keV	Bior 6.8
^{56}Fe	2.273	42 keV	Bior 6.8
^{40}Ca	2.273	47 keV	Bior 6.8

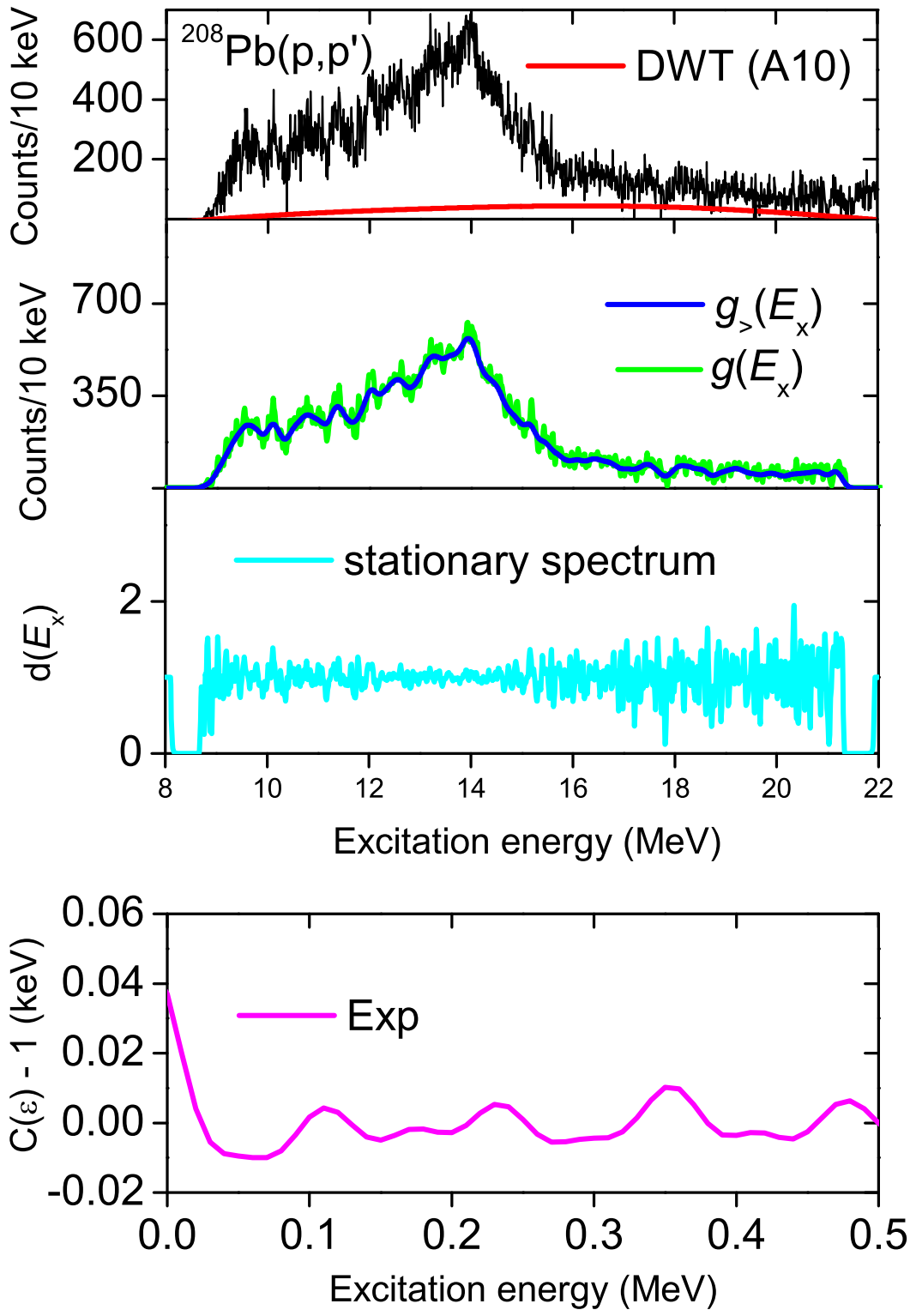

Figure 4.30: From top to bottom: Experimental ^{208}Pb(p,p′) excitation-energy spectrum including background obtained with the use of discrete wavelet transform, smoothed spectra g(E_x) and g$_>$(E_x), stationary fluctuating spectrum $d(E_x)$ obtained by dividing the two smoothed spectra, autocorrelation functions from experimental (purple solid line).

Figures 4.31, 4.33, 4.35 and 4.37 show the results from the DWT background determination after selecting $A10$ as the background. The estimates of the starting points of the $A10$ DWT backgrounds used in the extraction of experimental level densities were justified by the argument that below these excitation-energy points, the cross-sections were observed to be dropping to values close to zero (see Fig. 4.2), hence justifying the exclusion of these parts of the excitation-energy regions during level density extraction. In Fig. 4.32, results from the comparison of the extracted experimental level densities of 1^- states in ^{208}Pb nucleus with the theoretical model predictions are shown. One should note that the excitation-energy range displayed is restricted to the region where $\langle\Gamma\rangle/\langle D\rangle \ll 1$, neglecting the Ericson fluctuation region at higher excitation energies.

The red solid and green dashed lines indicate the result of the BSFG level density calculations using the parameterisations of [Rau97] and [Egi05], respectively. The spin- and parity-dependent level densities from the HFB model [Hil06] are shown as an orange dash-dotted line and finally the blue dotted line represents parameterisations of HF-BCS [Dem01].

The same level density extraction prescription as that in the case of ^{208}Pb nucleus was repeated for the measured excitation-energy spectra of ^{58}Ni, ^{56}Fe and ^{40}Ca nuclei. However, Fig. 4.34 shows the results of the extracted experimental level densities of $J^\pi = 1^-$ states in ^{58}Ni nucleus compared to the theoretical model predictions. It should be noted that the level densities were extracted after subtracting the DWT ($A10$) background from the experimentally measured (p,p$'$) excitation-energy spectrum (see top panel of the presented figures).

Figure 4.36 shows the results of the extracted experimental level densities in ^{56}Fe nucleus after subtracting the $A10$ background and then compared to the theoretical model predictions. Finally, Fig. 4.38 shows the results of experimental level densities

of $J^\pi = 1^-$ states in ^{40}Ca nucleus after background subtraction and then compared to the theoretical model predictions. For ease of comparison the level density figures for all the nuclei studied are grouped together at the end of this section.

4.7.4 Discussion of extracted $J^\pi = 1^-$ states

Examining each nucleus:

^{208}**Pb**: The experimental level density results increased by close to two orders of magnitude in the excitation-energy range, E_x = 8 – 14 MeV, and then started to fall indicating that the extraction method failed to work at higher excitation energies. From Fig. 4.32, one can see that the BSFG (Rauscher) with parametrisation from Ref. [Rau97] overestimates the extracted level densities of $J^\pi = 1^-$ states in ^{208}Pb nucleus while the BSFG (von Egidy) model from Ref. [Egi05] is in reasonable agreement with our data up to the excitation energy of 14 MeV. Moreover, the energy dependence of the BSFG (von Egidy) calculation is very similar to the experimental data and HF-BCS results in the energy range, $E_x \leqslant 14$ MeV.

^{58}**Ni**: Between 12 MeV $< E_x \leqslant 18.5$ MeV, an increase in experimental level densities by more than an order of magnitude was visualised and then followed by a drop in the level densities. Figure 4.34 reveals that two BSFG parametrisations [Rau97, Egi05] are in excellent agreement with the experimental level density results in the excitation-energy range considered, E_x = 12 – 18.5 MeV.

^{56}**Fe**: The experimentally obtained level densities were predicted to have increased by more than an order of magnitude in the excitation-energy region between 10 MeV and 18.5 MeV. Beyond this region, the extraction method failed to work, therefore supporting the decrease in the level densities. In Fig. 4.36, although the qualitative trend of the experimental data are well described, in general the HF-BCS parametri-

sation [Dem01] slightly overpredicts the extracted level densities.

^{40}Ca: Up to an excitation energy of $E_x \approx 20$ MeV, an increase by more than an order of magnitude was observed. In the doubly-magic ^{40}Ca nucleus, the magnitude of the level density pattern was found to be significantly smaller, as one would expect, and in addition, the HFB model [Hil06] failed to follow a smooth energy dependence as evidenced by the large fluctuations (see Fig. 4.38).

Summarising, we have extracted level densities of 1^- states in the GDR energy region of medium and heavy, magic and open shell nuclei. In general, the results are equally close to the predictions of the microscopic BSFG (Rauscher) and HFB models. Unfortunately, the method fails at high energy tail of the GDR when the level densities become too high. This failure is attributed to the fact that the experimental energy-resolution of the (p,p′) scattering measurement limits the level density to 10^3 MeV^{-1} for this method. The uncertainities of the extracted level densities were estimated by using different input parameters of the autocorrelation function. The following contributions, assumed to be independent of each other, were considered in the calculation of the experimental errors:

- Smoothing parameters: A variation by ± 10% led to a 2% error contribution,
- Range of the excitation energy interval: The analysis was repeated for interval sizes between 0.5 and 2 MeV. The corresponding uncertainty amounted to ± 10%, and
- Choice of wavelet functions: The variation between the different choices of the BIOR wavelets is taken as an estimate of the uncertainty of the background determination. Increasing the number of vanishing moments leads to larger backgrounds but approaching a constant magnitude and shape for the highest values used in the present analysis. The variation thus led to a systematic reduction of the level densities reaching 10%.

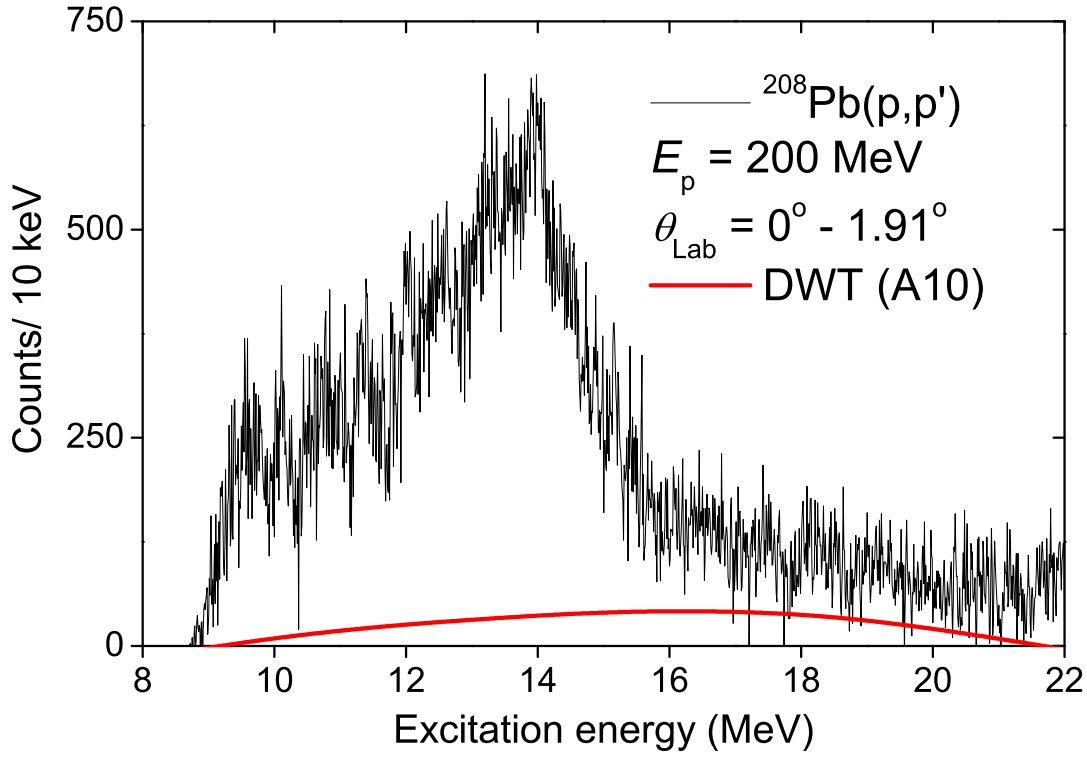

Figure 4.31: Excitation-energy spectrum of ^{208}Pb(p,p′) reaction at 0° before subtracting DWT (A10) background.

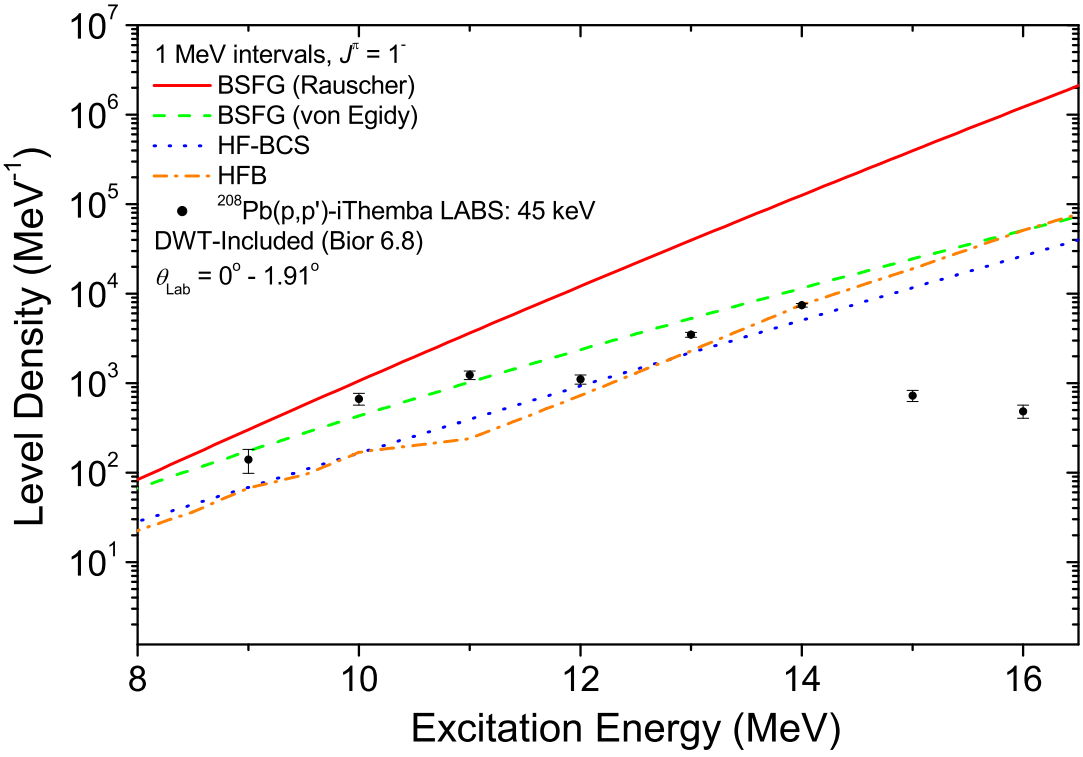

Figure 4.32: Comparison of the experimentally obtained level densities of 1^- states in ^{208}Pb in the energy range from 8 to 17 MeV with predictions from BSFG using the model of [Rau97] (red solid line) or from [Egi05] (green dashed line), HF-BCS [Dem01] (blue dotted line) and HFB [Hil06] (orange dash-dotted line).

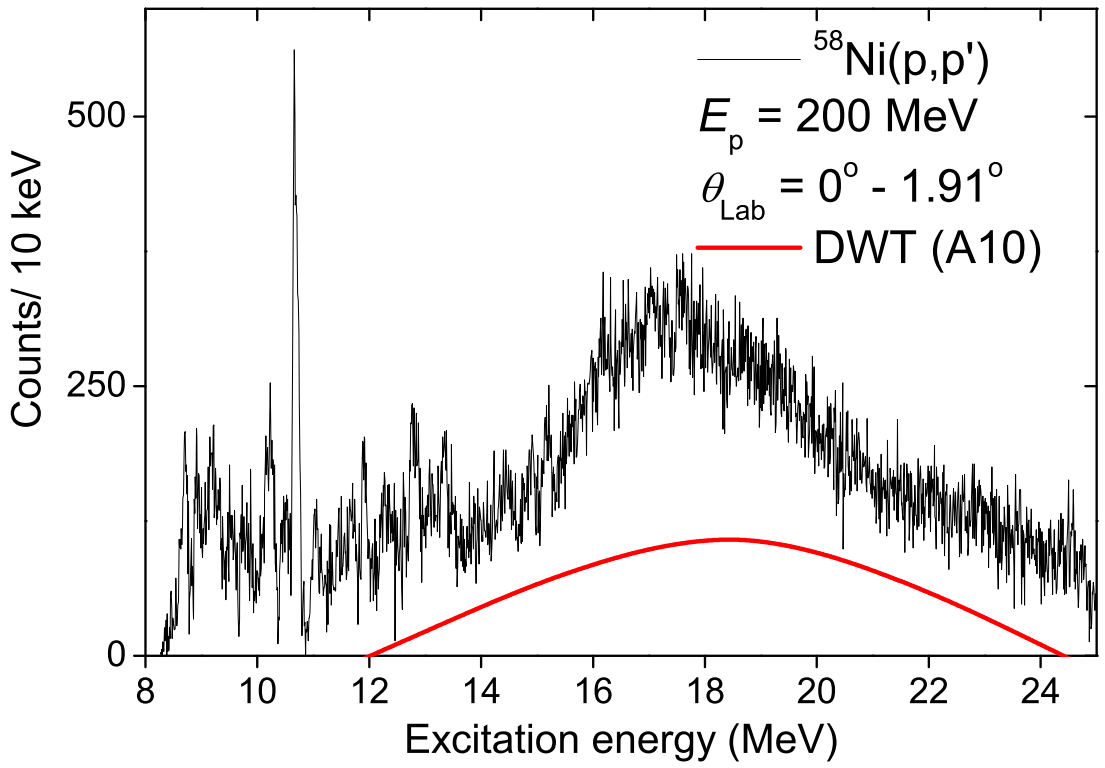

Figure 4.33: Excitation-energy spectrum of ^{58}Ni(p,p′) reaction at 0° before subtracting DWT (A10) background.

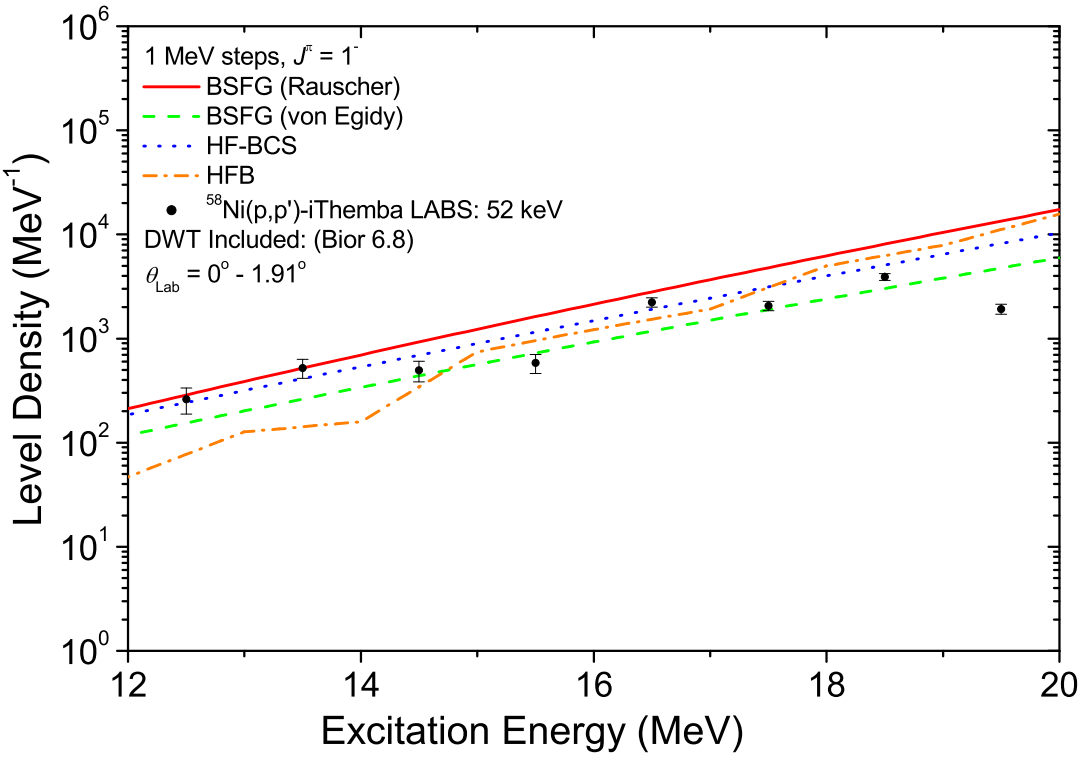

Figure 4.34: Comparison of the experimentally obtained level densities of 1^- states in ^{58}Ni in the energy range from 12 to 20 MeV with predictions from BSFG using the model of [Rau97] (red solid line) or from [Egi05] (green dashed line), HF-BCS [Dem01] (blue dotted line) and HFB [Hil06] (orange dash-dotted line).

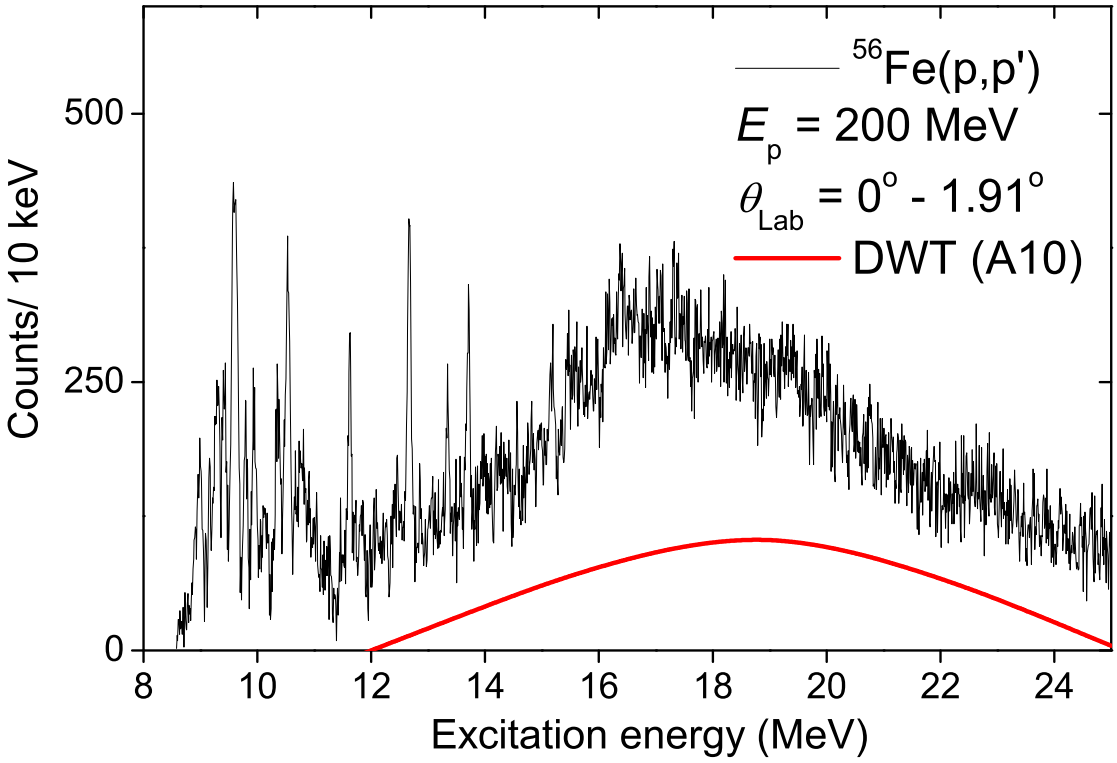

Figure 4.35: Excitation-energy spectrum of ^{56}Fe(p,p′) reaction at 0° before subtracting DWT (A10) background.

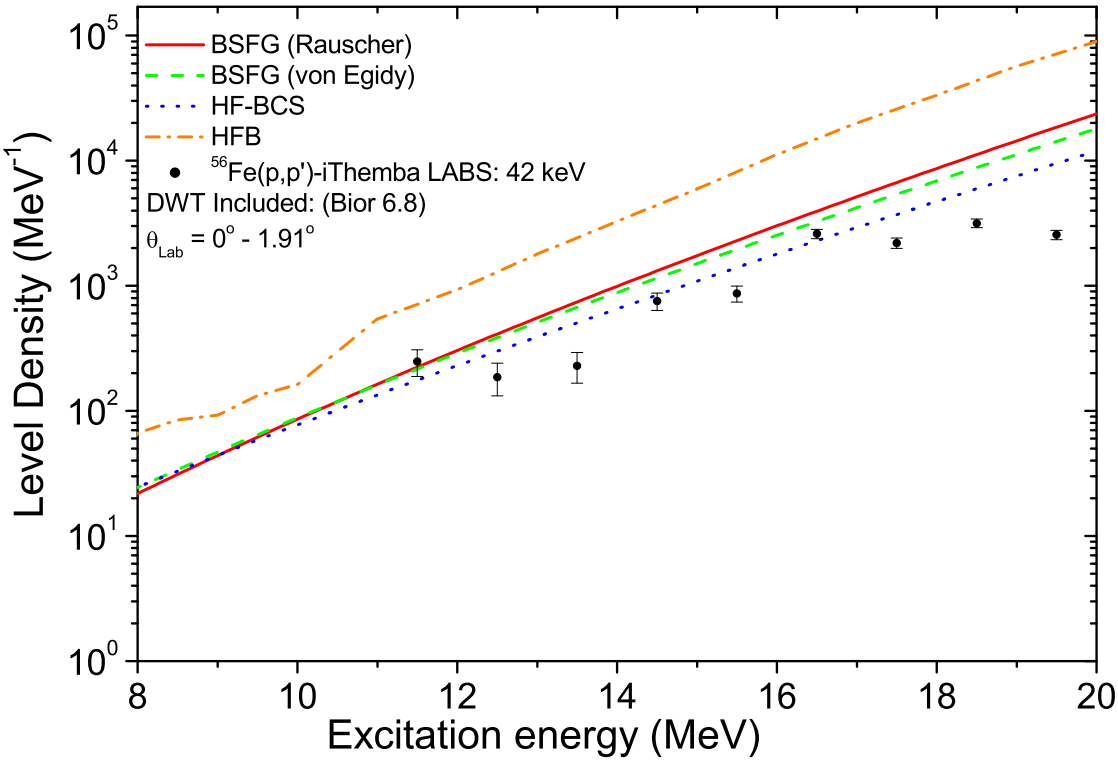

Figure 4.36: Comparison of the experimentally obtained level densities of 1^- states in ^{56}Fe in the energy range from 8 to 20 MeV with predictions from BSFG using the model of [Rau97] (red solid line) or from [Egi05] (green dashed line), HF-BCS [Dem01] (blue dotted line) and HFB [Hil06] (orange dash-dotted line).

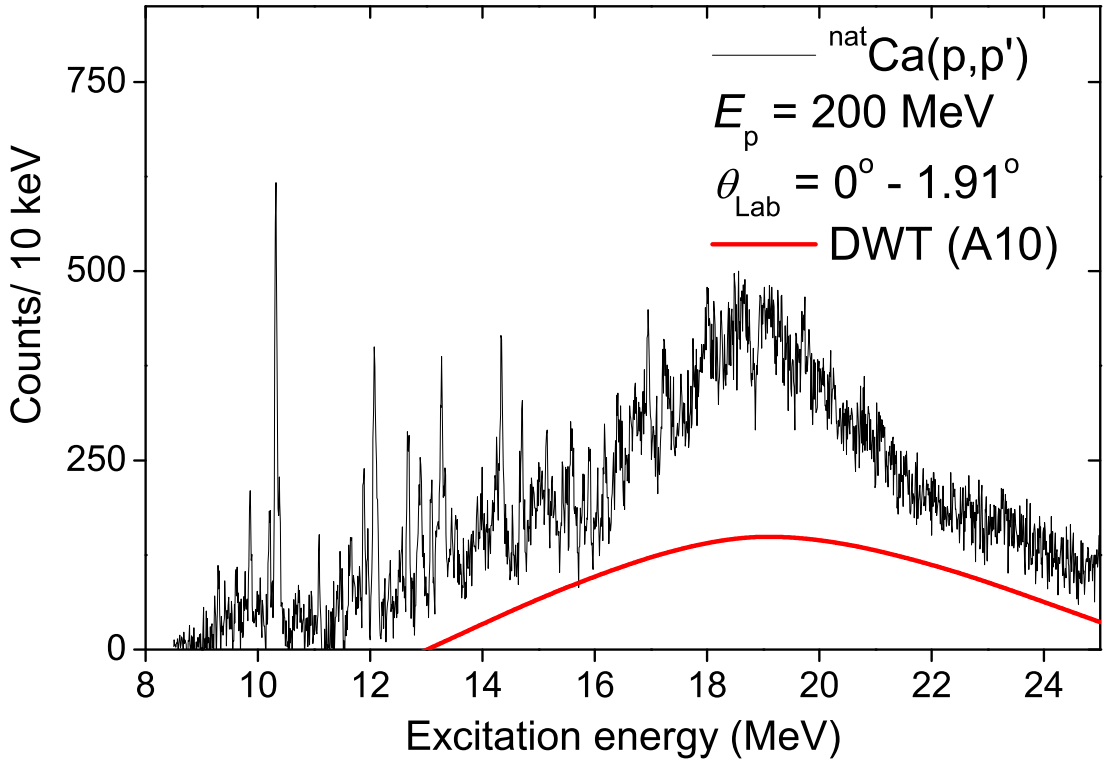

Figure 4.37: Excitation-energy spectrum of ^{40}Ca(p,p′) reaction at 0° before subtracting DWT (A10) background.

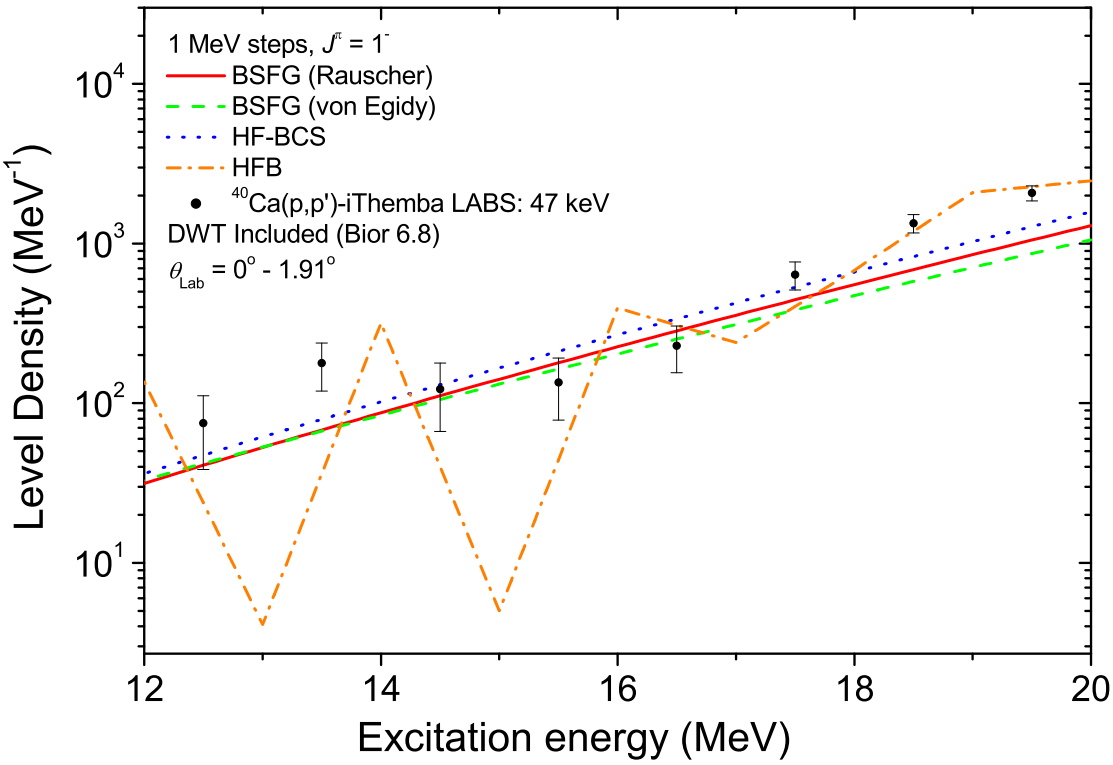

Figure 4.38: Comparison of the experimentally obtained level densities of 1^- states in ^{40}Ca in the energy range from 12 to 20 MeV with predictions from BSFG using the model of [Rau97] (red solid line) or from [Egi05] (green dashed line), HF-BCS [Dem01] (blue dotted line) and HFB [Hil06] (orange dash-dotted line).

Chapter 5

Conclusion

The present thesis focuses on the investigation of the phenomenon of fine structure of giant resonances in light, medium-heavy and heavy nuclei. Emphasis was placed on the extraction of the properties of the IVGDR. High energy-resolution inelastic proton scattering data were collected at the iThemba LABS cyclotron facility utilising an $E_{\mathrm{p}} = 200$ MeV proton beam and the K600 magnetic spectrometer for ^{208}Pb, ^{58}Ni, ^{56}Fe, ^{40}Ca and ^{27}Al target nuclei for kinematical conditions corresponding to the maximum of a $\Delta L = 1$ excitation. An experimental energy-resolution of $\Delta E \simeq 42$ keV FWHM was achieved using the faint-beam dispersion matching technique, which was crucial for the detection of the fine structure in the excitation-energy spectra. Fine structure was identified in all the nuclei investigated, hence proving it to be a global phenomenon. The present investigation supports the conclusions on fine structure reported in the (e,e′) work of [Str98, Die94] and later by [Kal05].

Since the cross-sections are of major interest, the first intermediate goal of the present experiment was to test the reproducibility of previously measured photo-absorption data. The measured cross-sections of the nuclei investigated were found to be consistent with the previously published Giant Dipole Resonance (GDR) data,

which allows us to gain confidence in the analysis results. Previous studies have revealed that knowledge of the cross-sections for partial photo-nuclear reactions (γ,p) and (γ,n) play a significant role isolating reliably the semi-direct branch of GDR decay (see Sect. 2.2.1). Concurrently, these partial photo-nuclear data were found to enable one to establish the shell structure of the dipole resonance being considered [Ish02b].

Several methods have been applied for the characterisation of fine structure and the extraction of energy scales. Techniques based on a wavelet transform were developed and utilised, which gave precise and model-independent information on the scales and their localisation in the excitation-energy spectrum. These features of the wavelet analysis allowed the confirmation that the experimentally identified energy scales are indeed characteristic for the IVGDR energy region. In this study, the complex Morlet mother wavelet was used to extract the characteristic energy scales. In order to enable a direct comparison between energy scales from experiment and theory, smoothing of B($E1$) strength distributions is vital. This is a process that involves folding the theoretical distributions with the experimental energy-resolutions before the application of wavelet analysis technique. However, a good agreement between the energy scales from the present experiment and theoretical predictions was observed. Three classes of energy scales were observed *viz* Class I contained energy scales below 300 keV. Several intermediate energy scales between 300 keV and 1000 keV belonged to Class II. Finally, Class III contained the largest observed energy scales above 1000 keV and these energy scales reflect the gross structure and the total width of the resonance. This classification of energy scales follows the recent work of Ref. [Usm09]. These energy scales can help in understanding the damping mechanism of the resonances (the origin of the width) in nuclei. In the present work, the calculations were performed on the RPA level and with accounting for coupling between $1p$-h and $2p$-$2h$ configurations. Since reasonably similar energy scales were detected in both RPA and QPM calculations, this allows us to conclude that Landau

damping is responsible for the main energy scales experimentally observed for the giant dipole resonance.

The extraction of spin- and parity-dependent level densities of 1^- states in ^{208}Pb, ^{58}Ni, ^{56}Fe, and ^{40}Ca nuclei in the GDR region was achieved by means of the fluctuation analysis technique and comparisons between the experimentally obtained level densities with those from theoretical models were done. In general, there is an overall fair agreement between results from experiment and theory.

Finally, the present work will also serve in the provision of information on the capabilities and limitations of the newly commissioned zero-degree facility of the K600 magnetic spectrometer. This will hopefully allow for better energy-resolution to be achieved in future experimental studies, thus uncovering the next levels in the hierarchy of couplings, which are expected to produce even finer structure and smaller energy scales.

References

[Agv03] U. Agvaanluvsan, G. E. Mitchell, J. F. Shriner Jr., and M. Pato, Phys. Rev. **C 67** (2003) 064608.

[Ahr75] J. Ahrens, H. Borchert, K. H. Czock, H. B. Eppler, H. Gimm, H. Gundrum, M. Kroning, P. Riehn, G. Sita Ram, A. Zieger, and B. Ziegler, Nucl. Phys. **A 251** (1975) 479.

[Aib99] H. Aiba and M. Matsuo, Phys. Rev. **C 60** (1999) 034307.

[Aib03] H. Aiba, M. Matsuo, S. Nishizaki, and T. Suzuki, Phys. Rev. **C 68** (2003) 054316.

[Ald75] K. Alder and A. Winther, *Electromagnetic Excitation: Theory of Coulomb Excitation with Heavy Ions*, North-Holland, Amsterdam (1975).

[Ale89] A. N. F. Aleixo and C. A. Bertulani, Nucl. Phys. **A 505** (1989) 448.

[Alh07] Y. Alhassid, S. Lui, and H. Nakada, Phys. Rev. Lett. **99** (2007) 162594.

[Ana81] N. Anantaraman, G. M. Crawley, and A. Galonsky, Phys. Rev. Lett. **46** (1981) 1318.

[And07] F. Andreozzi, F. Knapp, N. Lo ludice, A. Porrino, and J. Kvasil, Phys. Rev. **C 75** (2007) 044312.

[And08] F. Andreozzi, F. Knapp, N. Lo ludice, A. Porrino, and J. Kvasil, Phys. Rev. **C 78** (2008) 054308.

[Are79] H. Arenhövel, *Lecture Notes in Physics*, Vol. 108, Electromagnetic sum rules in nuclei, Springer, Berlin/Heidelberg (1979).

[astro-ulb] http : //www. - astro.ulb.ac.be/html/nld combp h.html.

[Aue75] N. Auerbach and A. Yeverechyahu, Ann. Phys. New York **95** (1975) 35.

[Bal47] G. C. Baldwin and G. S. Klaiber, Phys. Rev. **71** (1947) 3.

[Bau00] F. Bauwens, J. Bryssinck, D. De Frenne, K. Govaert, L. Govor, M. Hagemann, J. Heyse, E. Jacobs, W. Mondelaers, and V. Yu. Ponomarev, Phys. Rev. **C 62** (2000) 024302.

[Bel82] Z. W. Bell, L. S. Cardman, and P. Axel, Phys. Rev. **C 25** (1982) 791.

[Ben89] C. J. Benesh, B. C. Cook, and J. P. Vary, Phys. Rev. **C 40** (1989) 1198.

[Ber75] B. L. Berman and S. C. Fultz, Rev. Mod. Phys. **47** (1975) 713.

[Ber77] W. Bertozzi, M. V. Hynes, C. P. Sargent, C. Creswell, P.C. Dunn, A. Hirsch, M. Leitch, B. Norum, F. N. Rad, and T. Sasanuma, Nucl. Instr. Methods. **141** (1977) 457.

[Ber85] C. A. Bertulani and G. Baur, Nucl. Phys. **A 442** (1985) 739.

[Ber86] C. A. Bertulani and G. Baur, Nucl. Phys. **A 458** (1986) 725.

[Ber94] G. F. Bertsch and R. A. Broglia. *Oscillations in Finite Quantum Systems*, Cambridge Monographs on Mathematical Physics, Cambridge (1994).

[Ber99] C. A. Bertulani and V. Y. Ponomarev, Phys. Rep. **321** (1999) 139.

[Ber09] C. Bertulani, *Theory and Applications of Coulomb Excitation*, Texas A & M University, Commerce, Texas (2009).

[Bet36] H. A. Bethe and A. D. Bacher, Rev. Mod. Phys. **8** (1936) 82.

[Bet37] H. A. Bethe, Rev. Mod. Phys. **9** (1937) 69.

[Bha83] M. R. Bhat, IAEA *Advisory Group Meeting on Basic and Applied problems of Nuclear Level Densities*, Brookhaven National laboratory, Long Island, New York (1983).

[Bia12a] D. Bianco, F. Knapp, N. Lo ludice, F. Andreozzi, and A. Porrino, Phys. Rev. **C 85** (2012) 014313.

[Bia12b] D. Bianco, F. Knapp, N. Lo ludice, F. Andreozzi, and A. Porrino, Phys. Rev. **C 86** (2012) 044327.

[Blo63] B. Block and H. Feshbach, Ann. Phys. **23** (1963) 47.

[Boh75] A. Bohr, B. R. Mottelson, and W. A. Benjamin, *Nuclear Structure*, Vol. 2, Reading, Massachusetts (1975).

[Bor00] S. S. Borodina, A. V. Varlamov, V. V. Varlamov, B. S. Ishkhanov, and V. I. Mokeev, Moscow State Univ. Inst. of Nucl. Phys. Rep. **2000** (2000) 6/610.

[Bor98] P. F. Bortignon, A. Bracco, and R. A. Broglia, *Giant Resonances: Nuclear Structure at finite Temperature*, Harwood Academic, Amsterdam (1998).

[Bot37] W. Bothe and W. Z. Genther, Z. Phys. **106** (1937) 236.

[Bro64] G. Brown, *Unified Theory of Nuclear Models*, North-Holland, Amsterdam (1964).

[Bru95] R. Brun and F. Rademakers, ROOT Development Team, CERN, Geneva, Switzerland (1995).

[Con92] J. L. Conradie, Doctoral thesis, University of Stellenbosch (1992).

[Con06] J. L. Conradie, P. F. Rohwer, P. J. Celliers, M. J. van Niekerk, D. T. Fourie, P. T. Mansfield, J. L. G. Delsink, A. H. Botha, J. Dietrich, and I. Mohos, *Proc. on Beam Phase Measurement in a 200 MeV Cyclotron*, EPAC, Edinburgh, Scotland (2006).

[Cor92] C. Cornell, J. G. de Villiers, and D. T. Fourie, iThemba Laboratory for Accelerator Based Sciences, NAC-Report 92/4, Cape Town (1992).

[Dau94] I. Daubechies, *Ten Lectures on Wavelets*, Series in Applied Mathematics (SIAM), **61** (1994) 76.

[Dem01] P. Demetriou and S. Goriely, Nucl. Phys. **A 695** (2001) 95.

[Die94] H. Diesener, U. Helm, G. Herbert, V. Huck, P. von Neumann-Cosel, C. Rangacharyulu, A. Richter, G. Schrieder, A. Stascheck, and A. Stiller, Phys. Rev. Lett. **72** (1994) 1994.

[Die05] J. Dietrich, I. Mohos I, J. L. Conradie, Z. I. Kormny, P. F. Rohwer, P. T. Mansfield, D. T. Fourie, J. L. G. Delsink, and M. Sakildien *Proc. on Operational experience with beam alignment and monitoring using non-destructive beam position monitors in the cyclotron beamlines at iThemba LABS*, DIPAC 2005, Lyon, France (2005).

[Dil73] W. Dilg, W. Schantl, H. Vonach, and M. Uhl, Nucl. Phys. **A 217** (1973) 269.

[Dro86] S. Drozdz, V. Klent, J. Speth, and J. Wambach, Nucl. Phys. **A 451** (1986) 11.

[Egi05] T. von Egidy and D. Buchurescu, Phys. Rev. **C 72** (2005) 044311.

[Eng81] H. A. Enge, Nucl. Instr. Methods **187** (1981) 1.

[Eri60] T. E. O. Ericson, Adv. Phys. **9** (1960) 425.

[Eri63] T. Ericson, Ann. Phys **23** (1963) 390.

[Ero03] V. A. Erokhova, M. A. Elkin, A. V. Izotova, B. S. Ishkhanov, I. M. Kapitonov, E. I. Lileeva, and E. V. Shirokov, Izvi. Rossiiskoi Akademii Nauk, Ser. Fiz. **67** (2003) 1479.

[Fer24] E. Fermi, Z. Phys. **29** (1924) 315.

[Fes64] H. Feshbach, Rev. Mod. Phys. **36** (1964) 1076.

[Fes74] H. Feshbach, Rev. Mod. Phys. **46** (1974) 1.

[Fos89] C. Foster and G. Berg, IUCF Sci. and Tech. Report, Bloomington, Indiana (1989) 193.

[Fre65] J. B. French, *Proc. on Many-body description of nuclear structure and reactions*, International School of Physics 'Enrico Fermi', Course XXXVI, Varenna, Villa Monastero (1965).

[Fuj96] Y. Fujita, H. Akimune, I. Daito, M. Fujiwara, M. N. Harakeh, T. Inomata, J. Jänecke, K. Katori, H. Nakada, S. Nakayama, A. Tamii, M. Tanaka, H. Toyokawa, and M. Yosoi, Phys. Lett. **B 365** (1996) 29.

[Fuj00] Y. Fujita, H. Fujita, G. P. A. Berg, K. Harada, K. Hatanaka, T. Kawabata, T. Noro, H. Sakaguchi, T. Shinada, Y. Shimbara, T. Taki, H. Ueno, and M. Yosoi, J. Mass Spectrom. Soc. Jpn. **48** (2000) 306.

[Fuj02a] Y. Fujita, H. Fujita, T. Adachi, G. P. A. Berg, E. Caurier, H. Fujimura, K. Hara, K. Hatanaka, Z. Janas, J. Kamiya, T. Kawabata, K. Langanke, G. Martinez-Pinedo, T. Noro, E. Roeckl, Y. Shimbara, T. Shinada, S. Y. van der Werf, M. Yoshifuku, M. Yosoi, and R. G. T. Zegers, Eur. Phys. J. **A 13** (2002) 411.

[Fuj02b] H. Fujita, Y. Fujita, G. P. A. Berg, A. D. Bacher, C. C. Foster, K. Hara, K. Hatanaka, T. Kawabata, T. Noro, H. Sakaguchi, Y. Shimbara, T. Shinada, E. J. Stephenson, H. Ueno, and M. Yosoi, Nucl. Instr. Methods **A 484** (2002) 17.

[Fuj07] H. Fujita, Y. Fujita, T. Adachi, A. D. Bacher, G. P. A. Berg, T. Black, E. Caurier, C. C. Foster, H. Fujimura, K. Hara, K. Harada, K. Hatanaka, J.

Jänecke, J. Kamiya, Y. Kanzaki, K. Katori, T. Kawabata, K. Langanke, G. Martinez-Pinedo, T. Noro, D. A. Roberts, H. Sakaguchi, Y. Shimbara, T. Shinada, E. J. Stephenson, H. Ueno, T. Yamanaka, M. Yoshifuku, and M. Yosoi, Phys. Rev. **C 75** (2007) 034310.

[Ful62] E. G. Fuller, and E. Hayward, *Nuclear Reactions*, Vol. 2, John Wiley & Sons, New York (1962).

[Ful74] S. C. Fultz, R. A. Alvarez, B. L. Berman, and P. Meyer, Phys. Rev. **C 10** (1974) 608.

[Gad68] E. Gadioli and L. Zetta, Phys. Rev. **167** (1968) 1016.

[Goe82] K. Goeke and J. Speth, Ann. Rev. Nucl. Part. Sci. **32** (1982) 65.

[Gol48] M. Goldhaber and E. Teller, Phys. Rev. **74** (1948) 1046.

[Gor67a] B. I. Goryachev, B. S. Ishkhanov, V. G. Shevchenko, and B. A. Yuryev, Yad., Fiz. **5** (1967) 1138.

[Gor67b] B. I. Goryachev, B. S. Ishkhanov, I. M. Kapitonov, I. M. Piskarev, and V. G. Shevchenko, Zhurnal Eksper. iTeoret. Fiz., Pisma v Redakt, **5** (1967) 225.

[Gri04] D. J. Griffiths, *Introduction to Quantum Mechanics*, Pearson Prentice Hall, New Jersey (2004).

[Gro84] A. Grossman and J. Morlet, SIAM. J. Math. Anal. **15** (1984) 723.

[Guh98] T. Guhr, A. Müller-Groeling, and H. A. Weidenmüller, Phys. Rep. **299** (1998) 189.

[Hag04] M. Hagemann, A. M. van den Berg, D. De Frenne, V. M. Hannen, M. N. Harakeh, J. Heyse, M. A. de Huu, E. Jacobs, K. Langanke, G. Martinez-Pinedo, and H. J. Wörtche, Phys. Lett. **B 579** (2004) 259.

[Han79] P. G. Hansen, Ann. Rev. Nucl. Part. Sci. **29** (1979) 69.

[Han90] P. G. Hansen, B. Jonson, and A. Richter, Nucl. Phys. **A 518** (1990) 13.

[Haq82] R. U. Haq, A. Pandey, and O. Bohigas, Phys. Rev. Lett. **48** (1982) 1086.

[Har01] M. N. Harakeh and A. van der Woude, *Giant Resonances; Fundamental High-Frequency Modes of Nuclear Excitation*, Oxford University Press, Oxford (2001).

[Hil06] S. Hilaire and S. Goriely, Nucl. Phys. **A 779** (2006) 63.

[Hui69] J. R. Huizenga, H. K. Vonach, A. A. Katsanos, A. J. Gorski, and C. J. Stephan, Phys. Rev. **182** (1969) 1149.

[Ish70] B. S. Ishkhanov, I. M. Kapitonov, I. M. Piskarev, V. G. Shevchenko, and O. P. Shevchenko, Yad. Fiz. **11** (1970) 485.

[Ish02a] B. S. Ishkhanov, I. M. Kapitonov, E. I. Lileeva, E. V. Shirokov, V. A. Erokhova, M. A. Elkin, and A. V. Izotova, Moscow State Univ. Inst. of Nucl. Phys. Rep. **2002** (2002) 27/711.

[Ish02b] B. S. Ishkhanov, I. M. Kapitonov, I. A. Tutyn', and E. V. Shirokov, Yad. Fiz. **65** (2002) 3.

[Ito05] M. Itoh, Private communication (2005).

[Jac75] J. D. Jackson, *Classical Electrodynamics*, John Wiley & Sonc Inc., New York, (1975).

[Jac99] J. D. Jackson, *Classical Electrodynamics*, John Wiley & Sons Inc., New York, (1999).

[Jon76] B. Jonson, E. Hagberg, P. G. Hansen, P. Hornsöj, and P. Tidemand-Petersson, *Proc. on Nuclei far from Stability*, Cargese, CERN **76** (1976) 277.

[Jun08] A. R. Junghans, G. Rusev, R. Schwengner, A. Wagner, and E. Grosse, Phys. Lett. **B 670** (2008) 200.

[Kal05] Y. Kalmykov, Doctoral thesis D17, TU Darmstadt (2005).

[Kal06] Y. Kalmykov. T. Adachi, G. P. A. Berg, H. Fujita, K. Fujita, K. Hatanaka, J. Kamiya, K. Nakanishi, P. von Neumann-Cosel, V. Yu. Ponomarev, A. Richter, N. Sakamoto, Y. Sakemi, A. Shevchenko, Y. Shimbara, Y. Shimizu, F. D. Smit, T. Wakasa, J. Wambach, and M. Yosoi, Phys. Rev. Lett. **96** (2006) 01250.

[Kal07] Y. Kalmykov, C. Özen, K. Langanke, G. Martinez-Pinedo, P. von Neumann-Cosel, and A. Richter, Phys. Rev. Lett. **99** (2007) 202502.

[Kam97] S. Kamerdzhiev, J. Lisantti, P. von Neumann-Cosel, A. Richter, G. Tertychny, and J. Wambach, Phys. Rev. **C 55** (1997) 2101.

[Kat70] A. A. Katsanos, R. W. Shaw, R. van den Bosch, and D. Chamberlin, Phys. Rev. **C 1** (1970) 594.

[Khe10] N. Y. Kheswa, P. Papka, E. Z. Buthelezi, R. M. Lieder, R. Neveling, and R. T. Newman, Nucl. Instr. Methods. **613** (2010) 389c.

[Kon08] A. J. Koning, S. Hilaire, and S. Goriely, Nucl. Phys. **A 810** (2008) 13.

[Kne96] U. Kneissl, H. H. Pitz, and A. Zilges, *Investigation of Nuclear structure by Fluorescence Scattering*, Prog. Part. Nuc. Phys. **37** (1996) 349.

[Kno79] G. F. Knoll, *Radiation Detection and Measurement*, John Wiley & Sons, New York (1979).

[Kra88] K. S. Krane, *Introductory Nuclear Physics*, John Wiley & Sons, New York (1988).

[Kuh81] G. Kuhner, D. Meuer, S. Muller, A. Richter, E. Spamer, O. Titze, and W. Knupfer, Phys. Lett. **B 104** (1981) 189.

[Lac99] D. Lacroix and P. Chomaz, Phys. Rev. **C 60** (1999) 064307.

[Lac00] D. Lacroix, A. Mai, P. von Neumann-Cosel, A. Richter, and J. Wambach, Phys. Lett. **B 479** (2000) 15.

[Lac01] D. Lacroix, S. Ayik, and P. Chomaz, Phys. Rev. **C 63** (2001) 064305.

[Lag92] D. Lagoutte, J. C. Cerisier, J. L. Plagnaud, J. P. Villian, and B. Forget, J. Atm. Terr. Phys. **54** (1992) 1283.

[Law30] E. O. Lawrence and N. E. Edlefsen, Science **72** (1930) 376.

[Leo87] W. R. Leo, *Techniques for Nuclear and Particle Physics Experiments*, Springer-Verlag, Berlin/Heidelberg (1987).

[Lu72] C. C. Lu, L. C. Vaz, and J. R. Huizenga, Nucl. Phys. **A 190** (1972) 229.

[Mal92] S. Mallat and W. L. Hwang, IEEE Trans. Inf. Theory **38** (1992) 617.

[Mal98] S. G. Mallat, *A Wavelet tour of Signal Processing*, Academic Press, New York (1998).

[Mat07] The Mathworks, *Matlab, The Language of Technical Computing*, Version 7.4.0.287 (R2007a).

[Mig44] A. B. Migdal, J. Phys. Acad. Sci. USSR **8** (1944) 331.

[Mor76] H. Morinaga and T. Yamazaki, *In Beam Gamma Spectroscopy*, North Holland, Amsterdam (1976).

[Mor82] J. Morlet, G. Arens, E. Fourgeau, and D. Giard, *Wave propagation and sampling theory. Part II: Sampling theory and complex waves*, Geophysics (1982).

[Mor94] N. Morrison, *Introduction to Fourier Analysis*, John Wiley & Sons, New York (1994).

[Mye74] W. D. Myers and W. J. Swiatecki, Ann. Phys. **84** (1974) 186.

[Mul82] S. Müller, F. Beck, D. Meuer, and A. Richter, Phys. Lett.**B 113** (1982) 362.

[Mul83] S. Müller, Doctoral thesis D17, TU Darmstadt (1983).

[NAC92] NAC Annual Report NAC/AR/92-01, Cape Town (1992) 27.

[Nag10] M. Nagashima, Y. Shimbara, H. Fujita, Y. Fujita, T. Adachi, N. T. Botha, E. Ganioglu, K. Hatanaka, N. T. Kai, H. Matsubara, K. Nakanishi, R. Neveling, H. Okamura, H. J. Ong, Y. Sakemi, Y. Shimizu, G. Susoy, T. Suzuki, A. Tamii, J. Thies, and Yosoi, *High-resolution study of* $^{56}Fe \rightarrow ^{56}Mn$ *Gamow-Teller transition by the combined analysis of* $^{56}Fe(^{3}He,t)^{56}Co$ *and* $^{56}Fe(p,p')^{56}Fe$ *reactions*, *Proc. AIP Conf* (2010).

[Neu97] F. Neumeyer, Doctoral thesis D17, TU Darmstadt (1997).

[Nev11] R. Neveling, H. Fujita, F. D. Smit, T. Adachi, G. P. A. Berg, E. Z. Buthelezi, J. Carter, J. L. Conradie, M. Couder, R. W. Fearick, S. V. Förtsch, D. T. Fourie, Y. Fujita, J. Görres, K. Hatanaka, A. M. Heilmanh, J. P. Mira, S. H. T. Murray, P. von Neumann Cosel, S. O′Brien, P. Papka, I. Poltoratska, A. Richter, E. Sideras-Haddad, J. A. Swartz, A. Tamii, I. Usman, and J. J. van Zyl, Nucl. Instr. Methods **A 654** (2011) 29.

[New96] R. T. Newman, Doctoral thesis, University of Cape Town, (1996), unpublished.

[Pol11] I. Poltoratska, Doctoral thesis D17, TU. Darmstadt (2011).

[Pol12] I. Poltoratska, P. von Neumann-Cosel, A. Tamii, T. Adachi, C. A. Bertulani, J. Carter, M. Dozono, H. Fujita, K. Fujita, Y. Fujita, K. Hatanaka, M. Itoh, T. Kawabata, Y. Kalmykov, A. M. Krumbholz, E. Litvinova, H. Matsubara, K. Nakanishi, R. Neveling, H. Okamura, H. J. Ong, B.

Özel-Tashenov, V. Yu. Ponomarev, A. Richter, B. Rubio, H. Sakaguchi, Y. Sakemi, Y. Sasamoto, Y. Shimbara, Y. Shimizu, F. D. Smit, T. Suzuki, Y. Tameshige, J. Wambach, Mi. Yosoi, and J. Zenihiro, Phys. Rev. **C 85** (2012) 041304(R).

[Pon79] V. Yu. Ponomarev, V. G. Soloviev, C. Stoyanov, and A. I. Vdovin, Nucl. Phys. **A 323** (1979) 446.

[Pon99] V. Yu. Ponomarev and P. von Neumann-Cosel, Phys. Rev. Lett. **82** (1999) 501.

[Por65] C. E. Porter and R. G. Thomas, Phys. Rev. **A 518** (1965) 13.

[QDC] CAEN, Model V792NC, 32 Channel Charge-to-Digital Converter.

[Rau97] T. Rauscher, F. K. Thielemann, and K. L. Kratz, Phys. Rev. **C 58** (1997) 1613.

[Ray07] J. Raynal, Computing code DWBA07, NEA Data Service NEA1209/08.

[Rei00] B. Reitz, Doctoral thesis, D17, TU Darmstadt (2000).

[Rei02] B. Reitz, A. M. van den Berg, D. Frekers, F. Hofmann, M. de Huu, Y. Kalmykov, H. Lenske, P. von Neumann-Cosel, V. Yu. Ponomarev, S. Rakers, A. Richter, G. Schrieder, K. Schweda, J. Wambach, and H. J. Wörtche, Phys. Lett. **B 532** (2002) 179.

[Rin80] P. Ring and P. Schuck, *The Nuclear Many-Body Problem*, Springer-Verlag, Berlin/Heidelberg (1980).

[Ripl06] *Handbook for calculations of nuclear reaction data, (RIPL-2)* Reference Input Parameter Library-2, IAEA-TECDOC-1506 (2006).

[Rit93] S. Ritt, P. Amaudruz, and K. Olchanski, Maximum Integrated Data Acquisition System (MIDAS), Paul Scherrer Institute (PSI), Switzerland, TRUIMF, Canada (1993).

[Rus09] G. Rusev, R. Schwengner, R. Beyer, M. Erhard, E. Grosse, A. R. Junghans, K. Kosev, C. Nair, K. D. Schilling, A. Wagner, F. Dönau, and S. Frauendorf, Phys. Rev. **C 79** (2009) 061302(R).

[Rye02] N. Ryezayeva, T. Hartmann, Y. Kalmykov, H. Lenske, P. von Neumann-Cosel, V. Yu. Ponomarev, A. Richter, A. Shevchenko, S. Volz, and J. Wambach, Phys. Rev. Lett. **89** (2002) 272502.

[Sat83] G. R. Satchler, *Direct nuclear reactions*, Oxford University Press, New York (1983).

[Sch88] K. P. Schelhaas, J. M. Henneberg, M. Sanzone-Arenhövel, N. Wieloch-Laufenberg, U. Zurmühl, B. Ziegler, M. Schumacher, and F. Wolf, Nucl. Phys. **A 489** (1988) 189.

[Sch75] A. Schwierczinski, R. Frey, A. Richter, E. Spamer, H. Thiessen, O. Titze, T. Walcher, S. Krewald, and R. Rosenfeld, Phys. Rev. Lett. **35** (1975) 1255.

[She04] A. Shevchenko, J. Carter, R. W. Fearick, S. V. Förtsch, H. Fujita, Y. Fujita, Y. Kalmykov, D. Lacroix, J. J. Lawrie, P. von Neumann-Cosel, R. Neveling, V. Yu. Ponomarev, A. Richter, E. Sideras-Haddad, F. D. Smit, and J. Wambach, Phys. Rev. Lett **93** (2004) 122501.

[She05] A. Shevchenko, Doctoral thesis D17, TU. Darmstadt (2005).

[She08] A. Shevchenko, G. R. J. Cooper, J. Carter, R. W. Fearick, S. V. Förtsch, Y. Kalmykov, P. von Neumann-Cosel, V. Yu. Ponomarev, A. Richter, I. Usman, and J. Wambach, Phys. Rev. **C 77** (2008) 024302.

[She09] A. Shevchenko, O. Burda, J. Carter, G. R. J. Cooper, R. W. Fearick, S. V. Förtsch, H. Fujita, Y. Fujita, Y. Kalmykov, D. Lacroix, J. J. Lawrie, P. von Neumann-Cosel, R. Neveling, V. Yu. Ponomarev, A. Richter, E. Sideras-Haddad, F. D. Smit, and J. Wambach, Phys. Rev. **C 79** (2009) 044305.

[Sho62] K. Shoda, K. Abe, T. Ishizuka, N. Kawamura, and M. Kimura, J. Phys. Soc. Jpn. **17** (1962) 35.

[Sol92] V. G. Soloviev and V. I. Kisin, *Theory of Atomic Nuclei: Quasi-particles and Phonons*, IOP Publishing, Bristol (1992).

[Spe91] J. Speth and J. Wambach. *International Review of Nuclear Physics: Electric and Magnetic Giant Resonances in Nuclei*, Vol. 7, World Scientic, New Jersey (1991).

[Ste50] H. Steinwedel and J. H. D. Jensen, Phys. Rev. **79** (1950) 1019.

[Str98] S. Strauch, Doctoral thesis D17, TU Darmstadt (1998).

[Tam11] A. Tamii, I. Poltoratska, P. von Neumann-Cosel, Y. Fujita, T. Adachi, C. A. Bertulani, J. Carter, M. Dozono, H. Fujita, K. Fujita, K. Hatanaka, D. Ishikawa, M. Itoh, T. Kawabata, Y. Kalmykov, A. M. Krumbholz, E. Litvinova, H. Matsubara, K. Nakanishi, R. Neveling, H. Okamura, H. J. Ong, B. Özel-Tashenov, V. Yu. Ponomarev, A. Richter, B. Rubio, H. Sakaguchi, Y. Sakemi, Y. Sasamoto, Y. Shimbara, Y. Shimizu, F. D. Smit, T. Suzuki, Y. Tameshige, J. Wambach, R. Yamada, M. Yosoi, and J. Zenihiro, Phys. Rev. Lett. **107** (2011) 062502.

[TDC] CAEN, Model V1190A, 128 Channel Multi-event Time-to-Digital Converter.

[TechNo] Technoland Corporation, Model P-TM 005, 16 Channel Preamplier and Discriminator Card.

[Teo98] A. Teolis, *Computational signal processing with wavelets*, Birkhäuser (1998).

[Tof10] H. K. Toft, A. C. Larsen, U. Agvaanluvsan, A. Bürger, M. Guttormsen, G. E. Mitchell, H. T. Nyhus, A. Schiller, S. Siem, N. U. H. Syed, and A. Voinov, arXiv: 1006.4781v1 [nucl-ex] (2010).

[Var03] V. V. Varlamov, M. E. Stepanov, and V. V. Chesnokov, Izvi. Rossiiskoi Akademii Nauk, Ser. Fiz. **67** (2003) 656.

[Usm09] I. Usman, Doctoral thesis, University of the Witwatersrand, (2009).

[Vey70] A. Veyssiere, H. Beil, R. Bergre, P Carlos, and A. Lepretre, Nucl. Phys. **A 159** (1970) 561.

[Vey74] A. Veyssiere, H. Beil, R. Bergere, P. Carlos, A. Lepretre, and A. De Miniac, Nucl. Phys. **A 227** (1974) 513.

[Von69] H. Vonach and M. Hille, Nucl. Phys. **A 127** (1969) 289.

[VRA] V. Vrankovic and D. George, Program TRACK V8.6c, Paul Scherrer Institute, http://magnet.web.psi.ch/Analysis/track.html.

[Wei34] C. F. Weizsäcker, Z. Phys. **88** (1934) 612.

[Wei35] C. F. Weizsäcker, Z. Phys. **96** (1935) 431.

[Wig65] E. P. Wigner and C. E. Porter (Ed), *Statistical Theories of Spectra: Fluctuations*, Academic Press, New York (1965).

[Wil34] E. J. Williams, Phys. Rev. **45** (1934) 729.

[Win79] A. Winther and K. Alder, Nucl. Phys. **A 319** (1979) 518.

[Won90] S. M. Wong, *Introductory Nuclear Physics*, Prentice Hall, New Jersey (1990).